



Delft University of Technology

## Towards activity descriptors for the methane dehydroaromatization catalyst Mo/HZSM-

Vollmer, Ina

**DOI**

[10.4233/uuid:96989fc0-eafb-40c2-a622-f9f1a71faa29](https://doi.org/10.4233/uuid:96989fc0-eafb-40c2-a622-f9f1a71faa29)

**Publication date**

2019

**Document Version**

Final published version

**Citation (APA)**

Vollmer, I. (2019). *Towards activity descriptors for the methane dehydroaromatization catalyst Mo/HZSM- [Dissertation (TU Delft), Delft University of Technology]*. <https://doi.org/10.4233/uuid:96989fc0-eafb-40c2-a622-f9f1a71faa29>

**Important note**

To cite this publication, please use the final published version (if applicable).  
Please check the document version above.

**Copyright**

Other than for strictly personal use, it is not permitted to download, forward or distribute the text or part of it, without the consent of the author(s) and/or copyright holder(s), unless the work is under an open content license such as Creative Commons.

**Takedown policy**

Please contact us and provide details if you believe this document breaches copyrights.  
We will remove access to the work immediately and investigate your claim.

# **Towards activity descriptors for the methane dehydroaromatization catalyst Mo/HZSM-5**

**Ina VOLLMER**



# **Towards activity descriptors for the methane dehydroaromatization catalyst Mo/HZSM-5**

Dissertation

for the purpose of obtaining the degree of doctor  
at Delft University of Technology,  
by the authority of the Rector Magnificus prof.dr.ir. T.H.J.J. van der Hagen,  
chair of the Board of Doctorates,  
to be defended publicly on  
Monday 11 March 2019 at 15:00 o'clock

by

**Ina VOLLMER**

Master of Science in Chemical Engineering Practice, Massachusetts Institute  
of Technology (Massachusetts), United States of America

born in Freiburg im Breisgau, Baden-Württemberg, Germany

This dissertation has been approved by the promoters.

Composition of the doctoral committee:

Rector Magnificus	chairperson
Prof. dr. F. Kapteijn	Delft University of Technology, promotor
Prof. dr. J. Gascon Sabate	Delft University of Technology and King Abdullah University of Science and Technology, promotor

Independent members:

Prof. dr. E.J.R. Sudhölter	Delft University of Technology
Prof. dr. ir. J.R. van Ommen	Delft University of Technology
Prof. dr. J. Dedecek	J. Heyrovsky Institute
Prof. dr. ir. B.F. Sels	KU Leuven
Dr.-Ing. C. Dittrich	SABIC Geleen

The research presented in this thesis was performed at the Catalysis Engineering section of the Chemical Engineering at the faculty of Applied Sciences of Delft University of Technology. The research was funded by the Nederlandse Organisatie voor Wetenschappelijk Onderzoek and SABIC (NWO-731.014.302).

Dissertation, Delft University of Technology

With summary in Dutch

ISBN: 978-94-028-1396-8

Cover design: Ina Vollmer

Printed by Ipskamp Printing, Enschede

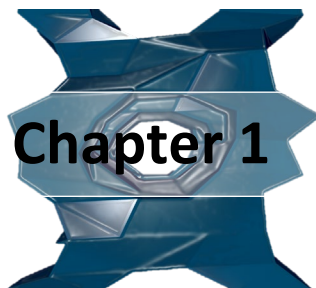
© 2019 Ina Vollmer

All rights reserved

*To my family*

## Table of Contents

<b>Chapter 1</b>	<b>Progress in developing a structure-activity-relationship for the direct aromatization of methane</b>	<b>1</b>
<b>Chapter 2</b>	<b>Relevance of the Mo-precursor state in H-ZSM-5 for Methane dehydroaromatization</b>	<b>41</b>
	<b>Annex chapter 2</b>	<b>59</b>
<b>Chapter 3</b>	<b>Quantifying the impact of dispersion, acidity and porosity of Mo/HZSM-5 on the performance in methane dehydroaromatization</b>	<b>79</b>
	<b>Annex chapter 3</b>	<b>103</b>
<b>Chapter 4</b>	<b>On the dynamic nature of Mo sites for methane dehydroaromatization</b>	<b>137</b>
	<b>Annex chapter 4</b>	<b>163</b>
<b>Chapter 5</b>	<b>A site-sensitive <i>quasi-in situ</i> strategy to characterize Mo/HZSM-5 during activation</b>	<b>197</b>
	<b>Annex chapter 5</b>	<b>227</b>
	<b>Summary and Outlook</b>	<b>243</b>
	<b>Samenvatting en vooruitblik</b>	<b>253</b>
	<b>Acknowledgements</b>	<b>263</b>
	<b>List of Publications</b>	<b>267</b>
	<b>About the Author</b>	<b>270</b>



---

**Progress in developing a structure-activity-  
relationship for the direct aromatization of  
methane**

---

To secure future supply of aromatics, methane is a commercially interesting alternative feedstock. Direct conversion of methane into aromatics combines the challenge of activating one of the strongest C-H bonds in all hydrocarbons with the selective aromatization over zeolites. To address these challenges, smart catalyst and process design are a must. And for that, understanding the most important factors leading to successful methane C-H bond activation and selective aromatization is needed. In this review, we summarize mechanistic insight that has been gained so far not only for this reaction, but also for other similar processes involving aromatization reactions over zeolites. With that, we highlight what can be learnt from similar processes. In addition, we provide an overview of characterization tools and strategies, which are useful to gain structural information about this particular metal-zeolite system at reaction conditions. Here we also aim to inspire future characterization work, by giving an outlook on characterization strategies that have not yet been applied for the methane dehydroaromatization catalyst, but are promising for this system.

---

This chapter is based on the following publication:  
Vollmer, I.; Yarulina I.; Kapteijn F.; Gascon J., (2019) "Progress in developing a structure-activity-relationship for the direct aromatization of methane." *ChemCatChem* **11** 39-52.  
*doi: 10.1002/cctc.201800880*

## 1.1 General Introduction

As the main building block of polystyrene and numerous consumer goods, such as pharmaceuticals, aromatics are essential to modern life. At the moment the main source of benzene, toluene and xylene (BTX) is steam-reforming of naphtha, but especially in North America naphtha is more and more replaced by shale gas liquids as a cheaper cracking feedstock for olefin production and this process does not yield aromatics [1]. There is high interest in using methane as an alternative feedstock to produce aromatics, because of its high availability from shale gas and clathrates [2]. Methane is an attractive feedstock also because 3.5 % of the global production of natural gas is currently flared as a by-product of crude oil facilities, because it cannot be utilized on-site due to a lack of convenient technology that is applicable on a small scale [3]. This represents a great economic opportunity. Utilizing instead of burning flare gas has the added environmental benefit of avoiding CO<sub>2</sub> emissions.

Methane however is hard to activate and is currently used mostly as an energy source, because of its high C-H bond energy of 104 kcal/mol. Indirect valorization of methane is possible via the syngas route, but requires many process steps. The direct aromatization of methane without addition of oxidants has gained interest since it was shown to be feasible first by Bragin and later Wang *et al* [4, 5]. It presents an alternative to the indirect valorization of methane via the syngas route, potentially applicable on a smaller scale and overall advantageous since it requires less process steps. Many challenges need to be overcome before this process can be commercialized. The reaction of methane to benzene and hydrogen is hampered by thermodynamics with  $\Delta G_r^0 = +104 \text{ kcal mol}^{-1}$  and  $\Delta H_r^0 = +127 \text{ kcal mol}^{-1}$  [6-8]. At the temperatures at which this reaction produces interesting yields of benzene (7.8 - 21.5 mol%), typically between 650 and 800 °C, coke formation experiences no such thermodynamic limitations leading to fast deactivation of the catalyst [6, 7]. Mo/HZSM-5, molybdenum (Mo) supported on an MFI zeolite remains the most investigated Methane Dehydroaromatization (MDA) catalyst to date, because of its superior performance [9, 10]. Both different metals[11, 12] and other supports[13] have not yielded improvements over this system. More insight into the mechanism and into the exact role and function of the metal active site are key to further improve this catalyst.

The many possible reaction mechanisms proposed for MDA have not yet converged to a common agreement [4, 5]. The number of pathways to consider is similarly unwieldy as in other reactions involving zeolites like the M2 process (aromatization of light hydrocarbons) and fluid catalytic cracking [14, 15]. Similarities can also be expected with the Methanol to Hydrocarbons (MTH) process, for which a hydrocarbon pool mechanism is widely accepted [16-25]. Indeed a hydrocarbon pool was recently also proposed to play a crucial role in MDA, although it was suggested to proceed via aromatic radicals instead of carbocations [26]. A series of dehydrogenation, cracking, isomerization, oligomerization, dehydrocyclization,  $\beta$ -scission, protolysis and hydride transfer reactions has to be considered [27]. Karakaya *et al.* in one of the few attempts to try to model this complex reaction network used 50 reaction steps and these did not even include pathways to carbonaceous deposits [28]. Kinetic modelling is also complicated by the fact that steady state conditions are never really reached during MDA, because of fast coking.

There is some consensus however, that the process has an activation period and proceeds via a two-step mechanism. A few transition metals are active for MDA, of which Mo was reported to be the most active [11, 12]. Mo species transform to an active phase during an initial period of the reaction where no desired products are observed [29-35]. The structure of this reduced active site is not yet fully revealed. Because the active phase of Mo forms at reaction conditions, characterization of the sites present and identification of the sites responsible for catalysis is difficult. A lot of publications agree that once the active site is formed, the reaction proceeds via a two-step mechanism on the bifunctional catalyst Mo/HZSM-5 [35-38]. According to this two-step mechanism methane is first activated on the Mo active site to form C<sub>2</sub> intermediates (ethane, ethylene or acetylene), which are then further dehydrocyclized to benzene and other aromatics on the Brønsted acid sites (BASs) of the zeolite. In the first part of this review, we will summarize the potential structures of the active site along with characterization techniques and strategies that can be applied to better understand this system at reaction conditions. In this part, we will also discuss proposed mechanisms for the C-H bond activation of methane on the active site.

The second part of the review focusses on the reaction steps following methane activation. The most mentioned

intermediates are ethylene and acetylene. Therefore, this part of the review is devoted to aromatization reactions of these two hydrocarbons and compares what has been reported for these reactions with observations about MDA. The catalytic role of the BAS on the catalyst will be at the center of this discussion. To summarize this part, we will discuss the two-step mechanism as a proposed reaction mechanism and address the question of whether it is possible to separate the two functions of the bifunctional catalyst.

## 1.2 Metal active site

Activation of methane is achieved over a transition metal supported on a zeolite, where the transition metal ion (TMI) anchors to the framework Al through oxygen, replacing the proton of the BAS.

The BAS itself can only very slowly activate methane, which was shown by feeding methane to bare HZSM-5[39, 40] and by CD<sub>4</sub> exchange with HZSM-5 to form CD<sub>3</sub>H [41]. Although the exchange of OH with D<sub>2</sub> was shown to be enhanced when Mo is present on HZSM-5, this activation still happens far too slow to play a major role in the mechanism of methane C-H bond activation [42]. To understand how methane interacts with the metal active site during activation, knowledge about the structure, nuclearity and oxidation state of the active site is crucial.

### 1.2.1 Understanding the structure of the metal site

Several TMIs are reported to be active for MDA. These TMIs, summarized in **Table 1.1.1**, can be separated into two categories: The first category comprises Mo, W, Fe, V, Cr, Re and Mn, which experience an activation period during which the TMI is reduced and most likely carburized to its active phase; for the second category, made up of Zn, In and Ag the active phase is reported to be a cation acting as a proton abstraction site. It has to be noted however that Ag and In were only reported to convert methane in the presence of ethylene. The most investigated metal for MDA is Mo, because of its superior activity, while almost no structural characterization is reported for other metals showing activity for MDA [12]. We will therefore focus on Mo specifically in the following although similar trends can also be expected for the other TMIs in the first category. Mo is present as an oxide on the as-synthesized catalyst. This catalyst pre-cursor

has received much research attention, which was reviewed earlier [9, 10, 43-48].

Table 1.1. Overview of transition metal ions supported on ZSM-5 used as a catalyst for MDA and their reported active phase.

Cation	Proposed active phase	
<b>Mo</b>	MoC, Mo <sub>2</sub> C, coke modified Mo <sub>2</sub> C[49], Mo <sub>2</sub> C[31, 50] on the outer surface and reduced oxides in the pores of the zeolite, any kind of Mo <sup>6+</sup> and partially reduced Mo <sup>6+</sup> as MoO <sub>(3-x)</sub> [43, 51].	Two-step mechanism[35-38]
<b>W</b>	Reduced with evolution of CO, CO <sub>2</sub> and H <sub>2</sub> O during activation[12]	
<b>Fe</b>	Reduced with evolution of CO, CO <sub>2</sub> and H <sub>2</sub> O during activation [12], carbide[52]	
<b>V</b>	Reduced with evolution of CO, CO <sub>2</sub> and H <sub>2</sub> O during activation[12]	
<b>Cr</b>	Reduced with evolution of CO, CO <sub>2</sub> and H <sub>2</sub> O during activation[12]	
<b>Re</b>	Metallic Re forming with evolution of CO, CO <sub>2</sub> and H <sub>2</sub> O[53]	
<b>Mn</b>	Carbide[54]	
<b>Zn</b>	Zn <sup>2+</sup> , Nano-ZnO[55-59]	Methoxy species pathway, where H is abstracted by Zn[55-59]
<b>Ag<sup>b</sup></b>	Ag <sup>+</sup> [55, 60, 61]	Methoxy species pathway, where H is abstracted by Ag[55, 60, 61]
<b>In<sup>a</sup></b>	InO <sup>+</sup> [62]	Methoxy species pathway, where H is abstracted by In[62]

<sup>a</sup>Conversion of CH<sub>4</sub> is only observed in the presence of ethylene

<sup>b</sup> significant conversion of CH<sub>4</sub> is only observed in the presence of ethylene or ethane

The as-synthesized oxidic Mo was shown to reduce to its active form in an initial period of the reaction where no gaseous hydrocarbons are formed yet [29-35]. It is poorly understood how the Mo precursor state influences the state of Mo at reaction conditions [63]. It is for instance conceivable that the Mo loses its ability to anchor to the zeolite framework, when it is being reduced [64, 65]. It is however commonly agreed that a better initial Mo dispersion leads to a more stable catalyst producing higher yields of benzene and naphthalene [66]. Therefore, the state of the catalyst pre-cursor has at least some influence on the active, reduced Mo phase formed at reaction conditions. For example, the Mo pre-cursor state can have an influence on its reducibility and its propensity to cluster or even form nanoparticles at reaction conditions.

The information listed below is needed to fully characterize the active site and to build up structure-activity relationships:

- Metal-support interaction: does the Mo detach from the zeolite during activation?
- Dispersion
- Location
- Nuclearity
- Stoichiometry (including heteroatoms)
- Geometry
- Charge

But characterizing the metal-zeolite system for MDA is highly challenging:

1) The metal pre-cursor takes on numerous configurations when supported on the zeolite, which leads to complicated and broadened signals for most spectroscopic techniques.

2) It is not the as-synthesized catalyst that is active, but the active site forms at reaction conditions, thus necessitating *operando* characterization techniques.

3) The characterization is further complicated by heavy coking in all stages of activation of the catalyst and during the reaction.

4) Not only the metal in the pre-catalyst can adopt different configurations, it is also not clear whether all the TMI transform to active sites and it is therefore difficult to distinguish between spectators and active sites. These aspects have hampered elucidation of the exact structure of the active sites present on the catalyst for MDA and understanding about which of the many possible structures are responsible for catalysis. The first three of

these complications are addressed below with ways to circumvent them and obtain information regarding the aspects listed above.

### 1.2.2 Inhomogeneity

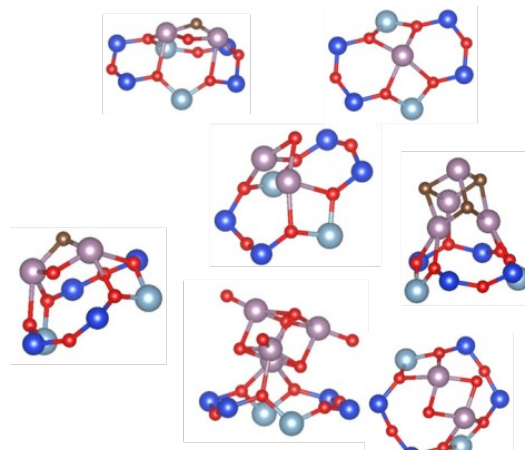


Figure 1.1. Various possible structures of (oxy-)carbidic Mo sites anchored on the HZSM-5 zeolite. Colors correspond to atom types (Mo: purple, Si: blue, Al: turquoise, O: red, C: brown).

This part aims to highlight the characterization difficulties that stem from the fact that Mo is present in varying nuclearity, oxidation state and geometry and how to overcome those challenges. The Mo/HZSM-5 system is compared to two well-known types of catalysts, the supported nanoparticle catalyst and the supported metal-organic catalyst to show that it belongs to neither category, but that inspiration for characterization techniques can be drawn especially from the latter category. Here we make a distinction between Mo species anchored to the zeolite inside the pores and bigger Mo species on the outer surface of the zeolite particles. The anchoring of Mo to the zeolite framework leads to different possible geometries and complicates spectroscopic characterization. The presence of bigger Mo species on the outer surface perturbs the signal for bulk characterization techniques. We discuss ways to address these two issues and provide a summary of techniques that can be applied to avoid bigger Mo clusters during the synthesis.

For a long time, the classical view of a heterogeneous catalyst involved an oxide support with nanoparticles of the active metal [67, 68]. The other extreme is a well-defined, usually monomeric

immobilized organometallic complex [69-72]. On zeolite supports, both bigger metal clusters and even nanoparticles[64] as well as mono-[65] or dimeric[73] sites coexist (see **Figure 1.1** for some examples). In recent years, a lot of work has moved towards single-site catalysts [74]. For MDA, this is reflected by the fact that reported metal loadings decreased over the years. Early studies reported metal loadings up to 10 wt.%, which represents a molar metal/Al ratio far above one, meaning that a large part of the metal cannot effectively be anchored to the zeolite and has to be present as bigger clusters. This represents the classical view of a nanoparticle supported on a support, where BAS were not yet valued for their anchoring role, but solely as an active site for the aromatization reactions. Later studies found that a loading of around 2 to 4 wt.%, depending on the Al content of the zeolite shows the highest activity per metal atom while most of the coke is formed on bulk Mo oxide, aluminium molybdate and other extra-framework species [35, 36, 75-77]. The metal to Al ratio at which anchoring to the framework Al is still effective seems to be far below one for most zeolites. The anchoring capacity of the zeolite has been investigated mostly for the oxidic catalyst pre-cursor. By combining XPS, TPO and UV Raman, Lim *et al.* showed that the amount of bulk surface Mo oxide species decreases with decreasing the Si/Al ratio thereby increasing the BAS density, Mo dispersion being proportional to the amount of BAS [75, 78]. Consequently, the highest benzene formation and the lowest deactivation rates were obtained over the catalyst with the highest amount of acid sites.

In some sense, the metal-zeolite system is comparable to *e.g.* an organometallic complex grafted on silica, where silanol OH groups serve as the anchor, while an acidic OH group serves this purpose on a zeolite [79]. Many studies suggest that only the Mo species anchored to the framework Al through oxygen bridges are actually able to activate methane [26, 65, 79]. This is consistent with what has been proposed for the methane to methanol reaction[80, 81] and for SCR of N<sub>2</sub>O [82].

Part of the metal is present as well-defined species and for those species some characterization techniques useful for supported organometallic compounds can be insightful for the metal on HZSM-5 system as well [69, 83]. Both CO FTIR and <sup>13</sup>C MAS NMR are often used to characterize metal-organics supported on silica. CO FTIR can distinguish between mono- or dimeric and species and bigger clusters. CO adsorbs only on the

reduced Mo species after activation [84, 85]. With FTIR distinct vibrations for different Mo sites present in the zeolite can be observed after activation of those sites has been completed [86, 87]. Using this technique combined with theory, information about the oxidation state as well as nuclearity of the reduced Mo can be gained for this system [85]. The chemical shift of  $^{13}\text{C}$  MAS NMR and its anisotropy can yield information about carbidic Mo species forming at reaction conditions, but often the signal is dominated by a big contribution from carbonaceous deposits [88-91]. We recently demonstrated that CO pre-treatment results in an active site equivalent to the one formed at reaction conditions, but without the presence of any carbonaceous deposits [92]. High resolution  $^{13}\text{C}$  MAS NMR then revealed three different carbidic resonances: a sharp one stemming from  $\text{Mo}_2\text{C}$  nanoparticles on the outer surface of the zeolite and two broad resonances corresponding to smaller species inside the pores of the zeolite. However, the interpretation of the spectra obtained for metal-zeolite systems compared to the ones obtained for supported metalorganics is much more complicated. This is because, in contrast to the metalorganic system, for Mo/HZSM-5 the anchoring zeolite OH groups are not uniform, but in different local geometries depending on the location of the framework Al inside the pores and cages of the material. It is likely that the confinement effect of the zeolite also stabilizes mono- and dimeric species at the OH-groups inside the porous structure of the zeolite [83]. Because of this, they can direct the cation to take on many different geometries [63]. This complicates characterization further, because it leads to rather broad contributions for spectroscopic techniques that probe the metal directly like EPR,[93]  $^{95}\text{Mo}$  NMR,[94] UV-Vis,[65, 66, 95] XAS,[96] UV-Raman[78, 97] and XPS[6, 98].

In addition, synthesis of a zeolite catalyst with perfect dispersion of the metal is still a challenge, and bigger clusters, especially at the external surface of the zeolite, are almost always present. They often dominate the signal in bulk spectroscopic techniques. Therefore, a way to avoid bigger clusters on the external surface could lead to a lot of insight about the active site. Silanation of the external BASs of the zeolite prior to Mo incorporation is one way to mitigate their formation [99]. This was found to increase the selectivity to products and slow down coking. For other metals, using chemical vapor deposition (CVD) techniques or cation exchange to incorporate the metal leads to

better dispersion compared to the predominantly used solid ion exchange (SIE) and Incipient Wetness Impregnation (IWI) [83, 100]. CVD was performed for MDA using  $\text{WCl}_6$ , but it is not known, if this improved the dispersion of the metal, because the catalyst synthesized this way was not compared to a catalyst prepared with the conventional method of IWI [73]. For zeolites with bigger cages,  $\text{Mo}(\text{CO})_6$  is often incorporated into the zeolite through CVD [101, 102]. Regulating pH level of the solution for impregnation[103, 104] or changing the atmosphere during calcination also influences metal dispersion [105].

A couple of indirect methods are available to characterize the dispersion of the metal, probing how many acid sites are replaced by a metal. This was effectively achieved by H/D exchange,[42, 73, 79]  $^1\text{H}$  NMR,[26, 106]  $^{27}\text{Al}$  NMR,[106]  $\text{NH}_3$ -TPD[56, 75, 107, 108] and probing adsorbed molecules by FTIR[39, 109].  $\text{CH}_4$ -TPR[110] and  $\text{H}_2$ -TPR[111] were also used to study the ease of reduction of the Mo species present on the zeolite. Reduction at lower temperatures is an indication of the presence of big Mo oxide clusters on the outer surface of the zeolite. Dispersion of Mo seems to be the most important factor for an active catalyst. A catalyst with Mo present only as mono- and dimeric species that do not cluster at reaction conditions has not been synthesized yet.

Understanding which sites are present on the catalyst is challenging, firstly because nanoparticles on the outer surface of the zeolite dominate the signal in bulk characterization techniques, and secondly because even the species in the pores of the zeolite can take on different geometries and nuclearities. It is clear that many sites coexist on the (pre-)catalyst and it is likely that only a fraction of them is actually responsible for all the catalysis [70, 112].

### 1.2.3 Operando is key

The as-synthesized oxidic Mo was shown to reduce to its active form in an initial period of the reaction where no gaseous hydrocarbon products are formed yet [29-35]. A variety of species have been observed on the catalyst at reaction conditions or after reaction and were proposed as active sites:  $\text{MoC}$ ,  $\text{Mo}_2\text{C}$ , coke modified  $\text{Mo}_2\text{C}$ [49],  $\text{Mo}_2\text{C}$ [31, 50] on the outside surface and reduced oxides in the pores of the zeolite, any kind of  $\text{Mo}^{6+}$  and partially reduced  $\text{Mo}^{6+}$  as  $\text{MoO}_{(3-x)}$  [43, 51]. Characterizing these carbidic species poses challenges, since many characterization techniques that are powerful in elucidating

oxides, like UV-Vis and UV-Raman cannot provide information about the reduced species. In addition, since the active species form at reaction conditions, *operando* characterization is necessary to spot them. It was by *operando* X-ray Absorption Spectroscopy (XAS) studies that the evolution of the Mo oxidation state during activation was first confirmed [26, 30, 92]. Another issue relates to the time-resolution. Depending on the Mo loading, the activation period can be rather short. Therefore experiments need to be designed carefully to properly follow the evolution of the active phase. This has been achieved by using a pulsed reaction technique [26, 29]. This powerful technique also in combination with *quasi-in-situ* studies enables the preparation of samples during particular phases of active site formation and allows studying the development of the active site with a variety of techniques [26, 92]. Next to XPS, NMR and EPR, FTIR spectroscopy using adsorbed probe molecules can characterize the oxidation state and even nuclearity of the reduced Mo [26, 87, 113]. In addition to a reduction, the Mo was proposed to also undergo clustering [65]. Bigger Mo clusters were observed on the outer surface of the catalyst after reaction,[64] but it is unclear if this Mo was already present as bigger clusters on the as-synthesized catalyst. To observe the clustering *operando* TEM could be performed [114]. However, zeolite samples are very sensitive to electron beam exposure and low dose imaging techniques are necessary[115, 116] not to damage the zeolite for the duration of an MDA experiment. Further, it remains to be determined if bigger Mo clusters also form inside the pores of the zeolite and whether these carbide clusters can activate methane.

#### 1.2.4 Coking

Another factor that complicates elucidation of the metal sites present, is the formation of carbonaceous deposits during the formation of the active site. This makes it difficult to probe the metal-support interaction at reaction conditions and also leads to a darkening of the sample, leading to a small signal of vibrational spectroscopy techniques. Knowing whether Mo detaches from the framework Al or stays anchored during initial reduction, limits the number of possible structures one has to consider in reconstructing the geometry of the metal site. On the as-synthesized catalyst, the interaction of the metal with the support can be probed indirectly by measuring acidity. This can be done using H/D exchange[42, 73, 79], <sup>1</sup>H NMR[117], <sup>27</sup>Al NMR[106, 118], NH<sub>3</sub>-TPD[56, 75, 107, 108] and probing

adsorbed molecules by FTIR[39, 109], but this is not possible when coke is also responsible for a loss in acidity. One cannot distinguish between a loss of acidity due to carbonaceous deposits and due to a metal replacing the acidic proton. We recently found that the formation of carbonaceous deposits during activation can be avoided using a treatment in CO to reduce Mo to its active phase. This treatment creates an active site equivalent to the one forming during regular MDA operation [92]. This technique has potential for studying the metal support interaction at reaction conditions without interference from aromatics.

**Table 1.2** summarizes the key information that is needed to fully characterize the Mo/HZSM-5 at reaction conditions, the characterization techniques that can be applied to obtain this information as well as their limitations. It can be concluded that most of the individual characterization techniques are insufficient to obtain a complete picture, but in combination and also in combination with theoretical calculations they yield a good description.

Table 1.2: Information that can be gained using different spectroscopic techniques and the difficulties encountered using them to characterize the Mo/HZSM-5 system.

Type of information	Spectroscopic Techniques	Difficulties
Metal-support interaction: does the Mo detach from the zeolite during activation?	Indirect methods probing acidity: H/D exchange,[42, 73, 79] $^1\text{H}$ NMR,[117] Al NMR,[106, 118] $\text{NH}_3$ -TPD[56, 75, 107, 108] and probing adsorbed molecules by FTIR,[39, 109]	Acid sites partly blocked by coke, which forms together with the transformation of Mo to its active phase
Dispersion		
Location		
Nuclearity	UV-Vis,[65, 66, 95] UV-Raman[78, 97, 106]	Difficult to get information on reduced/carbidic structures
	$^{13}\text{C}$ NMR	Signal rather broad
	Probing adsorbed molecules by FTIR[86, 87]	Only indirect information from full width at half maximum and together

		with theoretical calculation. Access can be blocked by coke
	H <sub>2</sub> -TPR[111]	Indirect method, nuclearity has to be inferred from reducibility
Stoichiometry	<sup>13</sup> C NMR, DNP <sup>13</sup> C NMR	Signal rather broad
	Information about removed oxygen: Temperature programmed reaction using CH <sub>4</sub> [110]	There will not only be carbidic carbon deposition but also carbonaceous carbon
	Information about deposited carbon: Temperature programmed reaction using CO	
Geometry	XANES[30, 39, 96]	Bulk technique, only an average over many structures is observed
	EXAFS[30, 39]	No long range structure for well dispersed species, only bulk Mo <sub>2</sub> C observed
Charge	XANES[30, 39, 70]	Bulk technique, only an average over many structures is observed
	EPR[93]	Only information about paramagnetic species
	XPS[6, 98]	Surface sensitive, only information about the surface is obtained
	Probing adsorbed molecules by FTIR[85, 119]	Only useful in combination with references or theoretical calculations

### 1.3 C-H bond activation

Various mechanisms by which the metal on the MDA catalyst activates methane are put forward, but uncertainty remains. It is however, crucial to know how the activation proceeds to design a better catalytic systems. One area of debate is whether hydrogen abstraction occurs only on the metal site or with the help of the BAS.

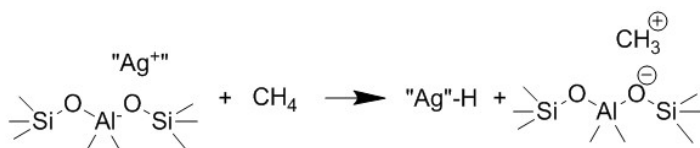


Figure 1.2. Mechanism of C-H bond activation proposed for Ag/HZSM-5, where the Ag Lewis acid site serves to abstract the proton from CH<sub>4</sub>. The resulting CH<sub>3</sub><sup>+</sup> forms an alkoxy-species with the oxygen from the BAS [55].

It is also not clear whether an adsorbed CH<sub>3</sub><sup>+</sup> species stays adsorbed on the active site and then further reacts with an incoming CH<sub>4</sub> or whether a CH<sub>3</sub>• radical is released immediately after H is abstracted and further reaction proceeds in the gas phase.

For TMIs which form carbidic species at reaction conditions, CH<sub>x</sub> species could also first form through reaction of H<sub>2</sub> with the carbidic carbon and then further react with incoming CH<sub>4</sub>. These possible pathways will be discussed below.

It has been proposed for Ag that the cationic species act as a Lewis acid that is able to abstract hydrogen from methane, while methane forms a methoxy-species with the BAS (**Figure 1.2**) [60]. A similar mechanism was proposed for In[62] and Zn[56]. The work by Kosinov et al. also underlines that both functionalities need to be in close proximity. They discovered that the bifunctional Mo/HZSM-5 cannot be separated into two catalysts, one carrying the Mo functionality and one carrying the BAS [120]. In contrast, for Ta grafted on silica, both CH<sub>3</sub> and H were proposed to coordinate to the metal, where the methyl species then dimerizes when a second CH<sub>4</sub> binds to Ta [121].

For Mo, most literature agrees that Mo first needs to be reduced (between 6+ and 4+) to be able to activate methane [29-34]. Theoretical calculations for methane activation have been performed on fully carbidic Mo clusters,[122] where methane adsorbs on the reduced Mo. In its carbidic form Mo has an electronic structure similar to that of noble metals and Mo carbide was also observed to behave similar to precious metals in

several reactions [123-125]. This would mean that the carbon serves merely to alter the electronic structure of Mo. In contrast to that, we recently found that the carbon that is present at the active site itself plays an important role in activating methane equivalent to oxygen in the Mars-van-Krevelen mechanism [126]. This is indicated by the fact that the carbon from the active site was found to be incorporated into the final products [92]. In the iron catalysed Fischer-Tropsch synthesis, iron carbide initiates the hydrocarbon chain growth[127, 128] and a similar mechanism can be envisaged for MDA. Both DFT studies and experimental work suggest that CH<sub>2</sub> fragments can easily be formed by reaction of the carbon from the active site with gas phase hydrogen [129].

It is conceivable that W and Fe behave similarly to Mo and that their active forms have similar structures, since they also exhibit an induction period and were shown to form carbidic phases at reaction conditions [12, 52, 73].

### 1.3 C2 intermediates

In this part, the assumption that C2 hydrocarbons are the main intermediates for the MDA reaction and which of ethane, ethylene or acetylene is the most likely C2 intermediate will be discussed. Activation of the C-H bond in methane is slow and difficult, but as soon as the first C-C bond is formed, further reaction becomes much easier, because C2 hydrocarbons are far more reactive than methane. At the same time, aromatics are thermodynamically more stable and are therefore observed as final products of the process. For these reasons, ethylene, ethane and acetylene have been proposed as the main reaction intermediates for MDA. For MTH, a reaction that shows many parallels with MDA, ethylene is often mentioned to be the main intermediate as well [130].

Ethylene and ethane are observed as final products of the reaction, while acetylene is not, likely because of its high reactivity. Wang et al. noted that the selectivity to ethylene increases when the contact time of CH<sub>4</sub> with Mo/ZSM-5 is shortened, demonstrating that the formation of ethylene is fast compared to the formation of aromatic products [32]. In addition, Wang et al. did not observe an activation period when feeding C<sub>2</sub>H<sub>4</sub> to Mo/HZSM-5.

Both ethylene as well as acetylene were shown to immediately oligomerize with near to 100% conversion when

contacted with a zeolite even at 300 °C,[131] while ethane reacts more slowly [132]. With both reactants, deactivation of the catalyst due to coking is fast [132]. Although most often ethylene, ethane and acetylene are proposed as reaction intermediates, higher intermediates are conceivable as well, especially if ethylene strongly adsorbs on the active metal and has to further react with gas-phase CH<sub>4</sub> to desorb. This was speculated for Ag [60]. Studying adsorption strength of ethylene at the active site however is difficult, since the structure of the active site formed at reaction conditions is unknown. Obtaining information about the dominant reaction intermediate is important, because knowledge about it facilitates designing the zeolite as a separate entity before focusing on the metal. Especially in designing superior supports factors like acidity (i.e. Si/Al, location of Al) and morphology (i.e. hierarchical zeolites, nanosheets) are essential. The most mentioned and reactive intermediates, ethylene and acetylene are discussed below.

### 1.3.1 Ethylene aromatization

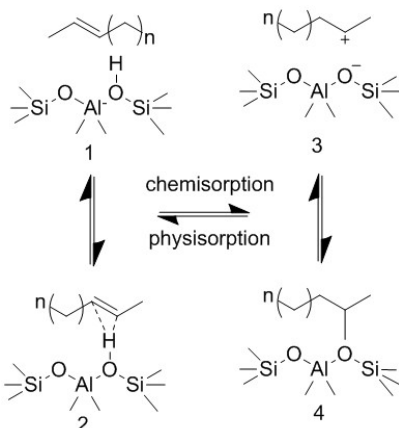


Figure 1.3. Four different modes of activation for an alkene – 1: Van der Waals complex, 2:  $\pi$ -complex, 3: carbenium ion, 4: alkoxide [133].

Ethylene aromatization easily occurs on the BAS of a zeolite. Four different possibilities for alkene activation are mentioned in the literature (**Figure 1.3**) [133]. But most papers assume that ethylene is activated by forming a carbocation (C<sub>2</sub>H<sub>5</sub><sup>+</sup>) with the help of the proton from the acid site [134]. Ethylene aromatization has been explored on HZSM-5 at 400 °C,[134, 135] 480 °C,[136] 500 °C[132, 137] and 540 °C[138] using very diluted streams of ethylene to slow down coking. Qiu et al. explored the

conversion of ethylene between 300 and 650 °C and found that the selectivity to aromatics increases with temperature [131]. However, only when introducing gallium (Ga) to the zeolite, immediate deactivation due to coking could be avoided at higher temperatures. When introducing metals into the zeolite, the proton at the BAS is replaced by the metal, thereby decreasing overall acidity, which leads to a lower activity, slower coking rates and with that a longer lifetime of the catalyst. But apart from slowing down coking, introducing a metal also increases the selectivity to aromatics, suggesting that the metal also plays a role in the aromatization steps [134, 135, 139].

The metal acts as a Lewis acid site (LAS) and its role is believed to be the abstraction of hydrogen. For Ga<sup>3+</sup> it was speculated that non-aromatic C4 and C6 are first formed on the BAS and then dehydrogenated on Ga<sup>3+</sup> to form aromatics [131]. Similarly, a DFT study revealed a lower activation energy for ethylene towards aromatics on BAS than on silver (Ag<sup>+</sup>), also suggesting that ethylene is first activated via the acidic proton and then dehydrocyclized on Ag<sup>+</sup> [134]. Interestingly, for methanol to aromatics (MTA), a linear relationship between Zn sites and aromatics selectivity was found for low loadings of Zn between 0.4 and 1.5 wt.% matching what was found for ethylene conversion [136, 140]. In contrast to this, when Zn is present as ZnO clusters at the mouth of the zeolite pores, it was suggested that it helps to expel hydrogen from the catalyst [141]. It was however also found that bigger ZnO clusters hydrogenate ethylene to ethane and therefore lower the aromatization activity [136]. For all metals an overall increase in ethylene conversion and aromatics selectivity was observed after introduction of the metal to HZSM-5, while even at 650 °C, the aromatics yield remained as low as 17 % on bare HZSM-5 [131].

### 1.3.2 Acetylene aromatization

Because of its high reactivity, the gas phase aromatization of acetylene over heterogeneous catalysts is hard to control and fast coking occurs even below 400 °C [142, 143]. The most recent report on this reaction investigated the effect of hierarchical zeolites at 700 °C, a temperature typically also applied for MDA [144]. A very diluted stream of acetylene was co-fed together with hydrogen and a BTX selectivity of up to 80 % was reached with benzene being the main product, and resembling the product distribution for MDA.

### 1.3.3 What is the most likely intermediate?

Mériaudeau et al. tried to determine what the dominant intermediate for MDA is, ethylene or rather acetylene [139, 145]. Acetylene, being the more reactive molecule, exhibited higher benzene formation rates than ethylene. They found that similar to Zn, Ga and Ag, the presence of Mo on HZSM-5 leads to four times higher benzene formation from ethylene than on the bare HZSM-5. Surprisingly, even Mo/SiO<sub>2</sub>, which possesses no BAS was much more active than H-ZSM-5 for benzene formation with a C<sub>2</sub>H<sub>4</sub>/H<sub>2</sub>/N<sub>2</sub> feed. Generally, when feeding ethylene, the selectivity to toluene (about the same as to benzene) seems to be higher than for MDA,[132] while the selectivity to toluene and benzene mimics those of MDA more closely for acetylene/H<sub>2</sub> mixtures [144]. Acetylene is not observed as a product of the MDA reaction, likely due to its high reactivity. It was also found that acetylene easily hydrogenates to ethylene in the presence of hydrogen, which can explain that ethylene is observed as a consecutive product [143]. Observing the intermediate at reaction conditions spectroscopically is very difficult and isotopic labelling studies only provide indirect information [146]. DFT studies of possible CH<sub>4</sub> dimerization pathways were attempted before, but are difficult to validate because of the lack of knowledge about the structure of the active site [147, 148]. Further insight on which C<sub>2</sub> hydrocarbon is the most likely intermediate can be gained from thermodynamic considerations. For this review, we investigated the thermodynamics of all three suggested intermediates, acetylene, ethylene and ethane using Aspen+ (**Figure 1.4**).

Excluding solid carbon, the following products were allowed to form: methane, naphthalene, benzene, toluene, propylene, propane, butylene, butane, pentane, the other C<sub>2</sub> hydrocarbons not defined as the reactant and hydrogen. The results for the three C<sub>2</sub> hydrocarbons were then compared to CH<sub>4</sub> conversion to the same products.

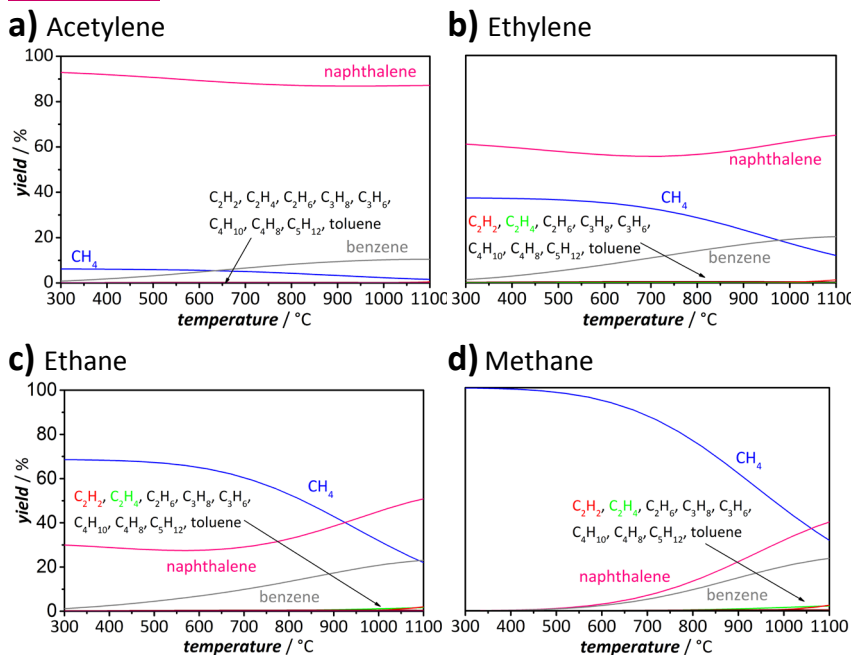


Figure 1.4. Equilibrium yields of methane, naphthalene, benzene, ethylene, acetylene, propylene, toluene, propane, pentane, butane, butylene and ethane with a) acetylene, b) ethylene, c) ethane and d) methane defined as reactant. Equilibrium concentrations were calculated using the *Aspen+* software.

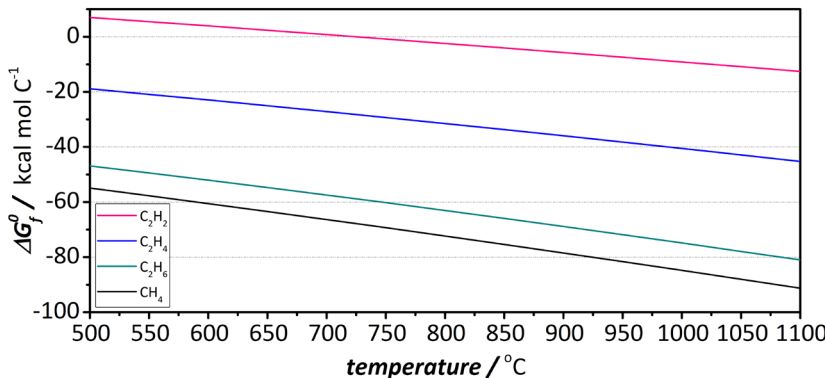


Figure 1.5. Standard Gibbs's free energy of formation of methane, acetylene, ethylene and ethane as a function of temperature, normalized by carbon number as obtained from the *HSC 6* database.

All three reactants form predominantly methane and naphthalene followed by benzene, all other products are formed in negligible amounts. This means that C2-C5 hydrocarbons, if observed during the catalytic tests are mostly kinetic products. The equilibria when acetylene, ethylene or ethane is defined as reactant only differ in the amount of methane and naphthalene formed, while benzene yields are fairly similar. **Figure 1.5** shows the standard Gibb's free energy of formation ( $\Delta G_f^0$ ) of methane, acetylene, ethylene and ethane as a function of temperature. The standard Gibb's free energy of reaction ( $\Delta G_r^0$ ) can be computed approximately from  $\Delta G_f^0$  using  $\Delta G_r^0 = \sum_B v_B \Delta G_f^0(B)$  [149]. The higher the hydrogen to carbon ratio of the C2 hydrocarbon, the more stable methane is compared to it and the reaction towards methane becomes more favourable (more negative  $\Delta G_r^0$ ). At the same time the propensity to form naphthalene decreases. As a consequence, the naphthalene to benzene ratio decreases with increasing H/C and is lowest, when pure methane is the reactant. The thermodynamic analysis shows that with all suggested intermediates naphthalene is the most dominant thermodynamic product followed by benzene. This provides an alternative explanation for why the aromatics selectivity increases upon introducing a metal to the zeolite. The metal acts to speed up the reaction and drive it more towards the thermodynamic product distribution.

#### 1.4 Topology, Brønsted acidity and the aromatization reactions

Shape selectivity and acidity are the two inherent properties of zeolites and the two main reasons of their vast utilization in catalysis [150]. Brønsted acidity in zeolites is represented by the proton counterbalancing the negative charge of the zeolite framework, created by substituting tetravalent Si by trivalent Al (or some other elements) [151]. Not only the amount of acid sites, but also their location and distribution are important parameters determining performance in zeolite catalysis [152]. In this paragraph we will discuss how they affect aromatization reactions.

There are many works dedicated to the effect of Brønsted acid site concentration on aromatization performance [10, 153]. Generally, Brønsted acid sites carry several functions. The first function is related to the dispersion of the active metal inside the zeolite micropores (vide supra). Only, if the metal is finely

dispersed inside the pores of the zeolite can it activate methane. It is generally recognized that the role of Mo species is to activate methane which results in C<sub>2</sub> formation, while the subsequent conversion of C<sub>2</sub> to benzene is performed on the acid site [9]. Thus, the second function of zeolite Brønsted acidity is to perform aromatization of intermediates formed on Mo sites. The decisive role of Brønsted acidity is further confirmed by the fact that Mo/Na-ZSM-5 is inactive in MDA [4]. To avoid excessive coking while retaining high benzene formation rate, it is generally recommended to use zeolites with moderate acidity. High Al content promotes condensation reactions of the products leading to the formation of the so-called hard coke (highly dehydrogenated polycyclic aromatics) [75]. On the other hand, it was shown that low Al content results in low benzene and toluene selectivity, yielding mainly ethylene in ethane aromatization [154].

Kosinov et al. recently hypothesized that MDA reaction mechanism might have features similar to methanol-to-hydrocarbons (MTH) mechanism claiming that primary C<sub>2</sub>H<sub>x</sub> fragments react with linear polycyclic aromatic species trapped in zeolitic microenvironment [155]. From such a perspective, the structure-performance relationship deduced from the MTH studies can be applied to MDA and paraffins/olefins aromatization reactions [21, 150]. It can be expressed in the following manner: *"the higher the density of acid sites, the closer these sites are to each other, the larger the number of successive chemical steps undergone by reactant molecules along the diffusion path within the zeolite crystallites and the more favourable the condensation reactions, hence the faster the coking rate."* [156, 157] To tackle high coking rates, a variety of methods are used to tune acidity and to passivate acid sites at the external surface. For example, Lu et al. performed dealumination of ZSM-5 by steaming which resulted in a significantly lower selectivity to coke (18.9 % vs 37.9 %), naturally leading to higher benzene yield [158]. Acid site concentration and acid strength is also altered by the high temperature applied for MDA similar to the heat-treatment applied to prepare silica for grafting [159-161].

In summary, while anchoring an active metal requires low Si/Al ratios, aromatization of active intermediates without high coking rates calls for zeolites with moderate acidity. According to Ma et al. an ideal MDA catalyst should have an appropriate balance between the free Brønsted acid sites and acid sites with

anchored Mo [162]. By utilizing Mo/MCM-22 with different Mo loading, they showed that the best catalyst possessed three Al per unit cell, where one framework Al was associated with aromatization reaction, while other two were used to anchor Mo.

To the best of our knowledge, for methane dehydroaromatization as well as aromatization of olefins/paraffins ZSM-5 and MCM-22-based catalysts show by far the highest performance compared to other zeolite topologies [163]. The ZSM-5 choice is dictated by a rather peculiar architecture of MFI topology, consisting of interconnecting straight ( $5.3 \times 5.6$  Å) and zig-zag ( $5.1 \times 5.5$  Å) channels able to accommodate aromatics up to methylated naphthalene or longer aromatic chains like anthracene. The fact that these two structures outperform other structures with similar pore sizes and acid strength for a lot of reactions, like FCC, MTH and alkane/alkene conversion was also assigned to confinement effects. They influence in which configuration reactants interact with the active site and are believed to play a significant role in determining the activity of those two zeolite topologies [164-166]. Kosinov *et al.* showed that in the absence of zeolite, molybdenum supported on different oxides such as  $\text{SiO}_2$  and  $\text{Al}_2\text{O}_3$ , can activate methane with minor formation of aromatics and aliphatics, but coke is the main product [39, 120].

Authors showed that the confinement of metal in zeolite pores shifts selectivity to benzene and its homologues increasing the overall yield of value-added products [167]. However, not all zeolite topologies are equally selective to aromatics. In small-pore zeolites with large cavities (8MR), any aromatic molecule is locked up in such a cavity making the catalyst selective almost exclusively to ethylene and ethane [168, 169]. Although such a catalyst does not have any perspective for practical application, it highlights the important role of ethylene as an intermediate.

Another extreme is utilization of large pore zeolites (12MR), such as X, Y, MOR, BEA and many others [39, 45, 169]. Their architectures with large pores and channels do not restrict benzene to react further and form polycondensed structures, which are coke pre-cursors. As a consequence, similar to oxide supports, this class of zeolites is selective to coke rather than benzene derivatives [168]. ZSM-5 belonging to 10MR family seems to be the optimal choice as its confinement allows formation of naphthalene, benzene, toluene and xylenes, while restricting further growth to polycondensed structures. Similarly to ZSM-5, many other 10MR zeolites exhibit high selectivity to

aromatics [153, 170]. Martinez *et al.*[171] compared the catalytic activity of Mo/MCM-22 and Mo/ITQ-2 (delaminated layered precursor of MCM-22) in MDA reaction. Both showed rather high selectivity to benzene, ITQ-2 being more selective to naphthalene. Further de-alumination of external surface of ITQ-2 resulted in an increase to benzene selectivity from 62 to 75% at the expense of naphthalene, suggesting that it is formed on the outer surface of the zeolite and confirming the profound effect of shape-selectivity. It is worth mentioning that Mo/MCM-22 (MWW) shows catalytic performance comparable to Mo/ZSM-5 in MDA reaction [9]. It possesses a set of 12MR cages connected through 10MR windows and a set of 10MR channels. It is not clear however which of the two pore systems is responsible for the catalytic performance [172].

### 1.5 A bifunctional catalyst and the two-step mechanism

The Mo in combination with the acidic zeolite support was proposed to make up the bifunctional nature of this catalyst. In a two-step process, the two sites are believed to fulfil two distinct functions. Mo achieves C-H activation of methane and leads to the formation of C2 intermediates, which then react over the BAS of the zeolite, where they aromatize. This mechanism was proposed early on[4] and was mostly accepted since then [35-38]. This proposed mechanism is supported by the fact that CH<sub>4</sub> activation solely over BAS is negligible,[39-41] and therefore a metal site is necessary to activate CH<sub>4</sub>. In contrast to the two-step mechanism, it was proposed that Mo does not achieve C-H bond activation on its own but in concert with the BAS, which helps in abstracting the proton from CH<sub>4</sub> [35, 58, 59]. This is also supported by the fact that there are only two active non-zeolite based catalysts reported for this reaction [121, 173]. A concerted action or at least the requirement of close proximity of the Mo and BAS is also suggested by the fact that physically mixing Mo carbides with zeolite only leads to very low activity [174].

Furthermore, in ethylene aromatization both ethylene conversion as well as aromatic selectivity was much enhanced when a metal was added to HZSM-5 [134, 135, 139]. This suggests that Mo also plays a crucial role in aromatics production. In conclusion, the separation of these functionalities is not possible [175]. Although some studies address the optimal loading of Mo, given a zeolite with certain acidity and vice versa,[35, 36, 75-77, 162] the optimal proximity of BAS to

Mo site and the optimal concentration of both sites per zeolite cage is only discussed for MCM-22 [162]. A careful study is necessary, both varying Mo/Al ratios as well as Si/Al ratios over a wide range while carefully characterizing how many well-dispersed Mo sites are created inside the pores of the zeolite. This could be achieved by probing how many BAS are replaced by Mo, probing acidity through H/D exchange,[42, 73, 79]  $^1\text{H}$  NMR,[117]  $^{27}\text{Al}$  NMR,[106, 118] NH<sub>3</sub>-TPD[56, 75, 107, 108] or probing adsorbed molecules by FTIR [39, 109].

An alternative reaction mechanism proposed proceeds via methyl radicals [35]. While their role for MDA over zeolite catalysts is mostly speculative, they have been shown to play a role above 1000 °C when a Fe@SiO<sub>2</sub> catalyst with a very low surface area was used. Methyl radicals were also observed to play an important role in the oxidative coupling of methane [146, 173, 176]. The presence of radicals can be investigated using operando electron spin resonance (ESR) or online vacuum ultraviolet soft photoionization molecular-beam mass spectrometry (VUVSPI-MBMS) [146, 173, 177].

## 1.6 Outlook

It is clear that significant research effort is necessary to further improve the performance of the MDA catalyst. To bring it to a stage where the development of a commercial process can be considered, the selectivity to coke has to be decreased, the catalyst needs to be resistant to degradation during regeneration and a catalyst more selective to benzene rather than naphthalene is required: on one hand, commercial interest in naphthalene is rather low, on the other hand, formation of such heavy product would bring serious operational issues in commercial plants. Spotting the metal sites that achieve methane activation among the plethora of metal sites present on the catalyst, however difficult, is crucial. A structure-activity relationship has however not been developed for the MDA system. This would have tremendous impact on catalyst design. Effort should be directed towards designing a catalyst containing only well-dispersed metal sites preventing metal nanoparticles and Mo clustering. Pre-treatments could play an important role in that regard as they can stabilize the active site and avoid coke formation in the initial periods of the reaction. In addition, elimination of the induction period through a pre-treatment could facilitate process operation especially during the startup of

the reaction [178]. Singling out the main reaction intermediate has not been achieved yet, but can aid in designing better supports by feeding reaction intermediates directly to the support without the metal. With this, the optimization of the catalyst system becomes easier, because several optimization parameters can be separated by first optimizing the support and then later the dispersion of the metal on the already optimized support. Metal-support interaction and inherent reactivity of the support can then be studied as two separate phenomena and optimized separately, making it a more manageable task.

## 1.7 Outline and scope of this thesis

Understanding of the methane dehydroaromatization reaction is particularly hard, because of the harsh reaction conditions and the fact that methane conversion to desired products goes in parallel with rapid deactivation. The research presented in this thesis is motivated by the goal of obtaining the information necessary to develop a structure-activity relationship.

The first half of this thesis addresses the metal-support interaction, the dispersion of the active metal and to some extent also the geometry of the active site. In **Chapter 2**, the location of the anchoring sites for Mo on the zeolite support is altered by the synthesis of the zeolite. The effect of the anchoring location on the geometry of the oxidic Mo is explored by DFT calculations and finally the effect on the anchoring on catalytic activity is investigated. This chapter shows that dispersion of Mo has a bigger influence on the catalytic behaviour than the exact location of Mo, thus in **Chapter 3**, the influence of dispersion on selectivity to aromatics and coke is quantified, where Py IR, ICP, UV-Vis and XPS are used to assess dispersion on the as-synthesized catalysts. Improved dispersion can be achieved by employing a synthesis method rarely mentioned in literature for MDA catalysts, chemical vapour deposition or sublimation, but the synthesis method was not very reproducible.

The second part (**Chapter 4** and **5**) focusses mostly on operando characterization of the active site. A new strategy for quasi-in-situ characterization is developed, where the key is to use a CO pre-treatment to produce the active site. *Operando* XAS, <sup>13</sup>C NMR, DNP and CO IR are used for characterization. The operando / quasi-in-situ strategy aims at obtaining the information listed in **section 1.2.1** of this introduction and at overcoming the challenges addressed in **section 1.2.2** to **1.2.4**.

Information is obtained about the nuclearity, the stoichiometry, the charge and partly also about the location of the active site at reaction conditions. In addition, the dynamic nature of the active site is highlighted and information about the interaction of the methane molecules with the active site is obtained using a pulsing reaction technique with labelled molecules.

Note that all chapters have been written as individual publications and can be read independently. As a result, the reader may find some overlap.

## 1.8 References

- [1] M. Bender, Global Aromatics Supply - Today and Tomorrow, in: New Technologies and Alternative Feedstocks in Petrochemistry and Refining DGMK Conference, Dresden, Germany, 2013.
- [2] N.E.T. Laboratory, An introduction to the science and energy potential of a unique resource, in: U.D.o. Energy (Ed.), US Department of Energy, US, 2011.
- [3] C. Elvidge, M. Zhizhin, K. Baugh, F.-C. Hsu, T. Ghosh, Methods for Global Survey of Natural Gas Flaring from Visible Infrared Imaging Radiometer Suite Data, *Energies*, 9 (2016) 14.
- [4] L. Wang, L. Tao, M. Xie, G. Xu, J. Huang, Y. Xu, Dehydrogenation and aromatization of methane under non-oxidizing conditions, *Catalysis Letters*, 21 (1993) 35-41.
- [5] O. Bragin, T. Vasina, Y.I. Isakov, B. Nefedov, A. Preobrazhenskii, N. Palishkina, K.M. Minachev, Catalytic aromatization of methane and ethane, *Russian Chemical Bulletin*, 31 (1982) 847-847.
- [6] B.S. Liu, L. Jiang, H. Sun, C.T. Au, XPS, XAES, and TG/DTA characterization of deposited carbon in methane dehydroaromatization over Ga-Mo/ZSM-5 catalyst, *Applied Surface Science*, 253 (2007) 5092-5100.
- [7] K. Honda, X. Chen, Z.-G. Zhang, Identification of the coke accumulation and deactivation sites of Mo<sub>2</sub>C/HZSM-5 catalyst in CH<sub>4</sub> dehydroaromatization, *Catalysis Communications*, 5 (2004) 557-561.
- [8] Y. Song, Y. Xu, Y. Suzuki, H. Nakagome, Z.-G. Zhang, A clue to exploration of the pathway of coke formation on Mo/HZSM-5 catalyst in the non-oxidative methane dehydroaromatization at 1073 K, *Applied Catalysis A: General*, 482 (2014) 387-396.
- [9] J.J. Spivey, G. Hutchings, Catalytic aromatization of methane, *Chemical Society Reviews*, 43 (2014) 792-803.
- [10] S. Ma, X. Guo, L. Zhao, S. Scott, X. Bao, Recent progress in methane dehydroaromatization: From laboratory curiosities to promising technology, *Journal of Energy Chemistry*, 22 (2013) 1-20.
- [11] B.M. Weckhuysen, D. Wang, M.P. Rosynek, J.H. Lunsford, Conversion of Methane to Benzene over Transition Metal Ion ZSM-5 Zeolites: II. Catalyst Characterization by X-Ray Photoelectron Spectroscopy, *Journal of Catalysis*, 175 (1998) 347-351.
- [12] B.M. Weckhuysen, D. Wang, M.P. Rosynek, J.H. Lunsford, Conversion of Methane to Benzene over Transition Metal Ion ZSM-5 Zeolites, *Journal of Catalysis*, 175 (1998) 338-346.
- [13] Y. Shu, M. Ichikawa, Catalytic dehydrocondensation of methane towards benzene and naphthalene on transition metal supported zeolite catalysts: templating role of zeolite micropores and characterization of active metallic sites, *Catalysis Today*, 71 (2001) 55-67.
- [14] N.Y. Chen, T.Y. Yan, M2 forming-a process for aromatization of light hydrocarbons, *Industrial & Engineering Chemistry Process Design and Development*, 25 (1986) 151-155.
- [15] T.F. Degnan, G.K. Chitnis, P.H. Schipper, History of ZSM-5 fluid catalytic cracking additive development at Mobil, *Microporous and Mesoporous Materials*, 35-36 (2000) 245-252.

- [16] J.F. Haw, D.M. Marcus, Well-defined (supra)molecular structures in zeolite methanol-to-olefin catalysis, *Topics in Catalysis*, 34 (2005) 41-48.
- [17] J.F. Haw, W. Song, D.M. Marcus, J.B. Nicholas, The Mechanism of Methanol to Hydrocarbon Catalysis, *Accounts of Chemical Research*, 36 (2003) 317-326.
- [18] U. Olsbye, M. Bjørgen, S. Svelle, K.-P. Lillerud, S. Kolboe, Mechanistic insight into the methanol-to-hydrocarbons reaction, *Catalysis Today*, 106 (2005) 108-111.
- [19] P.W. Goguen, T. Xu, D.H. Barich, T.W. Skloss, W. Song, Z. Wang, J.B. Nicholas, J.F. Haw, Pulse-Quench Catalytic Reactor Studies Reveal a Carbon-Pool Mechanism in Methanol-to-Gasoline Chemistry on Zeolite HZSM-5, *Journal of the American Chemical Society*, 120 (1998) 2650-2651.
- [20] K. Hemelsoet, J. Van der Mynsbrugge, K. De Wispelaere, M. Waroquier, V. Van Speybroeck, Unraveling the Reaction Mechanisms Governing Methanol-to-Olefins Catalysis by Theory and Experiment, *ChemPhysChem*, 14 (2013) 1526-1545.
- [21] U. Olsbye, S. Svelle, M. Bjørgen, P. Beato, T.V.W. Janssens, F. Joensen, S. Bordiga, K.P. Lillerud, Conversion of Methanol to Hydrocarbons: How Zeolite Cavity and Pore Size Controls Product Selectivity, *Angewandte Chemie International Edition*, 51 (2012) 5810-5831.
- [22] I. Yarulina, S. Bailleul, A. Pustovarenko, J.R. Martinez, K.D. Wispelaere, J. Hajek, B.M. Weckhuysen, K. Houben, M. Baldus, V. Van Speybroeck, F. Kapteijn, J. Gascon, Suppression of the Aromatic Cycle in Methanol-to-Olefins Reaction over ZSM-5 by Post-Synthetic Modification Using Calcium, *ChemCatChem*, 8 (2016) 3057-3063.
- [23] I. Yarulina, J. Goetze, C. Gucuyener, L. van Thiel, A. Dikhtierenko, J. Ruiz-Martinez, B.M. Weckhuysen, J. Gascon, F. Kapteijn, Methanol-to-olefins process over zeolite catalysts with DDR topology: effect of composition and structural defects on catalytic performance, *Catalysis Science & Technology*, 6 (2016) 2663-2678.
- [24] J. Goetze, F. Meirer, I. Yarulina, J. Gascon, F. Kapteijn, J. Ruiz-Martinez, B.M. Weckhuysen, Insights into the Activity and Deactivation of the Methanol-to-Olefins Process over Different Small-Pore Zeolites As Studied with Operando UV-vis Spectroscopy, *ACS Catalysis*, 7 (2017) 4033-4046.
- [25] I.M. Dahl, S. Kolboe, On the reaction mechanism for propene formation in the MTO reaction over SAPO-34, *Catalysis Letters*, 20 (1993) 329-336.
- [26] N. Kosinov, A.S.G. Wijpkema, E. Uslamin, R. Rohling, F.J.A.G. Coumans, B. Mezari, A. Parastaei, A.S. Poryvaev, M.V. Fedin, E.A. Pidko, E.J.M. Hensen, Confined Carbon Mediating Dehydroaromatization of Methane over Mo/ZSM-5, *Angewandte Chemie*, 57 (2018) 1016-1020.
- [27] K.S. Wong, J.W. Thybaut, E. Tangstad, M.W. Stöcker, G.B. Marin, Methane aromatisatation based upon elementary steps: Kinetic and catalyst descriptors, *Microporous and Mesoporous Materials*, 164 (2012) 302-312.
- [28] C. Karakaya, H. Zhu, R.J. Kee, Kinetic modeling of methane dehydroaromatization chemistry on Mo/Zeolite catalysts in packed-bed reactors, *Chemical Engineering Science*, 123 (2015) 474-486.

- [29] H. Jiang, L. Wang, W. Cui, Y. Xu, Study on the induction period of methane aromatization over Mo/HZSM-5: partial reduction of Mo species and formation of carbonaceous deposit, *Catalysis Letters*, 57 (1999) 95-102.
- [30] I. Lezcano-González, R. Oord, M. Rovezzi, P. Glatzel, S.W. Botchway, B.M. Weckhuysen, A.M. Beale, Molybdenum Speciation and its Impact on Catalytic Activity during Methane Dehydroaromatization in Zeolite ZSM-5 as Revealed by Operando X-Ray Methods, *Angewandte Chemie International Edition*, 55 (2016) 5215-5219.
- [31] F. Solymosi, A. Szöke, J. Cserényi, Conversion of methane to benzene over Mo<sub>2</sub>C and Mo<sub>2</sub>C/ZSM-5 catalysts, *Catalysis Letters*, 39 (1996) 157-161.
- [32] D. Wang, J. Lunsford, M. Rosynek, Catalytic conversion of methane to benzene over Mo/ZSM-5, *Topics in Catalysis*, 3 (1996) 289-297.
- [33] S. Liu, L. Wang, R. Ohnishi, M. Ichikawa, Bifunctional catalysis of Mo/HZSM-5 in the dehydroaromatization of methane with CO/CO<sub>2</sub> to benzene and naphthalene, *Kinetics and catalysis*, 41 (2000) 132-144.
- [34] W. Ding, S. Li, G. D Meitzner, E. Iglesia, Methane conversion to aromatics on Mo/H-ZSM5: structure of molybdenum species in working catalysts, *The Journal of Physical Chemistry B*, 105 (2001) 506-513.
- [35] L.Y. Chen, L.W. Lin, Z.S. Xu, X.S. Li, T. Zhang, Dehydro-oligomerization of Methane to Ethylene and Aromatics over Molybdenum/HZSM-5 Catalyst, *Journal of Catalysis*, 157 (1995) 190-200.
- [36] Y. Xu, S. Liu, X. Guo, L. Wang, M. Xie, Methane activation without using oxidants over Mo/HZSM-5 zeolite catalysts, *Catalysis Letters*, 30 (1994) 135-149.
- [37] Y. Xu, W. Liu, S.-T. Wong, L. Wang, X. Guo, Dehydrogenation and aromatization of methane in the absence of oxygen on Mo/HZSM-5 catalysts before and after NH<sub>4</sub>OH extraction, *Catalysis Letters*, 40 (1996) 207-214.
- [38] F. Solymosi, J. Cserényi, A. Szöke, T. Bánsági, A. Oszkó, Aromatization of Methane over Supported and Unsupported Mo-Based Catalysts, *Journal of Catalysis*, 165 (1997) 150-161.
- [39] S. Liu, L. Wang, R. Ohnishi, M. Ichikawa, Bifunctional Catalysis of Mo/HZSM-5 in the Dehydroaromatization of Methane to Benzene and Naphthalene XAFS/TG/DTA/MASS/FTIR Characterization and Supporting Effects, *Journal of Catalysis*, 181 (1999) 175-188.
- [40] V.T.T. Ha, L.V. Tiep, P. Meriaudeau, C. Naccache, Aromatization of methane over zeolite supported molybdenum: active sites and reaction mechanism, *Journal of Molecular Catalysis A: Chemical*, 181 (2002) 283-290.
- [41] R.E. Jentoft, B.C. Gates, H-D exchange between CD<sub>4</sub> and solid acids: AlCl<sub>3</sub>/sulfonic acid resin, promoted and unpromoted sulfated zirconia, and zeolite HZSM-5, *Catalysis Letters*, 72 (2001) 129-133.
- [42] Y.-H. Kim, R.W. Borry, E. Iglesia, Genesis of methane activation sites in Mo-exchanged H-ZSM-5 catalysts, *Microporous and Mesoporous Materials*, 35 (2000) 495-509.
- [43] Y. Xu, L. Lin, Recent advances in methane dehydro-aromatization over transition metal ion-modified zeolite catalysts under non-oxidative conditions, *Applied Catalysis A: General*, 188 (1999) 53-67.

- [44] Y. Xu, X. Bao, L. Lin, Direct conversion of methane under nonoxidative conditions, *Journal of Catalysis*, 216 (2003) 386-395.
- [45] Z.R. Ismagilov, E.V. Matus, L.T. Tsikoza, Direct conversion of methane on Mo/ZSM-5 catalysts to produce benzene and hydrogen: achievements and perspectives, *Energy & Environmental Science*, 1 (2008) 526-541.
- [46] S. Majhi, P. Mohanty, H. Wang, K.K. Pant, Direct conversion of natural gas to higher hydrocarbons: A review, *Journal of Energy Chemistry*, 22 (2013) 543-554.
- [47] R. Horn, R. Schlögl, Methane Activation by Heterogeneous Catalysis, *Catalysis Letters*, 145 (2015) 23-39.
- [48] A.I. Olivos Suarez, Á. Szécsényi, E.J.M. Hensen, J. Ruiz-Martínez, E.A. Pidko, J. Gascon, Strategies for the direct catalytic valorization of methane using heterogeneous catalysis: challenges and opportunities, *ACS Catalysis*, (2016).
- [49] B.M. Weckhuysen, M.P. Rosynek, J.H. Lunsford, Characterization of surface carbon formed during the conversion of methane to benzene over Mo/H-ZSM-5 catalysts, *Catalysis Letters*, 52 (1998) 31-36.
- [50] F. Solymosi, A. Erdöhelyi, A. Szöke, Dehydrogenation of methane on supported molybdenum oxides. Formation of benzene from methane, *Catalysis Letters*, 32 (1995) 43-53.
- [51] H. Liu, W. Shen, X. Bao, Y. Xu, Identification of Mo active species for methane dehydro-aromatization over Mo/HZSM-5 catalysts in the absence of oxygen:  $^{1}\text{H}$  MAS NMR and EPR investigations, *Journal of Molecular Catalysis A: Chemical*, 244 (2006) 229-236.
- [52] P. Tan, Active phase, catalytic activity, and induction period of Fe/zeolite material in nonoxidative aromatization of methane, *Journal of Catalysis*, 338 (2016) 21-29.
- [53] L. Wang, R. Ohnishi, M. Ichikawa, Selective Dehydroaromatization of Methane toward Benzene on Re/HZSM-5 Catalysts and Effects of CO/CO<sub>2</sub> Addition, *Journal of Catalysis*, 190 (2000) 276-283.
- [54] P.L. Tan, C.T. Au, S.Y. Lai, Methane dehydrogenation and aromatization over 4 wt% Mn/HZSM-5 in the absence of an oxidant, *Catalysis Letters*, 112 (2006) 239-245.
- [55] T. Baba, H. Sawada, Conversion of methane into higher hydrocarbons in the presence of ethylene over H-ZSM-5 loaded with silver cations, *Physical Chemistry Chemical Physics*, 4 (2002) 3919-3923.
- [56] B.S. Liu, Y. Zhang, J.F. Liu, M. Tian, F.M. Zhang, C.T. Au, A.S.C. Cheung, Characteristic and Mechanism of Methane Dehydroaromatization over Zn-Based/HZSM-5 Catalysts under Conditions of Atmospheric Pressure and Supersonic Jet Expansion, *The Journal of Physical Chemistry C*, 115 (2011) 16954-16962.
- [57] V. Abdelsayed, M.W. Smith, D. Shekhawat, Investigation of the stability of Zn-based HZSM-5 catalysts for methane dehydroaromatization, *Applied Catalysis A: General*, 505 (2015) 365-374.
- [58] V.B. Kazansky, A.I. Serykh, E.A. Pidko, DRIFT study of molecular and dissociative adsorption of light paraffins by HZSM-5 zeolite modified with zinc ions: methane adsorption, *Journal of Catalysis*, 225 (2004) 369-373.

- [59] G. Qi, Q. Wang, J. Xu, J. Trébosc, O. Lafon, C. Wang, J.P. Amoureux, F. Deng, Synergic Effect of Active Sites in Zinc-Modified ZSM-5 Zeolites as Revealed by High-Field Solid-State NMR Spectroscopy, *Angewandte Chemie*, (2016).
- [60] A.A. Gabrienko, S.S. Arzumanov, I.B. Moroz, A.V. Toktarev, W. Wang, A.G. Stepanov, Methane Activation and Transformation on Ag/H-ZSM-5 Zeolite Studied with Solid-State NMR, *The Journal of Physical Chemistry C*, 117 (2013) 7690-7702.
- [61] T. Baba, Y. Abe, Metal cation–acidic proton bifunctional catalyst for methane activation: conversion of  $^{13}\text{CH}_4$  in the presence of ethylene over metal cations-loaded H-ZSM-5, *Applied Catalysis A: General*, 250 (2003) 265-270.
- [62] A.A. Gabrienko, S.S. Arzumanov, I.B. Moroz, I.P. Prosvirin, A.V. Toktarev, W. Wang, A.G. Stepanov, Methane Activation on In-Modified ZSM-5: The State of Indium in the Zeolite and Pathways of Methane Transformation to Surface Species, *The Journal of Physical Chemistry C*, 118 (2014) 8034-8043.
- [63] I. Vollmer, G. Li, I. Yarulina, N. Kosinov, E.J. Hensen, K. Houben, D. Mance, M. Baldus, J. Gascon, F. Kapteijn, Relevance of the Mo-precursor state in H-ZSM-5 for methane dehydroaromatization, *Catalysis Science & Technology*, 8 (2018) 916-922.
- [64] E.V. Matus, I.Z. Ismagilov, O.B. Sukhova, V.I. Zaikovskii, L.T. Tsikoza, Z.R. Ismagilov, J.A. Moulijn, Study of Methane Dehydroaromatization on Impregnated Mo/ZSM-5 Catalysts and Characterization of Nanostructured Molybdenum Phases and Carbonaceous Deposits, *Industrial & Engineering Chemistry Research*, 46 (2007) 4063-4074.
- [65] J. Gao, Y. Zheng, J.-M. Jehng, Y. Tang, I.E. Wachs, S.G. Podkolzin, Identification of molybdenum oxide nanostructures on zeolites for natural gas conversion, *Science*, 348 (2015) 686-690.
- [66] C. Sun, S. Yao, W. Shen, L. Lin, Highly Dispersed Molybdenum Oxide Supported on HZSM-5 for Methane Dehydroaromatization, *Catalysis Letters*, 122 (2008) 84-90.
- [67] M. Bäumer, H.-J. Freund, Metal deposits on well-ordered oxide films, *Progress in Surface Science*, 61 (1999) 127-198.
- [68] H.J. Freund, M. Bäumer, H. Kuhlenbeck, Catalysis and surface science: What do we learn from studies of oxide-supported cluster model systems?, in: *Advances in Catalysis*, Academic Press, 2000, pp. 333-384.
- [69] J.C. Fierro-Gonzalez, S. Kuba, Y. Hao, B.C. Gates, Oxide- and Zeolite-Supported Molecular Metal Complexes and Clusters: Physical Characterization and Determination of Structure, Bonding, and Metal Oxidation State, *The Journal of Physical Chemistry B*, 110 (2006) 13326-13351.
- [70] C. Copéret, M. Chabanas, R. Petroff Saint-Arroman, J.-M. Basset, Homogeneous and Heterogeneous Catalysis: Bridging the Gap through Surface Organometallic Chemistry, *Angewandte Chemie International Edition*, 42 (2003) 156-181.
- [71] C. Copéret, A. Comas-Vives, M.P. Conley, D.P. Estes, A. Fedorov, V. Mougel, H. Nagae, F. Núñez-Zarur, P.A. Zhizhko, Surface Organometallic and Coordination Chemistry toward Single-Site Heterogeneous Catalysts: Strategies, Methods, Structures, and Activities, *Chemical reviews*, 116 (2016) 323-421.

- [72] C. Coperet, C-H Bond Activation and Organometallic Intermediates on Isolated Metal Centers on Oxide Surfaces, *Chemical reviews*, 110 (2010) 656-680.
- [73] W. Ding, G.D. Meitzner, D.O. Marler, E. Iglesia, Synthesis, Structural Characterization, and Catalytic Properties of Tungsten-Exchanged H-ZSM5, *The Journal of Physical Chemistry B*, 105 (2001) 3928-3936.
- [74] S. Liang, C. Hao, Y. Shi, The Power of Single-Atom Catalysis, *ChemCatChem*, 7 (2015) 2559-2567.
- [75] J.-P. Tessonnier, B. Louis, S. Rigolet, M.J. Ledoux, C. Pham-Huu, Methane dehydro-aromatization on Mo/ZSM-5: About the hidden role of Brønsted acid sites, *Applied Catalysis A: General*, 336 (2008) 79-88.
- [76] J. Gao, Y. Zheng, J.-M. Jehng, Y. Tang, I.E. Wachs, S.G. Podkolzin, Identification of molybdenum oxide nanostructures on zeolites for natural gas conversion, *Science*, (2015).
- [77] J. Shu, A. Adnot, B.P.A. Grandjean, Bifunctional Behavior of Mo/HZSM-5 Catalysts in Methane Aromatization, *Industrial & Engineering Chemistry Research*, 38 (1999) 3860-3867.
- [78] T.H. Lim, K. Nam, I.K. Song, K.-Y. Lee, D.H. Kim, Effect of Si/Al<sub>2</sub> ratios in Mo/H-MCM-22 on methane dehydroaromatization, *Applied Catalysis A: General*, 552 (2018) 11-20.
- [79] J.-P. Tessonnier, B. Louis, S. Walspurger, J. Sommer, M.-J. Ledoux, C. Pham-Huu, Quantitative Measurement of the Brønsted Acid Sites in Solid Acids: Toward a Single-Site Design of Mo-Modified ZSM-5 Zeolite, *The Journal of Physical Chemistry B*, 110 (2006) 10390-10395.
- [80] C. Hammond, M.M. Forde, M.H. Ab Rahim, A. Thetford, Q. He, R.L. Jenkins, N. Dimitratos, J.A. Lopez-Sanchez, N.F. Dummer, D.M. Murphy, A.F. Carley, S.H. Taylor, D.J. Willock, E.E. Stangland, J. Kang, H. Hagen, C.J. Kiely, G.J. Hutchings, Direct Catalytic Conversion of Methane to Methanol in an Aqueous Medium by using Copper-Promoted Fe-ZSM-5, *Angewandte Chemie International Edition*, 51 (2012) 5129-5133.
- [81] V.L. Sushkevich, D. Palagin, M. Ranocchiari, J.A. van Bokhoven, Selective anaerobic oxidation of methane enables direct synthesis of methanol, *Science*, 356 (2017) 523-527.
- [82] G. Centi, F. Vazzana, Selective catalytic reduction of N<sub>2</sub>O in industrial emissions containing O<sub>2</sub>, H<sub>2</sub>O and SO<sub>2</sub>: behavior of Fe/ZSM-5 catalysts, *Catalysis Today*, 53 (1999) 683-693.
- [83] N. Kosinov, C. Liu, E.J.M. Hensen, E.A. Pidko, Engineering of Transition Metal Catalysts Confined in Zeolites, *Chemistry of Materials*, (2018).
- [84] J. Raskó, J. Kiss, Infrared study of the adsorption of CO and CH<sub>3</sub> on silica-supported MoO<sub>3</sub> and Mo<sub>2</sub>C catalysts, *Applied Catalysis A: General*, 253 (2003) 427-436.
- [85] J.B. Peri, Computerized infrared studies of molybdenum/alumina and molybdenum/silica catalysts, *The Journal of Physical Chemistry*, 86 (1982) 1615-1622.
- [86] R.J. Lobo-Lapidus, B.C. Gates, Supported Rhenium Complexes: Almost Uniform Rhenium Tricarbonyls Synthesized from CH<sub>3</sub>Re(CO)<sub>5</sub> and HY Zeolite, *Langmuir*, 26 (2010) 16368-16374.

- [87] J.F. Goellner, B.C. Gates, G.N. Vayssilov, N. Rösch, Structure and Bonding of a Site-Isolated Transition Metal Complex: Rhodium Dicarbonyl in Highly Dealuminated Zeolite Y, *Journal of the American Chemical Society*, 122 (2000) 8056-8066.
- [88] T.-c. Xiao, A.P.E. York, V.C. Williams, H. Al-Megren, A. Hanif, X.-y. Zhou, M.L.H. Green, Preparation of Molybdenum Carbides Using Butane and Their Catalytic Performance, *Chemistry of Materials*, 12 (2000) 3896-3905.
- [89] T.M. Duncan, P. Winslow, A.T. Bell, The characterization of carbonaceous species on ruthenium catalysts with  $^{13}\text{C}$  nuclear magnetic resonance spectroscopy, *Journal of Catalysis*, 93 (1985) 1-22.
- [90] G.H. Yokomizo, A.T. Bell, Isotopic tracer and NMR studies of carbonaceous species present during CO hydrogenation over RuTiO<sub>2</sub>, *Journal of Catalysis*, 119 (1989) 467-482.
- [91] T. Xiao, A.P.E. York, K.S. Coleman, J.B. Claridge, J. Sloan, J. Charnock, M.L.H. Green, Effect of carburising agent on the structure of molybdenum carbides, *Journal of Materials Chemistry*, 11 (2001) 3094-3098.
- [92] I. Vollmer, B. van der Linden, S. Ould-Chikh, A. Aguilar-Tapia, I. Yarulina, E. Abou-Hamad, Y.G. Sneider, A.I. Olivos Suarez, J.-L. Hazemann, F. Kapteijn, J. Gascon, On the dynamic nature of Mo sites for methane dehydroaromatization, *Chemical Science*, 9 (2018) 4801-4807.
- [93] D. Ma, W. Zhang, Y. Shu, X. Liu, Y. Xu, X. Bao, MAS NMR, ESR and TPD studies of Mo/HZSM-5 catalysts: evidence for the migration of molybdenum species into the zeolitic channels, *Catalysis Letters*, 66 (2000) 155-160.
- [94] H. Zheng, D. Ma, X. Bao, J.Z. Hu, J.H. Kwak, Y. Wang, C.H.F. Peden, Direct Observation of the Active Center for Methane Dehydroaromatization Using an Ultrahigh Field  $^{95}\text{Mo}$  NMR Spectroscopy, *Journal of the American Chemical Society*, 130 (2008) 3722-3723.
- [95] R. Kumar Rana, B. Viswanathan, Mo incorporation in MCM-41 type zeolite, *Catalysis Letters*, 52 (1998) 25-29.
- [96] R.O. Savinelli, S.L. Scott, Wavelet transform EXAFS analysis of mono- and dimolybdate model compounds and a Mo/HZSM-5 dehydroaromatization catalyst, *Physical Chemistry Chemical Physics*, 12 (2010) 5660-5667.
- [97] J.P. Thielemann, T. Ressler, A. Walter, G. Tzolova-Müller, C. Hess, Structure of molybdenum oxide supported on silica SBA-15 studied by Raman, UV-Vis and X-ray absorption spectroscopy, *Applied Catalysis A: General*, 399 (2011) 28-34.
- [98] N. Kosinov, F.J. Coumans, G. Li, E. Uslamin, B. Mezari, A.S. Wijpkema, E.A. Pidko, E.J. Hensen, Stable Mo/HZSM-5 methane dehydroaromatization catalysts optimized for high-temperature calcination-regeneration, *Journal of Catalysis*, 346 (2017) 125-133.
- [99] W. Ding, G.D. Meitzner, E. Iglesia, The Effects of Silanation of External Acid Sites on the Structure and Catalytic Behavior of Mo/H-ZSM5, *Journal of Catalysis*, 206 (2002) 14-22.
- [100] H.-Y. Chen, W.M.H. Sachtl, Promoted Fe/ZSM-5 catalysts prepared by sublimation: de-NO<sub>x</sub> activity and durability in H<sub>2</sub>O-rich streams, *Catalysis Letters*, 50 (1998) 125-130.

- [101] B.R. Muller, G. Calzaferri, Thin Mo(CO)<sub>6</sub>-Y-zeolite layers: preparation and in situ transmission FTIR spectroscopy, *Journal of the Chemical Society, Faraday Transactions*, 92 (1996) 1633-1637.
- [102] Y. You-Sing, R.F. Howe, Adsorption and decomposition of Mo(CO)<sub>6</sub> in zeolite NaY, *Journal of the Chemical Society, Faraday Transactions 1: Physical Chemistry in Condensed Phases*, 82 (1986) 2887-2896.
- [103] J.L. Zeng, Z.T. Xiong, H.B. Zhang, G.D. Lin, K.R. Tsai, Nonoxidative dehydrogenation and aromatization of methane over W/HZSM-5-based catalysts, *Catalysis Letters*, 53 (1998) 119-124.
- [104] P.L. Tan, C.T. Au, S.Y. Lai, Effects of acidification and basification of impregnating solution on the performance of Mo/HZSM-5 in methane aromatization, *Applied Catalysis A: General*, 324 (2007) 36-41.
- [105] S. Lai, Y. She, W. Zhan, Y. Guo, Y. Guo, L. Wang, G. Lu, Performance of Fe-ZSM-5 for selective catalytic reduction of NO<sub>x</sub> with NH<sub>3</sub>: Effect of the atmosphere during the preparation of catalysts, *Journal of Molecular Catalysis A: Chemical*, 424 (2016) 232-240.
- [106] D. Ma, Y. Shu, X. Han, X. Liu, Y. Xu, X. Bao, Mo/HMCM-22 Catalysts for Methane Dehydroaromatization: A Multinuclear MAS NMR Study, *The Journal of Physical Chemistry B*, 105 (2001) 1786-1793.
- [107] A. Martínez, E. Peris, M. Derewinski, A. Burkat-Dulak, Improvement of catalyst stability during methane dehydroaromatization (MDA) on Mo/HZSM-5 comprising intracrystalline mesopores, *Catalysis Today*, 169 (2011) 75-84.
- [108] Y. Shu, D. Ma, L. Xu, Y. Xu, X. Bao, Methane dehydro-aromatization over Mo/MCM-22 catalysts: a highly selective catalyst for the formation of benzene, *Catalysis Letters*, 70 (2000) 67-73.
- [109] B. Rhimi, M. Mhamdi, V.N. Kalevaru, A. Martin, Synergy between vanadium and molybdenum in bimetallic ZSM-5 supported catalysts for ethylene ammoxidation, *RSC Advances*, 6 (2016) 65866-65878.
- [110] H. Liu, X. Bao, Y. Xu, Methane dehydroaromatization under nonoxidative conditions over Mo/HZSM-5 catalysts: Identification and preparation of the Mo active species, *Journal of Catalysis*, 239 (2006) 441-450.
- [111] H. Liu, Y. Xu, H<sub>2</sub>-TPR Study on Mo/HZSM-5 Catalyst for CH<sub>4</sub> Dehydroaromatization, *Chinese Journal of Catalysis*, 27 (2006) 319-323.
- [112] M. Nachtegaal, U. Hartfelder, J.A. van Bokhoven, From Spectator Species to Active Site Using X-ray Absorption and Emission Spectroscopy Under Realistic Conditions, in: J. Frenken, I. Groot (Eds.) *Operando Research in Heterogeneous Catalysis*, Springer International Publishing, Cham, 2017, pp. 89-110.
- [113] C. Lamberti, A. Zecchina, E. Groppo, S. Bordiga, Probing the surfaces of heterogeneous catalysts by in situ IR spectroscopy, *Chemical Society Reviews*, 39 (2010) 4951-5001.
- [114] P.A. Crozier, T.W. Hansen, In situ and operando transmission electron microscopy of catalytic materials, *MRS Bulletin*, 40 (2015) 38-45.
- [115] K. Yoshida, K. Toyoura, K. Matsunaga, A. Nakahira, H. Kurata, Y.H. Ikuhara, Y. Sasaki, Atomic sites and stability of Cs<sup>+</sup> captured within zeolitic nanocavities, *Scientific Reports*, 3 (2013) 2457.

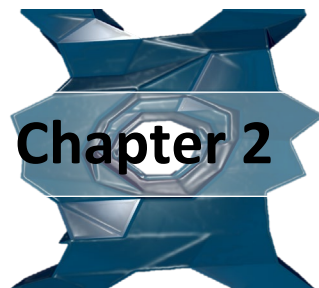
- [116] P. Kumar, K.V. Agrawal, M. Tsapatis, K.A. Mkoyan, Quantification of thickness and wrinkling of exfoliated two-dimensional zeolite nanosheets, *Nature Communications*, 6 (2015) 7128.
- [117] D. Ma, Y. Shu, W. Zhang, X. Han, Y. Xu, X. Bao, In Situ  $^1\text{H}$  MAS NMR Spectroscopic Observation of Proton Species on a Mo-Modified HZSM-5 Zeolite Catalyst for the Dehydroaromatization of Methane, *Angewandte Chemie International Edition*, 39 (2000) 2928-2931.
- [118] W. Zhang, D. Ma, X. Han, X. Liu, X. Bao, X. Guo, X. Wang, Methane Dehydroaromatization over Mo/HZSM-5 in the Absence of Oxygen: A Multinuclear Solid-State NMR Study of the Interaction between Supported Mo Species and HZSM-5 Zeolite with Different Crystal Sizes, *Journal of Catalysis*, 188 (1999) 393-402.
- [119] G. Doyen, G. Ertl, Theory of carbon monoxide chemisorption on transition metals, *Surface Science*, 43 (1974) 197-229.
- [120] N. Kosinov, F.J.A.G. Coumans, E.A. Uslamin, A.S.G. Wijpkema, B. Mezari, E.J.M. Hensen, Methane Dehydroaromatization by Mo/HZSM-5: Mono- or Bifunctional Catalysis?, *ACS Catalysis*, 7 (2017) 520-529.
- [121] D. Soulivong, S. Norsic, M. Taoufik, C. Coperet, J. Thivolle-Cazat, S. Chakka, J.-M. Basset, Non-Oxidative Coupling Reaction of Methane to Ethane and Hydrogen Catalyzed by the Silica-Supported Tantalum Hydride:  $(\equiv\text{SiO})_2\text{Ta}-\text{H}$ , *Journal of the American Chemical Society*, 130 (2008) 5044-5045.
- [122] F. Yin, G. Wang, M.-R. Li, A Periodic Density Functional Theory Analysis of Direct Methane Conversion into Ethylene and Aromatic Hydrocarbons Catalyzed by Mo<sub>4</sub>C<sub>2</sub>/ZSM-5, *Physical Chemistry Chemical Physics*, (2017).
- [123] C. Li, M. Zheng, A. Wang, T. Zhang, One-pot catalytic hydrocracking of raw woody biomass into chemicals over supported carbide catalysts: simultaneous conversion of cellulose, hemicellulose and lignin, *Energy & Environmental Science*, 5 (2012) 6383-6390.
- [124] W. Wu, Z. Wu, C. Liang, P. Ying, Z. Feng, C. Li, An IR study on the surface passivation of Mo<sub>2</sub>C/Al<sub>2</sub>O<sub>3</sub> catalyst with O<sub>2</sub>, H<sub>2</sub>O and CO<sub>2</sub>, *Physical Chemistry Chemical Physics*, 6 (2004) 5603-5608.
- [125] J.-S. Choi, J.-M. Krafft, A. Krzton, G. Djéga-Mariadassou, Study of Residual Oxygen Species over Molybdenum Carbide Prepared During In Situ DRIFTS Experiments, *Catalysis Letters*, 81 (2002) 175-180.
- [126] C. Doornkamp, V. Ponec, The universal character of the Mars and Van Krevelen mechanism, *Journal of Molecular Catalysis A: Chemical*, 162 (2000) 19-32.
- [127] V.P. Santos, T.A. Wezendonk, J.J.D. Jaén, A.I. Dugulan, M.A. Nasalevich, H.-U. Islam, A. Chojecki, S. Sartipi, X. Sun, A.A. Hakeem, A.C.J. Koeken, M. Ruitenbeek, T. Davidian, G.R. Meima, G. Sankar, F. Kapteijn, M. Makkee, J. Gascon, Metal organic framework-mediated synthesis of highly active and stable Fischer-Tropsch catalysts, *Nat Commun*, 6 (2015).
- [128] K. Xu, B. Sun, J. Lin, W. Wen, Y. Pei, S. Yan, M. Qiao, X. Zhang, B. Zong,  $\epsilon$ -Iron carbide as a low-temperature Fischer–Tropsch synthesis catalyst, 5 (2014) 5783.

- [129] V.V. Ordovsky, B. Legras, K. Cheng, S. Paul, A.Y. Khodakov, The role of carbon atoms of supported iron carbides in Fischer-Tropsch synthesis, *Catalysis Science & Technology*, 5 (2015) 1433-1437.
- [130] E.G. Derouane, J.B. Nagy, P. Dejaifve, J.H.C. van Hooff, B.P. Spekman, J.C. Védrine, C. Naccache, Elucidation of the mechanism of conversion of methanol and ethanol to hydrocarbons on a new type of synthetic zeolite, *Journal of Catalysis*, 53 (1978) 40-55.
- [131] P. Qiu, J.H. Lunsford, M.P. Rosyne, Characterization of Ga/ZSM-5 for the catalytic aromatization of dilute ethylene streams, *Catalysis Letters*, 52 (1998) 37-42.
- [132] A. Mehdad, R.F. Lobo, Ethane and ethylene aromatization on zinc-containing zeolites, *Catalysis Science & Technology*, 7 (2017) 3562-3572.
- [133] P. Cnudde, K. De Wispelaere, J. Van der Mynsbrugge, M. Waroquier, V. Van Speybroeck, Effect of temperature and branching on the nature and stability of alkene cracking intermediates in H-ZSM-5, *Journal of Catalysis*, 345 (2017) 53-69.
- [134] M.-F. Hsieh, Y. Zhou, H. Thirumalai, L.C. Grabow, J.D. Rimer, Silver-Promoted Dehydroaromatization of Ethylene over ZSM-5 Catalysts, *ChemCatChem*, (2017) n/a-n/a.
- [135] V.R. Choudhary, P. Devadas, S. Banerjee, A.K. Kinage, Aromatization of dilute ethylene over Ga-modified ZSM-5 type zeolite catalysts, *Microporous and Mesoporous Materials*, 47 (2001) 253-267.
- [136] X. Chen, M. Dong, X. Niu, K. Wang, G. Chen, W. Fan, J. Wang, Z. Qin, Influence of Zn species in HZSM-5 on ethylene aromatization, *Chinese Journal of Catalysis*, 36 (2015) 880-888.
- [137] H. Coqueblin, A. Richard, D. Uzio, L. Pinard, Y. Pouilloux, F. Epron, Effect of the metal promoter on the performances of H-ZSM5 in ethylene aromatization, *Catalysis Today*, 289 (2017) 62-69.
- [138] R. Le Van Mao, L.A. Dufresne, J. Yao, Y. Yu, Effects of the nature of coke on the activity and stability of the hybrid catalyst used in the aromatization of ethylene and n-butane, *Applied Catalysis A: General*, 164 (1997) 81-89.
- [139] P. Mériadeau, V.T.T. Ha, L.V. Tiep, Methane aromatization over Mo/H-ZSM-5: on the reaction pathway, *Catalysis Letters*, 64 (2000) 49-51.
- [140] X. Niu, J. Gao, Q. Miao, M. Dong, G. Wang, W. Fan, Z. Qin, J. Wang, Influence of preparation method on the performance of Zn-containing HZSM-5 catalysts in methanol-to-aromatics, *Microporous and Mesoporous Materials*, 197 (2014) 252-261.
- [141] L.A. Dufresne, R. Le Van Mao, Hydrogen back-spillover effects in the aromatization of ethylene on hybrid ZSM-5 catalysts, *Catalysis Letters*, 25 (1994) 371-383.
- [142] M. Berthelot, Action of Heat on some Hydrogenocarbon Compounds, *CR Acad. Sci.*, 62 (1866) 905.
- [143] P. Tsai, J.R. Anderson, Reaction of acetylene over ZSM-5-type catalysts, *Journal of Catalysis*, 80 (1983) 207-214.
- [144] W. Lee, T. Lee, H.-G. Jang, S.J. Cho, J. Choi, K.-S. Ha, Effects of hierarchical zeolites on aromatization of acetylene, *Catalysis Today*, 303 (2018) 177-184.

- [145] P. Mériadeau, L.V. Tiep, V.T.T. Ha, C. Naccache, G. Szabo, Aromatization of methane over Mo/H-ZSM-5 catalyst: on the possible reaction intermediates, *Journal of Molecular Catalysis A: Chemical*, 144 (1999) 469-471.
- [146] Y. Schuurman, C. Mirodatos, Uses of transient kinetics for methane activation studies, *Applied Catalysis A: General*, 151 (1997) 305-331.
- [147] D. Zhou, S. Zuo, S. Xing, Methane Dehydrogenation and Coupling to Ethylene over a Mo/HZSM-5 Catalyst: A Density Functional Theory Study, *The Journal of Physical Chemistry C*, 116 (2012) 4060-4070.
- [148] X. Gao, Q. Xin, Spectroscopic determination of oxidation and coordination states of Mo cations in the reduced MoAl<sub>2</sub>O<sub>3</sub> catalyst, *Journal of Catalysis*, 146 (1994) 306-309.
- [149] F. Larkins, A. Khan, Pyrolysis of methane to higher hydrocarbons: A thermodynamic study, *Australian Journal of Chemistry*, 42 (1989) 1655-1670.
- [150] I. Yarulina, A. Dutta Chowdhury, F. Meirer, B.M. Weckhuysen, J. Gascon, Recent Trends and Fundamental Insights in the Methanol-to-Olefins Process *Nature Catalysis*, (2018).
- [151] S.P. Yuan, J.G. Wang, Y.W. Li, H. Jiao, Brønsted Acidity of Isomorphously Substituted ZSM-5 by B, Al, Ga, and Fe. Density Functional Investigations, *Journal of Physical Chemistry A*, 106 (2002) 8167-8172.
- [152] I.L.C. Buurmans, B.M. Weckhuysen, Heterogeneities of individual catalyst particles in space and time as monitored by spectroscopy, *Nature Chemistry*, 4 (2012) 873-886.
- [153] P. Schwach, X. Pan, X. Bao, Direct Conversion of Methane to Value-Added Chemicals over Heterogeneous Catalysts: Challenges and Prospects, *Chemical reviews*, 117 (2017) 8497-8520.
- [154] Y. Xiang, H. Wang, J. Cheng, J. Matsubu, Progress and prospects in catalytic ethane aromatization, *Catalysis Science & Technology*, 8 (2018) 1500-1516.
- [155] N. Kosinov, A.S.G. Wijpkema, E. Uslamin, R. Rohling, F.J.A.G. Coumans, B. Mezari, A. Parastaei, A.S. Poryvaev, M.V. Fedin, E.A. Pidko, E.J.M. Hensen, Confined Carbon Mediating Dehydroaromatization of Methane over Mo/ZSM-5, *Angewandte Chemie International Edition*, 57 (2018) 1016-1020.
- [156] M. Guisnet, L. Costa, F.R. Ribeiro, Prevention of zeolite deactivation by coking, *Journal of Molecular Catalysis A: Chemical*, 305 (2009) 69-83.
- [157] I. Yarulina, K. De Wispelaere, S. Bailleul, J. Goetze, M. Radersma, E. Abou-Hamad, I. Vollmer, M. Goesten, B. Mezari, E.J.M. Hensen, J.S. Martínez-Espín, M. Morten, S. Mitchell, J. Perez-Ramirez, U. Olsbye, B.M. Weckhuysen, V. Van Speybroeck, F. Kapteijn, J. Gascon, Structure-performance descriptors and the role of Lewis acidity in the methanol-to-propylene process, *Nature Chemistry*, 10 (2018) 804-812.
- [158] Y. Lu, D. Ma, Z. Xu, Z. Tian, X. Bao, L. Lin, A high coking-resistance catalyst for methane aromatization, *Chemical Communications*, (2001) 2048-2049.
- [159] M.J. Nash, A.M. Shough, D.W. Fickel, D.J. Doren, R.F. Lobo, High-Temperature Dehydrogenation of Brønsted Acid Sites in Zeolites, *Journal of the American Chemical Society*, 130 (2008) 2460-2462.
- [160] H.E. Bergna, The colloid chemistry of silica, in, *American Chemical Society*, Washington, DC (United States), 1994.

- [161] P.L.J. Gunter, J.W. Niemantsverdriet, F.H. Ribeiro, G.A. Somorjai, Surface Science Approach to Modeling Supported Catalysts, *Catalysis reviews*, 39 (1997) 77-168.
- [162] D. Ma, Q. Zhu, Z. Wu, D. Zhou, Y. Shu, Q. Xin, Y. Xu, X. Bao, The synergic effect between Mo species and acid sites in Mo/HMCM-22 catalysts for methane aromatization, *Physical Chemistry Chemical Physics*, 7 (2005) 3102-3109.
- [163] J. Guo, H. Lou, X. Zheng, Energy-Efficient coaromatization of methane and propane, *Journal of Natural Gas Chemistry*, 18 (2009) 260-272.
- [164] T. Liang, J. Chen, Z. Qin, J. Li, P. Wang, S. Wang, G. Wang, M. Dong, W. Fan, J. Wang, Conversion of Methanol to Olefins over H-ZSM-5 Zeolite: Reaction Pathway Is Related to the Framework Aluminum Siting, *ACS Catalysis*, 6 (2016) 7311-7325.
- [165] G. Sastre, A. Corma, The confinement effect in zeolites, *Journal of Molecular Catalysis A: Chemical*, 305 (2009) 3-7.
- [166] D. Lesthaeghe, V. Van Speybroeck, M. Waroquier, Theoretical evaluation of zeolite confinement effects on the reactivity of bulky intermediates, *Physical Chemistry Chemical Physics*, 11 (2009) 5222-5226.
- [167] N. Kosinov, E.J.M. Hensen, Nonoxidative Dehydroaromatization of Methane, in: *Nanotechnology in Catalysis: Applications in the Chemical Industry, Energy Development, and Environment Protection*, Wiley, 2017, pp. 469 - 481.
- [168] C.-L. Zhang, S. Li, Y. Yuan, W.-X. Zhang, T.-H. Wu, L.-W. Lin, Aromatization of methane in the absence of oxygen over Mo-based catalysts supported on different types of zeolites, *Catalysis Letters*, 56 (1998) 207-213.
- [169] S.-T. Wong, Y. Xu, W. Liu, L. Wang, X. Guo, Methane activation without using oxidants over supported Mo catalysts, *Applied Catalysis A: General*, 136 (1996) 7-17.
- [170] K. Sun, D.M. Ginosar, T. He, Y. Zhang, M. Fan, R. Chen, Progress in Nonoxidative Dehydroaromatization of Methane in the Last 6 Years, *Industrial and Engineering Chemistry Research*, 57 (2018) 1768-1789.
- [171] A. Martínez, E. Peris, G. Sastre, Dehydroaromatization of methane under non-oxidative conditions over bifunctional Mo/ITQ-2 catalysts, *Catalysis Today*, 107-108 (2005) 676-684.
- [172] J. Bai, S. Liu, S. Xie, L. Xu, L. Lin, Shape Selectivity in Methane Dehydroaromatization Over Mo/MCM-22 Catalysts During a Lifetime Experiment, *Catalysis Letters*, 90 (2003) 123-130.
- [173] X. Guo, G. Fang, G. Li, H. Ma, H. Fan, L. Yu, C. Ma, X. Wu, D. Deng, M. Wei, D. Tan, R. Si, S. Zhang, J. Li, L. Sun, Z. Tang, X. Pan, X. Bao, Direct, Nonoxidative Conversion of Methane to Ethylene, Aromatics, and Hydrogen, *Science*, 344 (2014) 616-619.
- [174] F. Solymosi, A. Szoke, Study of the reactions of ethylene on supported Mo<sub>2</sub>C/ZSM-5 catalyst in relation to the aromatization of methane, in: *Studies in Surface Science and Catalysis*, 1998, pp. 355-360.
- [175] N. Kosinov, F.J.A.G. Coumans, E.A. Uslamin, A.S.G. Wijpkema, B. Mezari, E.J.M. Hensen, Methane Dehydroaromatization by Mo/HZSM-5: Mono- or Bifunctional Catalysis?, *ACS Catalysis*, (2016) 520-529.

- [176] K.D. Campbell, E. Morales, J.H. Lunsford, Gas-phase coupling of methyl radicals during the catalytic partial oxidation of methane, *Journal of the American Chemical Society*, 109 (1987) 7900-7901.
- [177] T. Ito, J. Wang, C.H. Lin, J.H. Lunsford, Oxidative dimerization of methane over a lithium-promoted magnesium oxide catalyst, *Journal of the American Chemical Society*, 107 (1985) 5062-5068.
- [178] L.L. Iaccino, T. Xu, J.S. Buchanan, N. Sangar, J.J. Patt, M.A. Nierode, K.R. Clem, M. Afeworki, Production of aromatics from methane, in, Google Patents, 2009.



---

**Relevance of the Mo-precursor state in H-ZSM-5  
for methane dehydroaromatization**

---

While the local geometry of Mo in Mo/HZSM-5 has been characterized before, we present a systematic way to manipulate the configuration of Mo and link it to its catalytic properties. The location and geometry of cationic Mo-complexes, the precursor of the active metal site for Methane Dehydroaromatization, is altered by directing the way they anchor to the framework of the zeolite. The handle used to direct the anchoring of Mo is the location of Al in the zeolite framework. According to DFT calculations, the local geometry of Mo should change, while UV-Vis and Pyridine FTIR indicated differences in the dispersion of Mo. Both aspects, however, did not influence the catalytic behaviour of Mo/HZSM-5, indicating that as long as enough isolated Mo species are present inside the pores of the zeolite, the catalytic behaviour is unaffected. This paves the way to better understand how the Mo oxo

---

This chapter is based on the following publication:  
Vollmer, I.; Li, G.; Yarulina, I.; Kosinov, N.; Hensen, E. J.; Houben, K.; Mance, D.; Baldus, M.; Gascon, J.; Kapteijn, F., (2018). "Relevance of the Mo-precursor state in H-ZSM-5 for methane dehydroaromatization." *Catalysis Science & Technology* **8**(3): 916-922. **doi: 10.1039/C7CY01789H**

## 2.1 Introduction

Interest and demand for a direct way to convert methane to valuable products is growing with the increasing availability of CH<sub>4</sub> sources and the inevitable depletion of oil. Such a process would enable flexible, on the spot, valorization of small-scale sources of methane, for example as by-product of oil fields which is currently flared or reinjected [1]. To date, methane is utilized via syngas chemistry, which is only economic at a large scale [2]. Oxidative methane coupling has attracted vast interest, but has inferior carbon efficiency when compared to nonoxidative methane conversion, because of the high selectivity towards CO<sub>2</sub> and CO. Since the pioneering work of Bragin and later Wang et al.,[3, 4] the direct aromatization of methane under reducing conditions has attracted a great deal of interest in the scientific community. In this process methane is converted to aromatics, mostly benzene as well as naphthalene, toluene and xylenes with simultaneous production of hydrogen. Ethylene and ethane are also produced in small quantities. The direct aromatization of CH<sub>4</sub> only occurs at harsh conditions, because of significant thermodynamic limitations. With a  $\Delta G_r^0 = +433 \text{ kJ/mol}$  and  $\Delta H_r^0 = +531 \text{ kJ/mol}$  it is only above 650 °C that conversion of CH<sub>4</sub> becomes significant [5]. The process has not been commercialized up to date. This is, to a large extent, due to the rapid deactivation of the Mo/HZSM-5 catalyst used (the best performing system so far) and to several important issues related with its regeneration [6-8].

Literature commonly agrees that methane is activated on Mo, which is present in a unique and highly dispersed form inside the channels of HZSM-5. However, Mo was shown to reduce in the beginning of the reaction suggesting that the reduced Mo-species is the active phase for methane dehydroaromatization [9-14]. Thus far, it is not entirely understood how the Mo oxide geometry of the as-synthesized catalyst transforms to the Mo carbide at reaction conditions and how the initial oxide structure influences the final carbide phase. Podkolzin *et al.* have used DFT calculations to find reasonable structures for the Mo carbide phase [15]. Certainty about the presence of these or other (oxy-)carbide structures at reaction conditions can only be reached by spectroscopic or other experimental observations, which are difficult to perform. Understanding this unique configuration is however crucial to guide Mo/HZSM-5 synthesis and to design new materials with similar catalytic behavior.

Regarding the influence of the Mo precursor on activity, the most important prerequisite is its presence inside the pores as isolated mono-[16] or bi-atomic[17] entities [18]. Because it is difficult to characterize the reduced Mo-species at reaction conditions, scientists often rely on characterizing the as-synthesized catalyst. The local geometry around Mo in Mo/HZSM-5 has been characterized by UV Raman using DFT calculations to match structures to the observed vibrations [16]. The dispersion of Mo has been investigated by UV Raman,[19] UV-Vis,[16, 20, 21] XANES[19, 22] and XPS[7, 23]. Both geometry and dispersion of the Mo-phase have been speculated to be important for catalysis [16, 18, 19, 21, 24, 25].

To shed more light on the relation between these well-dispersed Mo oxo units and catalytic performance, a promising approach is to manipulate their structure. To get a direct handle on the volatile Mo oxo species migrating into the pores during the synthesis is near to impossible. Thus, in this paper we chose to manipulate their siting instead. Since Mo is immobilized on the Brønsted acid sites (BASs) of the zeolite, which are made up of trivalent Al in the framework, Mo can be directed by synthesizing zeolites with those BAS in varied locations. With this, we present a systematic way to manipulate the local geometry of Mo and link it to its catalytic properties [16]. We aim to further understand which property of the precursor state: location, geometry or isolation is most important for the final performance of the Mo precursor.

## 2.2 Experimental Details

### 2.2.1 Catalyst Preparation

The synthesis procedure for the samples with low, medium and high concentration of Al pairs denoted HZ-L, HZ-M and HZ-H respectively was adapted from Dědecěk *et al* [26]. Solutions for the Al source, the Si source and the structure-directing agent (SDA) were prepared. The Al source solution was either  $\text{Al}(\text{NO}_3)_3 \cdot 9\text{H}_2\text{O}$  in DI-water (softened to 0.1°D, deionized via reverse-osmosis via a resistance of > 1 MOhm/cm, disinfected through an UV filter) keeping  $\text{H}_2\text{O}:\text{Al}(\text{NO}_3)_3 \cdot 9\text{H}_2\text{O}$  at 126 (solution A) or  $\text{AlCl}_3 \cdot 6\text{H}_2\text{O}$  in DI-water with  $\text{H}_2\text{O}:\text{AlCl}_3 \cdot 6\text{H}_2\text{O}$  = 128 (solution B). The Si source solution contained tetraethyl orthosilicate (TEOS) with ethanol keeping ethanol:TEOS = 1 and the SDA

containing solution was tetrapropylammonium hydroxide (TPAOH, 1 M in H<sub>2</sub>O) and DI-water keeping H<sub>2</sub>O:TPAOH = 101. In a typical synthesis, two solutions are mixed for 90 min after which the third solution is added to mix for another 90 min at ambient conditions. For **HZ-L**, Al-source solution A is mixed with the Si source solution first and then the SDA solution is added. For **HZ-M**, the Si source solution is mixed with Al source solution B and then the SDA is added. **HZ-H** was synthesized in the same manner as **HZ-M** only adding the SDA prior to the Si source. The Si/TPAOH ratio was kept at 2.65 and Si/Al at 25 for all syntheses. Subsequently, hydrothermal synthesis was performed at 170 °C in 45 ml Teflon liners in steel autoclaves with rotation for 10 days in the case of **HZ-L** and **HZ-H**. To obtain the same crystal size for all samples, a shorter duration for hydrothermal synthesis of 7 days was applied for **HZ-M**. The synthesized crystals were recovered by centrifugation and washing with DI-water 3 times. The so obtained crystals were left for drying overnight at 80 °C and then calcined at 550 °C for 7 h, heating at a rate of 2 °C/min.

**Na ion exchange** was achieved with 200 ml 1 M NaNO<sub>3</sub> solution per 1 g zeolite. The zeolite was exchanged for 7 h at 80 °C and afterwards recovered by centrifugation. Almost full Na ion exchange was achieved as confirmed by ICP (**Table A2.1**).

The samples were **exchanged with Co(NO<sub>3</sub>)<sub>2</sub>** following Na-exchange. The zeolite was left stirring in 200 ml 0.05 M solution per gram for 7 h at 80 °C and subsequently washed with DI-water and centrifuged 3 times. Co ion-exchange was repeated 3 times. Samples exchanged with Co are denoted by **CoHZ-x**, where x denotes the parent zeolites with a low (L), medium (M) or high (H) concentration of Al<sub>pairs</sub>.

**Mo was introduced** to the acid form of the zeolite through Incipient Wetness Impregnation (IWI) dissolving appropriate amounts of ammonium heptamolybdate (AHM) in a volume of water needed to fill the pores of the zeolite powder (210 µl/g). The samples are dried overnight at 80 °C and calcined at 550 °C for 7 h using a heating rate of 2 °C/min. Samples are thereafter denoted as **yMoHZ-x**, where y denotes the wt.% of Mo introduced. Catalysts were prepared with 2, 5 and 7.5 wt.% of Mo.

## 2.2.2 Catalyst characterization

**Low secondary Electron Imaging** (LEI) was used on a JEOL JSM-7500F Scanning Electron Microscope field emission scanning electron microscope (SEM) to produce high quality images of the catalysts. An acceleration voltage of 5 kV was used during image acquisition.

**Chemical composition** of the samples in terms of Mo, Co, Si and Al content was measured by digestion of approximately 50 mg sample in 4.5 ml 30 % HCl + 1.5 ml 65% HNO<sub>3</sub> + 0.2 ml 40 % HF using a microwave. The digestion time in the microwave was 60 min at 1000 W for 8 samples and 1300 W for 14 samples. After digestion, the samples were diluted to 50 ml with MQ and analyzed with ICP-OES on a PerkinElmer Optima 5300 (torch:Si+saffire injector). For Na a PerkinElmer AAS Modell AAnalyst 200 was used.

**X-ray powder diffraction** (XRD) data was collected on a Bruker D8 Advance diffractometer, operating in Bragg-Brentano geometry using Co K $\alpha$  radiation ( $\lambda = 0.179$  nm) and a Lynxeye position sensitive detector to collect data in the range of  $2\theta$  from 5° to 50° with a scan-speed of 0.2° s<sup>-1</sup> and a sample rotation rate of 30 rpm.

**N<sub>2</sub> adsorption** was performed on a TriStar II 3020 Version 3.02 (Micromeritics) at liquid nitrogen temperature,  $T = -196$  °C for determination of the BET area. The *t*-plot method was used to determine the micropore volume. Before adsorption, the catalyst was outgassed under a flow of N<sub>2</sub> at 350 °C for 16 h.

**Pyridine Transmission FTIR** spectroscopy was performed on a Nicolet 6700 spectrometer with a MCT/B detector. The sample was first activated in vacuum at 400 °C for 16 h to remove adsorbed species. After activation, the pyridine gas was fed to the pellets until saturated and further evacuated at 160 °C for 2 h. Spectra were recorded in 1000-4000 cm<sup>-1</sup> range at 4 cm<sup>-1</sup> resolution and co-addition of 128 scans. The spectra shown represent the subtraction result of the spectra collected before adsorption of pyridine from the one taken afterwards. All spectra were normalized by the framework absorbance at 1873 cm<sup>-1</sup>.

The **UV-Vis diffuse reflectance spectra** (UV-Vis-DRS) were collected on a Perkin-Elmer Lambda 900 spectrophotometer equipped with an integrating sphere ("Labsphere") in the 200–800 nm range. BaSO<sub>4</sub> was used as a white standard for **CoHZ-x** and the bare zeolite for **yMoHZ-x**.

Before measurement, the samples were degassed at 400 °C under N<sub>2</sub> flow for 12 h and then transferred to the sample

holders in the glovebox. The absorption intensity is expressed by the Schuster-Kubelka-Munk (**Equation 2.1**).

$$F(R_\infty) = (1 - R_\infty)^2 / 2R_\infty \quad (\text{Equation 2.1})$$

**Quantification of  $Al_{pairs}$  and determination of their location** is reported by Dědecěk *et al.*  $Al_F$  exists either as single Al or in pairs [26]. Co(II) ions selectively exchange with the Al in pairs at the applied exchange conditions [27]. Therefore, the following formula can be applied to calculate the number of  $Al_F$  in pairs.

$$Al_{pairs} = 2 * Co_{total} \quad (\text{Equation 2.2})$$

In addition, because Co replaces Na, the number of Al-pairs can also be calculated with:

$$Al_{single} = Na_{total} \quad (\text{Equation 2.3})$$

$$Al_F = Al_{single} + Al_{pairs} \quad (\text{Equation 2.4})$$

Where  $Co_{total}$  and  $Na_{total}$  represent the total amounts of exchanged  $Co^{2+}$  and  $Na^+$  cations present in the samples as determined by ICP. Co(II) ions can be either located in the straight or sinusoidal channels of the zeolite or at the intersection of the two. The distribution of  $Al_{pairs}$  among those sites is determined by deconvoluting the absorption bands of Co(II) in UV-Vis with Gaussians.

### 2.2.3 Catalytic Testing

Catalytic testing was performed in a quartz tube with an inner diameter of 6 mm, using 500 mg catalyst pelletized to pellets of 212 to 425  $\mu\text{m}$ . A weight hourly space velocity (WHSV) of 1.21  $\text{h}^{-1}$  was applied in all tests. Product analysis was achieved on an Interscience Trace GC with a TCD and two FIDs. A mixture 5 %  $N_2$  in  $CH_4$  was fed to the reactor. The reactor was brought to reaction temperature under the same flow with a heating rate of 10  $^\circ\text{C}/\text{min}$ . Although trace amount of many products were detected in the calculations the major products were considered (hydrogen, ethylene, ethane, propylene, benzene, toluene, xylenes and naphthalene).

Product yields were calculated according to **Equation 2.5**.

$$Y_{product} [\text{mol}\%] = \left( \frac{F_{C_i H_j}}{F_{CH_4,in}} \right) * i * 100\% \quad (\text{Equation 2.5})$$

### 2.2.4 DFT calculations

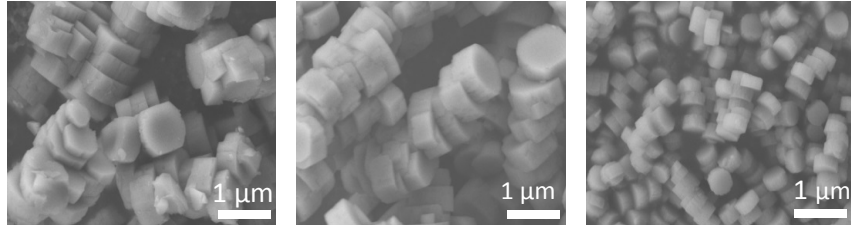
Periodic DFT calculations were performed using the Vienna Ab initio Simulation Package (VASP) [28, 29]. The exchange–correlation energy was described by the generalized gradient approximation PBE functional [30]. A plane-wave basis set with a cut-off of 500 eV in combination with the projected augmented wave (PAW) method was used [31, 32]. Brillouin zone-sampling was restricted to the  $\Gamma$  point. The orthogonal MFI unit cell with lattice parameters of  $a = 20.241 \text{ \AA}$ ,  $b = 20.015 \text{ \AA}$ , and  $c = 13.439 \text{ \AA}$  as optimized by DFT with an all-silica MFI periodic model was used for all calculations. The optimized unit cell parameters agree well with experimental data for calcined ZSM-5 [33]. To compensate for the positive charge of the extra-framework cationic Mo-oxo complexes, one or two framework  $\text{Si}^{4+}$  ions in MFI unit cell were substituted by  $\text{Al}^{3+}$ .

## 2.3 Results

In the Mo/HZSM-5 system, Mo oxide replaces the proton that balances trivalent Al in the HZSM-5 framework. The geometry of Mo oxide and its anchoring can be controlled by manipulating the location of Al in the framework. This  $\text{Al}_F$  siting was directed by the synthesis procedure, namely the source of Al used as well as the order of mixing of structure directing agent (SDA), Al source and silica source (see **Table 2.1**). Structural properties from  $\text{N}_2$  Adsorption are summarized in **Table 2.1**, while the morphology is shown in the SEM images in **Figure 2.1**. All zeolites synthesized exhibited the typical diffraction pattern of MFI (**Figure A2.1**). Structural properties (**Figure A2.2**), morphology and particle size are very similar for all three synthesized HZSM-5 zeolites.

Table 2.1. Synthesis mixture, Si/Al, and structural properties of the three synthesized zeolites.

Sample	Synthesis	Si/Al	$S_{\text{external}}$ $\text{m}^2/\text{g}$	$S_{\text{micro}}$ $\text{m}^2/\text{g}$	$S_{\text{total}}$ $\text{m}^2/\text{g}$	$V_{\text{micro}}$ $\text{cm}^3/\text{g}$
<b>HZ-L</b>	$\text{Al}(\text{NO}_3)_3 \cdot 9\text{H}_2\text{O}$ , TEOS, TPAOH	$24.2 \pm 2.4$	31	377	408	0.15
<b>HZ-M</b>	TEOS, $\text{AlCl}_3 \cdot 6\text{H}_2\text{O}$ , TPAOH	$24.5 \pm 2.4$	31	381	413	0.15
<b>HZ-H</b>	TPAOH, $\text{AlCl}_3 \cdot 6\text{H}_2\text{O}$ , TEOS	$22.0 \pm 2.2$	34	378	412	0.15


Figure 2.1. SEM images of **HZ-L** (left) **HZ-M** (middle) **HZ-H** (right).

In agreement with the similar structural properties, the three samples show virtually identical  $^{27}\text{Al}$  NMR spectra (**Figure A2.3**) where the majority of Al is in a tetrahedral conformation and about 4-5 % present as extra-framework Al. Only for **HZ-H** the peak corresponding to tetrahedral Al is shifted by 0.5 ppm, which can be explained by the slightly lower Si/Al ratio.

However, the three HZSM-5 differ greatly in terms of Al location. The three samples have different fractions of Al in pairs ( $\text{Al}_{\text{pairs}}$ ) vs.  $\text{Al}_{\text{single}}$ . Where  $\text{Al}_{\text{pairs}}$  consists of two framework Al ( $\text{Al}_F$ ) separated by two Si-O units ( $\text{Al}-\text{O}-(\text{Si}-\text{O})_2-\text{Al}$ ) and  $\text{Al}_{\text{single}}$  is an Al separated from another Al by more than two Si-O units. **Figure 2.2a** shows that **HZ-L** has the lowest percentage of  $\text{Al}_{\text{pairs}}$  (38% of  $\text{Al}_F$ ) and **HZ-H** the highest (72 % of  $\text{Al}_F$ ), while **HZ-M** lies in-between. This is determined by **Equation 2.3** according to the method developed by Dědecěk and co-workers to identify the location of  $\text{Al}_F$  using cobalt (Co) exchange. **Figure 2.2b** shows the UV-Vis absorption of all three samples, where the intensity of the bands characteristic for Co cations increase from **HZ-L** to **HZ-H**. We further utilized these bands to locate the  $\text{Al}_{\text{pairs}}$  in  $\alpha$ ,  $\beta$  and  $\gamma$  sites, positioned in the straight channel, at the intersection of straight and sinusoidal channels and in the sinusoidal channels, respectively. UV-Vis spectra and Gaussian deconvolution of those bands are shown in **Figure 2.2c-d**.

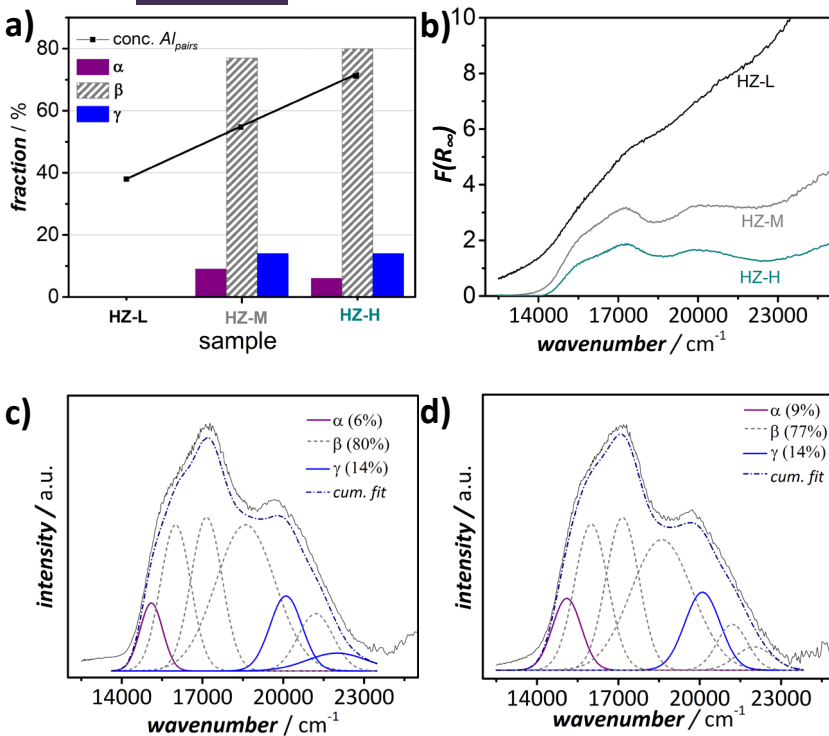


Figure 2.2 a) Percentage of Al in  $Al_{pairs}$  calculated using **Equation 2.3** and the distribution of  $Al_{pairs}$  in  $\alpha$ -,  $\beta$ - and  $\gamma$ -sites from deconvolution of UV-Vis DRS spectra; b) UV-Vis DRS spectra prior to baseline subtraction; c) baseline subtracted UV-Vis DRS spectra with deconvolution using Gaussians for **HZ-H** and d) **HZ-M**.

**Figure 2.2a** summarized the distribution of  $Al_{pairs}$  among the  $\alpha$ ,  $\beta$  and  $\gamma$  sites for **HZ-M** and **HZ-H** obtained from Gaussian deconvolution, where  $\alpha$ -sites are identified with the band at  $15100\text{ cm}^{-1}$ ,  $\beta$ -sites with the bands at  $16000$ ,  $17150$ ,  $18600$  and  $21200\text{ cm}^{-1}$ , while Co in  $\gamma$ -sites gives rise to bands  $20100$  and  $22000\text{ cm}^{-1}$ . The bands in **HZ-L** were not intense enough to achieve meaningful results from Gaussian deconvolution. Deconvolution for the other catalysts reveals a similar distribution of  $Al_{pairs}$  among the three different sites, with most  $Al_{pairs}$  located in the  $\beta$ -sites at the intersection of the straight and sinusoidal channels of MFI. Only about 20 % of  $Al_{pairs}$  are located in the straight ( $\alpha$ -site) and sinusoidal channels ( $\gamma$ -site) of the MFI structure.

Mo structures optimized by DFT calculations (**Figure 2.3**) show different geometries depending on whether they are anchored on  $Al_{pairs}$  or  $Al_{single}$ . Energies relative to the  $\gamma$ -site calculated for Mo oxide structures anchored to both  $Al_{pairs}$  or  $Al_{single}$  are low for all three sites considered here, namely  $\alpha$ ,  $\beta$  and  $\gamma$ . Because of these small energy differences, differences in location of  $Al_F$  can direct Mo to be present in varying dispersion (**Figure 2.4**) and geometry. To determine the size of Mo species or rather the number of Mo-O-Mo bonds formed, the edge energy of Mo, obtained from UV-Vis, was compared with known references as shown by Wachs et al [34].

**Figure 2.4a** shows that for all samples Mo is present as monomeric species at low (2 wt.%) Mo loading, corresponding to  $Mo/Al = 0.35$ . At higher loadings however, the zeolites show very different dispersion. While a significant amount of Mo is still present as monomeric species in **HZ-L**, in **HZ-M** and **HZ-H** Mo already starts forming Mo clusters at  $Mo/Al = 0.9$ . The more  $Al_{pairs}$  are present in the sample, the more clustering occurs, because one Mo will bind to two  $Al_F$  and therefore more  $Al_F$  is needed to incorporate the same amount of Mo. This is further confirmed by Pyridine FTIR quantification of the Lewis acid sites (LAS) absorbance at  $1455\text{ cm}^{-1}$  and the Brønsted acid sites (BAS) band at  $1546\text{ cm}^{-1}$  shown in **Figure 2.4b** (see **Figure A2.4-5** for full spectra) [35]. While the concentration of both LAS and BAS (**Figure 2.4b**) as well as the acid strength (**Figure A2.6**) of the pristine zeolites is similar, upon incorporating 2 wt.% Mo especially BAS decreases to a higher extent for **HZ-H** than for **HZ-L**. Acidity decreases to 65 % of the initial value for 2 wt.% Mo loading ( $Mo/Al = 0.35$ , see **Table A2.2** for ratios determined by ICP) for **HZ-L**, which means that one  $Al_F$  is blocked for each Mo incorporated. For **HZ-H** Brønsted acidity decreases by more than 65 %, leading to 1.5 acid sites neutralized per Mo incorporated (see right axis in **Figure 2.4b**) confirming that Mo binds to  $Al_{pairs}$  in this case. Incorporation of more Mo, does not decrease the acid site concentration any further, suggesting that instead of anchoring to the framework, Mo is increasingly present in clusters. XPS being a surface sensitive technique confirms these findings further (**Figure A2.7**). For 5 wt.% and 7.5 wt.% loading, a higher concentration of Mo is seen with this surface sensitive technique than what is determined by the bulk technique ICP (**Figure A2.7, Table A2.2**), which means that a significant amount of Mo is agglomerated at the surface of the zeolite for these high loadings.

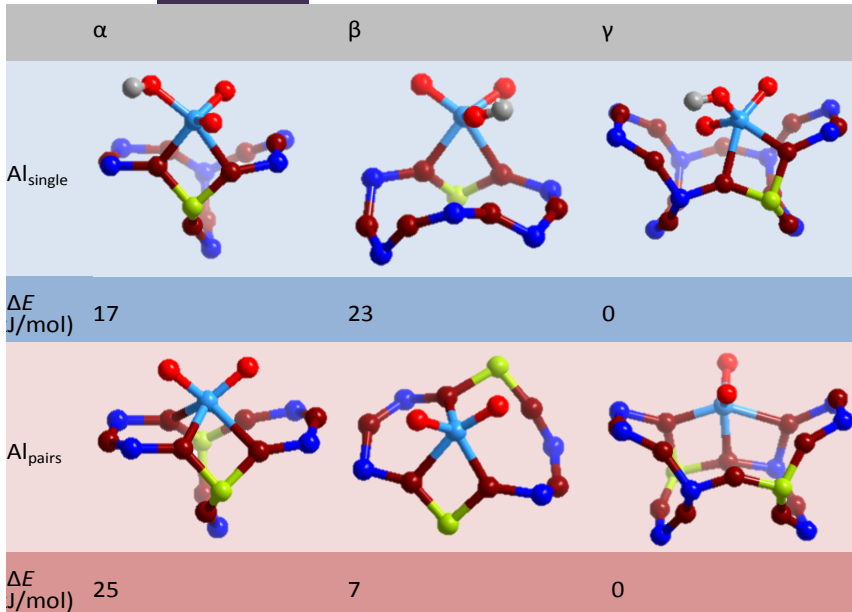


Figure 2.3 Results of geometry optimization with DFT for Mo oxide anchored either to  $Al_{single}$  (top) or  $Al_{pairs}$  (bottom) in  $\alpha$ ,  $\beta$  and  $\gamma$  positions. Energies relative to the  $\gamma$ -site are given below the images.

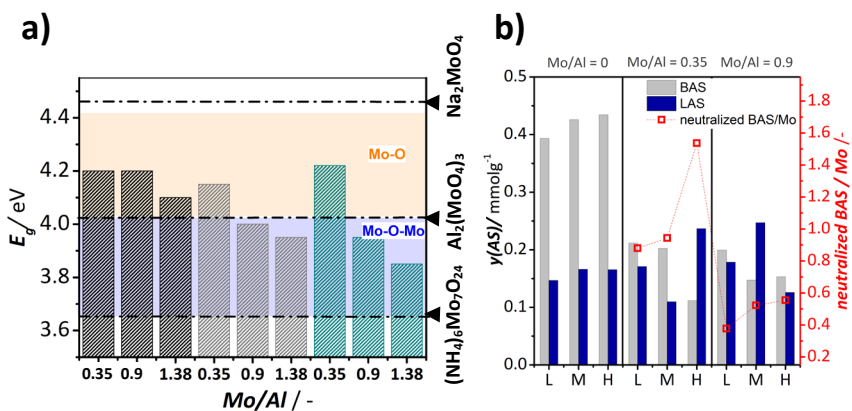


Figure 2.4 a)  $E_g$  obtained with the Tauc plot method for samples (black: HZ-L, grey: HZ-M, turquoise: HZ-H) with different Mo loadings and references. Full spectra in [Figure A2.8 to 11](#). b) Concentration of BAS and LAS in HZ-x for different Mo-loading. Mo/Al = 0.35 and 0.9 correspond to 2 wt.% and 5 wt.% of Mo respectively.

In contrast, the Mo loadings obtained from ICP and XPS match very well for 2 wt.% again confirming that Mo is very well dispersed for these catalysts. This was also observed by Liu *et al.* [22]. DFT structure optimization (**Figure 2.3**) revealed the different geometries for Mo oxide anchoring to  $Al_{pairs}$  vs.  $Al_{single}$ . This difference in geometry arises from the difference of one negative charge present when binding to two vs. one  $Al_F$ , which is compensated by another dangling oxygen.

This systematic approach to altering the geometry and dispersion of Mo finally allows drawing the crucial connection to catalytic performance in MDA. The three zeolites with 2 wt.% and 5 wt.% Mo loading were tested at 650 °C. The methane conversion reaches 4.5 % for 2 wt.% Mo and around 7 % for 5 wt.% Mo in the initial period of the reaction, but decreases to about 1 % during the initial 2 hours on stream for both Mo loadings (**Figure 2.5**). Benzene is formed with the highest yield, followed by naphthalene. Only negligible amounts of toluene, ethane and ethylene are formed. Within experimental accuracy the catalytic performance (activity, selectivity and deactivation) of all three zeolites is the same. This was also observed when testing the catalysts at 760 °C (**Figure A.12**), although deactivation is faster in that case (**Figure A2.13**). This is explained by the fact that the bonds the Mo precursor forms with the framework and its geometry transform significantly at reaction conditions. It was shown that the Mo gets reduced under these conditions which is likely to break at least one bond of the Mo with the framework thereby changing its geometry, as demonstrated for Tungsten [17]. The catalytic results also imply that both Mo anchoring to  $Al_{pairs}$  as well as  $Al_{single}$  reduce easily enough leading to a similar delay in onset of the reaction. In all catalysts prepared in this work, enough isolated Mo oxo units are inside the pores of the zeolite to lead to similar catalytic behavior, so that seems to be the more important factor for this particular system.

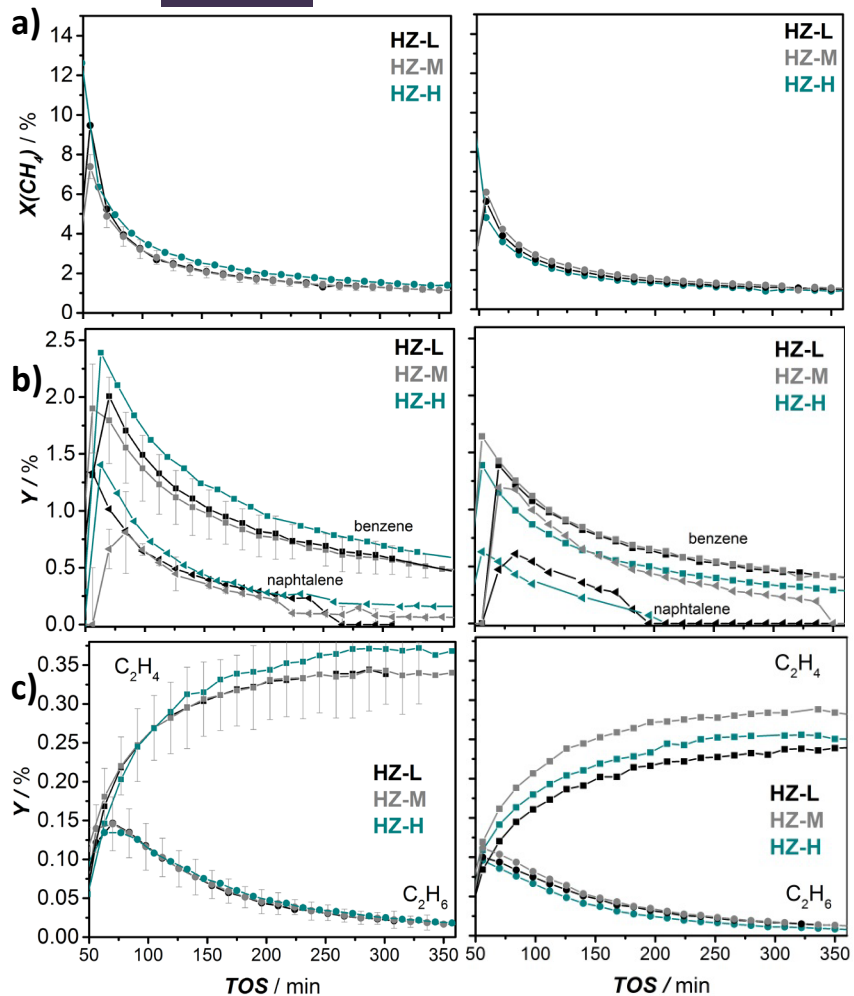


Figure 2.5 a) CH<sub>4</sub> conversion, b) naphthalene and benzene yield, c) ethylene and ethane yield, for 5MoHZ-x (left) and 2MoHZ-x (right) at 650 °C with WHSV = 1.21 h<sup>-1</sup> and 500 mg catalyst.

## 2.4 Conclusions

These results suggest that the precursor state of the Mo and the aluminum distribution in the three ZSM-5 samples plays no decisive role in the final performance for methane dehydroaromatization. We attribute this effect to the significant transformation of the local environment and binding of Mo at reaction conditions. At the reaction temperatures methane converts the Mo oxide into Mo (oxy-)carbide, which was shown to be the active phase in this reaction [9-14]. In this sense, the isolation of the Mo oxo units and their location inside the channels of the zeolite seem to be crucial in the development of an efficient pre-catalyst. The geometry does not play a role, likely because it is transformed upon carburization. With this work, we bridge the gap between the Mo precursor state and catalytic performance. So far research has either focused on extensive characterization of the Mo precursor[16, 18, 21] or on measuring the effect of other factors on the catalytic performance [36-38]. Our results underscore the necessity to develop appropriate characterization tools for methane dehydroaromatization catalysts that elucidate how the actual catalytic site forms under reaction conditions [21, 25].

## 2.5 References

- [1] J.H. Lunsford, Catalytic conversion of methane to more useful chemicals and fuels: a challenge for the 21st century, *Catalysis Today*, 63 (2000) 165-174.
- [2] J. Raskó, J. Kiss, Infrared study of the adsorption of CO and CH<sub>3</sub> on silica-supported MoO<sub>3</sub> and Mo<sub>2</sub>C catalysts, *Applied Catalysis A: General*, 253 (2003) 427-436.
- [3] L. Wang, L. Tao, M. Xie, G. Xu, J. Huang, Y. Xu, Dehydrogenation and aromatization of methane under non-oxidizing conditions, *Catalysis Letters*, 21 (1993) 35-41.
- [4] O. Bragin, T. Vasina, Y.I. Isakov, B. Nefedov, A. Preobrazhenskii, N. Palishkina, K.M. Minachev, Catalytic aromatization of methane and ethane, *Russian Chemical Bulletin*, 31 (1982) 847-847.
- [5] S. Ma, X. Guo, L. Zhao, S. Scott, X. Bao, Recent progress in methane dehydroaromatization: From laboratory curiosities to promising technology, *Journal of Energy Chemistry*, 22 (2013) 1-20.
- [6] K. Honda, X. Chen, Z.-G. Zhang, Identification of the coke accumulation and deactivation sites of Mo<sub>2</sub>C/HZSM-5 catalyst in CH<sub>4</sub> dehydroaromatization, *Catalysis Communications*, 5 (2004) 557-561.
- [7] N. Kosinov, F.J. Coumans, G. Li, E. Uslamin, B. Mezari, A.S. Wijpkema, E.A. Pidko, E.J. Hensen, Stable Mo/HZSM-5 methane dehydroaromatization catalysts optimized for high-temperature calcination-regeneration, *Journal of Catalysis*, 346 (2017) 125-133.
- [8] A. Jens, B. Rainer, M. Leslaw, Methane Direct Aromatization Process from an Industrial Perspective: Technical Catalyst and Conceptual Design for Reactor and Process, in: *Small-Scale Gas to Liquid Fuel Synthesis*, CRC Press, 2015, pp. 531-560.
- [9] H. Jiang, L. Wang, W. Cui, Y. Xu, Study on the induction period of methane aromatization over Mo/HZSM-5: partial reduction of Mo species and formation of carbonaceous deposit, *Catalysis Letters*, 57 (1999) 95-102.
- [10] I. Lezcano-González, R. Oord, M. Rovezzi, P. Glatzel, S.W. Botchway, B.M. Weckhuysen, A.M. Beale, Molybdenum Speciation and its Impact on Catalytic Activity during Methane Dehydroaromatization in Zeolite ZSM-5 as Revealed by Operando X-Ray Methods, *Angewandte Chemie International Edition*, 55 (2016) 5215-5219.
- [11] F. Solymosi, A. Szöke, J. Cserényi, Conversion of methane to benzene over Mo<sub>2</sub>C and Mo<sub>2</sub>C/ZSM-5 catalysts, *Catalysis Letters*, 39 (1996) 157-161.
- [12] D. Wang, J. Lunsford, M. Rosynek, Catalytic conversion of methane to benzene over Mo/ZSM-5, *Topics in Catalysis*, 3 (1996) 289-297.
- [13] S. Liu, L. Wang, R. Ohnishi, M. Lchikawa, Bifunctional catalysis of Mo/HZSM-5 in the dehydroaromatization of methane with CO/CO<sub>2</sub> to benzene and naphthalene, *Kinetics and catalysis*, 41 (2000) 132-144.
- [14] W. Ding, S. Li, G. D Meitzner, E. Iglesia, Methane conversion to aromatics on Mo/H-ZSM5: structure of molybdenum species in working catalysts, *The Journal of Physical Chemistry B*, 105 (2001) 506-513.
- [15] J. Gao, Y. Zheng, G.B. Fitzgerald, J. de Joannis, Y. Tang, I.E. Wachs, S.G. Podkolzin, Structure of Mo<sub>2</sub>C<sub>x</sub> and Mo<sub>4</sub>C<sub>x</sub> Molybdenum Carbide

- Nanoparticles and Their Anchoring Sites on ZSM-5 Zeolites, *The Journal of Physical Chemistry C*, 118 (2014) 4670-4679.
- [16] J. Gao, Y. Zheng, J.-M. Jehng, Y. Tang, I.E. Wachs, S.G. Podkolzin, Identification of molybdenum oxide nanostructures on zeolites for natural gas conversion, *Science*, 348 (2015) 686-690.
- [17] W. Ding, G.D. Meitzner, D.O. Marler, E. Iglesia, Synthesis, Structural Characterization, and Catalytic Properties of Tungsten-Exchanged H-ZSM5, *The Journal of Physical Chemistry B*, 105 (2001) 3928-3936.
- [18] J.-P. Tessonnier, B. Louis, S. Walspurger, J. Sommer, M.-J. Ledoux, C. Pham-Huu, Quantitative Measurement of the Brönsted Acid Sites in Solid Acids: Toward a Single-Site Design of Mo-Modified ZSM-5 Zeolite, *The Journal of Physical Chemistry B*, 110 (2006) 10390-10395.
- [19] J.P. Thielemann, T. Ressler, A. Walter, G. Tzolova-Müller, C. Hess, Structure of molybdenum oxide supported on silica SBA-15 studied by Raman, UV-Vis and X-ray absorption spectroscopy, *Applied Catalysis A: General*, 399 (2011) 28-34.
- [20] R. Kumar Rana, B. Viswanathan, Mo incorporation in MCM-41 type zeolite, *Catalysis Letters*, 52 (1998) 25-29.
- [21] C. Sun, S. Yao, W. Shen, L. Lin, Highly Dispersed Molybdenum Oxide Supported on HZSM-5 for Methane Dehydroaromatization, *Catalysis Letters*, 122 (2008) 84-90.
- [22] S. Liu, L. Wang, R. Ohnishi, M. Ichikawa, Bifunctional Catalysis of Mo/HZSM-5 in the Dehydroaromatization of Methane to Benzene and Naphthalene XAFS/TG/DTA/MASS/FTIR Characterization and Supporting Effects, *Journal of Catalysis*, 181 (1999) 175-188.
- [23] B.S. Liu, L. Jiang, H. Sun, C.T. Au, XPS, XAES, and TG/DTA characterization of deposited carbon in methane dehydroaromatization over Ga-Mo/ZSM-5 catalyst, *Applied Surface Science*, 253 (2007) 5092-5100.
- [24] J.-Z. Zhang, M.A. Long, R.F. Howe, Molybdenum ZSM-5 zeolite catalysts for the conversion of methane to benzene, *Catalysis Today*, 44 (1998) 293-300.
- [25] D. Wang, J.H. Lunsford, M.P. Rosynek, Characterization of a Mo/ZSM-5 Catalyst for the Conversion of Methane to Benzene, *Journal of Catalysis*, 169 (1997) 347-358.
- [26] J. Dedecek, V. Balgová, V. Pashkova, P. Klein, B. Wichterlová, Synthesis of ZSM-5 Zeolites with Defined Distribution of Al Atoms in the Framework and Multinuclear MAS NMR Analysis of the Control of Al Distribution, *Chemistry of Materials*, 24 (2012) 3231-3239.
- [27] J. Dědeček, B. Wichterlová, Co<sup>2+</sup> Ion Siting in Pentasil-Containing Zeolites. I. Co<sup>2+</sup> Ion Sites and Their Occupation in Mordenite. A Vis-NIR Diffuse Reflectance Spectroscopy Study, *The Journal of Physical Chemistry B*, 103 (1999) 1462-1476.
- [28] G. Kresse, J. Hafner, Ab initio molecular dynamics for liquid metals, *Physical Review B*, 47 (1993) 558.
- [29] G. Kresse, J. Furthmüller, Efficiency of ab-initio total energy calculations for metals and semiconductors using a plane-wave basis set, *Computational Materials Science*, 6 (1996) 15-50.

- [30] J.P. Perdew, K. Burke, M. Ernzerhof, Generalized gradient approximation made simple, *Physical review letters*, 77 (1996) 3865.
- [31] G. Kresse, D. Joubert, From ultrasoft pseudopotentials to the projector augmented-wave method, *Physical Review B*, 59 (1999) 1758.
- [32] P.E. Blöchl, Projector augmented-wave method, *Physical Review B*, 50 (1994) 17953.
- [33] H. Van Koningsveld, J. Jansen, H. Van Bekkum, The monoclinic framework structure of zeolite H-ZSM-5. Comparison with the orthorhombic framework of as-synthesized ZSM-5, *Zeolites*, 10 (1990) 235-242.
- [34] H. Tian, C.A. Roberts, I.E. Wachs, Molecular Structural Determination of Molybdena in Different Environments: Aqueous Solutions, Bulk Mixed Oxides, and Supported MoO<sub>3</sub> Catalysts, *The Journal of Physical Chemistry C*, 114 (2010) 14110-14120.
- [35] I. Yarulina, S. Bailleul, A. Pustovarenko, J.R. Martinez, K.D. Wispelaere, J. Hajek, B.M. Weckhuysen, K. Houben, M. Baldus, V. Van Speybroeck, F. Kapteijn, J. Gascon, Suppression of the Aromatic Cycle in Methanol-to-Olefins Reaction over ZSM-5 by Post-Synthetic Modification Using Calcium, *ChemCatChem*, 8 (2016) 3057-3063.
- [36] J.-P. Tessonnier, B. Louis, S. Rigolet, M.J. Ledoux, C. Pham-Huu, Methane dehydro-aromatization on Mo/ZSM-5: About the hidden role of Brønsted acid sites, *Applied Catalysis A: General*, 336 (2008) 79-88.
- [37] A. Martínez, E. Peris, A. Vidal-Moya, Modulation of zeolite acidity by post-synthesis treatments in Mo/HZSM-5 catalysts for methane dehydroaromatization, in: P.M. Antoine Gédéon, B. Florence (Eds.) *Studies in Surface Science and Catalysis*, Elsevier, 2008, pp. 1075-1080.
- [38] H. Liu, Y. Li, W. Shen, X. Bao, Y. Xu, Methane dehydroaromatization over Mo/HZSM-5 catalysts in the absence of oxygen: effects of silanation in HZSM-5 zeolite, *Catalysis Today*, 93–95 (2004) 65-73.



## Annex chapter 2

**Relevance of the Mo-precursor state in H-ZSM-5  
for methane dehydroaromatization**

**Contents**

<b>A2.1 Catalyst characterization</b>	61
A2.1.1 Na exchange (ICP)	61
A2.1.2 Morphology	61
A2.1.3 $^{27}\text{Al}$ NMR	62
A2.1.4 Acidity	63
A2.1.5 $^{31}\text{P}$ NMR of adsorbed TMPO	66
A2.1.6 Mo content (ICP)	68
A2.1.7 X-ray photoelectron spectroscopy	68
A2.1.8 UV-Vis	69
<b>A2.2 Catalytic performance at 760 °C</b>	72
<b>A2.3 References</b>	75

**A2. 1 Catalyst characterization**

**A2.1.1 Na exchange (ICP)**

ICP was performed on **HZ-M** after Na-exchange to confirm the complete exchange of protons with Na. **Table A2.1** shows that the Na/Al ratio is between 0.8 and 0.86. From Pyridine IR it is known that about 20 % of Al is present as EFAI, which means that all BAS are associated with Na after the Na-exchange method applied here.

Table A2.1. Molar ratio Na/Al after sodium exchange as determined by ICP.

	Na/Al
NaHZ-M	0.80
NaHZ-M duplicate	0.86

### A2.1.2 Morphology

**X-ray powder diffraction** (XRD) data was collected on a Bruker D8 Advance diffractometer, operating in Bragg-Brentano geometry using Co  $K\alpha$  radiation ( $\lambda = 0.179$  nm) and a Lynxeye position sensitive detector to collect data in the range of  $2\theta$  from 5° to 50° with a scan-speed of  $0.2^\circ s^{-1}$  and a sample rotation of 30 rpm.

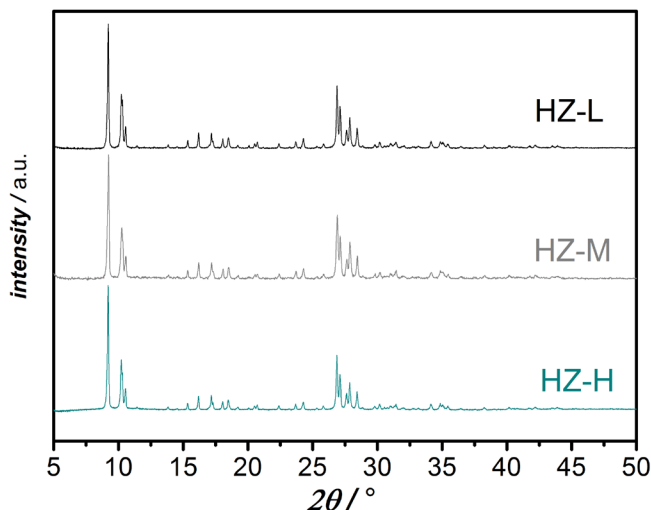


Figure A2.1. Normalized XRD patterns of all samples with the typical diffraction peaks for MFI zeolite.

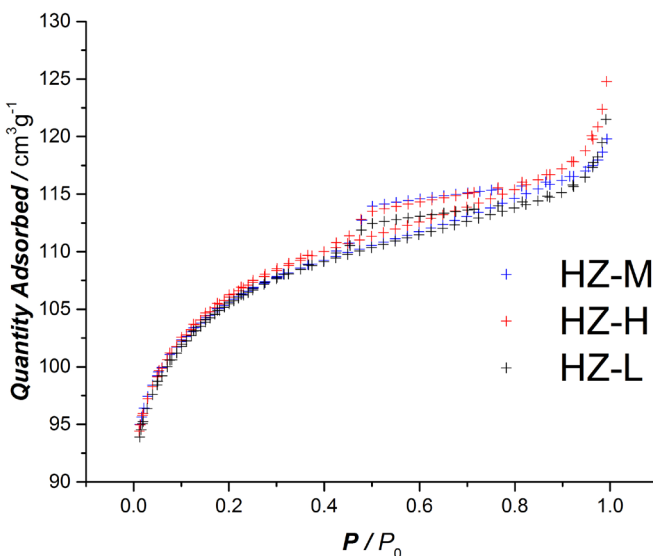


Figure A2.2. N<sub>2</sub> Adsorption Isotherms at -169 °C for the three different H-ZSM-5 zeolites.

### A2.1.3 <sup>27</sup>Al NMR

<sup>27</sup>Al solid-state NMR (ssNMR) measurements were recorded on a wide-bore Bruker Avance III 500 MHz spectrometer equipped with 3.2 mm magic angle spinning (MAS) probe. The temperature was set to 25 °C and the MAS frequency was 18 kHz, resulting in an effective temperature of approximately 30 °C. <sup>27</sup>Al spectra were referenced externally to the <sup>27</sup>Al signal at 0 ppm of a non-spinning Al(NO<sub>3</sub>)<sub>3</sub> solution. The spectra were recorded using a 0.78 us pi/12 excitation pulse and an acquisition time of 6.6 ms. 1024 Scans were accumulated with a recycle delay of 0.8 s. Spectra were processed using a 20 Hz line-broadening window.

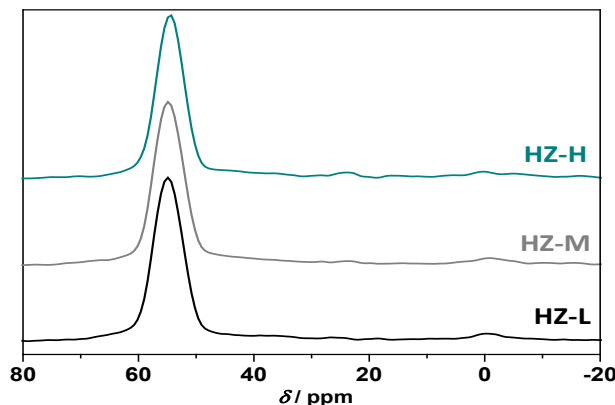


Figure A2.3.  $^{27}\text{Al}$  NMR for the three different zeolites.

#### A2.1.4 Acidity

FTIR with the probe molecule pyridine was performed to characterize both Lewis (LAS) as well as Brønsted acidity (BAS). 50 mg of zeolite sample was pressed into round wafers with a diameter 80 mm using 4.29 bar pressure. Quantification was achieved by assuming an acid concentration of 0.6 mmol/g for the bare zeolite as this is the value corresponding to the Al content of a zeolite with Si/Al = 25. It was assumed that all Al contributes to the acidity only 4-5% of Al was present as extra-framework Al (EFAl) as shown by  $^{27}\text{Al}$  NMR. All other samples were quantified in relation to this value. The error of the measurements can be estimated comparing the values obtained for the three pristine zeolites. Since we know from the TMPO study as well as  $^{27}\text{Al}$  NMR that the three pristine zeolites have very similar acidity, differences seen with Py IR can be estimated to represent the error. This amounts to 0.052 mmol/g. **Figure A2.4** shows the spectra of the samples before incorporation of Mo and with 2 wt.% as well as with 5 wt.% Mo. The fresh samples before Mo incorporation show a band for BAS at  $1546 \text{ cm}^{-1}$  as well as one for Lewis acidity at  $1455 \text{ cm}^{-1}$ , probably arising from EFAl [1]. The bands at  $1621 \text{ cm}^{-1}$  and  $1635 \text{ cm}^{-1}$  also correspond to LAS and BAS, respectively. Comparing spectra before and after incorporation of Mo, a new band appears ( $1612 \text{ cm}^{-1}$ ) corresponding to Lewis acidity arising from Mo oxide species anchored to the zeolite. Upon incorporation of more Mo, the LAS band at  $1455 \text{ cm}^{-1}$  shifts to  $1452 \text{ cm}^{-1}$  while a new band appears at  $1440 \text{ cm}^{-1}$  for 2 wt.% loading and disappears

again at 5 wt.% Mo loading. To confirm the adequacy of the degassing pre-treatment at 400 °C, one sample, **2MoHZ-M** was subjected to 10 min of re-calcination at 550 °C, followed by degassing for 1 h at the same temperature. For this a custom-made quartz cell that could withstand such high temperatures was developed. A pellet with a diameter of 10 mm was prepared from 50 mg and pressed at 4 tonne. After the re-calcination treatment, the sample was subjected to pyridine treatment, then left under excess of pyridine for 1 h at 160 °C after which it was evacuated for 5 h. For comparison, the same sample degassed under the same conditions as the samples shown in **Figure A2.4**, but in the custom-made quartz cell and then subjected to pyridine as described above. **Figure A2.5** shows the spectra for both treatments. It can be seen that the re-calcination leads to an increase in acidity accompanied by changes in the LAS bands. This is likely due to clustering happening during the re-calcination treatment. It is clear that a re-calcination treatment does lead to the unwanted redistribution of Mo, which is hard to control at such high temperatures. We conclude that degassing the sample at 400 °C is a more suitable pre-treatment for Py IR, if one wants to compare different Mo/HZSM-5 catalysts.

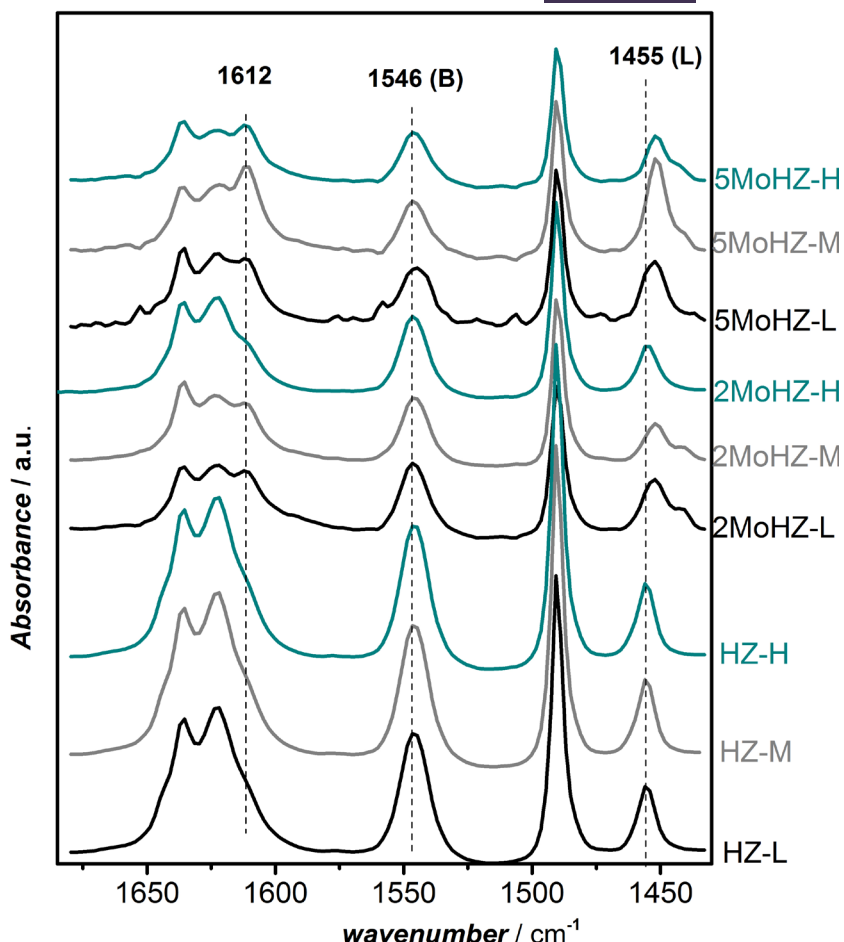


Figure A2.4 Transmission pyridine FTIR spectra of (from bottom to top) increasing amounts of Mo incorporated into the samples

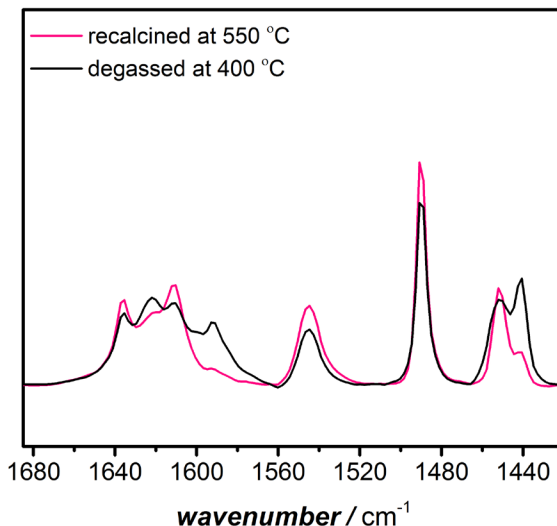


Figure A2.5. Transmission pyridine FTIR spectra of **2MoHZ-M** re-calcined at 550 °C compared to the same sample degassed in the same manner as the samples shown in **Figure A2.4**.

#### A2.1.5 $^{31}\text{P}$ NMR of adsorbed TMPO

To confirm that not only concentration of LAS and BAS are similar for the three parent zeolites, we performed additional characterization by solid-state NMR spectrometry using trimethylphosphine oxide (TMPO) as a probe molecule (**Figure A2.6**). For solid-state NMR measurements using trimethoxyphosphine oxide (TMPO) as a probe molecule, the preparation procedure was adapted from Wiper *et al.* [2]. TMPO (17 mg) was dissolved in anhydrous  $\text{CH}_2\text{Cl}_2$  (5 mL) in an Ar glove box. A 5 mL volume of this solution was added to 150 mg of the zeolite, dehydrated at 400 °C for 16 h, and left under stirring for 1 h. Subsequently, materials were evacuated under cooling to -10 °C and subsequently heated at 150 °C for 1 h under vacuum to allow homogeneous distribution of TMPO. Finally, cooled down samples were transferred into a zirconia MAS rotor (3.2 mm).  $^{31}\text{P}$  solid-state NMR measurements were recorded on a wide-bore Bruker Avance III 500 MHz spectrometer equipped with 3.2 mm magic angle spinning (MAS) probe. The temperature was set to 298K and the MAS frequency was set to 19 kHz.  $^{31}\text{P}$  spectra were acquired using a  $^1\text{H}$ - $^{31}\text{P}$  cross-polarization transfer by using a

46 kHz field on  $^{31}\text{P}$  and a ramped (70 to 100%) 94 kHz field on  $^1\text{H}$  with a contact time of 4.2 ms. During acquisition 83 kHz  $^1\text{H}$  decoupling was employed using SPINAL64.

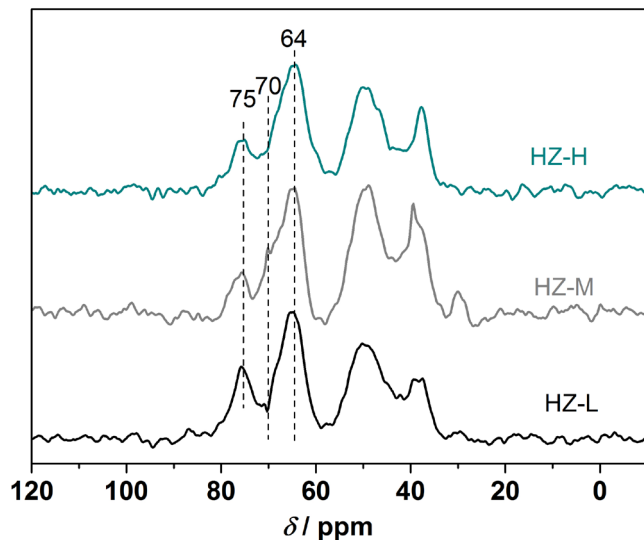


Figure A2.6.  $^1\text{H}$ - $^{31}\text{P}$  CP MAS NMR spectra for TMPO adsorbed on **HZ-x**.

The  $^{31}\text{P}$  spectra were referenced externally to the  $^{31}\text{P}$  signal at 0 ppm of a non-spinning  $\text{H}_3\text{PO}_4$  solution. Each experiment was acquired with 256 scans and a recycle delay of 4 s [3].

The  $^{31}\text{P}$  resonance peaks at 75, 70, 64, 50, 38 and 30 ppm are observed for all three zeolites. The resonance peak at 30 ppm is ascribed to “mobile” TMPO, and peaks at 50 and 38 ppm are characteristic for physisorbed TMPO [4, 5]. Peaks in the range between 60 and 90 ppm are arising from  $\text{TMPOH}^+$  complexes on Brønsted acid sites [6]. The location of the peaks as well as the intensities are very similar for the three parent zeolite, confirming that not only acid site concentration, but also acid strength is very similar for the three parent zeolites.

### A2.1.6 Mo content (ICP)

Table A2.2. Molar ratio Mo/Al as determined by ICP.

	Mo/Al
<b>2MoHZ-L</b>	0.35
<b>2MoHZ-M</b>	0.34
<b>2MoHZ-H</b>	0.29
<b>5MoHZ-L</b>	0.86
<b>5MoHZ-M</b>	0.76
<b>5MoHZ-H</b>	0.70

### A2.1.7 X-ray photoelectron spectroscopy (XPS)

X-ray photoelectron spectroscopy (XPS) analysis was performed in order to identify any agglomeration of Mo on the zeolite surface. A Thermo Scientific K-alpha spectrometer equipped with a monochromatic Al  $K\alpha$  X-ray source and a  $180^\circ$  double-focusing hemispherical analyzer with a 128-2 channel detector was used.

Since XPS is a surface sensitive technique and only propagates a few nm into the material,[7] comparing the Mo loading obtained from XPS with ICP results, which is a bulk technique can give information about agglomeration and clustering on the zeolite surface. In **Figure A2.7** the ratio Mo/(Al+Si) obtained from XPS is compared to the one measured with ICP. For 2wt.% Mo loadings, the two techniques lead to approximately the same value, while XPS reveals far higher loadings of Mo on the surface for 5 wt.% and 7.5 wt.% loading of Mo.

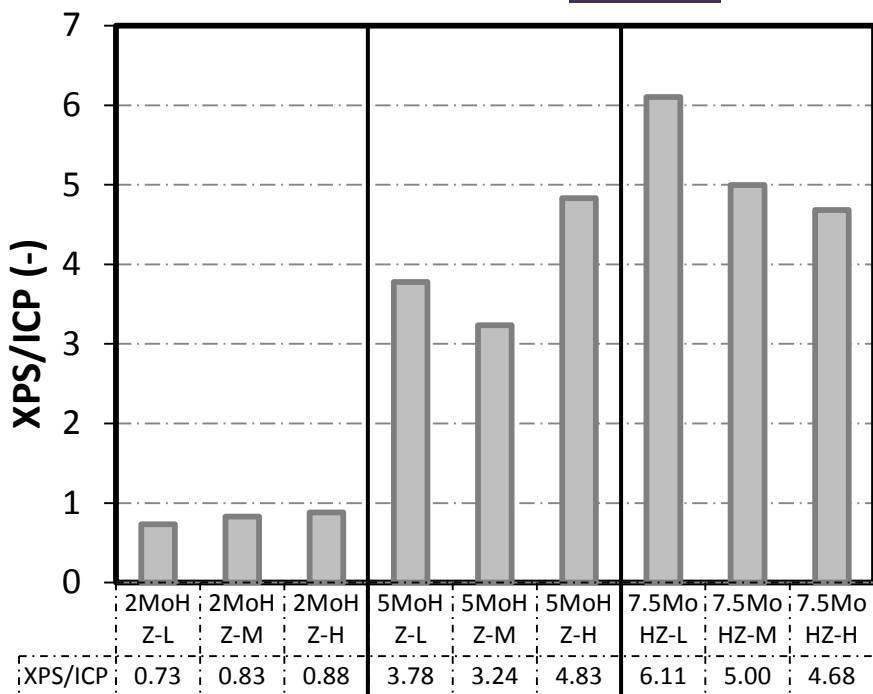


Figure A2.7. The molar ratio Mo/(Al+Si) obtained from ICP compared to the same ratio obtained by XPS. Values are compared by again taking another ratio of the two ratios obtained from the different techniques.

#### A2.1.8 UV-Vis

UV-Vis spectra of the Mo reference compounds were collected using the undiluted compound measured against BaSO<sub>4</sub> as a white standard. The edge energy ( $E_g$ ) was determined by fitting a straight line to  $(F(R_\infty)h\nu)^2$  plotted against the incident photon energy  $h\nu$  in the low energy rise region [8].

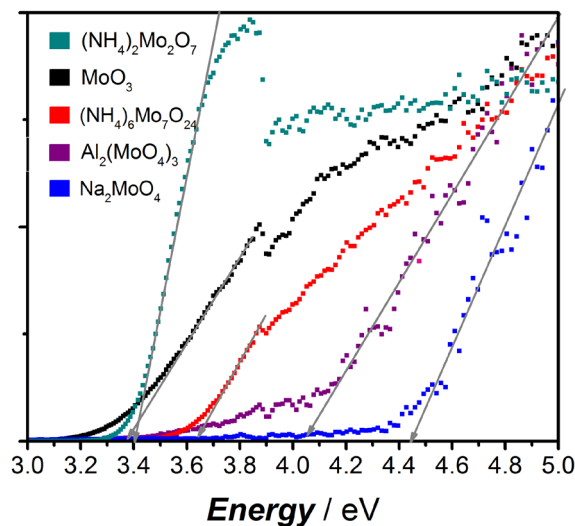


Figure A2.8. Tauc plots for determination of the edge energy  $E_g$  for references.

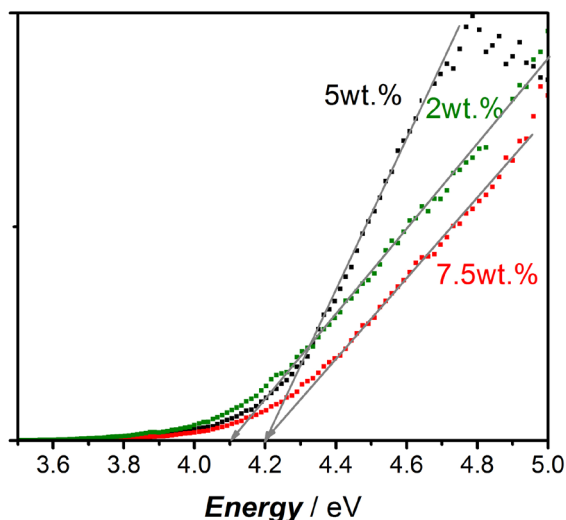


Figure A2.9. Determination of the edge energy  $E_g$  for HZ-L with 2, 5, 7.5 wt.% loading of Mo.

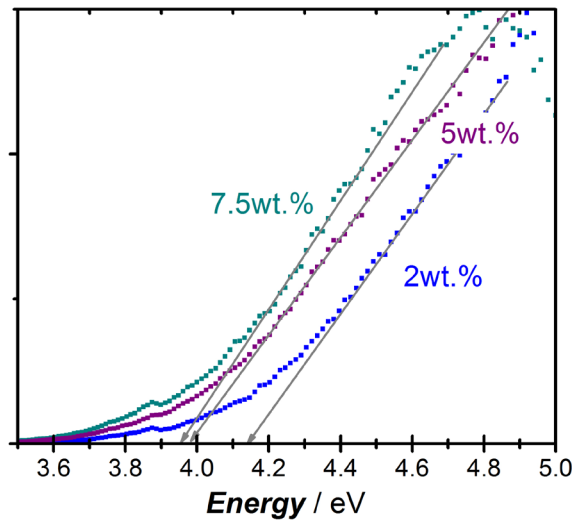


Figure A2.10. Tauc plots for determination of the edge energy  $E_g$  for **HZ-M** with 2, 5, 7.5 wt.% loading of Mo.

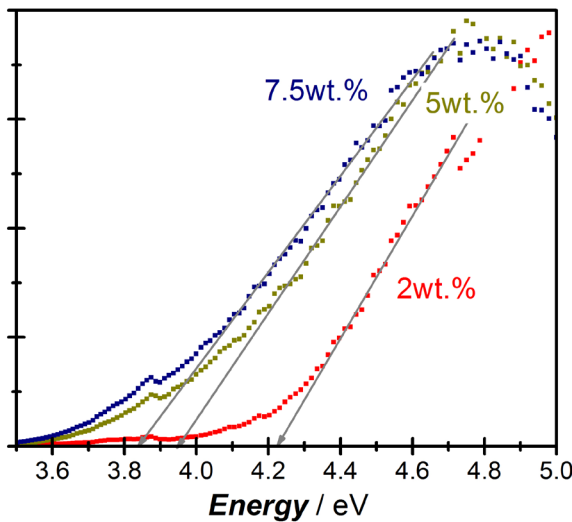


Figure A2.11. Tauc plots for determination of the edge energy  $E_g$  for **HZ-H** with 2, 5, 7.5 wt.% loading of Mo.

## A2.2 Catalytic performance at 760 °C

To investigate, the influence of reaction temperature on the performance of the catalysts, all three **5MoHZ-x** samples were also tested at 760 °C. The methane conversion reaches 20 % in the initial period of the reaction, but decreases to about 4.5 % during the initial 2 h on stream (**Figure A2.12**). Benzene is formed with the highest yield, followed by naphthalene. Only negligible amounts of toluene, ethane and ethylene are formed. Within experimental accuracy the catalytic performance (activity, selectivity and deactivation) of all three zeolites is the same. While conversion is increased by a factor of 2.7, the deactivation rate is increased simultaneously. This can be seen in **Figure A2.13**, where the benzene yield normalized by its maximum value is compared for both temperatures. The benzene yield at 760 °C decreased to 11 % of its maximum value after 238 min, while it only decreased to 33 % of its initial value for 650 °C.

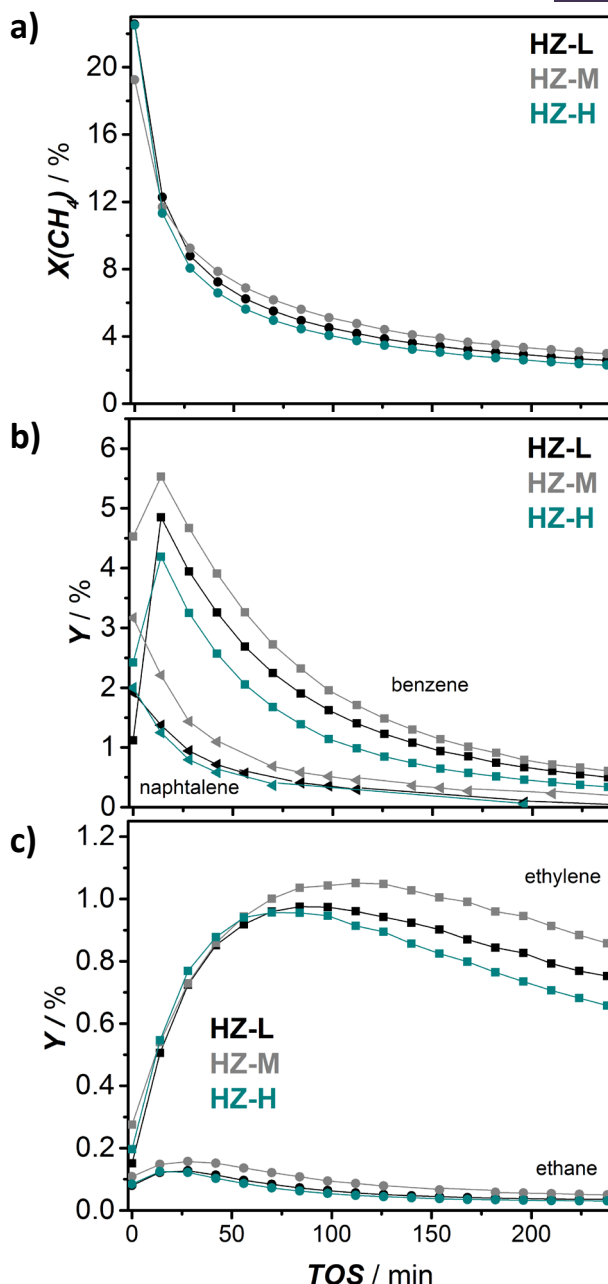


Figure A2.12. a)  $\text{CH}_4$  conversion, b) naphthalene and benzene yield, c) ethylene and ethane yield for  $5\text{MoHZ-x}$  at  $760^\circ\text{C}$  with  $\text{WHSV} = 1.21 \text{ h}^{-1}$  and 500 mg catalyst.

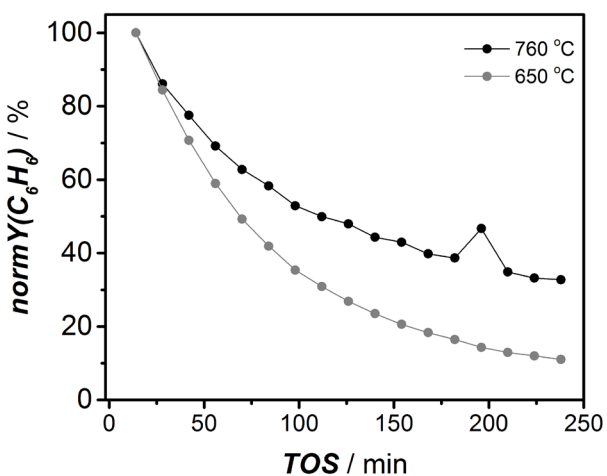
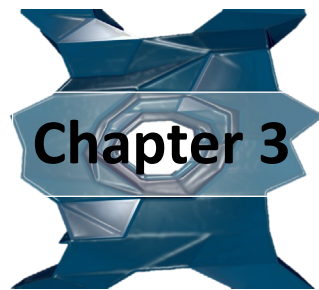


Figure A2.13. Benzene yield normalized by its maximum value with time on stream for **5HZ-M** tested at 650 °C and 760 °C with WHSV = 1.21 h<sup>-1</sup> and 500 mg catalyst.

### A2.3 References

- [1] B. Rhimi, M. Mhamdi, V.N. Kalevaru, A. Martin, Synergy between vanadium and molybdenum in bimetallic ZSM-5 supported catalysts for ethylene ammoxidation, RSC Advances, 6 (2016) 65866-65878.
- [2] P.V. Wiper, J. Amelse, L. Mafra, Multinuclear solid-state NMR characterization of the Brønsted/Lewis acid properties in the BP HAMS-1B (H-[B]-ZSM-5) borosilicate molecular sieve using adsorbed TMPO and TBPO probe molecules, Journal of Catalysis, 316 (2014) 240-250.
- [3] B.M. Fung, A.K. Khitrin, K. Ermolaev, An Improved Broadband Decoupling Sequence for Liquid Crystals and Solids, Journal of Magnetic Resonance, 142 (2000) 97-101.
- [4] Q. Zhao, W.-H. Chen, S.-J. Huang, Y.-C. Wu, H.-K. Lee, S.-B. Liu, Discernment and Quantification of Internal and External Acid Sites on Zeolites, The Journal of Physical Chemistry B, 106 (2002) 4462-4469.
- [5] A. Zheng, S.-J. Huang, W.-H. Chen, P.-H. Wu, H. Zhang, H.-K. Lee, L.-C. de Ménorval, F. Deng, S.-B. Liu, <sup>31</sup>P Chemical Shift of Adsorbed Trialkylphosphine Oxides for Acidity Characterization of Solid Acids Catalysts, The Journal of Physical Chemistry A, 112 (2008) 7349-7356.
- [6] S. Hayashi, K. Jimura, N. Kojima, Acid property of MFI-type zeolites probed by trimethylphosphine oxide studied by solid-state NMR, Microporous and Mesoporous Materials, 186 (2014) 101-105.
- [7] C.J. Powell, A. Jablonski, Surface sensitivity of X-ray photoelectron spectroscopy, Nuclear Instruments and Methods in Physics Research Section A: Accelerators, Spectrometers, Detectors and Associated Equipment, 601 (2009) 54-65.
- [8] H. Tian, C.A. Roberts, I.E. Wachs, Molecular Structural Determination of Molybdena in Different Environments: Aqueous Solutions, Bulk Mixed Oxides, and Supported MoO<sub>3</sub> Catalysts, The Journal of Physical Chemistry C, 114 (2010) 14110-14120.





**Quantifying the impact of dispersion, acidity  
and porosity of Mo/HZSM-5 on the  
performance in methane**

---

The catalytic performance of the bifunctional catalyst Mo/HZSM-5 for methane dehydroaromatization (MDA) depends on the Mo dispersion and on zeolite acidity. Here we separately quantify the effect of dispersion and the effect of acidity on aromatic yields and coke selectivity. Also, the effect of porosity on the same is quantitatively assessed. For that, a suite of 17 samples with varying Mo dispersion were synthesized by means of several methods, including chemical vapor deposition with  $\text{MoCl}_5$ ,  $\text{MoO}_2\text{Cl}_2$  and  $\text{Mo}(\text{CO})_6$  as precursors and the conventional methods, incipient wetness impregnation and solid ion exchange. These catalysts were characterized with pyridine IR-spectroscopy, XPS, UV-Vis spectroscopy,  $\text{N}_2$  adsorption, XRD, TGA and  $^{27}\text{Al}$  MAS NMR. The combined results yielded a measure of how much Mo is anchored to the zeolite as well-defined cationic species and how much is present as bigger clusters on the outer surface of the zeolite. Through relating these characterization results to the catalytic behavior of the catalysts, it was found that the maximum instantaneous benzene and naphthalene yields as well as the integral selectivities during methane dehydroaromatization linearly increase with the amount of Mo present as mono- or dimeric species. At the same time, the selectivity to coke increases with the amount of Mo present as bigger clusters or nanoparticles on the outer surface of the zeolite. The number of Mo cationic sites is the most important factor determining the activity of Mo/HZSM-5 for low loadings of Mo. But at higher loadings, the high rate of aromatics formation requires an easily accessible pre structure as well.

---

This chapter is based on the following publication:  
Vollmer, I., Mondal, A., Yarulina, I., Abou-Hamad, E., Kapteijn, F., Gascon, J., (2019). "Quantifying the impact of dispersion, acidity and porosity of Mo/HZSM-5 on the performance in methane dehydroaromatization", *Applied Catalysis A: General* **574**: 144-150. doi: [10.1016/j.apcata.2019.01.022](https://doi.org/10.1016/j.apcata.2019.01.022)

### 3.1 Introduction

Converting methane to aromatics, an important building block of many consumer goods and pharmaceuticals, is desirable because this small and very stable hydrocarbon is highly available [1]. For valorizing methane, steam reforming combined with Fischer-Tropsch synthesis is one of the indirect routes already applied industrially. However, there is great commercial interest in directly converting methane to aromatics. A process that can achieve this without the addition of oxidants is preferred, as the production of CO and CO<sub>2</sub> can be avoided and carbon efficiency is superior in that case. Thermodynamically, however, the direct non-oxidative conversion of methane to benzene is limited, with values for  $\Delta G_r^0 = +104 \text{ kcal mol}^{-1}$  and  $\Delta H_r^0 = +127 \text{ kcal mol}^{-1}$  [2-4]. Thus, considerable conversion of methane and yields of benzene (7.8-21.5 mol<sub>c</sub>%) can only be achieved at high temperature, practically between 923 and 1073 K, while coke formation is much less limited at these temperatures. This usually leads to fast deactivation of the catalyst. Catalyst deactivation and regeneration is the biggest concern when designing a catalyst for the methane dehydroaromatization (MDA) reaction. The best performing catalysts for this system, Mo/HZSM-5 and Mo/MCM-22[5-9] almost reach the thermodynamic limit in the beginning of the reaction operation, but their activity immediately decreases once it reached its maximum [2, 3].

The most important aspects that were found to influence catalytic activity and stability were Mo dispersion, acidity[10-14] and porosity[15, 16] of the zeolite support. The catalyst is believed to be most active when Mo is anchored to the framework Al inside the pores of the zeolite via oxygen bridges, (partially) replacing the proton of the Brønsted acid site (BAS) [17-19]. Mo was found to be either mono-[17] or dimeric[20] when anchoring to the zeolite. The anchoring capacity is therefore limited by the concentration of framework Al and its distribution in the framework [21]. Several studies reported optimal activity per Mo atom for Mo loadings between 2 and 4 wt.%, corresponding to Mo/Al ratios far below 1 [10, 22-24]. The Mo that does not anchor to the framework is left as polymeric structures inside the pores or as nanoparticles on the outer surface of the zeolite, which is hard to avoid and believed to be the main cause of coking [10, 17, 22-24]. Some approaches exist to minimize the presence of Mo nanoparticles on the outer surface of the zeolite: silanation of the external surface of the zeolite prior to introduction of Mo[13] or adding small amounts

of ammonia to the impregnation solution[25]. X-ray photoelectron spectroscopy (XPS) can be used to detect Mo on the outer surface of the zeolite, as it is a surface sensitive technique, while UV Raman and UV-Visible spectroscopy (UV-Vis) yield information about the Mo state in the whole particle [10, 26]. Tian *et al.* related the electronic edge energy ( $E_g$ ) of the ligand-to-metal charge transfer transitions of Mo cations determined by UV-Vis to the number of bridging Mo-O-Mo and thereby developed a way to determine the average cluster size of Mo [27]. Further, the dispersion of Mo can be probed indirectly by probing the acidity of the catalyst using H/D exchange,[18, 20, 28]  $^1\text{H}$  NMR,[29, 30]  $^{27}\text{Al}$  MAS NMR,[31, 32] NH<sub>3</sub>-TPD[10, 15, 33, 34] or probing adsorbed molecules by IR-spectroscopy[35, 36] (Py IR). The more the BAS concentration decreases compared to the pristine zeolite, the higher is the achieved dispersion. At the same time, it has to be carefully assessed that the BAS decrease is not partly due to destruction of the zeolite by extraction of the framework Al (FAI) during introduction of Mo. This is best achieved by  $^{27}\text{Al}$  MAS NMR.

Mo/HZSM-5 is most commonly prepared by incipient wetness impregnation (IWI), where an aqueous solution containing (NH<sub>4</sub>)<sub>6</sub>Mo<sub>7</sub>O<sub>24</sub> (ammonium heptamolybdate, AHM) with a volume to just fill the pores of the zeolite is added dropwise to the dry zeolite. Mo is present as Mo<sub>7</sub>O<sub>24</sub><sup>6-</sup> in the impregnation solution, an ion that does not fit into the pores of the zeolite and remains at the outer surface of the particle. Only upon increasing the temperature MoO<sub>3</sub> moieties can form in air, which are able to migrate into the pore channels of the zeolite and anchor there [30]. This calcination step is performed with low heating rates (0.5 to 2 K/min) to avoid fast expansion of the liquid in the zeolite pores, which would impair their integrity and to facilitate migration of Mo, while avoiding agglomeration. The final temperature applied is between 773 and 973 K, where 873 K was found to lead to good dispersion of Mo, while maintaining decent integrity of the zeolite structure and limiting the extraction of framework Al to form Al<sub>2</sub>MoO<sub>4</sub>, which is catalytically inactive [37, 38]. In some publications MoO<sub>3</sub> powder is mixed with the zeolite directly and then calcined. This is usually referred to as solid ion exchange (SIE) [39, 40]. It is clear that Mo has to form some volatile or mobile species that can migrate into the pores of the zeolite in order to achieve good dispersion and with that a good catalytic activity. MoO<sub>3</sub> however has a very high melting point of 1068 K and was observed to start to evaporate at around 973 K in

inert atmosphere [41]. Therefore, here we also employ another synthesis approach using Mo precursors with very low melting points in combination with chemical vapor deposition (CVD). Two chloride precursors,  $\text{MoCl}_5$  (m.p. 467 K) and  $\text{MoO}_2\text{Cl}_2$  (m.p. 448 K) as well as  $\text{Mo}(\text{CO})_6$  (m.p. 423 K) are explored. Here, we compare the Mo dispersion achieved with the different synthesis techniques and relate it to benzene and naphthalene selectivities and yields as well as coke selectivity. Dispersion of Mo is determined by a combination of XPS, pyridine IR-spectroscopy, UV-Vis spectroscopy and  $^{27}\text{Al}$  MAS NMR. Using  $\text{N}_2$  adsorption, the role of the porosity of the as-synthesized catalysts is assessed on catalytic performance. From this we determine the most important parameters determining the performance of Mo/HZSM-5 for MDA and how that can be influenced by the synthesis.

## 3.2 Experimental Details

### 3.3.2.1 Catalyst synthesis

Mo was introduced into the H-form of a commercial HZSM-5 zeolite (PQCorporation, CBV 5020E) with Si/Al = 24 (denoted **HZ**) using IWI, SIE or CVD. Samples are denoted as **yMoHZ-x**, where **y** denotes the Mo/Al ratio and **x** the synthesis method. Catalysts were prepared with Mo/Al = 0.3 and 1. If a precursor other than  $\text{MoCl}_5$  is used for the synthesis, this is specifically indicated. The synthesis methods are described in detail in the appendix.

### 3.3.2.2 Catalyst characterization

**Pyridine transmission FTIR** spectroscopy was performed on a Nicolet 6700 spectrometer with a MCT/B detector. A 10 mm wafer using 50 mg sample is pressed using 4.29 bar. The sample was first activated in vacuum at 673 K for 16 h to remove adsorbed species. After activation, the pyridine gas was fed to the pellets until saturated and further evacuated at 433 K for 2 h. Spectra were recorded in 1000–4000  $\text{cm}^{-1}$  range at 4  $\text{cm}^{-1}$  resolution and co-addition of 128 scans. The spectra shown represent the subtraction result of the spectra collected before adsorption of pyridine from the one taken afterwards. All spectra were normalized by the framework absorbance at 1873  $\text{cm}^{-1}$ . The decrease in peak area characteristic for Brønsted acidity (BAS) at 1455  $\text{cm}^{-1}$  is expressed by **Equation 1**, where  $A$  represent the

area of the absorbance with a certain vibration of either the catalyst containing Mo or the bare zeolite.

$$(Mo/Al)_{Py\ FTIR} = 1 - \left( \frac{A_{1546\text{cm}^{-1},\text{sample}}}{A_{1546\text{cm}^{-1},\text{bare\ zeolite}}} \right) \quad (\text{Equation 3.1})$$

$(Mo/Al)_{Py\ FTIR}$  is a measure for how many BAS protons got replaced by Mo. The increase in Lewis acid sites (LASs) with respect to the bare zeolite due to the formation of Mo cations is expressed by **Equation 3.2**.

$$LAS_{extra} = A_{1455\text{cm}^{-1},\text{sample}} - A_{1455\text{cm}^{-1},\text{bare\ zeolite}} \quad (\text{Equation 3.2})$$

The UV-Vis diffuse reflectance spectra (UV-Vis-DRS) were collected on a Perkin–Elmer Lambda 900 spectrophotometer equipped with an integrating sphere (“Labsphere”) in the 200–800 nm range. The bare zeolite was used as a white standard. Before measurement, the samples were degassed at 673 K under dynamic vacuum for 12 h and then transferred to the sample holders in the glovebox. The absorption intensity is expressed by the Schuster-Kubelka-Munk equation (**Equation 3.3**).

$$F(R_\infty) = (1 - R_\infty)^2 / 2R_\infty \quad (\text{Equation 3.3})$$

The edge energy ( $Eg$ ) was determined by fitting a straight line to  $(F(R_\infty)hv)^2$  plotted against the incident photon energy  $h\nu$  in the low energy rise region [27].

**Chemical composition** of the samples in terms of Mo, and Al content was measured by digestion of approximately 50 mg sample in 4.5 ml 30 % HCl + 1.5 ml 65 %  $\text{HNO}_3$  + 0.2 ml 40 % HF using a microwave. The digestion time in the microwave was 60 min at 1000 W for 8 samples and 1300 W for 14 samples. After digestion, the samples were diluted to 50 ml with MQ and analysed with ICP-OES on a PerkinElmer Optima 5300 (torch:Si+saffire injector). For Na a PerkinElmer AAS Modell AAnalyst 200 was used.

**X-ray photoelectron spectroscopy** (XPS) analysis was performed in order to identify any agglomeration of Mo on the zeolite surface. A Thermo Scientific K-alpha spectrometer equipped with a monochromatic Al  $K\alpha$  X-ray source and a 180° double-focusing hemispherical analyzer with a 128-2 channel detector was used. Measurements were performed at ambient temperature and chamber pressure of about  $10^{-8}$  mbar. The spot size was 400 mm. A flood gun was always used for charge

compensation. The spectra were analyzed and processed by using Thermo Avantage v5.903 software (Thermo Fisher Scientific). Smart background (derived from the Shirley background) was used over the peak width.  $(Mo/Al)_{XPS}$  was determined by quantifying the amount of Mo and Al from the XPS measurement as an average of two measurement points.

**Catalytic testing** was performed in a quartz reactor tube with an inner diameter of 6 mm, using 500 mg catalyst pelletized and sieved to 212 to 355  $\mu\text{m}$ . A weight hourly space velocity (WHSV) of 1.21  $\text{h}^{-1}$  (based only on methane flow) and a reaction temperature of 973 K was applied in all tests. Product analysis was achieved on an Interscience Trace GC with one TCD and two FIDs. A mixture 5 %  $\text{N}_2$  in  $\text{CH}_4$  was fed to the reactor, where  $\text{N}_2$  was used as an internal standard according to **Equation 3.4**, where  $A_{i,in}$  ( $i = \text{CH}_4$  or  $\text{N}_2$ ), the integrated peak area from the GC analysis is determined from three initial GC calibration injections before increasing the temperature for each run. The reactor was brought to reaction temperature under the same flow with a heating rate of 10 K/min. Product yields were calculated according to **Equation 3.5**, where  $F_n$  denotes the molar flow of molecule  $n$ ,  $x$  the number of carbons and  $y$  the number of hydrogens in a product molecule. The integral selectivity to each gaseous product  $i$  over the whole time on stream (TOS) is obtained using **Equation 3.6**, where the number of the GC injection is denoted by  $j$ . Coke selectivity over the whole TOS calculated with **Equation 3.7**.

$$X_{\text{CH}_4} = \frac{\left(\frac{A_{\text{CH}_4,\text{in}}}{A_{\text{N}_2,\text{in}}}\right) - \left(\frac{A_{\text{CH}_4,\text{out}}}{A_{\text{N}_2,\text{out}}}\right)}{\frac{A_{\text{CH}_4,\text{in}}}{A_{\text{N}_2,\text{in}}}} * 100\% \quad (\text{Equation 3.4})$$

$$Y_i[\text{mol}\%] = \frac{F_{C_xH_y,\text{out}}}{F_{\text{CH}_4,\text{in}}} * x * 100\%, \quad i = \text{product}, C_xH_y \quad (\text{Equation 3.5})$$

$$\Sigma_{\text{TOS}} S_i[\text{mol}\%] = \frac{\sum_j Y_i}{\sum_j X_{\text{CH}_4}} * 100\%, \quad j = \text{GC injection\#} \quad (\text{Equation 3.6})$$

$$\Sigma_{\text{TOS}} S_{\text{coke}}[\text{mol}\%] = \sum_j X_{\text{CH}_4} - \Sigma_i \Sigma_{\text{TOS}} S_i \quad (\text{Equation 3.7})$$

Samples of spent catalysts were analyzed for porosity by  $\text{N}_2$  adsorption and their coke content by thermogravimetric analysis (TGA, heating in air at 10 K/min, see appendix **section A3.5.8**).

### 3.3 Results

#### 3.3.1 Effect of Mo loading

A suite of 17 catalysts was prepared using several CVD methods found in literature as well as SIE and IWI. Three different precursors,  $\text{MoCl}_5$ ,  $\text{MoO}_2\text{Cl}_2$  and  $\text{Mo}(\text{CO})_6$  were used for CVD, while  $\text{MoO}_3$  and  $\text{MoCl}_5$  were tested for SIE and AHM for IWI. A detailed description and discussion of the synthesis methods and the catalytic performance achieved can be found in the supplementary information **sections A3.1 to A3.3**. While a better dispersion was achieved with CVD compared to IWI it also has to be noted that the synthesis was hard to reproduce and more consistent results were obtained with IWI.

Samples with two different loadings of Mo were prepared with a Mo/Al ratio of 0.3 and 1.0. The high loading corresponds to the theoretical limit of Mo incorporation, because each Al can theoretically anchor one Mo. This high loading was used to test how well the different synthesis methods perform, because it is hard to disperse Mo at the limit of how much Mo can be anchored. Generally, a better dispersion is achieved for  $\text{Mo/Al} = 0.3$  as is evident from XPS as well as UV-Vis (*vide infra*). The integrity of the zeolite is also less impaired by the synthesis method for  $\text{Mo/Al} = 0.3$  compared to when the catalysts are prepared with  $\text{Mo/Al} = 1$ . This is concluded from the  $\text{N}_2$  adsorption isotherms, XRD and  $^{27}\text{Al}$  MAS NMR. For  $\text{Mo/Al} = 0.3$ , the  $\text{N}_2$  adsorption isotherms (**Figure A3.7a**) retain the same shape as the isotherm for the bare zeolite, while for catalysts prepared with  $\text{Mo/Al} = 1$  a decrease in BET surface area is observed accompanied with, in some cases, increased mesoporosity (**Figure A3.7b**). XRD patterns (**Figure A3.8**) also show a more significant decrease in crystallinity for  $\text{Mo/Al} = 1$  than for  $\text{Mo/Al} = 0.3$ . The diffraction peaks characteristic for  $\text{MoO}_3$  are observed for more catalysts with  $\text{Mo/Al} = 1$  than for  $\text{Mo/Al} = 0.3$  showing that there is a higher chance of Mo agglomeration for high Mo loadings.  $^{27}\text{Al}$  MAS NMR (**Figure A3.9**) shows that some samples with  $\text{Mo/Al} = 1$  experienced significant extraction of framework Al, while only moderate extraction is observed for  $\text{Mo/Al} = 0.3$ . Both EFAI as well as  $\text{Al}_2(\text{MoO}_4)_3$  are observed especially for  $\text{Mo/Al} = 1$ . EFAI leads to an increase in LAS, which in some cases was shown to have a beneficial effect on catalyst lifetime, [42] while  $\text{Al}_2(\text{MoO}_4)_3$  was generally agreed to be inactive for MDA [37, 43, 44]. At the same time BAS are removed leading to a lower acidity, which was shown to decrease

the formation of coke [10-14]. Generally, extraction of Al from the framework leads to a decrease in crystallinity, because some microporous structures are destroyed. This can also result in mesoporosity as observed in the N<sub>2</sub> adsorption measurements. Some mesoporosity can be beneficial for the reaction, but there seems to be an optimum of how many mesopores should exist [16, 45-47]. Finally, catalytic performance varies more at higher loadings (compare left and right of **Figure A3.2**), also because it becomes harder to disperse Mo.

### 3.3.2 Effect of dispersion

#### 3.3.2.1 Measuring dispersion

A combination of Py IR, XPS and UV-Vis is used to elucidate the nature of Mo species present on the catalysts after synthesis. Py IR indirectly probes the amount of cationic sites of Mo inside the pores of the zeolite particles, XPS only probes the outer surface of the zeolite and UV-Vis is a bulk technique giving an average of all Mo species present on the catalyst. Thus a combination of all three techniques is insightful for distinguishing between bigger clusters of Mo on the outer surface of the zeolite particle and Mo anchored inside the pores.

Py IR was used to determine how many active Mo sites are created. **Figures 3.1a, A3.10b and A3.11b** show the absorbance bands of pyridine adsorbed on the acid sites of the bare zeolite and the catalysts containing Mo. Three contributions are observed corresponding to Lewis acid sites (LAS) at 1455 cm<sup>-1</sup>, a mixture of LAS and BAS at 1490 cm<sup>-1</sup> and BAS at 1546 cm<sup>-1</sup> [48-50]. In addition several absorbances are observed between 1612 and 1635 cm<sup>-1</sup> that represents a mixture of LAS and BAS as well. The intensity for the BAS absorbance at 1546 cm<sup>-1</sup> decreases for the catalysts with Mo, because the Mo cations replace the acidic protons [21]. Through this exchange new Lewis acid sites are created. One of the absorbances around 1635 cm<sup>-1</sup> decreases together with the BAS absorbance at 1546 cm<sup>-1</sup> and is therefore assigned to BASs. Both the absorbance at 1623 cm<sup>-1</sup> as well as at 1612 cm<sup>-1</sup> are assigned to LASs. For the bare zeolite, LASs stem from extra-framework Al (EFAI), while on the zeolite containing Mo both LASs from EFAI and from Mo cations are observed. The absorbance at 1612 cm<sup>-1</sup> only appears for the zeolite containing Mo, therefore this wavenumber is assigned to LAS arising from Mo cations while the absorbance at 1623 cm<sup>-1</sup> likely stems from EFAI [21]. Comparing **Figures A3.10a and A3.11a**, it can be seen that for Mo/Al = 1, the OH absorbance corresponding to Si-OH

and Al-OH almost disappeared. This is because Mo is also anchored on those groups for high loadings. A complete table containing the fraction of BAS covered and the amount of extra LAS created for each sample can be found in the appendix (**Table A3.1**). In **Figure 3.1b**, the amount of additional LASs created,  $LAS_{extra}$  is plotted against the ratio of BAS covered,  $(Mo/Al)_{Py\ FTIR}$ . Proportionally the more LASs are created, the more acidic protons are replaced by Mo cations. Some EFAI is created during the synthesis of the zeolite, likely during the calcination step, as was discussed in the appendix, **section A3.3**. This explains why the bare zeolite, **HZ** does not follow the same linear trend as the other samples. The catalysts with Mo however, follow one trend, because the amount of EFAI created is similar for most samples as shown by  $^{27}\text{Al}$  MAS NMR in **Figure A3.9**. **1MoHZ-CVD1** presents an outlier, as no extra LASs are created in that case during the incorporation of Mo. This indicates that most of the decrease in the characteristic BAS absorbance is not because Mo replaced the acidic proton, but because the BASs got destroyed during the synthesis. Similarly for **1MoHZ-SIE** the decrease in BAS is partly due to extraction of FAI and forming  $\text{Al}_2(\text{MoO}_4)_3$ .

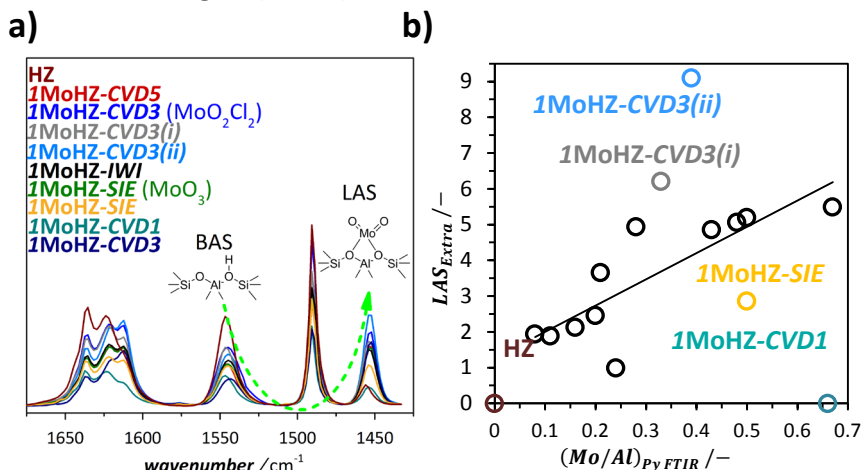


Figure 3.1. a) Py IR spectra of **1MoHZ-x** samples with illustration of how the Mo cation replaces the proton at the BAS to create LAS. b)  $LAS_{extra}$  as determined by integrating the absorbance at the IR wavenumber characteristic for pyridine adsorption on LAS and subtracting the area of the absorbance at the same location on the bare zeolite plotted against  $(Mo/Al)_{Py\ FTIR}$  as determined by integrating the absorbance at the IR wavenumber characteristic for pyridine adsorption on BAS for a sample containing Mo and comparing it to the area of the same absorbance measured for the bare zeolite. Results for all samples are plotted and outliers highlighted. For all values refer to **Table A3.1**.

In contrast, for **1MoHZ-CVD3(i)** and **1MoHZ-CVD3(ii)**, more EFAI was created during the synthesis compared to other samples.

Since XPS is a surface sensitive technique, which for our specific experimental configuration has a mean escape depth of around 3-4 nm (details in appendix **section A3.5.5**),[51-53] it can inform about agglomeration and clustering of Mo on the external surface of the catalyst particles. An agglomeration on the outer surface of the zeolite crystal will yield an increased amount of Mo detected by XPS. XPS confirms that Mo does not significantly cluster on the outer surface of the catalyst particle for catalysts synthesized with  $\text{Mo}/\text{Al} = 0.3$ , as the  $\text{Mo}/\text{Al}$  ratios obtained from XPS for those samples are all below 0.33, while they can be as high as 1.44 for catalysts synthesized with  $\text{Mo}/\text{Al} = 1$  (**Table A3.1**). The more Mo anchors to the BAS, the less Mo is expected to be present as bigger clusters and nanoparticles on the outer surface of the zeolite and the lower the expected  $(\text{Mo}/\text{Al})_{XPS}$ . Indeed, a decrease in the  $\text{Mo}/\text{Al}$  ratio obtained from XPS with  $\text{Mo}/\text{Al}$  ratio determined by Py IR is observed for the same Mo loading (**Figure 3.2a**). The  $(\text{Mo}/\text{Al})_{XPS}$  was determined as an average of two measurement locations. These values for the different locations on the same sample can vary considerably at high Mo loadings (**Table A3.1**), demonstrating local clustering of Mo on the external surface revealed by the XPS measurement.

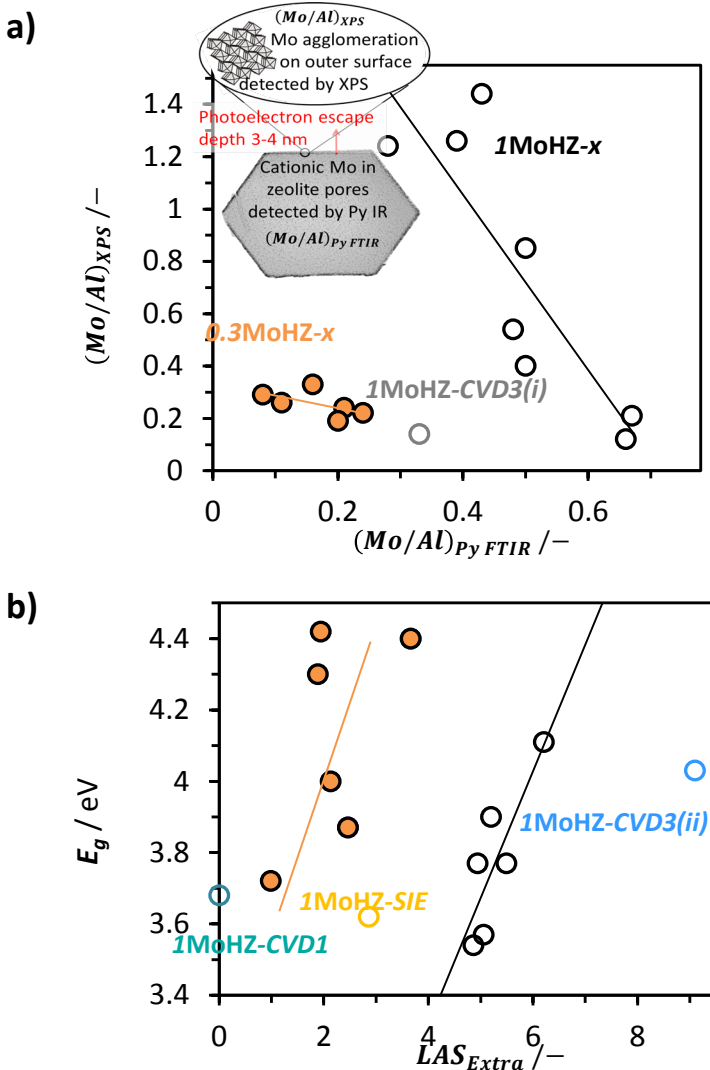


Figure 3.2. a)  $(\text{Mo}/\text{Al})_{\text{XPS}}$  on the outer surface of the catalyst particle as determined by quantifying the amount of Mo and Al from the XPS measurement plotted against  $(\text{Mo}/\text{Al})_{\text{Py FTIR}}$  as determined by integrating the absorbance at the IR wavenumber characteristic for pyridine adsorption on BAS for a sample containing Mo to the same absorbance measured for the bare zeolite. Results for all samples are plotted and outliers highlighted. For all values refer to **Table A3.1**. b) Edge energy  $E_g$  determined from UV-Vis (**Figure A3.19**, **Table A3.2**) plotted against  $LAS_{\text{Extra}}$  as determined by integrating the absorbance at the IR wavenumber characteristic for pyridine adsorption on LAS and subtracting the area of the absorbance at the same location on the bare zeolite.

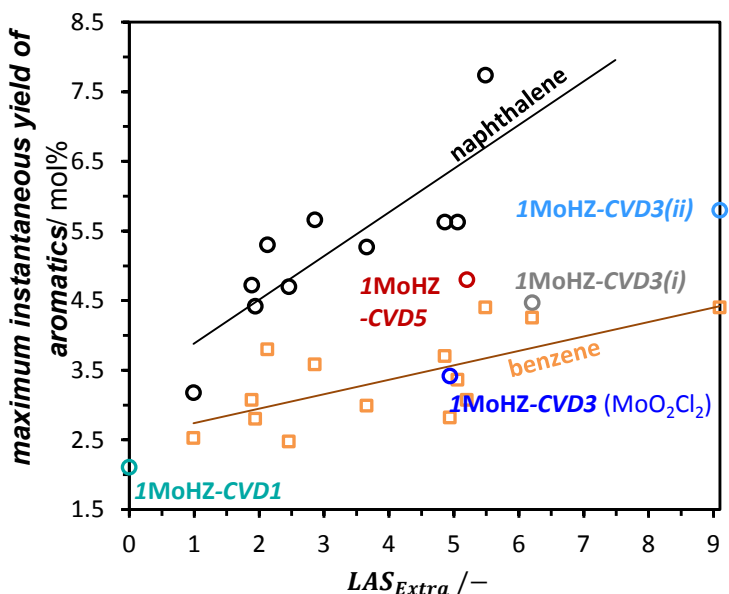
UV-Vis can be used to determine the electronic edge energy ( $E_g$ ) of the charge transfer from oxygen to molybdenum. For samples with Mo/Al = 0.3,  $E_g$  is generally between 4.00 and 4.42 (**Table A3.2**) suggesting that with such low loadings, Mo is almost exclusively present as mono- or dimeric species [27]. For Mo/Al = 1,  $E_g$  is generally a bit lower, because this ratio is at the limit of how much Mo can be anchored to the BAS of the zeolite framework and Mo oxide polymers will always be present to some extent. **Figure 3.2b** shows that  $E_g$  generally increases with the number of extra Lewis acid sites created compared to the bare zeolite, confirming that these LASs correspond to mono- or dimeric Mo cations. The limitations of using  $E_g$  as an indicator of dispersion however are also clear, as many outliers can be found in **Figure 3.2b**. Even worse correlations were found when trying to correlate the results from UV-Vis with results from XPS.

### 3.3.2.2 Relating dispersion to catalytic activity

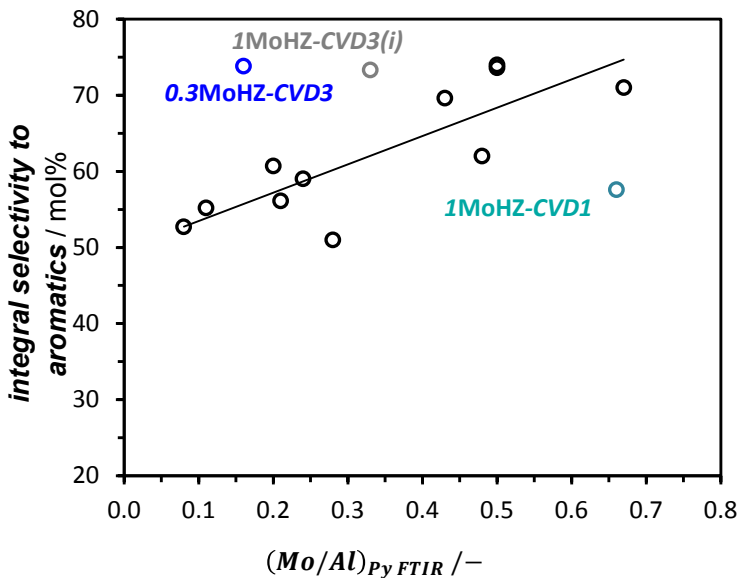
Finally, the measure for dispersion ( $(Mo/Al)_{Py\ FTIR}$ ) determined with pyridine IR can directly be related to catalytic performance. The overall activity is increased when more well-dispersed cationic Mo sites are created. This is evident from the increase in the instantaneous yield of naphthalene and benzene with  $(Mo/Al)_{Py\ FTIR}$  shown in **Figure 3.3a**. More benzene and naphthalene are produced leading to an increased integral selectivity to aromatics (**Figure 3.3b**), and a decreased integrated selectivity to coke (**Figure 3.3c**). **1MoHZ-CVD1** presents an outlier in all three relationships, because of the significant destruction of the zeolite during synthesis as discussed in **section 3.3.1**. The other outliers in the trend for selectivity to aromatics can be explained by the particularly low selectivity to C2-C3 hydrocarbons, effectively increasing aromatics selectivity. The other outliers in **Figure 3.3c** correspond with a prolonged activation period. During the activation period, the oxidic Mo present on the as-synthesized catalysts is carburized to its active phase, which leads to a delay in the onset of aromatics production [54]. This is observed for **1MoHZ-CVD3(MoO<sub>2</sub>Cl<sub>2</sub>)** and **0.3MoHZ-CVD3(MoO<sub>2</sub>Cl<sub>2</sub>)** (**Figure A3.2**). This prolonged activation period leads to an increased coke production already in the beginning of the reaction. Carburization takes longer, because of the presence of bigger Mo particles on **1MoHZ-CVD3(MoO<sub>2</sub>Cl<sub>2</sub>)** and **0.3MoHZ-CVD3(MoO<sub>2</sub>Cl<sub>2</sub>)**, which are observed as MoO<sub>3</sub> diffraction peaks in the XRD pattern (**Figure A3.8**) and as a weight increase in the TGA curve right before the onset of coke

combustion on the spent catalyst (**Figure A3.13**), which occurs when bigger Mo<sub>2</sub>C particles are oxidized (**Figure A3.14**). The **1MoHZ-CVD1** sample suffered from severe Al extraction from the framework, resulting in structural changes (**Figure A3.8b**) and formation of inactive Al<sub>2</sub>(MoO<sub>4</sub>)<sub>3</sub> (**Figure A3.9a**). Brønsted acidity was therefore reduced considerably and no Lewis acidity created (**Figure A3.11**).

a)



b)



c)

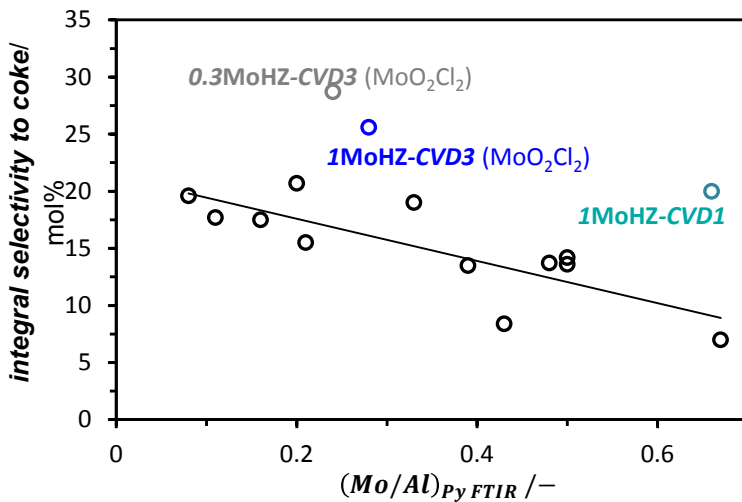


Figure 3.3. a) Instantaneous maximum yield to benzene and naphthalene (**Table A3.3**). b) The integral selectivity to aromatics (**Table A3.3**) plotted against the ratio of BAS covered,  $(Mo/Al)_{Py\ FTIR}$  (**Table A3.1**). c) The integral selectivity to coke (**Table A3.3**) plotted against the ratio of BAS covered,  $(Mo/Al)_{Py\ FTIR}$  (**Table A3.1**).

### 3.3.3 Effect of acidity and porosity

When exchanging the proton at the BAS with Mo, Mo active sites are created while simultaneously decreasing the acidity [30]. That is why it is difficult to separate the effect of more Mo sites from the effect of lowering the amount of acid sites. Although it has been shown that coke selectivity decreases when the Brønsted acidity of the zeolite is lowered,[10-14] this is not the sole reason as might be suggested by **Figure 3.3c**. Additionally, the aromatics formation rate increases, because there are more well-dispersed Mo sites on which methane can be activated (**Figure 3.3a**). As a consequence, it is not enough to create a zeolite support with low acidity to enhance aromatic selectivity as has been suggested[47], but the amount of well-dispersed Mo sites has to be increased as well. This is similar to what has been shown for Ca species for the methanol to olefins reaction [42, 48].

We further assessed the effect of porosity on catalytic performance. Pore volume, especially micropore volume decreases with  $(Mo/Al)_{PyFTIR}$ , because more Mo is anchored inside the pores of the zeolite (**Figure 3.4a**). For  $Mo/Al = 0.3$ , maximum instantaneous yields to aromatics decrease with pore volume, because more Mo cationic sites are present (orange points, **Figure 3.4b**). In contrast, for a higher loading of Mo, the maximum instantaneous yields to aromatics are higher for higher pore volumes. The rate of aromatics formation for these catalysts with a lot of active Mo sites is very high and thus diffusion of the products starts to impact catalyst performance. A longer catalyst lifetime can also be expected for a higher pore volume, because more coke can be accommodated before access to the active sites of the catalyst is blocked. The total amount of coke deposited after 364 min on stream increases with pore volume (**Figure A3.15**), but this is not due to a complete filling of the pores, since the pore volume of the catalysts decreased by less than 40 % during the 364 min on stream and mesopore volume decreased relatively more than micropore volume (**Table A3.7**). Total coke amounts instead increase because the concentration of BASs is also higher at higher pore volumes (**Figure 3.4a**). Coke formation is thus clearly associated with acidity. This is supported by the fact that for the catalysts with lower loadings of Mo and thus higher acidity, activity drops around by 70 % and only by 30 to 60 % for the high loadings. The drop in benzene formation is also much higher than the decrease in pore volume indicating that coking might not be the only cause of deactivation, but

agglomeration of Mo could play a role as well, as has been suggested before [17, 55]. The integrated aromatic selectivities follow a similar trend as the maximum instantaneous yields (**Figure A3.16**), demonstrating that more cationic Mo sites increase activity at low Mo loadings and that it is important to increase accessibility for high Mo loadings.

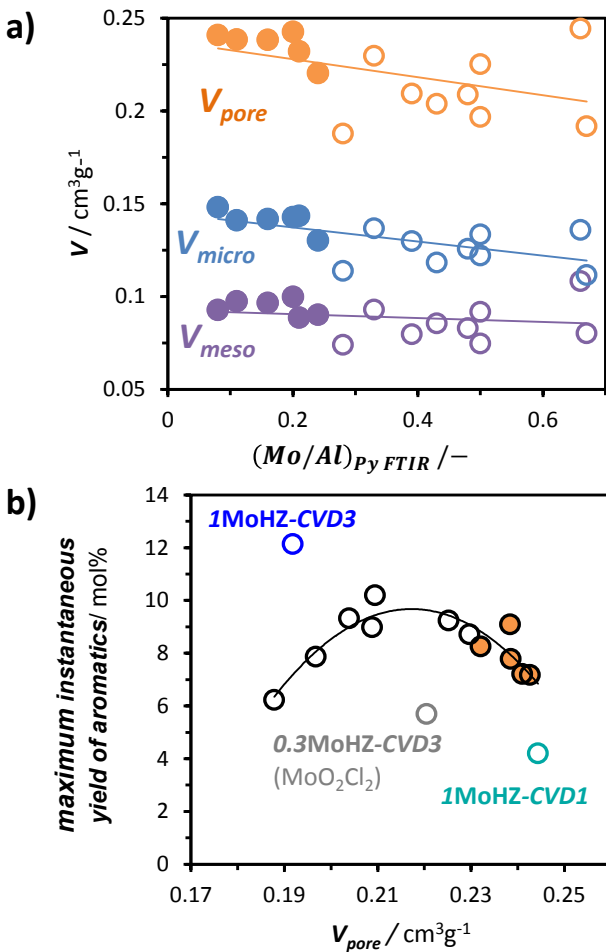


Figure 3.4. a) Meso- micro- and total pore volume (**Table A3.5**) as a function of  $(Mo/Al)_{Py\text{FTIR}}$ . Catalysts with  $\text{Mo}/\text{Al} = 0.3$  are indicated by solid symbols. b) Maximum instantaneous yield to aromatics (**Table A3.3**) as a function of total pore volume (**Table A3.5**). Samples with  $\text{Mo}/\text{Al} = 0.3$  are indicated in orange.

### 3.4 Conclusions

Comparing and adapting several CVD techniques from literature and using the conventional preparation techniques, IWI and SIE, a suite of 17 catalysts were synthesized, characterized and their catalytic performance tested for MDA. The synthesis method had a greater effect on catalyst performance for the high Mo loading corresponding to a Mo/Al ratio of 1, while the different synthesis methods lead to more similar performance for Mo/Al = 0.3. Mo/Al = 1, which corresponds to a loading of 5.8 wt.% Mo on a zeolite with Si/Al = 25, represents the theoretical maximum of Mo that can be anchored to the framework Al of the zeolite. At this loading, dispersing Mo while avoiding the formation of Mo nanoparticles is difficult to achieve. Full exchange of the acidic protons with Mo is controlled by migration of the Mo precursor into the pores of the zeolite. This migration can be enhanced by using a Mo precursor with a lower melting point.

Characterization with pyridine IR, XPS, UV-Vis and  $^{27}\text{Al}$  MAS NMR allowed determining the amount of Mo present as mono- or dimeric species inside the pores of the zeolite as well as the fraction of Mo that formed nanoparticles and bigger clusters on the outer surface of the zeolite. Py IR showed to be the most informative technique in that regard, as XPS shows a high local measurement variation, and edge energies determined from UV-Vis do not correlate well with results from other characterization techniques. The information from Py IR can be related well with catalytic behavior. A linear relationship was found between the rate of aromatics formation (benzene and naphthalene) and the concentration of Mo cations inside the channels of HZSM-5. Hence, when more Mo cations are present the integral selectivity to aromatics also increases and at the same time the selectivity to coke decreases due to a simultaneously reduced acidity.

Both the dispersion of Mo as well as overall acidity influence catalytic performance. Thus, it is not sufficient to create a zeolite support with low acidity to enhance aromatic selectivity as has been suggested [47], the amount of well-dispersed Mo sites has to be increased as well. Coking can clearly be associated with the acid sites. In addition bigger Mo nanoparticles prolong the induction period and the catalyst deactivates faster. Deactivation also occurs because of agglomeration of Mo and thus a decrease in the number of cationic Mo sites. The number of cationic Mo-sites is the most important factor determining the activity of

## CHAPTER 3

Mo/HZSM-5 for low loadings of Mo, but at higher loadings, catalysts design should also provide for enough porosity to enhance diffusion of products.

### 3.5 References

- [1] N.E.T. Laboratory, An introduction to the science and energy potential of a unique resource, in: U.D.o. Energy (Ed.), US Department of Energy, US, 2011.
- [2] B.S. Liu, L. Jiang, H. Sun, C.T. Au, XPS, XAES, and TG/DTA characterization of deposited carbon in methane dehydroaromatization over Ga–Mo/ZSM-5 catalyst, *Applied Surface Science*, 253 (2007) 5092-5100.
- [3] K. Honda, X. Chen, Z.-G. Zhang, Identification of the coke accumulation and deactivation sites of Mo<sub>2</sub>C/HZSM-5 catalyst in CH<sub>4</sub> dehydroaromatization, *Catalysis Communications*, 5 (2004) 557-561.
- [4] Y. Song, Y. Xu, Y. Suzuki, H. Nakagome, Z.-G. Zhang, A clue to exploration of the pathway of coke formation on Mo/HZSM-5 catalyst in the non-oxidative methane dehydroaromatization at 1073 K, *Applied Catalysis A: General*, 482 (2014) 387-396.
- [5] Y. Xu, L. Lin, Recent advances in methane dehydro-aromatization over transition metal ion-modified zeolite catalysts under non-oxidative conditions, *Applied Catalysis A: General*, 188 (1999) 53-67.
- [6] J.J. Spivey, G. Hutchings, Catalytic aromatization of methane, *Chemical Society Reviews*, 43 (2014) 792-803.
- [7] Z.R. Ismagilov, E.V. Matus, L.T. Tsikoza, Direct conversion of methane on Mo/ZSM-5 catalysts to produce benzene and hydrogen: achievements and perspectives, *Energy & Environmental Science*, 1 (2008) 526-541.
- [8] Y. Xu, X. Bao, L. Lin, Direct conversion of methane under nonoxidative conditions, *Journal of Catalysis*, 216 (2003) 386-395.
- [9] S. Majhi, P. Mohanty, H. Wang, K.K. Pant, Direct conversion of natural gas to higher hydrocarbons: A review, *Journal of Energy Chemistry*, 22 (2013) 543-554.
- [10] J.-P. Tessonner, B. Louis, S. Rigolet, M.J. Ledoux, C. Pham-Huu, Methane dehydro-aromatization on Mo/ZSM-5: About the hidden role of Brønsted acid sites, *Applied Catalysis A: General*, 336 (2008) 79-88.
- [11] P. Schwach, X. Pan, X. Bao, Direct Conversion of Methane to Value-Added Chemicals over Heterogeneous Catalysts: Challenges and Prospects, *Chemical reviews*, 117 (2017) 8497-8520.
- [12] S. Ma, X. Guo, L. Zhao, S. Scott, X. Bao, Recent progress in methane dehydroaromatization: From laboratory curiosities to promising technology, *Journal of Energy Chemistry*, 22 (2013) 1-20.
- [13] H. Liu, Y. Li, W. Shen, X. Bao, Y. Xu, Methane dehydroaromatization over Mo/HZSM-5 catalysts in the absence of oxygen: effects of silanation in HZSM-5 zeolite, *Catalysis Today*, 93–95 (2004) 65-73.
- [14] F. Denardin, O.W. Perez-Lopez, Tuning the acidity and reducibility of Fe/ZSM-5 catalysts for methane dehydroaromatization, *Fuel*, 236 (2019) 1293-1300.
- [15] A. Martínez, E. Peris, M. Derewinski, A. Burkat-Dulak, Improvement of catalyst stability during methane dehydroaromatization (MDA) on Mo/HZSM-5 comprising intracrystalline mesopores, *Catalysis Today*, 169 (2011) 75-84.

- [16] D. Ma, Y. Lu, L. Su, Z. Xu, Z. Tian, Y. Xu, L. Lin, X. Bao, Remarkable Improvement on the Methane Aromatization Reaction: A Highly Selective and Coking-Resistant Catalyst, *The Journal of Physical Chemistry B*, 106 (2002) 8524-8530.
- [17] J. Gao, Y. Zheng, J.-M. Jehng, Y. Tang, I.E. Wachs, S.G. Podkolzin, Identification of molybdenum oxide nanostructures on zeolites for natural gas conversion, *Science*, 348 (2015) 686-690.
- [18] J.-P. Tessonnier, B. Louis, S. Walspurger, J. Sommer, M.-J. Ledoux, C. Pham-Huu, Quantitative Measurement of the Brönsted Acid Sites in Solid Acids: Toward a Single-Site Design of Mo-Modified ZSM-5 Zeolite, *The Journal of Physical Chemistry B*, 110 (2006) 10390-10395.
- [19] N. Kosinov, A.S.G. Wijpkema, E. Uslamin, R. Rohling, F.J.A.G. Coumans, B. Mezari, A. Parastaei, A.S. Poryvaev, M.V. Fedin, E.A. Pidko, E.J.M. Hensen, Confined Carbon Mediating Dehydroaromatization of Methane over Mo/ZSM-5, *Angewandte Chemie*, 57 (2018) 1016-1020.
- [20] W. Ding, G.D. Meitzner, D.O. Marler, E. Iglesia, Synthesis, Structural Characterization, and Catalytic Properties of Tungsten-Exchanged H-ZSM5, *The Journal of Physical Chemistry B*, 105 (2001) 3928-3936.
- [21] I. Vollmer, G. Li, I. Yarulina, N. Kosinov, E.J. Hensen, K. Houben, D. Mance, M. Baldus, J. Gascon, F. Kapteijn, Relevance of the Mo-precursor state in H-ZSM-5 for methane dehydroaromatization, *Catalysis Science & Technology*, 8 (2018) 916-922.
- [22] L.Y. Chen, L.W. Lin, Z.S. Xu, X.S. Li, T. Zhang, Dehydro-oligomerization of Methane to Ethylene and Aromatics over Molybdenum/HZSM-5 Catalyst, *Journal of Catalysis*, 157 (1995) 190-200.
- [23] Y. Xu, S. Liu, X. Guo, L. Wang, M. Xie, Methane activation without using oxidants over Mo/HZSM-5 zeolite catalysts, *Catalysis Letters*, 30 (1994) 135-149.
- [24] J. Shu, A. Adnot, B.P.A. Grandjean, Bifunctional Behavior of Mo/HZSM-5 Catalysts in Methane Aromatization, *Industrial & Engineering Chemistry Research*, 38 (1999) 3860-3867.
- [25] P.L. Tan, C.T. Au, S.Y. Lai, Effects of acidification and basification of impregnating solution on the performance of Mo/HZSM-5 in methane aromatization, *Applied Catalysis A: General*, 324 (2007) 36-41.
- [26] T.H. Lim, K. Nam, I.K. Song, K.-Y. Lee, D.H. Kim, Effect of Si/Al<sub>2</sub> ratios in Mo/H-MCM-22 on methane dehydroaromatization, *Applied Catalysis A: General*, 552 (2018) 11-20.
- [27] H. Tian, C.A. Roberts, I.E. Wachs, Molecular Structural Determination of Molybdena in Different Environments: Aqueous Solutions, Bulk Mixed Oxides, and Supported MoO<sub>3</sub> Catalysts, *The Journal of Physical Chemistry C*, 114 (2010) 14110-14120.
- [28] Y.-H. Kim, R.W. Borry, E. Iglesia, Genesis of methane activation sites in Mo-exchanged H-ZSM-5 catalysts, *Microporous and Mesoporous Materials*, 35 (2000) 495-509.

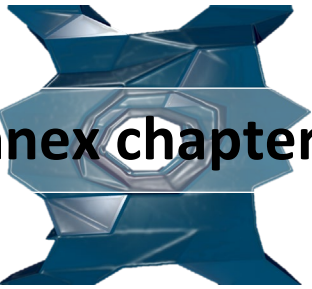
## CHAPTER 3

- [29] D. Ma, Y. Shu, W. Zhang, X. Han, Y. Xu, X. Bao, In Situ  $^1\text{H}$  MAS NMR Spectroscopic Observation of Proton Species on a Mo-Modified HZSM-5 Zeolite Catalyst for the Dehydroaromatization of Methane, *Angewandte Chemie International Edition*, 39 (2000) 2928-2931.
- [30] D. Ma, W. Zhang, Y. Shu, X. Liu, Y. Xu, X. Bao, MAS NMR, ESR and TPD studies of Mo/HZSM-5 catalysts: evidence for the migration of molybdenum species into the zeolitic channels, *Catalysis Letters*, 66 (2000) 155-160.
- [31] D. Ma, Y. Shu, X. Han, X. Liu, Y. Xu, X. Bao, Mo/HMCM-22 Catalysts for Methane Dehydroaromatization: A Multinuclear MAS NMR Study, *The Journal of Physical Chemistry B*, 105 (2001) 1786-1793.
- [32] W. Zhang, D. Ma, X. Han, X. Liu, X. Bao, X. Guo, X. Wang, Methane Dehydroaromatization over Mo/HZSM-5 in the Absence of Oxygen: A Multinuclear Solid-State NMR Study of the Interaction between Supported Mo Species and HZSM-5 Zeolite with Different Crystal Sizes, *Journal of Catalysis*, 188 (1999) 393-402.
- [33] B.S. Liu, Y. Zhang, J.F. Liu, M. Tian, F.M. Zhang, C.T. Au, A.S.C. Cheung, Characteristic and Mechanism of Methane Dehydroaromatization over Zn-Based/HZSM-5 Catalysts under Conditions of Atmospheric Pressure and Supersonic Jet Expansion, *The Journal of Physical Chemistry C*, 115 (2011) 16954-16962.
- [34] Y. Shu, D. Ma, L. Xu, Y. Xu, X. Bao, Methane dehydro-aromatization over Mo/MCM-22 catalysts: a highly selective catalyst for the formation of benzene, *Catalysis Letters*, 70 (2000) 67-73.
- [35] B. Rhimi, M. Mhamdi, V.N. Kalevaru, A. Martin, Synergy between vanadium and molybdenum in bimetallic ZSM-5 supported catalysts for ethylene ammonoxidation, *RSC Advances*, 6 (2016) 65866-65878.
- [36] S. Liu, L. Wang, R. Ohnishi, M. Ichikawa, Bifunctional Catalysis of Mo/HZSM-5 in the Dehydroaromatization of Methane to Benzene and Naphthalene XAFS/TG/DTA/MASS/FTIR Characterization and Supporting Effects, *Journal of Catalysis*, 181 (1999) 175-188.
- [37] N. Kosinov, F.J. Coumans, G. Li, E. Uslamin, B. Mezari, A.S. Wijpkema, E.A. Pidko, E.J. Hensen, Stable Mo/HZSM-5 methane dehydroaromatization catalysts optimized for high-temperature calcination-regeneration, *Journal of Catalysis*, 346 (2017) 125-133.
- [38] P.L. Tan, Y.L. Leung, S.Y. Lai, C.T. Au, The effect of calcination temperature on the catalytic performance of 2 wt.% Mo/HZSM-5 in methane aromatization, *Applied Catalysis A: General*, 228 (2002) 115-125.
- [39] I. Lezcano-González, R. Oord, M. Rovezzi, P. Glatzel, S.W. Botchway, B.M. Weckhuysen, A.M. Beale, Molybdenum Speciation and its Impact on Catalytic Activity during Methane Dehydroaromatization in Zeolite ZSM-5 as Revealed by Operando X-Ray Methods, *Angewandte Chemie International Edition*, 55 (2016) 5215-5219.
- [40] R.W. Borry, Y.H. Kim, A. Huffsmith, J.A. Reimer, E. Iglesia, Structure and density of Mo and acid sites in Mo-exchanged H-ZSM5 catalysts for nonoxidative methane conversion, *The Journal of Physical Chemistry B*, 103 (1999) 5787-5796.

- [41] N. Kosinov, F.J.A.G. Coumans, E.A. Uslamin, A.S.G. Wijpkema, B. Mezari, E.J.M. Hensen, Methane Dehydroaromatization by Mo/HZSM-5: Mono- or Bifunctional Catalysis?, *ACS Catalysis*, (2016) 520-529.
- [42] I. Yarulina, K. De Wispelaere, S. Bailleul, J. Goetze, M. Radersma, E. Abou-Hamad, I. Vollmer, M. Goesten, B. Mezari, E.J.M. Hensen, J.S. Martínez-Espín, M. Morten, S. Mitchell, J. Perez-Ramirez, U. Olsbye, B.M. Weckhuysen, V. Van Speybroeck, F. Kapteijn, J. Gascon, Structure-performance descriptors and the role of Lewis acidity in the methanol-to-propylene process, *Nature Chemistry*, 10 (2018) 804-812.
- [43] J.-Z. Zhang, M.A. Long, R.F. Howe, Molybdenum ZSM-5 zeolite catalysts for the conversion of methane to benzene, *Catalysis Today*, 44 (1998) 293-300.
- [44] W. Liu, Y. Xu, S.-T. Wong, L. Wang, J. Qiu, N. Yang, Methane dehydrogenation and aromatization in the absence of oxygen on MoHZSM-5: A study on the interaction between Mo species and HZSM-5 by using 27Al and 29Si MAS NMR, *Journal of Molecular Catalysis A: Chemical*, 120 (1997) 257-265.
- [45] L. Su, L. Liu, J. Zhuang, H. Wang, Y. Li, W. Shen, Y. Xu, X. Bao, Creating Mesopores in ZSM-5 Zeolite by Alkali Treatment: A New Way to Enhance the Catalytic Performance of Methane Dehydroaromatization on Mo/HZSM-5 Catalysts, *Catalysis Letters*, 91 (2003) 155-167.
- [46] Y. Wu, L. Emdadi, Z. Wang, W. Fan, D. Liu, Textural and catalytic properties of Mo loaded hierarchical meso-/microporous lamellar MFI and MWW zeolites for direct methane conversion, *Applied Catalysis A: General*, 470 (2014) 344-354.
- [47] Y. Lu, D. Ma, Z. Xu, Z. Tian, X. Bao, L. Lin, A high coking-resistance catalyst for methane aromatization, *Chemical Communications*, (2001) 2048-2049.
- [48] I. Yarulina, S. Bailleul, A. Pustovarenko, J.R. Martinez, K.D. Wispelaere, J. Hajek, B.M. Weckhuysen, K. Houben, M. Baldus, V. Van Speybroeck, F. Kapteijn, J. Gascon, Suppression of the Aromatic Cycle in Methanol-to-Olefins Reaction over ZSM-5 by Post-Synthetic Modification Using Calcium, *ChemCatChem*, 8 (2016) 3057-3063.
- [49] S. Bordiga, C. Lamberti, F. Bonino, A. Travert, F. Thibault-Starzyk, Probing zeolites by vibrational spectroscopies, *Chemical Society Reviews*, 44 (2015) 7262-7341.
- [50] C.A. Emeis, Determination of Integrated Molar Extinction Coefficients for Infrared Absorption Bands of Pyridine Adsorbed on Solid Acid Catalysts, *Journal of Catalysis*, 141 (1993) 347-354.
- [51] C.J. Powell, A. Jablonski, Surface sensitivity of X-ray photoelectron spectroscopy, *Nuclear Instruments and Methods in Physics Research Section A: Accelerators, Spectrometers, Detectors and Associated Equipment*, 601 (2009) 54-65.
- [52] A.J. C. J. Powell, NIST Electron Inelastic-Mean-Free-Path Database, Version 1.2, SRD 71, National Institute of Standards and Technology, Gaithersburg, MD, 2010.
- [53] J.C. Ashley, V.E. Anderson, Interaction of low-energy electrons with silicon dioxide, *Journal of Electron Spectroscopy and Related Phenomena*, 24 (1981) 127-148.

## CHAPTER 3

- [54] H. Jiang, L. Wang, W. Cui, Y. Xu, Study on the induction period of methane aromatization over Mo/HZSM-5: partial reduction of Mo species and formation of carbonaceous deposit, *Catalysis Letters*, 57 (1999) 95-102.
- [55] E.V. Matus, I.Z. Ismagilov, O.B. Sukhova, V.I. Zaikovskii, L.T. Tsikoza, Z.R. Ismagilov, J.A. Moulijn, Study of Methane Dehydroaromatization on Impregnated Mo/ZSM-5 Catalysts and Characterization of Nanostructured Molybdenum Phases and Carbonaceous Deposits, *Industrial & Engineering Chemistry Research*, 46 (2007) 4063-4074.



## **Annex chapter 3**

**Quantifying the impact of dispersion, acidity  
and porosity of Mo/HZSM-5 on the  
performance in methane**

## Contents

<b>A3.1 Synthesis method</b>	105
<b>A3.2 Catalytic Results</b>	108
<b>A3.3 Detailed discussion of catalytic results</b>	109
<b>A3.3.1 CVD</b>	109
<b>A3.3.1.1 CVD3</b>	109
<b>A3.3.1.2 Effect of <i>in-vacuo</i> sublimation</b>	110
<b>A3.3.1.3 MoCl<sub>5</sub> versus MoO<sub>2</sub>Cl<sub>2</sub></b>	112
<b>A3.3.1.4 Influence of drying prior to introduction of Mo</b>	112
<b>A3.3.1.5 Influence of mixing the precursor with the zeolite</b>	112
<b>A3.3.1.6 Effect of calcination treatment</b>	113
<b>A3.3.2 Other synthesis approaches</b>	114
<b>A3.3.2.1 Solid ion exchange (SIE)</b>	114
<b>A3.3.2.2 Mo(CO)<sub>6</sub></b>	114
<b>A3.4 Summary of characterization and catalytic results</b>	115
<b>A3.5 Characterization</b>	119
<b>A3.5.1 N<sub>2</sub> adsorption</b>	119
<b>A3.5.2 X-ray powder diffraction</b>	120
<b>A3.5.3 <sup>27</sup>Al MAS NMR</b>	122
<b>A3.5.4 Infrared spectra</b>	124
<b>A3.5.5 Calculation of mean escape depth</b>	128
<b>A3.5.6 UV-Vis spectra</b>	129
<b>A3.5.7 TGA</b>	130
<b>A3.5.8 N<sub>2</sub> adsorption on spent catalyst</b>	134
<b>A3.6 References</b>	135

### A3.1 Synthesis methods

**Incipient wetness impregnation** (IWI) was performed dissolving appropriate amounts of ammonium heptamolybdate ( $(\text{NH}_4)_6\text{Mo}_7\text{O}_{24}$ , AHM) in a volume of water needed to fill the pores of the zeolite powder (400  $\mu\text{l/g}$ ). The AHM solution is introduced to the zeolite previously dried at 293 K for 10 h and mixing. The impregnated samples are dried overnight at 353 K and calcined under static air at 823 K for 5 h using a heating rate of 2 K/min.

For **Solid ion exchange** (SIE) the Mo precursor, either  $\text{MoCl}_5$  or  $\text{MoO}_3$  mixed with the zeolite until a homogeneous colour was achieved using a mortar and pestle and then calcined under static air at 823 K for 5 h using a heating rate of 2 K/min.

### Chemical vapor deposition (CVD)

Different synthesis methods found in literature were compared and different synthesis steps assessed for their impact on catalyst performance. **CVD1**, adapted from Ding *et al.* and was the most elaborate synthesis method found and was therefore used as a starting point for optimization [1]. **Figure A3.1** illustrates this procedure in 7 steps. 2 g of zeolite are filled into an ampule (1), which is connected to flexible tubing equipped with a valve. This tubing is connected to a vacuum pump to keep the ampule under dynamic vacuum while heating slowly to 673 K for 10 to 16 h to dry the zeolite (2). With the valve closed, the ampule is transferred to an Ar glovebox and the dried zeolite is mixed well with the appropriate amount of anhydrous Mo precursor until a homogeneous color is achieved (3). The mixture is then filled back into the ampule connected to the flexible tubing with the valve closed in order to avoid contact with the atmosphere, while the ampule is transferred back to the vacuum pump. After thorough evacuation the ampule is flame-sealed (4). The sealed ampule is slowly heated to 673 K and kept there for 4 h. After this step the zeolite adopts a very homogeneous color (5). The ampule is broken inside the glovebox and the powder filled on top of the frit of a U-shaped quartz reactor, which is connected to flexible tubing with closed valves (6). The reactor is placed into a custom-made setup and a 100 ml/min flow of 0.6% $\text{H}_2\text{O}$ /19.7% $\text{O}_2$ /79.7% $\text{N}_2$  is sent to the sample from the bottom (upflow). Water is added to the flow using a saturator kept at 273 K with an ice bath. The temperature is ramped to 523 K with 10 K/min and kept there for 0.5 h after which the flow is switched to pure synthetic air (100 ml/min, 20% $\text{O}_2$ /80% $\text{N}_2$ ).

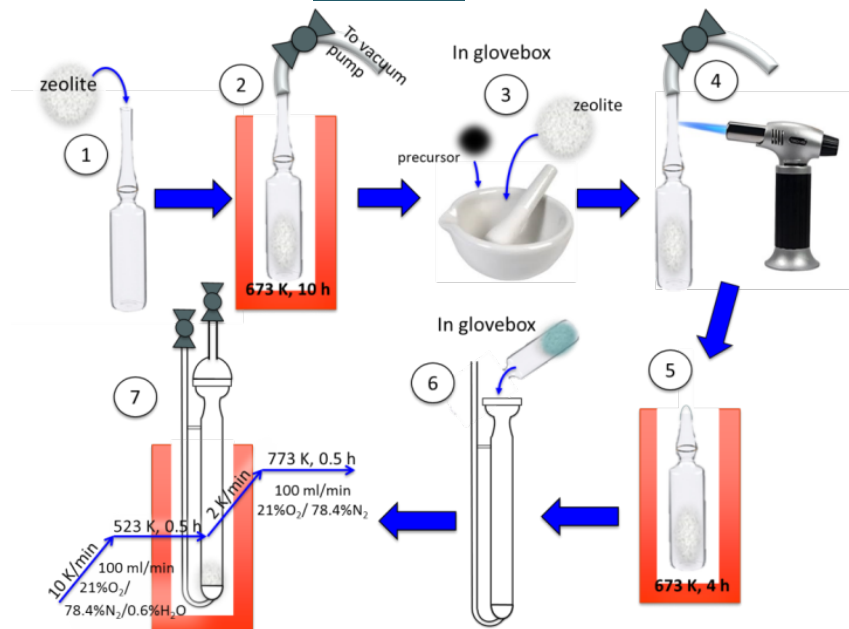


Figure A3.1. Illustration of the CVD1 synthesis.

The temperature is then further increased to 773 K with 2 K/min with a dwell time of 0.5 h (7).

Different steps of **CVD1** were then assessed by omitting them or changing the conditions:

**CVD3** is an alteration of **CVD1** leaving out steps (4) and (5). For **CVD3(i)** water was added to the 100 ml/min synthetic air flow for the entire duration of step (7), while no water was added for **CVD3(ii)**.

**CVD5** is an alteration of **CVD3** leaving out steps (1) and (2) as well and performing step (3) under ambient conditions.

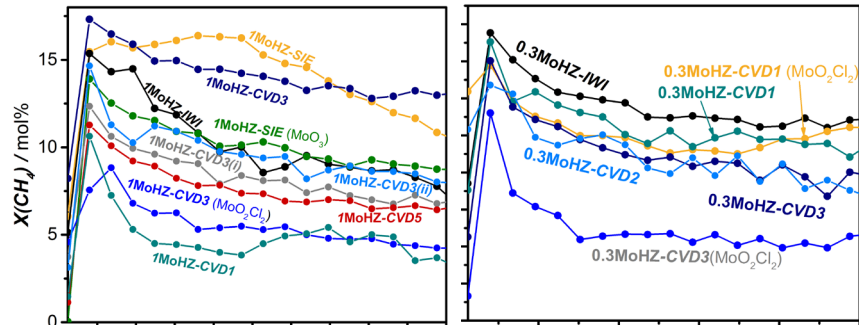
For **CVD4a**, The zeolite is filled into an ampule and evacuated as in step (1) and (2) of **CVD1**. The dried zeolite is filled into the same U-shaped reactor as used for **CVD1** inside the glovebox. The zeolite is placed on top of the quartz frit, while the Mo precursor is filled into the thinner part of the reactor below the quartz frit. Tubing, equipped with valves on inlet and outlet is connected and with valves closed the reactor is connected to a homemade setup where it is subjected to the same calcination treatment as in step (7) of **CVD1**.

For **CVD4b**. The zeolite is filled into an ampule and evacuated as in step (1) and (2) of **CVD1**. The dried zeolite is filled into a U-shaped reactor (i.d. 4 mm) inside the glovebox (**Figure A3.6**). The zeolite is placed on one side of a piece of quartz wool, while the Mo precursor is filled into the other side. Tubing, equipped with valves on inlet and outlet is connected and with valves closed the reactor is connected to a homemade setup where it is subjected to a 30 ml/min Ar flow. The reactor is heated to 523 K with a ramp of 10 K/min and kept there for 0.5 h after which it is further heated to 773 K with 2 K/min.

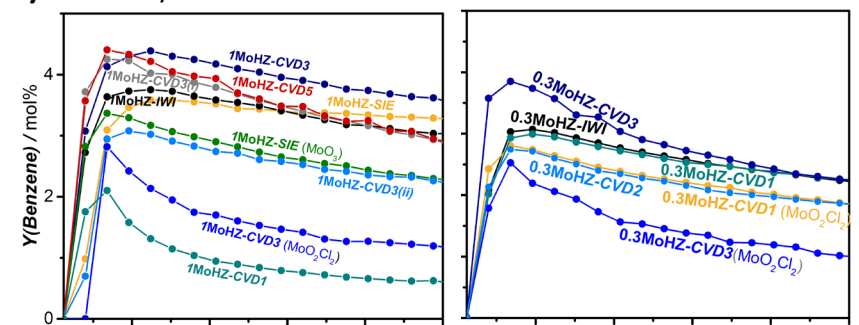
**CVD2** is only used for  $\text{Mo}(\text{CO})_6$ , because of its low boiling point. 2 g zeolite is dried in an ampule and transferred to the glovebox as in step (1) and (2) of **CVD1**. In the glovebox  $\text{Mo}(\text{CO})_6$  is ground well with the zeolite and transferred to a Schlenk reaction tube. The Schlenk reaction tube containing the mixture is transferred to a vacuum pump without exposure to the atmosphere, evacuated and closed with a valve. The closed Schlenk reaction tube is put into a sonication bath for 0.5 h after which it is heated in an oil bath at 353 K for 2 h. The zeolite with the deposited Mo is then calcined under static air at 823 K for 7 h heating with 2 K/min.

## A3.2 Catalytic Results

### a) methane conversion



### b) benzene yield



### c) naphthalene yield

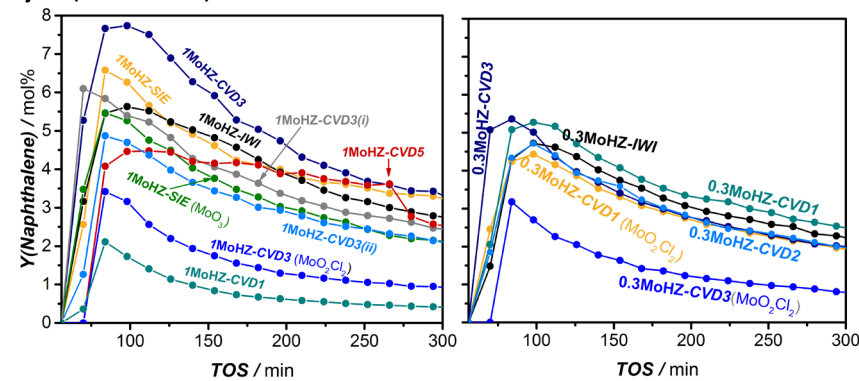


Figure A3.2. a) Methane conversion, b) benzene yields and c) naphthalene yields of **1MoHZ-x** samples (left) and **0.3MoHZ-CVDx** samples (right). Catalysts are prepared using  $MoCl_5$  as a precursor unless otherwise indicated in the brackets.

### A3.3 Detailed discussion of catalytic results

#### A3.3.1 CVD

##### A3.3.1.1 CVD3

**CVD3** is an alteration of **CVD1**, omitting the sublimation step in the flame-sealed ampule (step(4) and (5), **Figure A3.1**) and initially led to a best performing catalyst (**Figure A3.2**) however with very low reproducibility. **Figure A3.3** shows the UV-Vis absorption spectrum of **1MoHZ-CVD3** and **1MoHZ-IWI** together with the precursor, MoCl<sub>5</sub>. The absorption of MoCl<sub>5</sub>, which absorbs at 313 nm and 245 nm is very different from **1MoHZ-CVD3** and **1MoHZ-IWI** with absorption at around 230 and 270 nm, demonstrating that no significant amount of chloride remains on the sample and that Mo is present in oxidic form. This was also confirmed by XPS, where no Cl was detected in the survey spectrum (**Figure A3.4**).

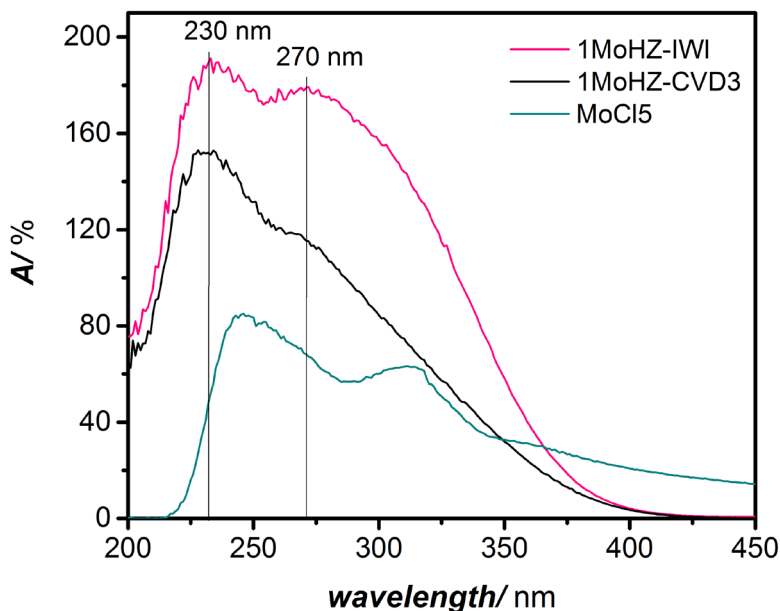


Figure A3.3. UV-Vis spectra of **1MoHZ-IWI** and **1MoHZ-CVD3** compared to the MoCl<sub>5</sub> reference.

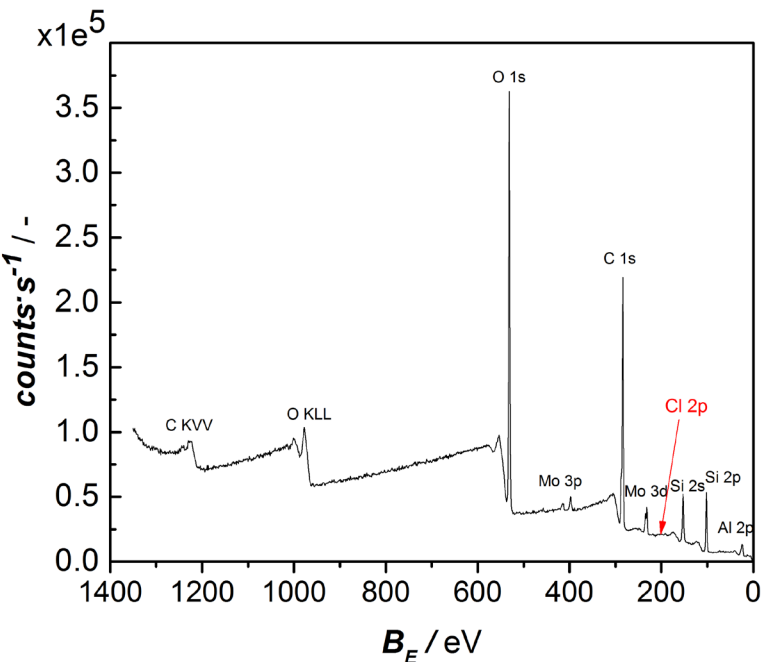
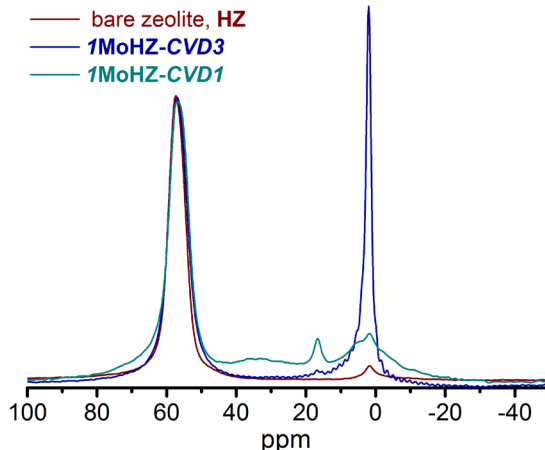


Figure A3.4. XPS survey spectrum of **1MoHZ-CVD3**.

#### A3.3.1.2 Effect of *in-vacuo* sublimation

*In-vacuo* deposition of Mo has a negative effect on catalyst performance, because the BAS are largely destroyed during this step (step (4) and (5), **Figure S1**). The catalyst is subjected to a harsh acid and or chlorine treatment due to the HCl and Cl<sub>2</sub> that form when MoCl<sub>5</sub> reacts with the acidic protons of the zeolite and cannot escape the flame-sealed ampule. **Figure A3.5a** shows that the contribution for BAS (57 ppm) is much broadened for **1MoHZ-CVD1** compared to the bare zeolite and a new resonance appears at 16 ppm stemming from Al<sub>2</sub>(MoO<sub>4</sub>)<sub>3</sub>, which is formed through extraction of framework Al by strongly binding and reacting with Mo [2]. There are also several broad contributions. In contrast, the BAS contribution is only slightly broadened for **1MoHZ-CVD3** and the resonance for Al<sub>2</sub>(MoO<sub>4</sub>)<sub>3</sub> is not observed. Quite some EFAL formed on this sample, which does however not seem to affect catalytic performance negatively. This goes hand-in-hand with an increase in mesoporosity for this sample (**Figure A3.7b**). The N<sub>2</sub>-isotherm of **1MoHZ-CVD1** shows a step at about 0.2 relative pressure also suggesting that the morphology of the zeolite was altered through the harsh acid treatment.

a)



b)

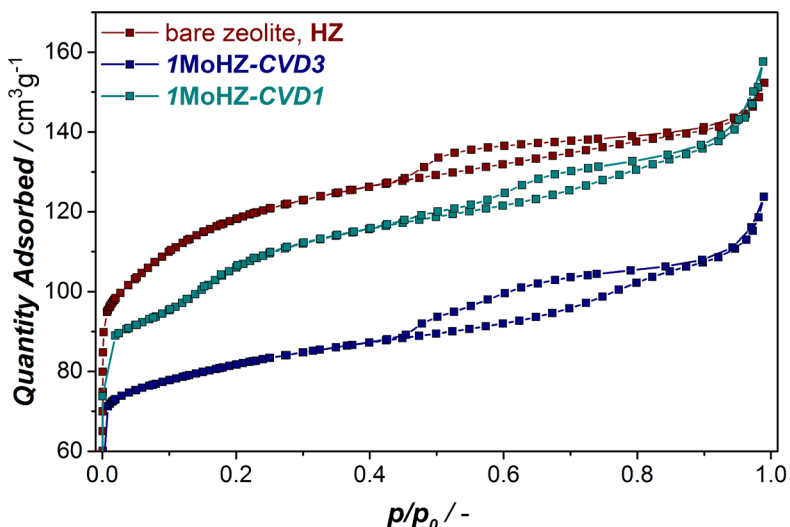


Figure A3.5. a)  $^{27}\text{Al}$  MAS spectra and b) N<sub>2</sub>-adsorption isotherms of the bare zeolite, 1MoHZ-CVD3 and 1MoHZ-CVD1.

### A3.3.1.3 MoCl<sub>5</sub> versus MoO<sub>2</sub>Cl<sub>2</sub>

The catalytic performance of catalysts prepared using two different chlorine Mo precursors, MoCl<sub>5</sub> and MoO<sub>2</sub>Cl<sub>2</sub> was compared for **CVD3**. Figure A3.3 shows that a better catalyst was obtained using MoCl<sub>5</sub> for Mo/Al = 1. The same observation was made for Mo/Al = 0.3 using **CVD3**. For **CVD1** with Mo/Al = 0.3, a

catalyst prepared with  $\text{MoCl}_5$  only shows slightly higher yields to aromatics than a catalyst prepared using  $\text{MoO}_2\text{Cl}_2$ , but the preparation with the oxychloride leads to a much higher overall selectivity to coke of 29 mol% compared to 18 mol% for **0.3MoHZ-CVD1**( $\text{MoCl}_5$ ).

#### A3.3.1.4 Influence of drying prior to introduction of Mo

For **CVD5**, the wet zeolite was directly ground with  $\text{MoCl}_5$  and subjected to the same calcination treatment as in **CVD3** (step (7)). Benzene and naphthalene yields as well as methane conversion do not reach the level of the catalyst prepared with **CVD3** (**Figure A3.2**), suggesting the importance of steps (1) and (2).

#### A3.3.1.5 Influence of mixing the precursor with the zeolite

In other synthesis methods, **CVD4a** and **CVD4b** the zeolite was not mixed with the Mo precursor, but the precursor was filled below the frit of the U-shaped quartz reactor (**Figure A3.6**), while the dried zeolite was put on top of the frit. Using these methods only traces of Mo were found on the zeolite with both ICP and XPS. Thus step (3) was determined to be the most important step.

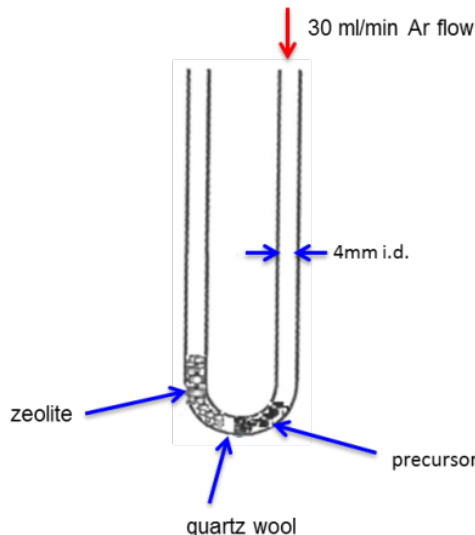


Figure A3.6. Illustration of the reactor configuration used for synthesis **CVD4b**.

#### A3.2.1.6 Effect of the calcination treatment

The effect of adding 0.6vol.% water during the calcination treatment of step (7) in **CVD3** was explored by adding water

throughout the entire treatment (**CVD3(i)**) and by not adding water through step (7) (**CVD3(ii)**). **CVD3** leads to the best performance, especially in terms of naphthalene yields. When water is left out (**CVD3(ii)**), the initial yield of benzene is similar, but the catalyst deactivates faster and less naphthalene is produced. The catalyst treated with water throughout the whole duration of step (7) (**CVD3(i)**), produces even less naphthalene; the naphthalene production is delayed, which indicates that this catalyst already experiences more coking during the induction period. In addition, benzene production decreases faster than for **CVD3**. The comparison of the three catalysts illustrates that adding water throughout the first phase of step (7) has a positive effect on the performance, but that adding water is not strictly necessary to produce an active catalyst. We speculate that adding water at relatively mild temperatures up to 523 K creates some mesoporosity, which positively affects catalyst performance, but that adding water throughout the whole calcination treatment leads to agglomeration of Mo, which negatively affects performance.

### A3.3.2 Other synthesis approaches

#### A3.3.2.1 Solid ion exchange (SIE)

Apart from IWI another synthesis method often used in literature is SIE. Despite the simplicity of this method, it leads to better catalytic performance than IWI both when using  $\text{MoO}_3$  as a precursor and when using  $\text{MoCl}_5$  as is shown in **Figure A3.2**. When using  $\text{MoCl}_5$ , a better performance is achieved compared to  $\text{MoO}_3$ , likely because  $\text{MoCl}_5$  has a far lower boiling point than  $\text{MoO}_3$  and migrates more easily into the pores of the zeolite.

#### A3.3.2.2 $\text{Mo}(\text{CO})_6$

Since  $\text{Mo}(\text{CO})_6$  is well investigated for introducing Mo into Y zeolites,[3-5] this precursor is also explored using synthesis method **CVD2**. **Figure A3.2** shows that a similar performance can be achieved using this synthesis method as when using the conventional IWI.

### A3.4 Summary of characterization and catalytic results

Table A3.1. List of samples and different characterization results relating to the dispersion of Mo.

$(Mo/Al)_{syn}$ a.	Synthesis method	Pre-cursor	$(Mo/Al)_{ICP}$ b.	$(Mo/Al)_{Py FTIR}$ c.	$(Mo/Al)_{XPS}$ d.	$LAS_{extra}$ c.
0.3	IWI	AHM	0.30±0.12	0.11	0.26±0.02	1.89
0.3	CVD1	MoCl <sub>5</sub>	0.30±0.12	0.21	0.24±0.07	3.66
0.3	CVD1	MoO <sub>2</sub> Cl <sub>2</sub>	0.31±0.12	0.08	0.29±0.13	1.94
0.3	CVD3	MoCl <sub>5</sub>	0.39±0.03	0.16	0.33±0.02	2.13
0.3	CVD3	MoO <sub>2</sub> Cl <sub>2</sub>	1.31±0.20	0.24	0.22±0.02	0.99
0.3	CVD2	Mo(CO) <sub>6</sub>	0.27±0.12	0.20	0.19±0.04	2.46
1.0	IWI	AHM	1.06±0.12	0.43	1.44±0.26	4.86
1.0	SIE	MoO <sub>3</sub>	1.25±0.12	0.48	0.54±0.12	5.06
1.0	SIE	MoCl <sub>5</sub>	1.25±0.12	0.50	0.85±0.34	2.86
1.0	CVD1	MoCl <sub>5</sub>	2.35±0.12	0.66	0.12±0.02	0.00
1.0	CVD3	MoCl <sub>5</sub>	1.02±0.12	0.67	0.21±0.15	5.49
1.0	CVD3	MoO <sub>2</sub> Cl <sub>2</sub>	2.38±0.18	0.28	1.24±0.16	4.94
1.0	CVD3 (i)	MoCl <sub>5</sub>	0.58±0.06	0.33	0.38±0.27	6.21
1.0	CVD3 (ii)	MoCl <sub>5</sub>	0.80±0.08	0.39	1.26±0.65	9.10
1.0	CVD5	MoCl <sub>5</sub>	1.20±0.06	0.50	0.40±0.13	5.20
1.0	CVD4a	MoO <sub>2</sub> Cl <sub>2</sub>	0.00±0.12	-	0.00	-
1.0	CVD4b	MoO <sub>2</sub> Cl <sub>2</sub>	0.01±0.12	-	0.00	-

- a. Molar ratio of Mo to Al as aimed at during the synthesis.
- b. Molar ratio of Mo to Al as determined by ICP. For details refer to **Chemical composition** in the experimental part.
- c. Determined by pyridine IR-spectroscopy for details refer to **Pyridine transmission FTIR** in the experimental part.
- d. Molar ratio of Mo to Al as determined by XPS. For details refer to **X-ray photoelectron spectroscopy** in the experimental part. The error represented is the absolute difference between two measurements on two different points on the sample.

Table A3.2. The edge energy ( $E_g$ ) for all samples, determined by fitting a straight line to  $(F(R_\infty)hv)^2$  plotted against the incident photon energy  $hv$  in the low energy rise region [6]. For details refer to **Figure A3.12**.

$(Mo/Al)_{syn}$ a.	Synthesis method	$E_g$ e.
0.3	IWI	4.30
0.3	CVD1	4.40
0.3	CVD1	4.42
0.3	CVD3	4.00
0.3	CVD3	3.72
0.3	CVD2	3.87
1.0	IWI	3.54
1.0	SIE	3.57
1.0	SIE	3.62
1.0	CVD1	3.68
1.0	CVD3	3.77
1.0	CVD3	3.77
1.0	CVD3 (i)	4.11
1.0	CVD3 (ii)	4.03
1.0	CVD5	3.90
1.0	CVD4a	-
1.0	CVD4b	-

Table A3.3. Summary of integral selectivity to different products after 364 min of reaction. For details of the calculation of selectivities refer to **Catalytic testing** in the experimental part.

$(Mo/Al)_{syn}$	Synthesis method	precursor	$S_{C2-C3}/mol\%$	$S_{Benzene}/mol\%$	$S_{Naphthalene}/mol\%$	$S_{coke}/mol\%$
0.3	IWI	AHM	27.1	25.2	30.0	17.7
0.3	CVD1	MoCl <sub>5</sub>	28.4	23.7	32.4	15.5
0.3	CVD1	MoO <sub>2</sub> Cl <sub>2</sub>	24.6	23.4	29.3	19.6
0.3	CVD3	MoCl <sub>5</sub>	8.7	37.6	36.2	17.5
0.3	CVD3	MoO <sub>2</sub> Cl <sub>2</sub>	12.3	30.8	28.2	28.7
0.3	CVD2	Mo(CO) <sub>6</sub>	18.6	27.0	33.7	20.7
1.0	IWI	AHM	22.0	32.4	37.2	8.4
1.0	SIE	MoO <sub>3</sub>	24.3	28.0	34.0	13.7
1.0	SIE	MoCl <sub>5</sub>	12.8	33.0	40.6	13.6
1.0	CVD1	MoCl <sub>5</sub>	11.2	31.7	25.9	20.0
1.0	CVD3	MoCl <sub>5</sub>	22.0	31.8	39.2	7.0
1.0	CVD3	MoO <sub>2</sub> Cl <sub>2</sub>	23.4	25.8	25.2	25.6
1.0	CVD3(i)	MoCl <sub>5</sub>	7.7	35.8	37.5	19.0
1.0	CVD3(ii)	MoCl <sub>5</sub>	6.8	39.0	40.7	13.5
1.0	CVD5	MoCl <sub>5</sub>	11.8	33.9	40.1	14.2

Table A3.4. Summary of maximum instantaneous yields to benzene and naphthalene in the beginning of reaction. For details of the calculation of instantaneous yields refer to **Catalytic testing** in the experimental part.

$(Mo/Al)_{syn}$	Synthesis method	precursor	$Y_{Benzene}/mol\%$	$Y_{naphthalene}/mol\%$
0.3	IWI	AHM	3.07	4.72
0.3	CVD1	MoCl <sub>5</sub>	2.99	5.27
0.3	CVD1	MoO <sub>2</sub> Cl <sub>2</sub>	2.8	4.42
0.3	CVD3	MoCl <sub>5</sub>	3.8	5.3
0.3	CVD3	MoO <sub>2</sub> Cl <sub>2</sub>	2.526	3.176
0.3	CVD2	Mo(CO) <sub>6</sub>	2.474	4.7
1.0	IWI	AHM	3.7	5.63
1.0	SIE	MoO <sub>3</sub>	3.36	5.63
1.0	SIE	MoCl <sub>5</sub>	3.583	5.660
1.0	CVD1	MoCl <sub>5</sub>	2.1	2.107
1.0	CVD3	MoCl <sub>5</sub>	4.4	7.74
1.0	CVD3	MoO <sub>2</sub> Cl <sub>2</sub>	2.818	3.419
1.0	CVD3(i)	MoCl <sub>5</sub>	4.253	4.47
1.0	CVD3(ii)	MoCl <sub>5</sub>	4.4	5.8
1.0	CVD5	MoCl <sub>5</sub>	3.07	4.8

## A3.5 Characterization

### A3.5.1 N<sub>2</sub> Adsorption

N<sub>2</sub> adsorption was performed on a TriStar II 3020 Version 3.02 (Micromeritics) at liquid nitrogen temperature,  $T = 77\text{ K}$  for determination of the BET area. The  $t$ -plot method was used to determine the micropore volume. Before adsorption, the catalyst was outgassed under a flow of N<sub>2</sub> at 673 K for 16 h.

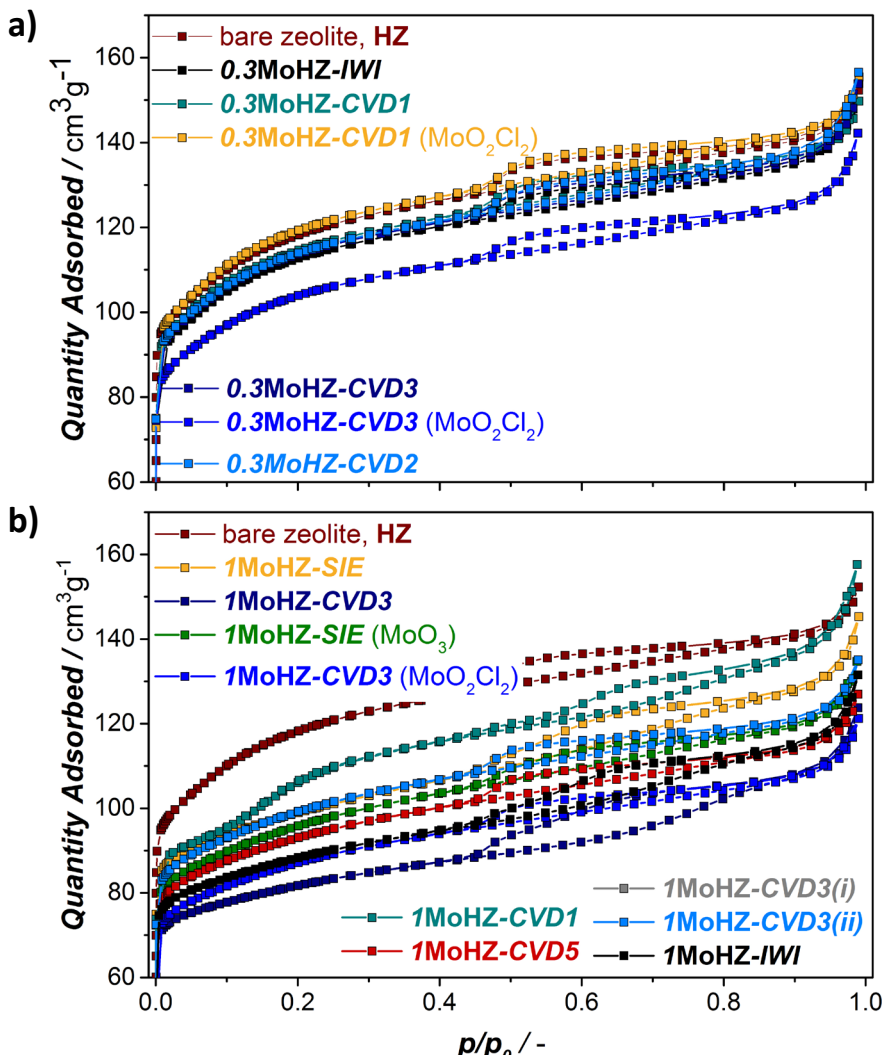


Figure A3.7. N<sub>2</sub> Adsorption isotherms of a) 0.3MoHZ-x and b) 1MoHZ-x.

Table A3.5. Total pore volume, micropore volume and BET surface area determined from N<sub>2</sub> adsorption measurements.

(Mo/Al) <sub>syn</sub>	Synthesis method	precursor	$V_{pore}$ /cm <sup>3</sup> g <sup>-1</sup>	$V_{micro}$ /cm <sup>3</sup> g <sup>-1</sup>	$S_{BET}$ /m <sup>2</sup> g <sup>-1</sup>
0.3	IWI	AHM	0.239	0.141	409
0.3	CVD1	MoCl <sub>5</sub>	0.232	0.143	415
0.3	CVD1	MoO <sub>2</sub> Cl <sub>2</sub>	0.241	0.148	434
0.3	CVD3	MoCl <sub>5</sub>	0.238	0.142	412
0.3	CVD3	MoO <sub>2</sub> Cl <sub>2</sub>	0.220	0.130	376
0.3	CVD2	Mo(CO) <sub>6</sub>	0.243	0.143	413
1.0	IWI	AHM	0.204	0.118	315
1.0	SIE	MoO <sub>3</sub>	0.209	0.126	342
1.0	SIE	MoCl <sub>5</sub>	0.225	0.134	353
1.0	CVD1	MoCl <sub>5</sub>	0.244	0.136	368
1.0	CVD3	MoCl <sub>5</sub>	0.192	0.112	292
1.0	CVD3	MoO <sub>2</sub> Cl <sub>2</sub>	0.188	0.114	312
1.0	CVD3(i)	MoCl <sub>5</sub>	0.230	0.137	392
1.0	CVD3(ii)	MoCl <sub>5</sub>	0.209	0.130	355
1.0	CVD5	MoCl <sub>5</sub>	0.197	0.122	333

### A3.5.2 X-ray powder diffraction

X-ray powder diffraction (XRD) data was collected on a Bruker D8 Advance diffractometer, operating in Bragg-Brentano geometry using Co K $\alpha$  radiation ( $\lambda = 0.179$  nm) and a Lynxeye position sensitive detector to collect data in the range of  $2\theta$  from 5° to 50° with a scan-speed of 0.2°s<sup>-1</sup> and a sample rotation rate of 30 rpm.

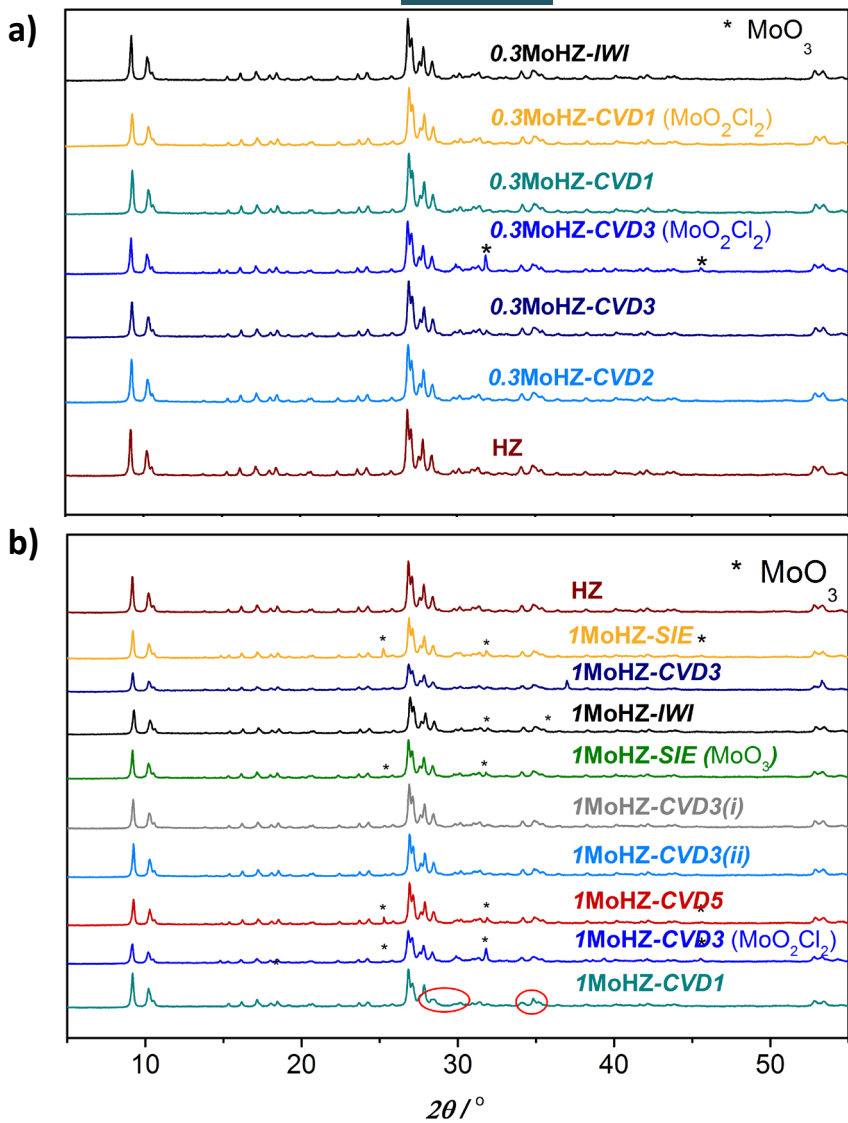
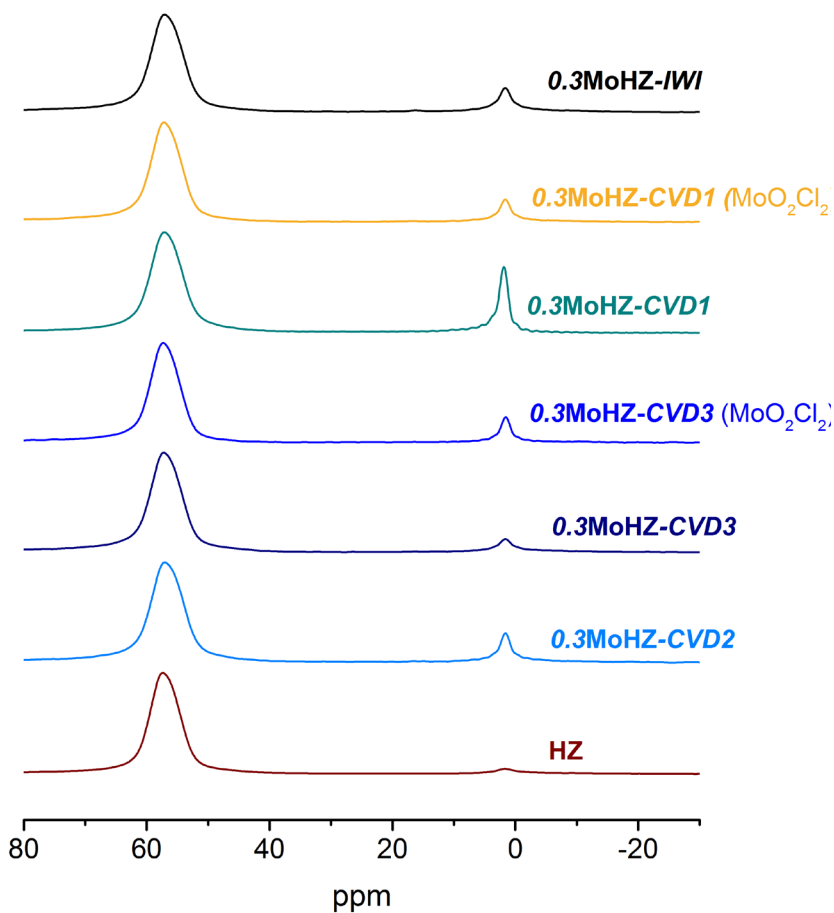


Figure A3.8. XRD patterns of a) **0.3MoHZ-x** and b) **1MoHZ-x**.

### A3.5.3 $^{27}\text{Al}$ MAS NMR

$^{27}\text{Al}$  solid-state NMR spectra were recorded on a wide-bore Bruker Avance III 600 MHz spectrometer equipped with 3.2 mm magic angle spinning (MAS) probe. The temperature was set to 298 K and the MAS frequency was 20 kHz, resulting in an effective temperature of approximately 303 K.  $^{27}\text{Al}$  spectra were referenced externally to the  $^{27}\text{Al}$  signal at 0 ppm of a non-spinning  $\text{Al}(\text{NO}_3)_3$  solution. The spectra were recorded using a 0.78  $\mu\text{s}$   $\pi/12$  excitation pulse and an acquisition time of 6.6 ms. 1024 Scans were accumulated with a recycle delay of 0.8 s. Spectra were processed using a 20 Hz line-broadening window.

a)



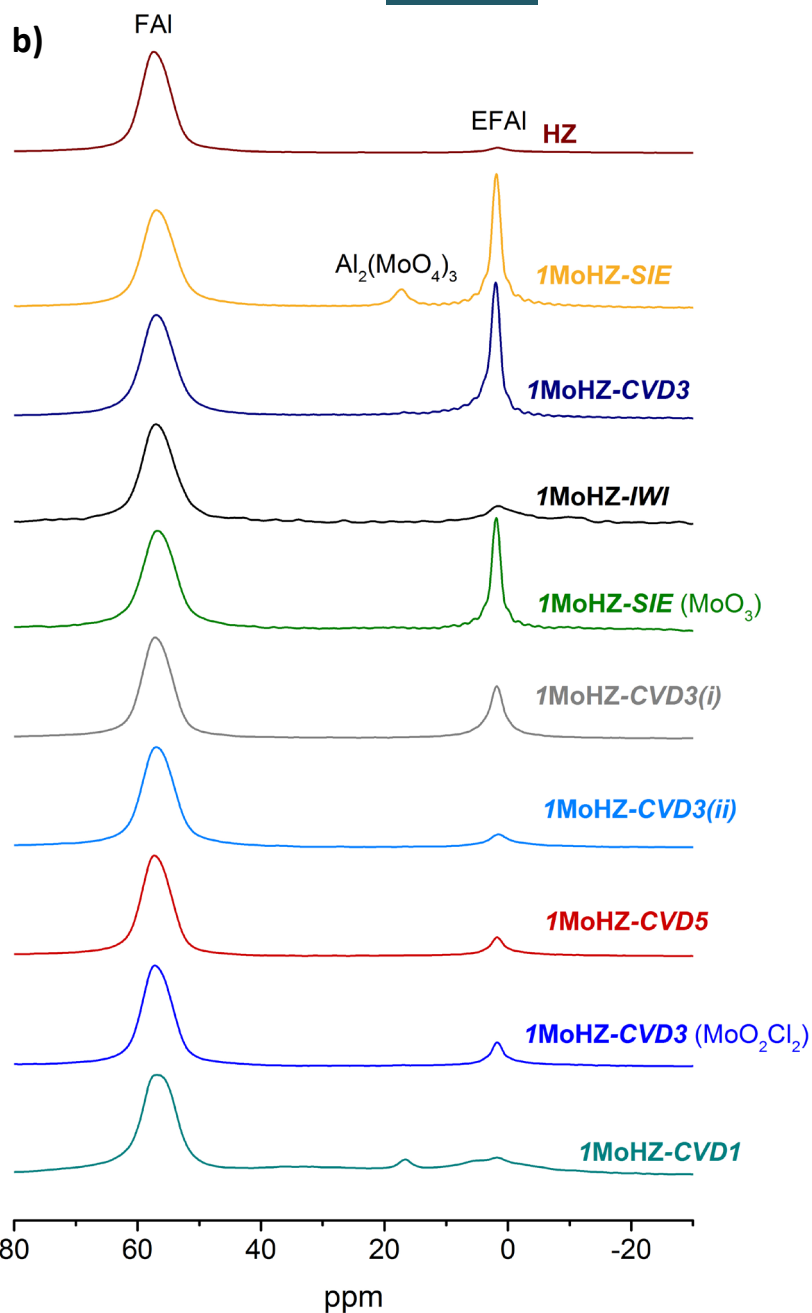
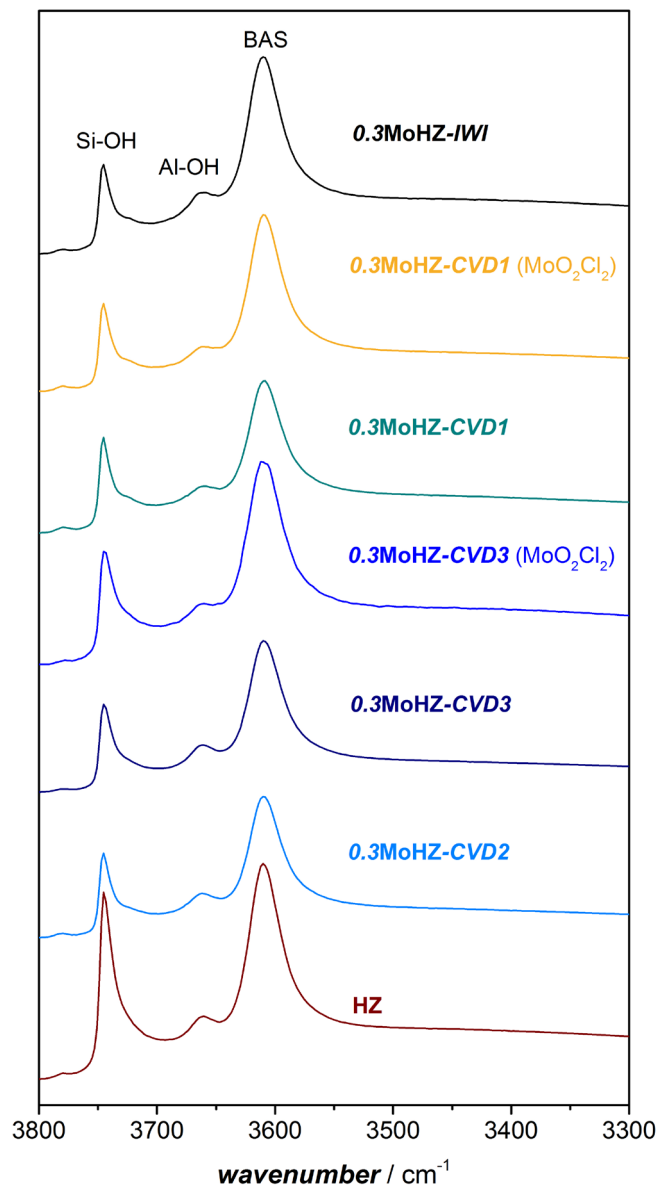


Figure A3.9.  $^{27}\text{Al}$  MAS NMR spectra for a)  $0.3\text{MoHZ-x}$  and b)  $1\text{MoHZ-x}$ .

## A3.5.4 Infrared spectra

a)



b)

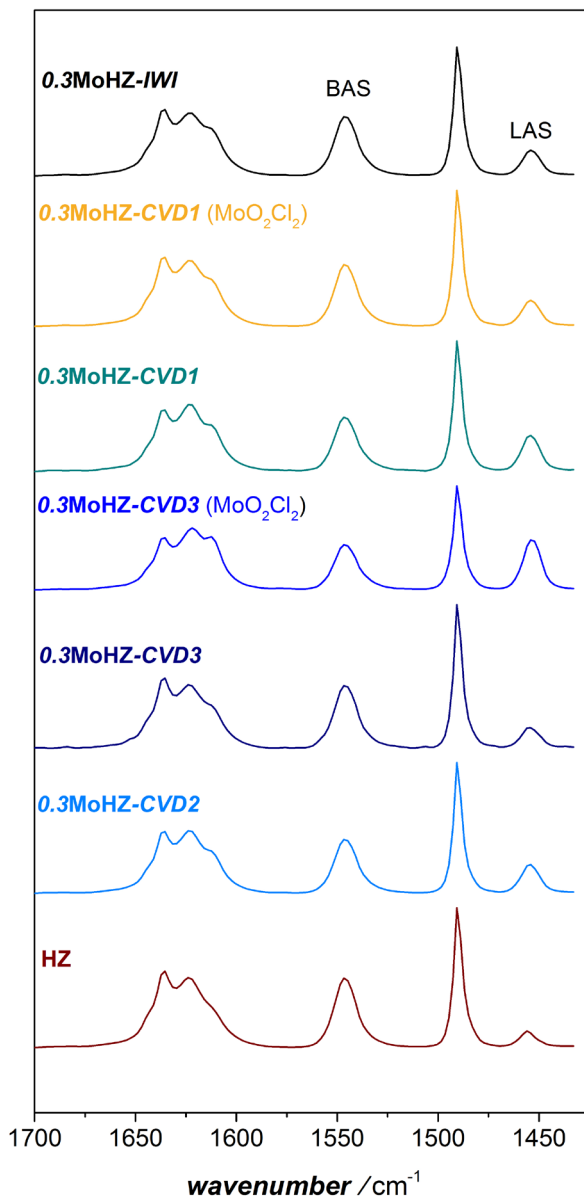
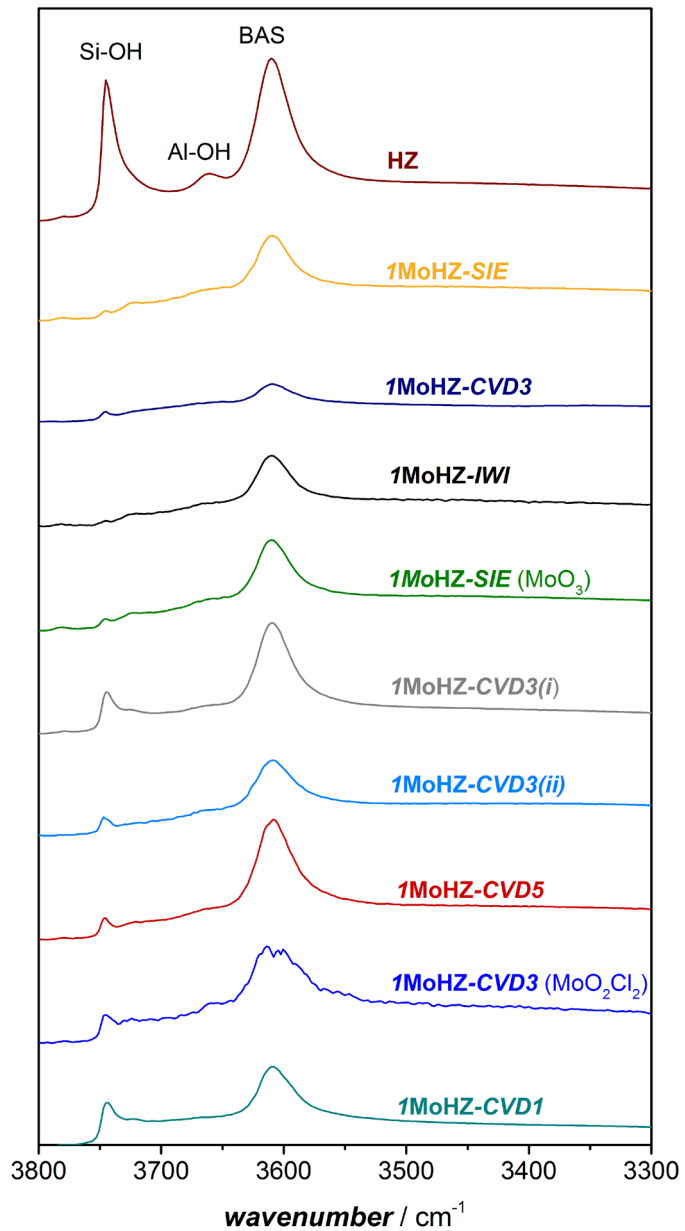


Figure A3.10. a) IR-spectra of OH-region before pyridine adsorption and b) IR-spectra of pyridine adsorbed on **0.3MoHZ-x** samples.

a)



b)

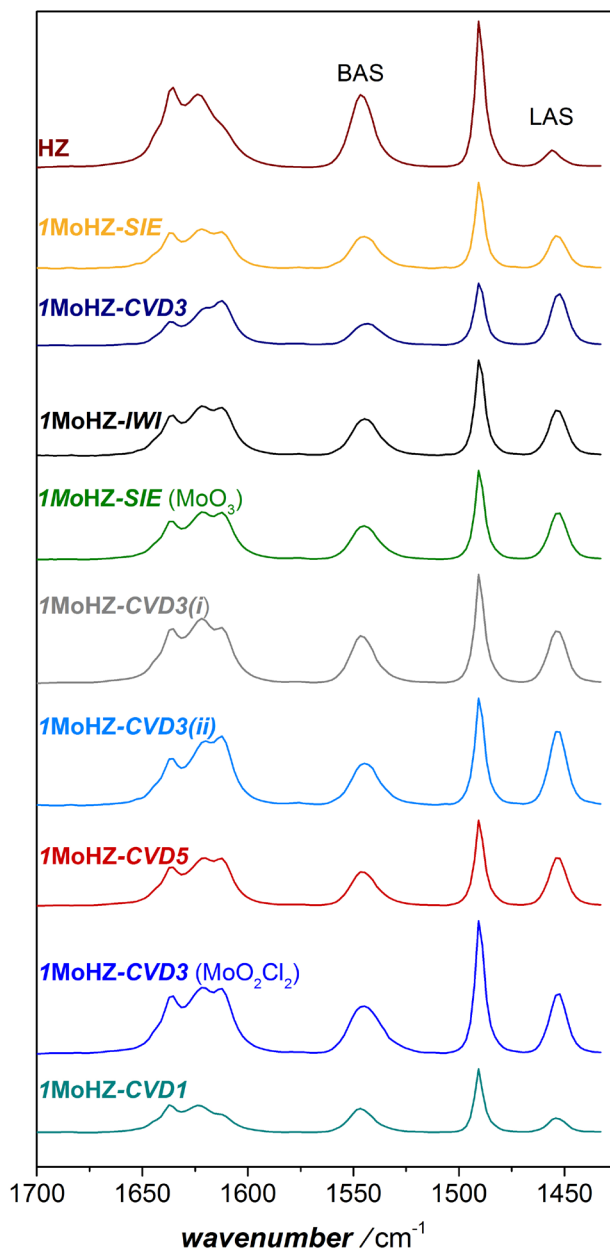


Figure A3.11. a) IR-spectra of OH-region before pyridine adsorption and b) IR-spectra of pyridine adsorbed on **1MoHZ-x** samples.

### A3.5.5 Calculation of mean escape depth

As described by Powell *et al.*[7], the mean escape depth (MED) can be used as a measure of surface sensitivity for a particular experimental configuration and material. The MED can be calculated using **Equation A3.1**, if inelastic scattering is neglected.

$$\Delta = \lambda_i \cos(\alpha) \quad \text{Equation A3.1}$$

In **Equation A3.1**,  $\lambda_i$  denotes the inelastic mean free path and  $\alpha$  denotes the emission angle of the photoelectrons. While  $\alpha$  is  $0^\circ$  for the setup used,  $\lambda_i$  is specific to the investigated material and can be obtained from the NIST database [8]. Since data on zeolite is not available the  $\lambda_i$  for  $\text{SiO}_2$  was used [9]. As  $\lambda_i$  is a function of energy, the kinetic energy of the detected photoelectrons needed to be determined according to **Equation A3.2**, where  $E_{binding}$  is the binding energy ( $B_E$ ) of the electron,  $E_{photon}$  is the energy of the X-ray photons being used, which is 1486.7 eV for Al  $K_\alpha$  X-rays and  $E_{kinetic}$  is the kinetic energy of the electrons as measured by the instrument.  $\Phi$  is the work function dependent on the spectrometer and the material.

$$E_{binding} = E_{photon} - (E_{kinetic} + \Phi) \quad \text{Equation A3.2}$$

**Table A3.6** shows the values obtained for  $E_{kinetic}$  and  $\lambda_i$  for Mo and Al respectively.

Table A3.6. Kinetic energy of the photoelectrons and inelastic mean free path obtained from **Equation A3.2** and ref. [8].

element	$E_{kinetic}/\text{eV}$	$\lambda_i/\text{\AA}^\circ$	$\Delta/\text{\AA}^\circ$
Mo	~1255	~33.0	~33.0
Al	~1413	~36.5	~36.5

## A3.5.6 UV-Vis spectra

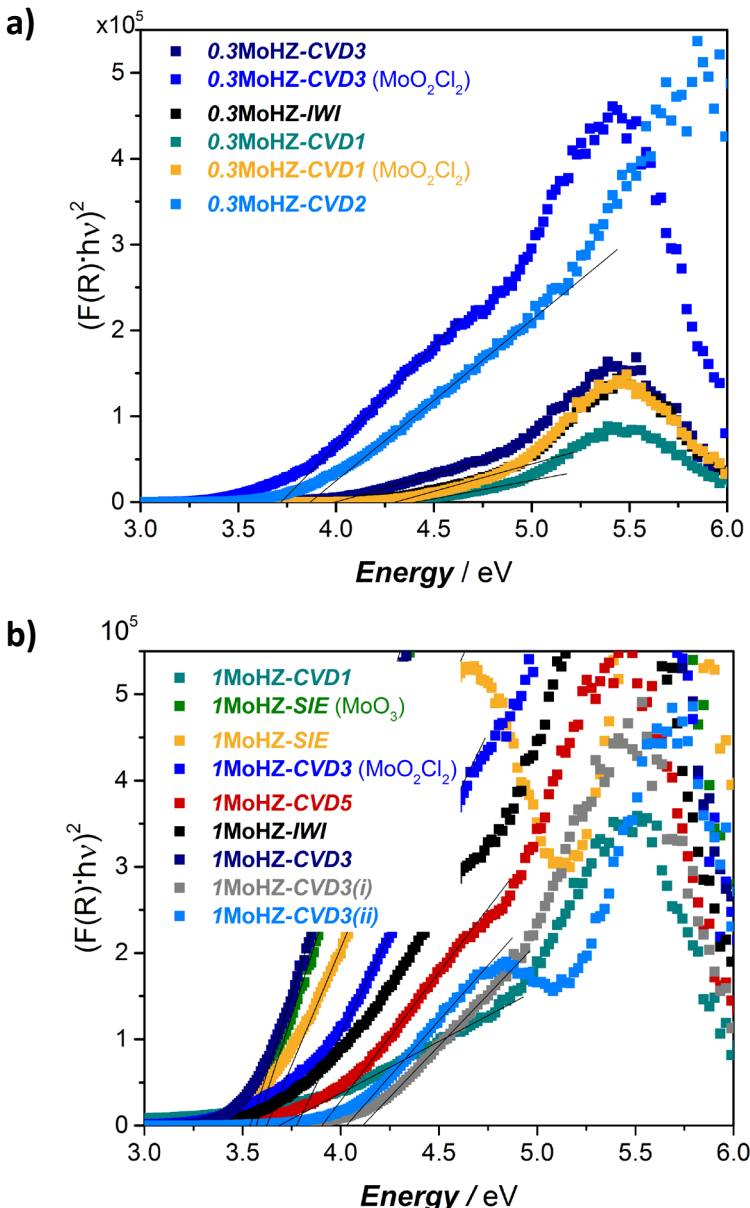
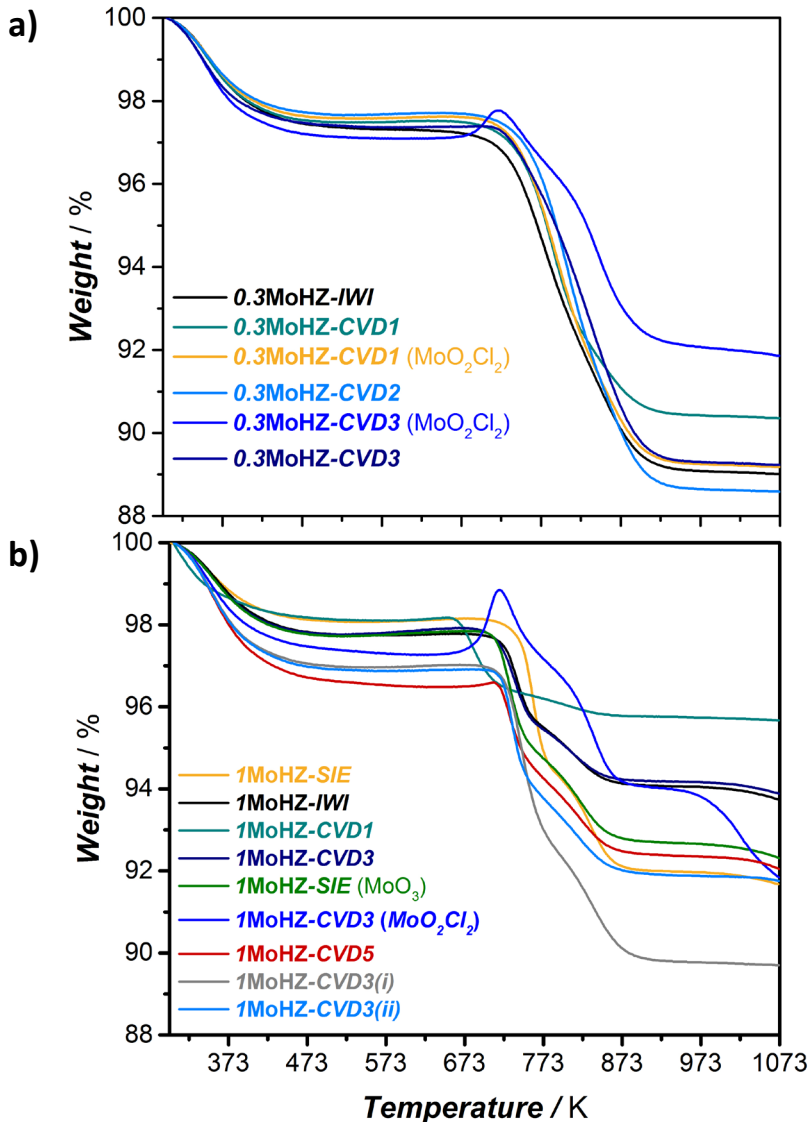


Figure A3.12.  $E_g$  determination from UV-Vis measurements by fitting a straight line to  $(F(R_\infty)\cdot h\nu)^2$  plotted as a function of the incident photon energy  $h\nu$  in the low energy rise region<sup>[18]</sup> for a) **0.3MoHZ-x** samples and b) **1MoHZ-x** samples.

**A3.5.7 TGA**

Thermogravimetric analysis (TGA) is performed on a Mettler Toledo TGA/SDTA851e using 10 to 20 mg of sample under flowing 100 ml/min of air at a heating rate of 10 K/min up to 1073 K. The amount of coke formed during the reaction is calculated from the weight loss between 573 K and 1073 K of the catalyst after 7 h of reaction.



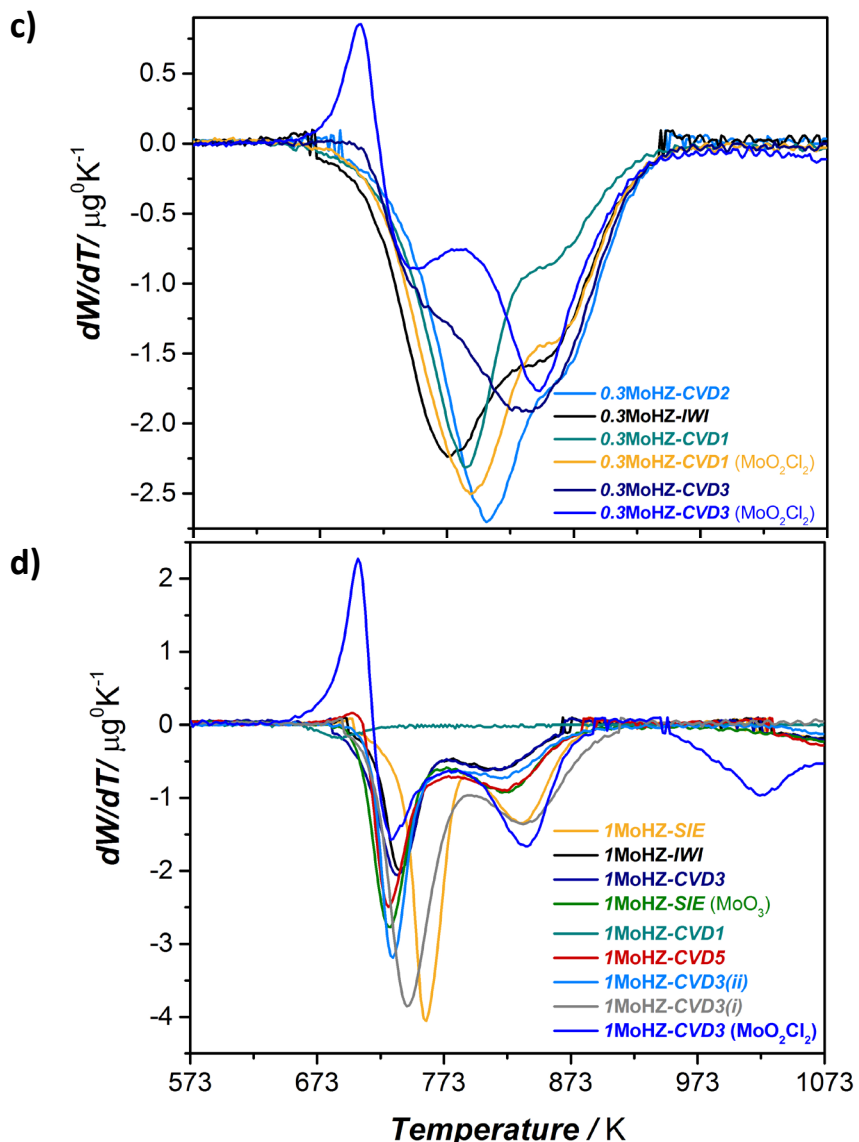


Figure A3.13. TGA of a) spent catalysts **0.3MoHZ-x** and b) spent catalysts **1MoHZ-x** as well as DTGA c) spent catalysts **0.3MoHZ-x** and d) spent catalysts **1MoHZ-x** after 364 min of reaction. Heating rate 10 K/min in air.

A positive peak is observed in the DTGA of **1MoHZ-CVD3 (MoO<sub>2</sub>Cl<sub>2</sub>)** and **1MoHZ-CVD3 (MoO<sub>2</sub>Cl<sub>2</sub>)**. This represents a mass increase due to the oxidation of bigger  $\beta$ -Mo<sub>2</sub>C particles present on those catalysts. This assignment is made by comparison with a TGA and DTGA profile of a pure  $\beta$ -Mo<sub>2</sub>C reference (Figure S15). There is a mass increase in the air oxidation at 673-723 K, which matches with what we observe on the Mo catalysts. A much larger peak centered around 873 K is also observed representing the oxidation of bulk Mo<sub>2</sub>C. The pre-peak at 723 K could correspond to either some smaller particles present in the bulk sample or to (partially) oxidized surface carbide.

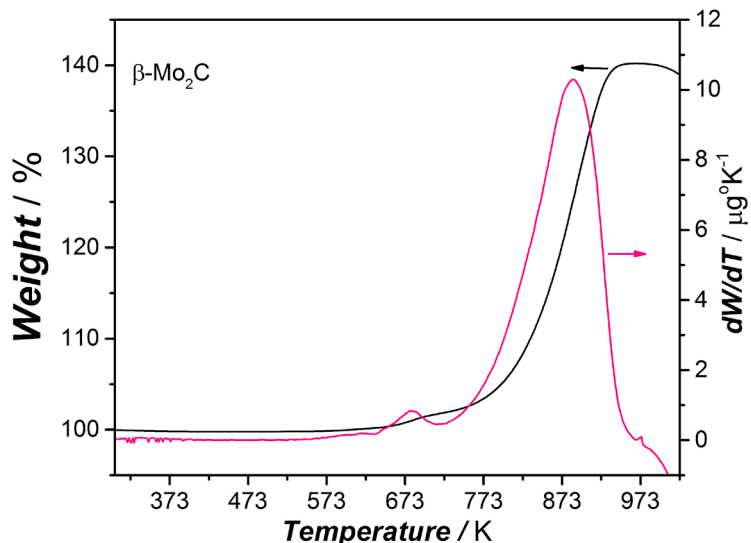


Figure A3.14. TGA and DTGA profile of a pure  $\beta$ -Mo<sub>2</sub>C reference sample. Heating rate 10 K/min in air.

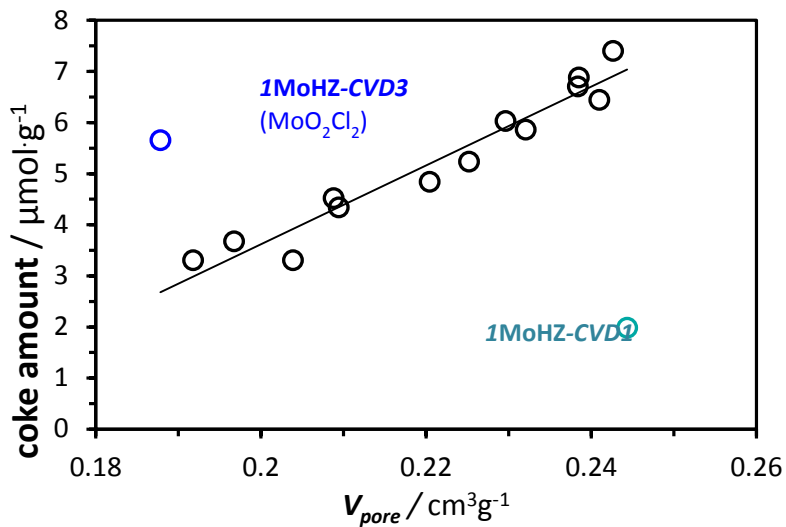


Figure A3.16. Integrated aromatics selectivity as a function of total pore volume as determined by N<sub>2</sub> Adsorption (Figure A3.7, Table A3.5). Samples with Mo/Al=0.3 are represented by the symbols with orange fill.

### A3.5.8 N<sub>2</sub> Adsorption on spent catalyst

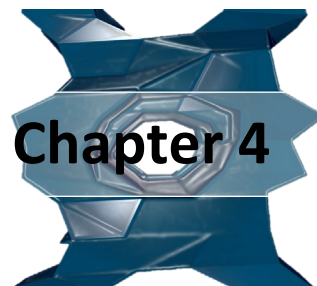
Table A3.7. Total pore volume, micro- and mesopore volume and BET area measured on catalyst after 364 min of reaction. The percentage loss in comparison to the fresh catalyst is indicated in the brackets. In addition, the total amount of coke as determined by TGA in air (see **Figure A3.13** for TGA curves).

$(Mo/Al)_{syn}$	Synthesis method	Precursor	$V_{pore}/cm^3 g^{-1}$	$V_{micro}/cm^3 g^{-1}$	$V_{meso}/cm^3 g^{-1}$	$S_{BET}/m^2 g^{-1}$	Total amount of coke / $\mu\text{mol g}^{-1}$
0.3	IWI	AHM	0.168 (30%)	0.110 (22%)	0.058 (41%)	276 (33%)	6.88
0.3	CVD1	MoCl <sub>5</sub>					5.86
0.3	CVD1	MoO <sub>2</sub> Cl <sub>2</sub>					6.44
0.3	CVD3	MoCl <sub>5</sub>					6.70
0.3	CVD3	MoO <sub>2</sub> Cl <sub>2</sub>	0.177 (20%)	0.112 (14%)	0.065 (28%)	285 (40%)	4.80
0.3	CVD2	Mo(CO) <sub>6</sub>	0.155 (36%)	0.100 (30%)	0.055 (45%)	249 (40%)	7.40
1.0	IWI	AHM					3.30
1.0	SIE	MoO <sub>3</sub>	0.159 (24%)	0.103 (18%)	0.056 (33%)	259 (24%)	4.52
1.0	SIE	MoCl <sub>5</sub>					5.23
1.0	CVD1	MoCl <sub>5</sub>					1.98
1.0	CVD3	MoCl <sub>5</sub>					3.30
1.0	CVD3	MoO <sub>2</sub> Cl <sub>2</sub>	0.164 (13%)	0.096 (16%)	0.068 (8%)	257 (18%)	5.65
1.0	CVD3(i)	MoCl <sub>5</sub>					6.02
1.0	CVD3(ii)	MoCl <sub>5</sub>					4.33
1.0	CVD5	MoCl <sub>5</sub>					3.67

### A3.6 References

- [1] W. Ding, G.D. Meitzner, D.O. Marler, E. Iglesia, Synthesis, Structural Characterization, and Catalytic Properties of Tungsten-Exchanged H-ZSM5, The Journal of Physical Chemistry B, 105 (2001) 3928-3936.
- [2] N. Kosinov, F.J. Coumans, G. Li, E. Uslamin, B. Mezari, A.S. Wijpkema, E.A. Pidko, E.J. Hensen, Stable Mo/HZSM-5 methane dehydroaromatization catalysts optimized for high-temperature calcination-regeneration, Journal of Catalysis, 346 (2017) 125-133.
- [3] T. Shido, A. Yamaguchi, A. Suzuki, Y. Inada, K. Asakura, M. Nomura, Y. Iwasawa, DXAFS study on the decarbonylation process of Mo (CO) 6 in NaY supercages, Journal of synchrotron radiation, 8 (2001) 628-630.
- [4] B.R. Muller, G. Calzaferri, Thin Mo(CO)6-Y-zeolite layers: preparation and in situ transmission FTIR spectroscopy, Journal of the Chemical Society, Faraday Transactions, 92 (1996) 1633-1637.
- [5] Y. You-Sing, R.F. Howe, Adsorption and decomposition of Mo(CO)6 in zeolite NaY, Journal of the Chemical Society, Faraday Transactions 1: Physical Chemistry in Condensed Phases, 82 (1986) 2887-2896.
- [6] H. Tian, C.A. Roberts, I.E. Wachs, Molecular Structural Determination of Molybdena in Different Environments: Aqueous Solutions, Bulk Mixed Oxides, and Supported MoO<sub>3</sub> Catalysts, The Journal of Physical Chemistry C, 114 (2010) 14110-14120.
- [7] C.J. Powell, A. Jablonski, Surface sensitivity of X-ray photoelectron spectroscopy, Nuclear Instruments and Methods in Physics Research Section A: Accelerators, Spectrometers, Detectors and Associated Equipment, 601 (2009) 54-65.
- [8] A.J. C. J. Powell, NIST Electron Inelastic-Mean-Free-Path Database, Version 1.2, SRD 71, National Institute of Standards and Technology, Gaithersburg, MD, 2010.
- [9] J.C. Ashley, V.E. Anderson, Interaction of low-energy electrons with silicon dioxide, Journal of Electron Spectroscopy and Related Phenomena, 24 (1981) 127-148.





---

**On the dynamic nature of Mo sites for methane dehydroaromatization**

---

The mechanism of methane activation on Mo/HZSM-5 is not yet fully understood, despite the great interest in methane dehydroaromatization (MDA) to replace aromatics production in oil refineries. It is difficult to assess the exact nature of the active site due to fast coking. By pre-carburizing Mo/HZSM-5 with carbon monoxide (CO), the MDA active site formation was isolated from coke formation. With this a clear  $^{13}\text{C}$  NMR signal solely from the active site and not obscured by coke was obtained and revealed two types of likely molecular Mo (oxy-)carbidic species in addition to the  $\beta\text{-Mo}_2\text{C}$  nanoparticles often mentioned in literature. Furthermore, separating the active site formation from coking by pre-carburization helped us examine how methane is activated on the catalytic site by carrying out MDA using isotopically labelled methane ( $^{13}\text{CH}_4$ ). Carbon originating from the pre-formed carbide was incorporated into the main products of the reaction, ethylene and benzene, demonstrating the dynamic behaviour of the (oxy-)carbidic active sites. Following the signal of an on-line mass spectrometer during treatment with either  $^{13}\text{C}^{16}\text{O}$  or  $^{12}\text{C}^{18}\text{O}$ , the amount of oxygen removed from and carbon deposited on the Mo site was determined.

---

This chapter is based on the following publication:

Vollmer, I.; van der Linden, B.; Ould-Chikh, S.; Aguilar-Tapia, A.; Yarulina, I.; Abou-Hamad, E.; Sneider, Y. G.; Olivos Suarez, A. I.; Hazemann, J-L.; Kapteijn, F. and Gascon, J., (2018). "On the dynamic nature of Mo sites for methane dehydroaromatization." *Chemical Science* 9(21): 4801-4807.  
**doi: 10.1039/C8SC01263F**

## 4.1 Introduction

Due to depletion of oil reserves and the increasing availability of cheap methane as a major component of shale gas as well as in methane hydrates, processes to valorize methane are in high demand [1]. Up to date, some indirect routes of methane conversion based on syngas from methane reforming have been commercialized. Requiring less process steps, direct conversion of methane is a desired alternative. Among them, non-oxidative methods have attracted interest since the pioneering work of Bragin and later Wang *et al* [2, 3]. A great deal of research effort has focused on the most promising systems Mo/HZSM-5 and Mo/HMCM-22, typically achieving 10 to 12 % conversion with a benzene selectivity of 60 to 70 % at 700 °C [4, 5]. Other products include, in order of decreasing selectivity, naphthalene, ethylene, ethane, xylene and toluene. The reaction is hampered by thermodynamics with  $\Delta G_r^\varrho = +433 \text{ kJmol}^{-1}$  and  $\Delta H_r^0 = +531 \text{ kJmol}^{-1}$  and coke formation is very favorable at high temperatures, leading to fast deactivation [6-8]. In Mo/HZSM-5, both the Brønsted acid site (BAS) and Mo make up the bifunctional catalytic nature of the system: CH<sub>4</sub> is activated on the exchanged Mo active site, forming C<sub>2</sub>H<sub>x</sub> [9]. Then, the intermediate C<sub>2</sub>H<sub>x</sub> moieties react on the BAS and are further converted into aromatic compounds [4, 10-13].

There is a delay for the onset of the reaction, in which mono[14] and dimeric[15] MoO<sub>x</sub> species from the as-synthesized Mo/HZSM-5 were shown to carburize, suggesting that reduced Mo is the active phase for methane dehydroaromatization [12, 15-19]. This delay is usually coined 'induction period'. A wide range of species have been reported to be active for MDA: MoC, Mo<sub>2</sub>C, coke modified Mo<sub>2</sub>C[20], Mo<sub>2</sub>C[18, 21] on the outside surface and reduced oxides in pores, any kind of Mo<sup>6+</sup> and partially reduced Mo<sup>6+</sup> as MoO<sub>(3-x)</sub> [11, 22]. However, thus far the exact nature of those reduced Mo species and which one of them dominates activity in the reaction is unknown. The observation of the active phase is difficult. <sup>13</sup>C MAS NMR[16, 23-25] and UV Raman[26, 27] can be used to look at the carbon in the Mo carbide, but due to the dominant signal coming from carbonaceous species, it is hard to observe. This leaves only quite expensive or less available options, like synchrotron techniques[15, 28], EPR or <sup>95</sup>Mo MAS NMR[29, 30], which, regrettably, are not conclusive either. Since the active phase forms at reaction conditions, *operando* techniques are necessary to get more insight about the structure of the active site.

*Operando* X-ray Absorption Spectroscopy (XAS) was used to show the gradual carburization of the molybdenum sites during the early stage of the reaction. While this yields a lot of insight on the oxidation state of Mo, structural information to be gained is limited, because XAS represents a bulk technique, making it difficult to distinguish between the plethora of active sites present on the zeolite. The signal is dominated by the bigger clusters of Mo, which are always present on the catalyst. Information on mono- or dimeric species, believed to be responsible for catalysis is mostly lost [31].

In another economically very interesting reaction, Fischer-Tropsch, it is proposed that the carbide phase of iron is active for the reaction and is involved in initiating the chain-growth of hydrocarbons [32, 33]. Both DFT studies as well as experiments with labelled reactants suggest that the carbide is easily hydrogenated to CH<sub>2</sub> species, which then further react with gas-phase species to form hydrocarbons [34]. Afterwards the carbide is replenished again in a way similar to the oxides in the Mars-van-Krevelen mechanism [35]. Although the Fe-carbide is present as nanoparticles in the Fischer-Tropsch catalyst and the initial active phase for Mo/HZSM-5 is expected to present itself either as molecular MoO<sub>x</sub>C<sub>y</sub> or cluster species, it is of high interest to consider a similar mechanism for this system. Especially, since the catalyst considered here, Mo/HZSM-5 was also found to be active for the Fischer-Tropsch reaction [36]. In a few publications, understanding the activation of CH<sub>4</sub> on the carbidic form of Mo/HZSM-5 is only theoretically approached [37-39].

In this work, we experimentally investigate the interaction of methane with the relevant Mo active sites during MDA reaction. Because of the aforementioned induction period of MDA, it is not possible to separate in time the formation of the Mo active phase via CH<sub>4</sub> carburization and the MDA reaction itself. Furthermore, the MDA reaction produces coke surrounding the active site and prevents the possibility to probe the interaction of CH<sub>4</sub> solely with the active Mo-carbide phase [40]. To circumvent this issue, our study involves the prior synthesis of the Mo carbide by contacting the Mo/HZSM-5 pre-catalyst with carbon monoxide (CO) at a high temperature (780 °C). Indeed, carbon monoxide has been reported to carburize Mo oxides to Mo<sub>2</sub>C [41-43]. We will demonstrate by a combination of online mass spectrometry (MS) and *operando* X-ray absorption spectroscopy that the Mo (oxy-)carbide produced *via* CO carburization and CH<sub>4</sub> activation

are equivalent. We report more direct structural characterization of the active site using  $^{13}\text{C}$  NMR. Then, the use of isotope labelling experiments and online-MS will highlight the dynamic behavior of the Mo active phase when contacted with methane.

## 4.2 Experimental Methods

For catalyst preparation 1, 2 and 5 wt.% of molybdenum (Mo) were introduced into a commercial zeolite with Si/Al = 13 (Südchemie), denoted as **yMoHZ-13**, where  $y$  denotes the wt.% of Mo introduced.  $(\text{NH}_4)_6\text{Mo}_7\text{O}_{24} \cdot 4\text{H}_2\text{O}$  was dissolved in 210  $\mu\text{l}$  of de-ionized water per gram of catalyst and introduced dropwise to the ammonia form of the zeolite dehydrated at 150 °C in vacuum. After mixing solution and zeolite well, the sample was dried overnight at 80 °C and subsequently calcined at 550 °C for 7 h with a heating rate of 2 °C/min. Another sample denoted as **2MoS** was produced for  $^{13}\text{C}$  NMR measurements introducing 2 wt.% of Mo into silicalite-1 using the same method as described above. Silicalite-1 was synthesized mixing 25.6 g of TPAOH with 30.0 g of distilled water, after which 36.9 g of TEOS was added dropwise to the solution. The obtained mixture is aged at room temperature overnight. Afterwards the mixture was transferred into autoclaves to perform further crystallization at 150 °C for 10 days. After cooling down, the product was collected by filtration and washing, and dried in air overnight. The dried product was calcined at 550 °C for 5 h (2 °C/min) to remove the residue template [44].

**CO carburization** was performed on a custom-made setup, where a 30 ml/min flow of 2.5 % CO in He was continuously fed to the reactor. Effluent gasses were analyzed by a quadrupole mass spectrometer (Balzers) connected on-line with the reactor. Mass Spectra were recorded in multiple ion detection (MID) mode using a channeltron detector. Quantification of CO and  $\text{CO}_2$  was achieved by calibrating signals with calcium oxalate [45]. Signals were normalized with the signal of He and the fragmentation contribution of  $\text{CO}_2$   $m/z = 44$  was subtracted from  $m/z = 28$ . The catalyst was pre-treated at 350 °C in He overnight to desorb any adsorbed gasses from the pores of the zeolite.

**$\text{CH}_4$  pulsing Experiments** were performed on the same setup as CO carburization and  $\text{H}_2$ -reduction. It was equipped with an injection loop in the feed line kept at atmospheric pressure, injecting 223  $\mu\text{mol}$  by switching a multi-position valve to the reactor. The loop was refilled every 200 s into 30 ml/min flow of

He. 300 mg Catalyst was pelletized and sieved to 212 to 425  $\mu\text{m}$  particles and filled in a quartz tube with a 6 mm inner diameter.

The structural analysis of the Mo/HZSM-5 catalyst with **X-ray Absorption spectroscopy (XAS)** was performed *operando* with a pulsing gas set-up at the CRG-FAME UHD beamline (BM16) at the European Synchrotron Radiation Facility (ESRF) in Grenoble [46]. The XAS cell previously described consists of a vitreous carbon reactor i.d. 4 mm. 100 mg of **2MoHZ-13** catalyst sieved to 250 - 300  $\mu\text{m}$  were loaded into the reactor. The effluent gas composition was monitored on-line by an EcoCat-P portable mass spectrometer (ESS). XANES spectra on the MDA catalyst were recorded either in fluorescence with a Silicon Drift Detector (Vortex-60EX) with a 50  $\text{mm}^2$  active area (energy resolution: 250 eV) or in transmission mode for the references at the Mo K-edge (20.0 keV).

For these experiments the CO carburization was performed by heating the fresh sample up to 780  $^{\circ}\text{C}$  ( $10\ ^{\circ}\text{C}/\text{min}$ ) with a 30 ml/min flow of 2.5 % CO in He. For the  $\text{CH}_4$  pulsing experiments, the **2MoHZ-13** catalyst (either CO carburized or untreated) was first heated under an helium flow (10 ml/min) up to 700  $^{\circ}\text{C}$  with a heating rate of ( $20\ ^{\circ}\text{C}/\text{min}$ ). Then, 223  $\mu\text{mol}$   $\text{CH}_4$  pulses were introduced into a He flow of 10 ml/min while maintaining a temperature of 700  $^{\circ}\text{C}$ .

In addition, XANES spectra were measured ex-situ at the Mo K-edge in transmission at the BM26B DUBBLE beamline of the European Synchrotron Radiation Facility (ESRF), Grenoble, France. Those measurements on pelletized samples provide XANES spectra with a better signal to noise ratio compared to spectra measured in the previous *operando* set-up. Prior to measurement, the fresh samples were dehydrated under a flow of  $\text{N}_2$  at 400  $^{\circ}\text{C}$  for 16 h. Samples carburized as described in section “CO carburization” were transferred from the carburization setup to the glovebox without exposure to the atmosphere, where they were packed into custom-made holders under inert atmosphere.

The samples for  **$^{13}\text{C}$  MAS NMR** were prepared as described in section “CO carburization” using  $^{13}\text{CO}$  and transferred from the carburization setup to the glovebox without exposure to the atmosphere. A known amount of sample was filled into zirconia rotors inside the glovebox and tightly closed. 1D  $^{13}\text{C}$  MAS NMR spectra were recorded on a Bruker AVANCE III spectrometer operating at resonance frequencies of 100 MHz, and using a conventional double resonance 4 mm CPMAS probe. The

spinning frequency was set to 15 kHz. NMR chemical shifts are reported with respect to TMS as the external reference. Spectra were recorded by a spin echo pulse sequence (pulse length 3.4  $\mu$ s) with four-phase alternation synchronized with the spinning rate for the MAS experiments. The interscan delay was set to 30 s to allow the complete relaxation, and 5,000-30,000 scans were performed. An apodization function (exponential) corresponding to a line broadening of 80 Hz was applied prior to the Fourier transformation. For quantitative analysis, Mo<sub>2</sub>C was used as an external reference. Amount of carbon ( $\mu\text{mol}\cdot\text{g}^{-1}$ ) was derived from the deconvoluted Mo<sub>2</sub>C spectrum normalized by the amount of scans, weight of the sample and natural abundance of <sup>13</sup>C.

**Temperature Programmed Oxidation (TPO)** was performed on a custom-made setup, where a 30 ml/min flow of 5 % O<sub>2</sub> in He was continuously fed to the reactor. Effluent gasses were analyzed by a quadrupole mass spectrometer (Balzers) connected on-line with the reactor. Mass Spectra were recorded in multiple ion detection (MID) mode using a channeltron detector. Quantification of CO and CO<sub>2</sub> was achieved by calibrating signals with calcium oxalate [45]. Signals were normalized with the signal of He and the fragmentation contribution of CO<sub>2</sub>  $m/z = 44$  was subtracted from  $m/z = 28$ . The catalyst was pre-treated by TPC.

## 4.3 Results and discussion

### 4.3.1 Temperature programmed carburization

To understand the conditions necessary to prepare the active Mo site by CO carburization, CO consumption and simultaneous  $\text{CO}_2$  production were monitored by MS during Temperature Programmed Carburization (TPC) with  $^{13}\text{CO}$ . **Figure 4.1a** shows that carburization starts at  $450\text{ }^\circ\text{C}$  and continues until the maximum temperature is reached. After Mo carburization is complete, CO consumption and  $\text{CO}_2$  production continue at a lower level, which can be seen as a sign for completed carburization. From this we concluded that 1 h of carburization at  $780\text{ }^\circ\text{C}$  is sufficient to complete catalyst activation. The reproducibility of this experiment is demonstrated in **Figure A4.1**.

**Figure 4.1b** shows the same experiment, but using CO with labelled oxygen,  $\text{C}^{18}\text{O}$ . This experiment demonstrates that the extent of carbon deposition due to the reverse Boudouard reaction is negligible as this would lead to the formation of  $\text{C}^{18}\text{O}_2$ , which is only observed in very small amounts. **Figure 4.1b** shows the net consumption of  $\text{C}^{18}\text{O}$ , which was calculated by adding the signals for CO and  $\text{C}^{18}\text{O}$  shown in **Figure 4.2**. Large amounts of  $\text{C}^{18}\text{O}$  are ‘consumed’ while CO is ‘produced’, attributed to a high degree of exchange of unlabelled framework oxygen with labelled oxygen from  $\text{C}^{18}\text{O}$ . To the best of our knowledge, this was not reported previously with CO, but Voskoboinikov *et. al.*[47] as well as Valyon *et. al.*[48] observed an exchange of  $^{18}\text{O}_2$  with framework oxygen for an iron on ZSM-5 catalyst. To explore whether a similar extent of exchange of framework oxygen occurs without the presence of Mo, a bare zeolite **HZ-13** was exposed to the same treatment in  $^{18}\text{CO}$ . As can be seen in **Figure 4.2** an extensive exchange is observed in this case as well, without any net consumption of CO or production of  $\text{CO}_2$ . Quantification (see section A4.1.1 in the Appendix) of  $\text{C}^{18}\text{O}$  consumed and CO produced shows that 12 mol% of framework O is replaced by  $^{18}\text{O}$  in the case of **2MoHZ-13** and 25 mol% in when no Mo is present (**HZ-13**).

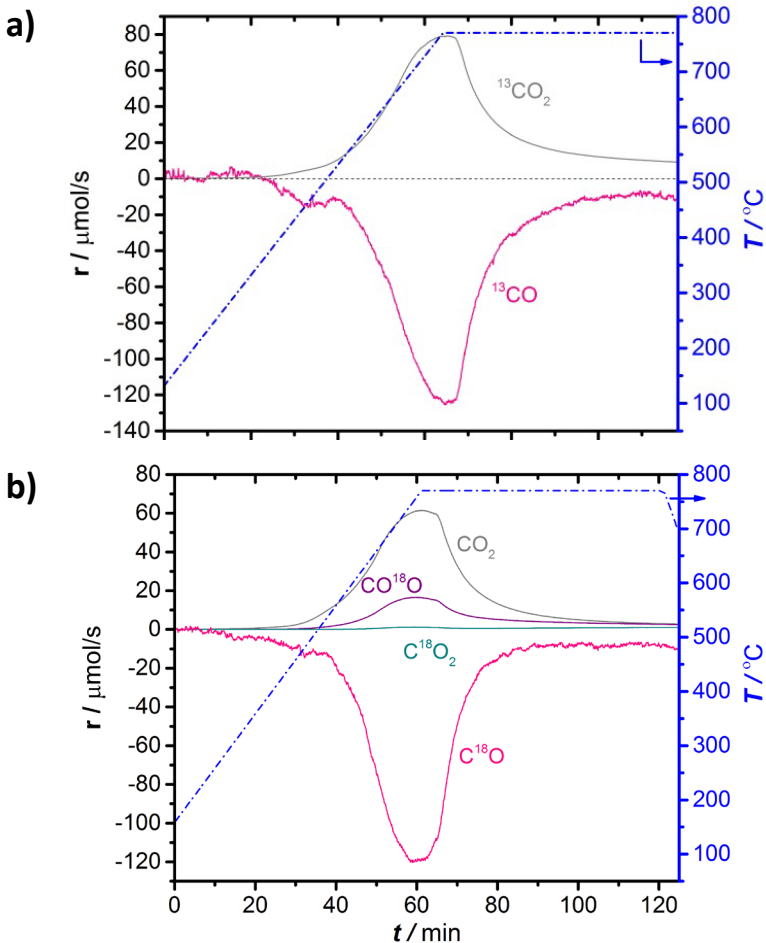


Figure 4.1. a)  $^{13}\text{CO}$  consumption and simultaneous  $^{13}\text{CO}_2$  production in TPC with 30 ml/min, 2.5%  $^{13}\text{CO}$  in He. b) Net  $\text{C}^{18}\text{O}$  (sum of  $\text{C}^{18}\text{O}$  and  $\text{CO}^{18}\text{O}$  signals) consumption and simultaneous  $\text{CO}_2$ ,  $\text{C}^{18}\text{O}_2$  and  $\text{CO}^{18}\text{O}$  production in TPC with 30 ml/min, 2.5%  $\text{C}^{18}\text{O}$  in He. 300 mg **2MoHZ-13** catalyst was used and the temperature was increased to  $780^\circ\text{C}$  at a rate of  $10^\circ\text{C}/\text{min}$  (right axis). (cf. Figure A4.2 for TPC for all Mo loadings).

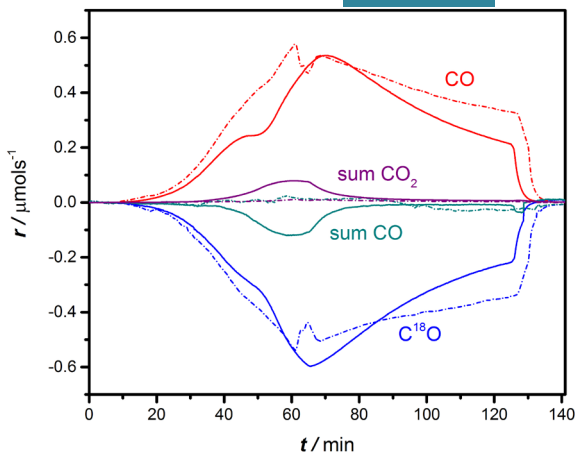


Figure 4.2.  $\text{C}^{18}\text{O}$  consumption, CO production and net CO consumption as well as net  $\text{CO}_2$  production for carburization of **2MoHZ-13** (solid lines) and **HZ-13** (dotted lines). 300 mg catalyst was treated with 30 ml/min, 2.5%  $\text{C}^{18}\text{O}$  in He. The temperature was increased to 780 °C at a rate of 10 °C/min.

#### 4.3.2 Probing the induction period - $\text{CH}_4$ pulsing

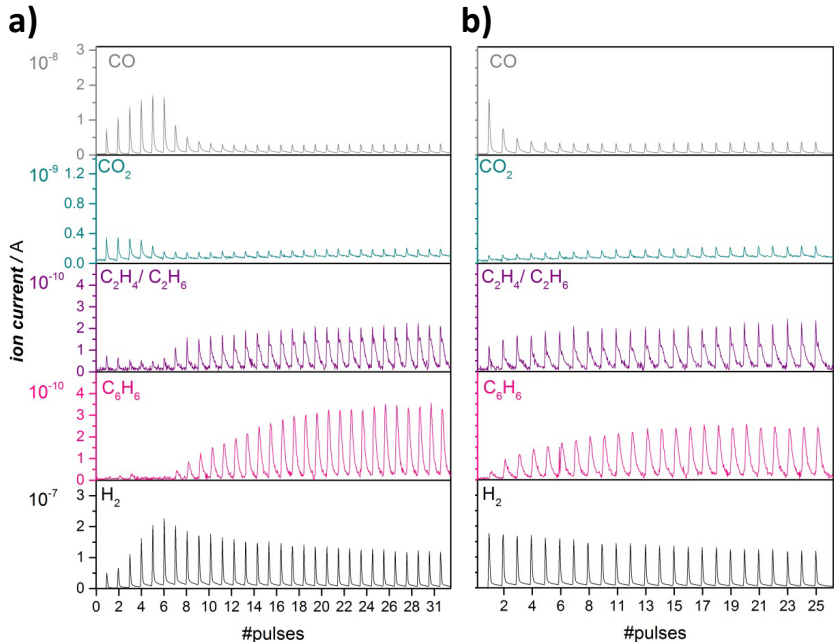


Figure 4.3. a) Evolution of CO,  $\text{C}_2\text{H}_4/\text{C}_2\text{H}_6$ ,  $\text{CO}_2$ ,  $\text{C}_6\text{H}_6$  and  $\text{H}_2$  under consecutive pulsing of 223  $\mu\text{mol}$   $\text{CH}_4$  at 700 °C to a 300 mg of an untreated **2MoHZ-13** and b) the same catalyst pre-carburized with a 30 ml/min flow of 2.5 % CO in He at 780 °C for 1 h

Pulsing CH<sub>4</sub> to the catalyst is a quantitative way to look at the length of the activation period [16]. We performed pulsing experiments both on the untreated as well as the same catalyst carburized in CO for 1 h at 780 °C (**Figure 4.3**). The untreated Mo/HZSM-5 started to produce benzene after 2-15 pulses of methane depending on the Mo loading (**Figure 4.3a** and **A4.3**), while benzene was formed immediately on the CO-carburized catalyst (**Figure 4.b** and **A4.3**). Similar conclusions are made for ethane and ethylene formation. These observations attest the immediate activity of the CO carburized catalyst. In another experiment, a H<sub>2</sub>-treatment at 700 °C was used to verify if carbidic carbon needs to be present at the active site for it to be able to activate CH<sub>4</sub> or whether a merely reduced species is sufficient (see **Figure A4.4**). This pre-treatment did not lead to instantaneous activity in the same manner as the CO treatment did. This was also observed previously[12, 16] and leads us to conclude that the carbon atoms incorporated into the active Mo phase play an essential role in activating the C-H bond of methane.

#### 4.3.3 Same reduction with CO as with CH<sub>4</sub> - *Operando* XANES

The CH<sub>4</sub> pulsing experiments show that the CO-treatment can effectively eliminate the induction period and should lead to a reduced Mo species equivalent to the one forming during the initial pulses of CH<sub>4</sub> where no benzene is observed.

To confirm this spectroscopically, the CH<sub>4</sub> pulsing experiments were reproduced at the BM16 beamline (ESRF) and the evolution of Mo species was followed *operando* by X-ray absorption spectroscopy (cf. section A4.3 in the Appendix for experimental details and **Figures A4-A4.12**). **Figure A4.8b** shows a similar pulsing experiment to what is depicted in **Figure 4.3a**. Benzene is only detected at the 6<sup>th</sup> pulse of methane. It is therefore interesting to investigate what happens during the first five pulses of methane spectroscopically. This is depicted by the pink XANES spectra in **Figure 4.4**. The XANES spectra collected during the initial five pulses of methane show a strong pre-edge peak at 20,008 eV attributable to a 1s-4d quadrupole/dipole transition, characteristic for distorted oxidic Mo species,[17] and a 1s-5p dipole transition at 20,025 eV followed by a relatively flat post-edge region. Clear changes in the pre-edge peak were detected especially between the 4<sup>th</sup> and 5<sup>th</sup> pulses accompanied by a total a shift of the rising absorption edge of about 4.2 eV. Those spectral changes have been previously studied by HERFD-XANES

and vtc-XES and correspond to a gradual carburization of the molybdenum sites during the early stage of the reaction [17].

Since the detection of benzene happened just at the 6<sup>th</sup> CH<sub>4</sub> pulse (**Figure A4.8b**), it is particularly interesting to compare the spectrum corresponding to the 5<sup>th</sup> CH<sub>4</sub> pulses of methane (bold pink curve, **Figure 4.4**) with the spectrum of the CO treated catalyst uncontacted with methane (black curve, **Figure 4.4**).

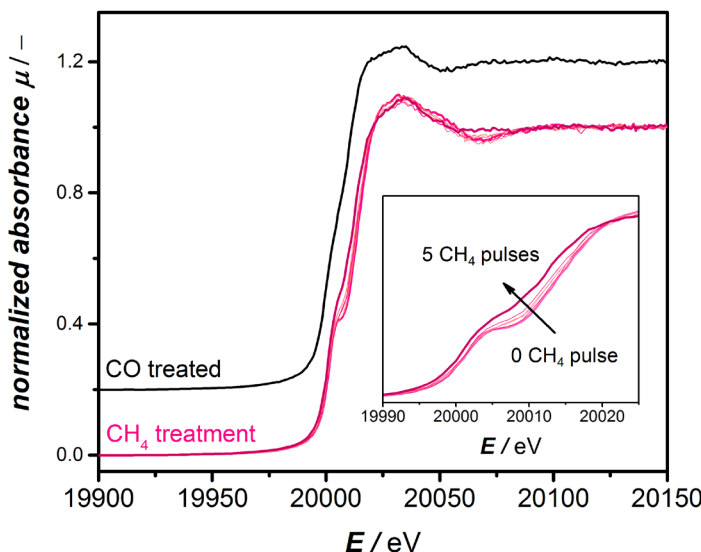


Figure 4.4. Comparison of *operando* XANES spectra recorded at Mo K-edge for a **2MoHZ-13** catalyst during consecutive pulsing of CH<sub>4</sub> at 700 °C (pink curves) and a **2MoHZ-13** catalyst carburized at 780 °C with a 2.5 % CO/He gas flow (black curve).

Both spectra present the same spectral features with comparable intensity. This is also confirmed by EXAFS and FT-EXAFS of those two samples represented in **Figures A4.11-12**. Thus, *operando* X-ray absorption spectroscopy provides a convincing evidence of a similar Mo chemical environment when the catalyst is CO pre-treated or activated over time by CH<sub>4</sub>.

If temperatures below 780 °C, applied for all experiments herein, are used for the CO-treatment, the induction period is not eliminated completely. This can be explained by insufficient reduction at those temperatures confirmed by the XANES spectra measured *quasi-in-situ* on samples carburized at 600 °C, 700 °C and 780 °C (**Figure 4.5**): only the spectra of the samples carburized at 780 °C is equivalent to the spectra of a sample

activated in methane, while the spectra of the catalysts carburized at 600 °C still shows a significant pre-edge feature representative of the 1s–5p transitions allowed for distorted oxidic Mo species. This would explain that previous attempts at pre-carburizing Mo/HZSM-5 with CO at 700 °C[12] did not lead to an elimination of the activation period.

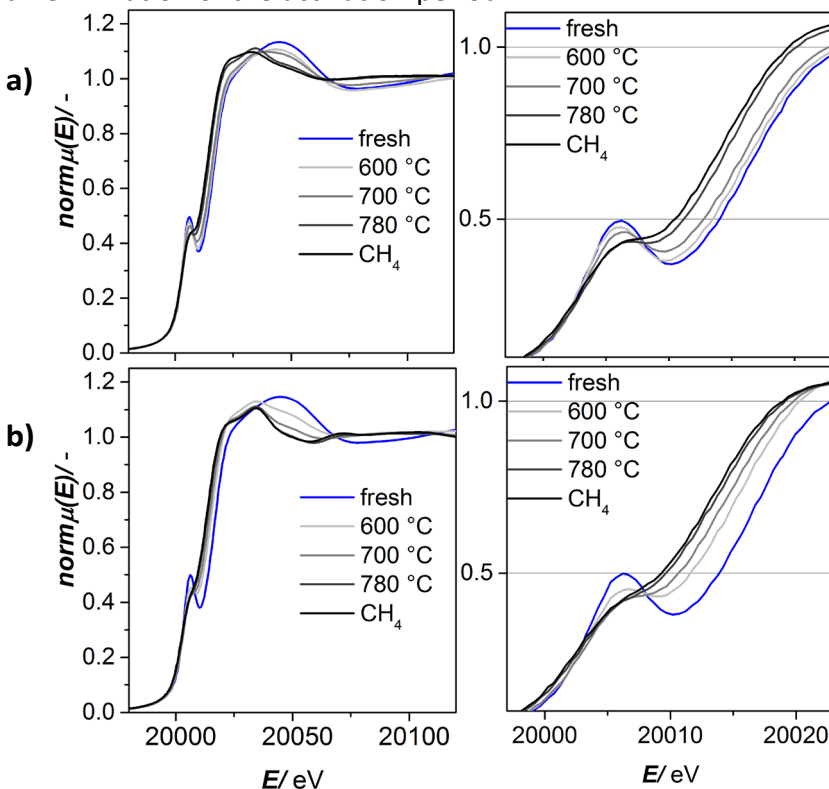


Figure 4.5. XANES spectra of a) **2MoHZ-13** and b) **5MoHZ-13** collected at the Mo K-edge carburized at 600, 700 and 780 °C as described in the appendix section A4.1 compared to a sample taken from the reaction with methane, which was quenched right at the onset of benzene formation (indicated as “CH<sub>4</sub>”) and a sample degassed at 400 °C. All samples were transferred to the glovebox after treatment, where they were packed into XAS sample holders. The right graph presents a zoom-in of the edge.

#### 4.3.4 Distinguishing among different Mo species – $^{13}\text{C}$ NMR

The above presented TPC, *operando* XAS and pulsing experiments confirm that CO carburization can be used to produce an active Mo phase that is equivalent to the one forming during the activation period of the reaction with  $\text{CH}_4$ . This opens up new possibilities for characterization, especially with  $^{13}\text{C}$  NMR, because the carbidic carbon from the active site can be probed directly without any interference from the signal of aromatic carbons. Indeed the  $^{13}\text{C}$  NMR results presented in **Figure 4.6** are devoid of non-carbidic carbon, since there is no resonance around 100 ppm characteristic for aromatic carbon [24]. In contrast to XAS, these spectra can distinguish between different Mo carbide species present on the catalyst, showing distinct peaks for each species. Three main carbidic species can be detected. A sharp contribution exists at a chemical shift of  $\delta_3 \sim 270$  ppm as well as two more broad resonances in the range of 400-250 ppm. The resonance of  $\beta\text{-Mo}_2\text{C}$  at 270 ppm is assigned to hcp type  $\beta\text{-Mo}_2\text{C}$  [23, 24, 49, 50]. Its rather sharp shape points towards nanoparticles. The fact that this resonance characteristic for bulk  $\beta\text{-Mo}_2\text{C}$  is only significantly observed for the highest loadings of Mo, **5MoHZ-13** suggests an accumulation of the Mo at the outer surface of the zeolite crystal for the high loading. An excess of Mo cannot effectively be anchored inside the pores of the zeolite. During synthesis Mo anchors to the Al of the framework through oxygen, replacing the proton of the active site, which leads to a high dispersion of Mo inside the pores of the zeolite [51]. The importance of this anchoring was further demonstrated, by preparing a sample of Mo supported on the same zeolite, but containing no framework Al and therefore no anchoring sites. For this sample, (Mo on silicalite-1, **2MoS**) only the resonance at  $\sim 270$  ppm can be observed [31].

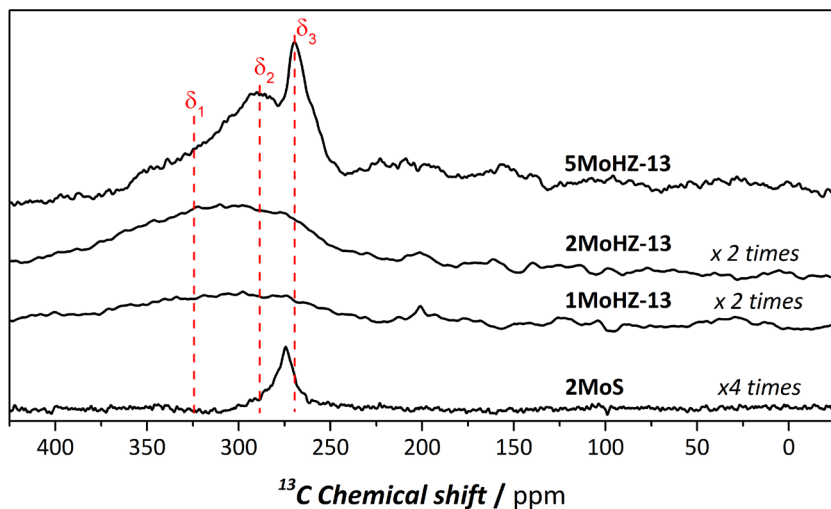


Figure 4.6.  $^{13}\text{C}$  MAS NMR spectra of Mo loaded HZ-13 after  $^{13}\text{CO}$  carburization at  $780\text{ }^\circ\text{C}$  for 1 h using 30 ml/min, 2.5 %  $^{13}\text{CO}$  in He. Deconvolution results of the spectra can be found in **Figure A4.14**.

The other two broad resonances are centered at  $\delta_1 \sim 338\text{ ppm}$  and  $\delta_2 \sim 290\text{ ppm}$  and show a large anisotropy, probably arising from several similar species with slightly varying geometry and orientation. In addition, these two resonances,  $\delta_1$  and  $\delta_2$  show a strong up-field shift compared to  $\text{Mo}_2\text{C}$  species. This could be due to deshielding by an electronegative atom (oxygen) and could be further indication that oxygen is present at the Mo active site, as was previously claimed [17, 18, 52]. The extent of the chemical shift (20 ppm and 68 ppm) makes quantum size effects an unlikely cause for this shift, as the shifts arising from quantum size effects are smaller, i.e. 12 ppm for a difference of 24 Å [53]. We propose an oxycarbide structure rather than a carbonylic one, considering that carbon in  $\text{Mo}(\text{CO})_6$  grafted on zeolites resonates at  $\sim 200\text{ ppm}$  while we observe resonances much more upfield [54].

Three different Mo (oxy-)carbide species are also observed in the Temperature Programmed Oxidation (TPO) experiment shown in **Figure 4.7**. The first peak between  $84\text{ }^\circ\text{C}$  and  $142\text{ }^\circ\text{C}$  likely corresponds to small Mo (oxy-)carbide species inside the pores of the zeolite, which are easy to oxidize, since this is most significant peak for **1MoHZ-13** and it is known that Mo only exists as mono- or dimeric species in **1MoHZ-13** [31]. This amount is about the same for all three loadings. The second peak between

281 °C and 251 °C increases with Mo-loading attributed to slightly bigger species still inside the pores of the zeolite corresponding to  $\delta_2$  from  $^{13}\text{C}$  NMR.

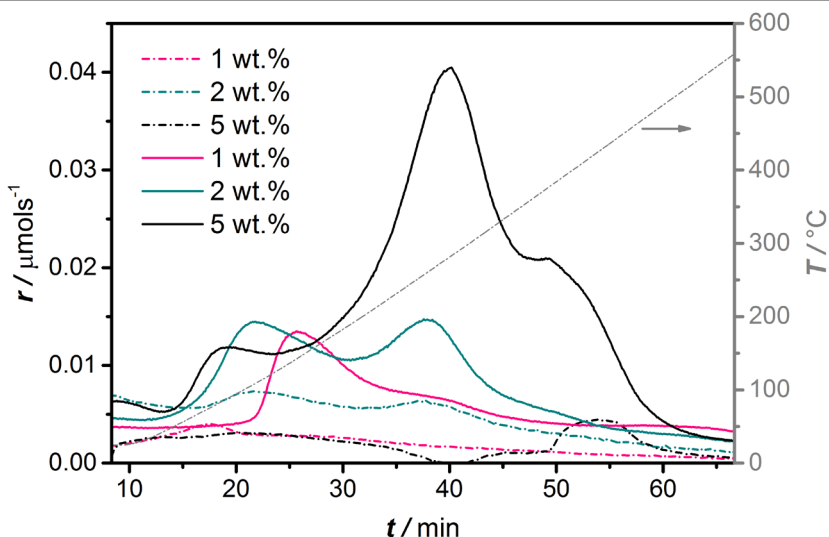


Figure 4.7. CO (dashed lines) and  $\text{CO}_2$  (solid lines) evolution for 1, 2 and **5MoHZ-13**, previously carburized in CO during TPO with 30 ml/min of 5 %  $\text{O}_2$  in He heating to 770 °C with 10 °C/min.

The third peak at 377 °C is only observed for **5MoHZ-13**, which is small compared to the other two peaks for **5MoHZ-13**, and matching the results from  $^{13}\text{C}$  NMR well, where  $\delta_3$  only makes up 4 % of all the carbon in that catalyst. This peak is attributed to  $\text{Mo}_2\text{C}$  nanoparticles at the external surface of the zeolite. The presence of oxygen at the active site is suggested by the limited amount of oxygen removed during CO carburization based on quantification of MS signals (c.f. section A4.1.1 in the appendix). According to this analysis, only one oxygen is removed per Mo site, while depending on the geometry of the initially present Mo oxide two or three oxygens have to be removed in order to fully reduce the active site [55]. While both quantification of the MS signals during CO carburization as well as  $^{13}\text{C}$  NMR suggest an oxycarbide, XAS shows high similarity with a fully carbidic  $\beta$ - $\text{Mo}_2\text{C}$ . Comparing XANES spectra of a sample carburized in CO with the reference spectra measured for  $\beta$ - $\text{Mo}_2\text{C}$  in Figure A4.12 they look similar, although the post-edge features differ. Also FT-EXAFS shows that Mo-Mo distances on the samples activated in CO as well as in  $\text{CH}_4$  match the one for  $\beta$ - $\text{Mo}_2\text{C}$ , while being much

less intense (**Figure A4.12**). We speculate that this is due to the presence of some bigger Mo clusters forming at reaction conditions, which are fully reduced, while a majority of species still pertain their oxycarbodic form leading to a flattening of the post-edge features but not giving rise to significant additional signal due to the many configuration these molecular species can take on inside the pores of the zeolite. Importantly, the resonance representing bulk  $\beta$ -Mo<sub>2</sub>C ( $\delta_3 \sim 270$  ppm) is missing for the  $^{13}\text{C}$  NMR spectra for both **1MoHZ-13** and **2MoHZ-13**. These two catalysts are immediately active to form benzene after being treated in CO (**Figure A4.3**). We therefore conclude that these broader species are active sites. Furthermore, there is a linear relation between total carbon content determined by deconvolution of the  $^{13}\text{C}$  NMR spectra and the initial conversion of methane in the reaction (**Figure A4.15**), while the initial conversion does not linearly correlate with Mo content (**Figure A4.16**). This indicates that Mo does not constitute an active site unless carbon is present at the active site. This is similar to what was found for a Ru/SiO<sub>2</sub> in Fischer-Tropsch [56]. Note that the amount of carbon increases with Mo loading, but the C/Mo ratio decreases (see **Table A4.2** and **Figure A4.14**).

#### 4.3.5 Interaction of CH<sub>4</sub> with active site – $^{13}\text{CH}_4$ pulsing

Preparation of the active carbodic phase of Mo without any coke surrounding it further allows probing the interaction of CH<sub>4</sub> solely with the active Mo-carbide phase isolating this interaction from interactions with undefined (hydro-)carbonaceous species [31].

To understand how methane interacts with the formed active Mo species, we performed a series of pulsing experiments using labelled methane,  $^{13}\text{CH}_4$ . Prior to this pulsing, the catalyst was carburized using  $^{12}\text{CO}$ , forming  $^{12}\text{C}$  based carbodic or oxycarbodic Mo structures. This way, it was possible to track the incorporation of  $^{12}\text{C}$  from the catalytic Mo site into the products. Firstly, masses 84 to 78 arising from fragmentation of labelled benzene,  $^{13}\text{C}_6\text{H}_6$  as well as benzene where some  $^{12}\text{C}$  is incorporated, were recorded on the MS. **Figure 4.8** shows the development of the abundance of the masses normalized by the one with highest abundance,  $m/z = 84$ , while **Figure A4.20** shows the control experiment where both CO pre-treatment and methane pulsing was performed with the same isotope of carbon,  $^{13}\text{C}$ .

The ratio 83/84 is most informative in assessing the incorporation of  $^{12}\text{C}$  into the observed benzene, because  $m/z = 83$  is the most abundant mass for  $^{12}\text{C}^{13}\text{C}_5\text{H}_6$  and should lead to a higher 83/84 ratio than for the control experiment where  $m/z = 83$  only represents the  $^{13}\text{C}_6\text{H}_5$  fragment. When using  $^{12}\text{C}$  for carburization and  $^{13}\text{C}$  for methane pulsing (**Figure 4.8**), the ratio of 83/84 reaches a value of 0.67 for the first pulse and decreases to 0.28 over the next 8 methane pulses. This value of 0.28 is the constant fragmentation ratio in the control experiment. The higher value of 83/84 during the initial pulses can clearly be attributed to the presence of  $^{12}\text{C}^{13}\text{C}_5\text{H}_6$ .

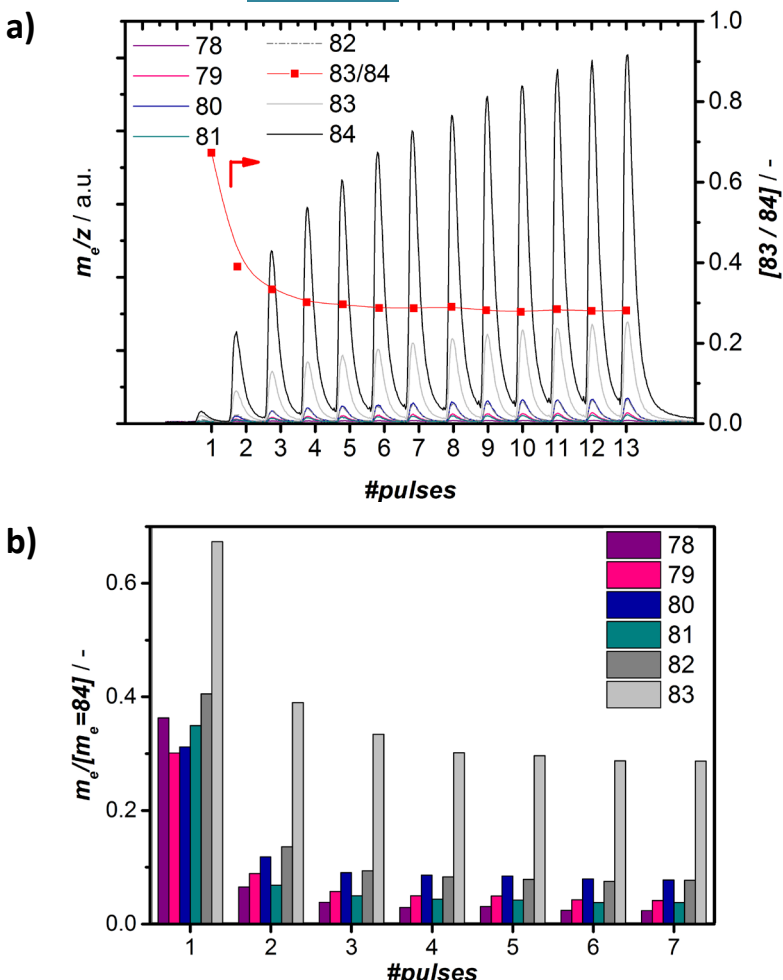


Figure 4.8. a) Evolution of masses typical for the fragmentation of benzene under consecutive pulsing of 223  $\mu\text{mol}$   $^{13}\text{CH}_4$  to 300 mg **2MoHZ-13** catalyst carburized at 780  $^{\circ}\text{C}$  with 30 ml/min 2.5 %  $^{12}\text{CO}$  in He. b) shows the area under each pulse for masses 78 to 83 normalized by  $m/z = 84$ .

The increased abundance of masses 82 to 78 further supports the incorporation of  $^{12}\text{C}$  into benzene. Similarly, incorporation of  $^{12}\text{C}$  into ethylene and ethane was investigated by tracking masses 26 to 30. **Figure 4.9a** demonstrates that mostly ethylene with one carbon from the active site,  $^{12}\text{C}^{13}\text{CH}_4$  is produced, evidenced by the increased abundance of mass 29. More information can be obtained, because of the use of CO with labelled oxygen,  $^{12}\text{C}^{18}\text{O}$ . It helped to determine how much oxygen of the as-synthesized

catalyst is exchanged during the CO treatment (**Figure 4.2**). This leads to the conclusion that all oxygen staying behind on the catalyst should be labelled  $^{18}\text{O}$ . Therefore, most of the CO that is released during the initial pulses of  $\text{CH}_4$ , should be  $\text{C}^{18}\text{O}$  with  $m/z = 30$ . In addition, in **Figure 4.9a** mass 30 is slowly decreasing with each pulse, while mass 28 stays constant starting from pulse 1. Both of these observations lead to the conclusion that mass 28 arises from ethylene in this case. Since the level of  $m/z = 28$  in **Figure 4.9a** follows the same trend and intensity as  $m/z = 28+30$  in **Figure 4.9b**, none of  $m/z = 29$  seems to stem from  $^{13}\text{CO}$ , because the amount of CO produced should be the same in both experiments.

These findings demonstrate that in both benzene and ethylene at least one carbon from the active site is incorporated as long as  $^{12}\text{C}$  is still available at this site. In analogy to what is proposed for Fischer-Tropsch, the carbon from the Mo-carbide could easily be hydrogenated by the abundant  $\text{H}_2$  in the reaction atmosphere arising from dehydrogenation of methane already during the induction period [35].

The  $\text{CH}_x$  formed in this way easily reacts with gas-phase or nearby adsorbed  $\text{CH}_x$  species to form ethylene, in literature suggested as the main reaction intermediate [4, 10-13]. Because of the high reactivity of this intermediate at the reaction conditions, it quickly reacts with other ethylene in its proximity [57]. In addition, the small extent of incorporation of carbon from the active site into benzene can be explained by the small amount of carbidic  $^{12}\text{C}$  present compared to the  $^{13}\text{CH}_4$  fed. According to quantification of the amount of carbon left on **2MoHZ-13** (**Figure 4.1**), the number of moles of  $\text{CH}_4$  fed in the first 4 pulses, where significant amounts of  $^{12}\text{C}^{13}\text{C}_5\text{H}_6$  are observed, is  $\sim 9.6$  times the amount of carbidic carbon on the catalyst. Through these labelling experiments the activation of methane on the catalytic Mo site could be studied at such a detailed level. Our work provides a good starting point for finding the precise molecular structure of the reduced Mo formed. The carbon in this structure is easily replaced by another carbon from methane, pointing at a dynamic active site. The high reactivity of the carbidic carbon is also evident from TPO experiments (**Figure 2.7**) showing that some of the carbidic species already oxidize at  $50^\circ\text{C}$ .

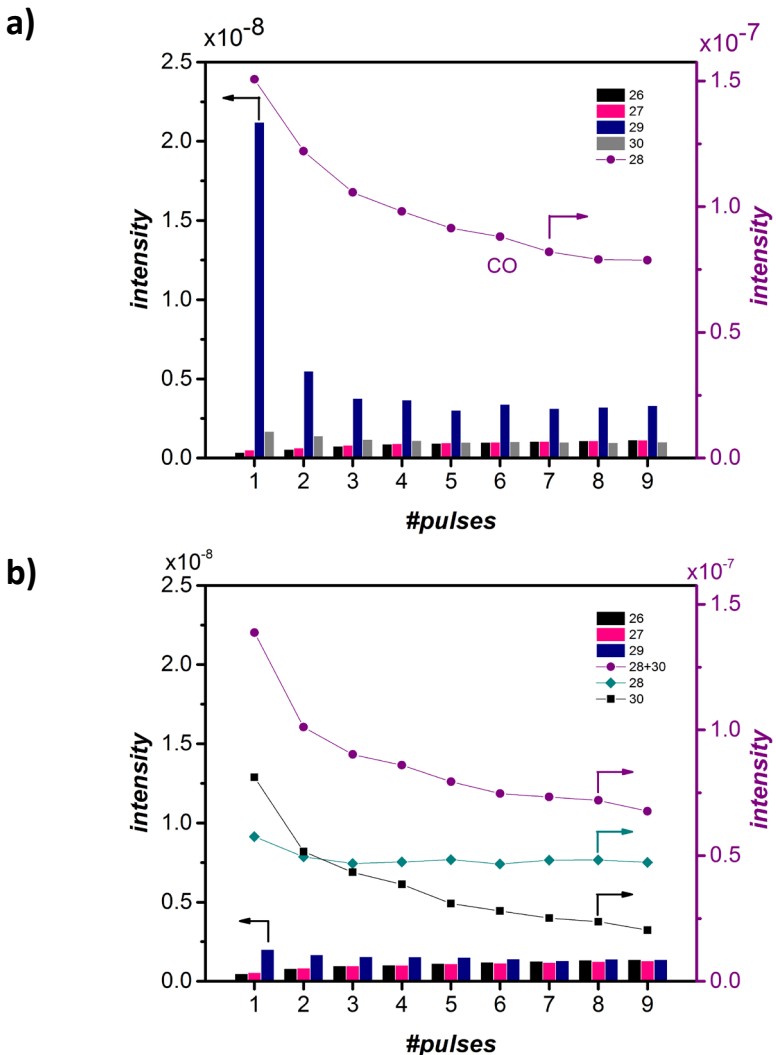


Figure 4.9. Integrated peak areas per pulse for MS readouts for masses 26 to 30 during consecutive pulsing of  $^{12}\text{CH}_4$  at  $700\text{ }^\circ\text{C}$  to **2MoHZ-13** carburized with 30 ml/min with 2.5 % of either a)  $^{13}\text{CO}$  or b)  $^{12}\text{C}^{18}\text{O}$  in He at  $780\text{ }^\circ\text{C}$  for 1 h.

#### 4.4 Conclusions

In summary, we demonstrate that CO carburization is a powerful approach to isolate the formation of the active site on Mo/HZSM-5 for non-oxidative methane conversion from the catalytic cycle without undesired catalyst coking. This strategy allowed us to distinguish between three different structures for the active site with  $^{13}\text{C}$  NMR, obtaining high resolution spectra of the (oxy-)carbidic species present that are usually obscured by aromatic carbon [16, 23-25]. This provides a useful structural characterization tool furthering our understanding beyond that from bulk techniques like XAS. Further, it was possible to study the activation of methane on the Mo catalytic active site at the molecular level. Rapid exchange reactions with the active Mo-site result in the incorporation of carbidic carbon into the products ethylene and benzene. This demonstrates that the carbon at the metal site in this structure is easily replaced by another carbon from methane, pointing at a dynamic active site. There are three observations that provide hard evidence on the mechanistic role of carbidic Mo species in the Mo/HZSM-5 catalyst: a) Carbon from the active site is incorporated into the final products. b) There is a linear relationship between carbon present at the active site and initial activity of the catalyst. c)  $\text{H}_2$ -reduction treatment during which no carbon is deposited at the active site does not lead to an elimination of the induction period. This lets us conclude that the catalytic Mo site actively takes part in the catalytic reaction rather than acting as an adsorption site to lower the activation barrier of  $\text{CH}_4$ , similar to what was observed for the Mars-van-Krevelen mechanism.

## 4.5 References

- [1] B.L. Farrell, V.O. Igenegbai, S. Linic, A Viewpoint on Direct Methane Conversion to Ethane and Ethylene Using Oxidative Coupling on Solid Catalysts, *ACS Catalysis*, 6 (2016) 4340-4346.
- [2] L. Wang, L. Tao, M. Xie, G. Xu, J. Huang, Y. Xu, Dehydrogenation and aromatization of methane under non-oxidizing conditions, *Catalysis Letters*, 21 (1993) 35-41.
- [3] O. Bragin, T. Vasina, Y.I. Isakov, B. Nefedov, A. Preobrazhenskii, N. Palishkina, K.M. Minachev, Catalytic aromatization of methane and ethane, *Russian Chemical Bulletin*, 31 (1982) 847-847.
- [4] J.J. Spivey, G. Hutchings, Catalytic aromatization of methane, *Chemical Society Reviews*, 43 (2014) 792-803.
- [5] S. Ma, X. Guo, L. Zhao, S. Scott, X. Bao, Recent progress in methane dehydroaromatization: From laboratory curiosities to promising technology, *Journal of Energy Chemistry*, 22 (2013) 1-20.
- [6] B.S. Liu, L. Jiang, H. Sun, C.T. Au, XPS, XAES, and TG/DTA characterization of deposited carbon in methane dehydroaromatization over Ga-Mo/ZSM-5 catalyst, *Applied Surface Science*, 253 (2007) 5092-5100.
- [7] K. Honda, X. Chen, Z.-G. Zhang, Identification of the coke accumulation and deactivation sites of Mo<sub>2</sub>C/HZSM-5 catalyst in CH<sub>4</sub> dehydroaromatization, *Catalysis Communications*, 5 (2004) 557-561.
- [8] Y. Song, Y. Xu, Y. Suzuki, H. Nakagome, Z.-G. Zhang, A clue to exploration of the pathway of coke formation on Mo/HZSM-5 catalyst in the non-oxidative methane dehydroaromatization at 1073 K, *Applied Catalysis A: General*, 482 (2014) 387-396.
- [9] S. Liu, L. Wang, R. Ohnishi, M. Ichikawa, Bifunctional Catalysis of Mo/HZSM-5 in the Dehydroaromatization of Methane to Benzene and Naphthalene XAFS/TG/DTA/MASS/FTIR Characterization and Supporting Effects, *Journal of Catalysis*, 181 (1999) 175-188.
- [10] V.T.T. Ha, L.V. Tiep, P. Meriaudeau, C. Naccache, Aromatization of methane over zeolite supported molybdenum: active sites and reaction mechanism, *Journal of Molecular Catalysis A: Chemical*, 181 (2002) 283-290.
- [11] Y. Xu, L. Lin, Recent advances in methane dehydro-aromatization over transition metal ion-modified zeolite catalysts under non-oxidative conditions, *Applied Catalysis A: General*, 188 (1999) 53-67.
- [12] D. Wang, J. Lunsford, M. Rosynek, Catalytic conversion of methane to benzene over Mo/ZSM-5, *Topics in Catalysis*, 3 (1996) 289-297.
- [13] Y. Xu, X. Bao, L. Lin, Direct conversion of methane under nonoxidative conditions, *Journal of Catalysis*, 216 (2003) 386-395.
- [14] J. Gao, Y. Zheng, J.-M. Jehng, Y. Tang, I.E. Wachs, S.G. Podkolzin, Identification of molybdenum oxide nanostructures on zeolites for natural gas conversion, *Science*, 348 (2015) 686-690.
- [15] W. Ding, S. Li, G. D Meitzner, E. Iglesia, Methane conversion to aromatics on Mo/H-ZSM5: structure of molybdenum species in working catalysts, *The Journal of Physical Chemistry B*, 105 (2001) 506-513.

- [16] H. Jiang, L. Wang, W. Cui, Y. Xu, Study on the induction period of methane aromatization over Mo/HZSM-5: partial reduction of Mo species and formation of carbonaceous deposit, *Catalysis Letters*, 57 (1999) 95-102.
- [17] I. Lezcano-González, R. Oord, M. Rovezzi, P. Glatzel, S.W. Botchway, B.M. Weckhuysen, A.M. Beale, Molybdenum Speciation and its Impact on Catalytic Activity during Methane Dehydroaromatization in Zeolite ZSM-5 as Revealed by Operando X-Ray Methods, *Angewandte Chemie International Edition*, 55 (2016) 5215-5219.
- [18] F. Solymosi, A. Szöke, J. Cserényi, Conversion of methane to benzene over Mo<sub>2</sub>C and Mo<sub>2</sub>C/ZSM-5 catalysts, *Catalysis Letters*, 39 (1996) 157-161.
- [19] S. Liu, L. Wang, R. Ohnishi, M. Lchikawa, Bifunctional catalysis of Mo/HZSM-5 in the dehydroaromatization of methane with CO/CO<sub>2</sub> to benzene and naphthalene, *Kinetics and catalysis*, 41 (2000) 132-144.
- [20] B.M. Weckhuysen, M.P. Rosynek, J.H. Lunsford, Characterization of surface carbon formed during the conversion of methane to benzene over Mo/H-ZSM-5 catalysts, *Catalysis Letters*, 52 (1998) 31-36.
- [21] F. Solymosi, A. Erdöhelyi, A. Szöke, Dehydrogenation of methane on supported molybdenum oxides. Formation of benzene from methane, *Catalysis Letters*, 32 (1995) 43-53.
- [22] H. Liu, W. Shen, X. Bao, Y. Xu, Identification of Mo active species for methane dehydro-aromatization over Mo/HZSM-5 catalysts in the absence of oxygen: <sup>1</sup>H MAS NMR and EPR investigations, *Journal of Molecular Catalysis A: Chemical*, 244 (2006) 229-236.
- [23] J. Yang, D. Ma, F. Deng, Q. Luo, M. Zhang, X. Bao, C. Ye, Solid state <sup>13</sup>C NMR studies of methane dehydroaromatization reaction on Mo/HZSM-5 and W/HZSM-5 catalysts, *Chem. Commun.*, (2002) 3046-3047.
- [24] N. Kosinov, F.J.A.G. Coumans, E.A. Uslamin, A.S.G. Wijpkema, B. Mezari, E.J.M. Hensen, Methane Dehydroaromatization by Mo/HZSM-5: Mono- or Bifunctional Catalysis?, *ACS Catalysis*, (2016) 520-529.
- [25] H. Zheng, D. Ma, X. Liu, W. Zhang, X. Han, Y. Xu, X. Bao, Methane dehydroaromatization over Mo/HZSM-5: A study of catalytic process, *Catalysis Letters*, 111 (2006) 111-114.
- [26] Y. Song, Y. Xu, Y. Suzuki, H. Nakagome, X. Ma, Z.-G. Zhang, The distribution of coke formed over a multilayer Mo/HZSM-5 fixed bed in H<sub>2</sub> co-fed methane aromatization at 1073 K: Exploration of the coking pathway, *Journal of Catalysis*, 330 (2015) 261-272.
- [27] D. Ma, Y. Shu, X. Han, X. Liu, Y. Xu, X. Bao, Mo/HMCM-22 Catalysts for Methane Dehydroaromatization: A Multinuclear MAS NMR Study, *The Journal of Physical Chemistry B*, 105 (2001) 1786-1793.
- [28] D. Ma, W. Zhang, Y. Shu, X. Liu, Y. Xu, X. Bao, MAS NMR, ESR and TPD studies of Mo/HZSM-5 catalysts: evidence for the migration of molybdenum species into the zeolitic channels, *Catalysis Letters*, 66 (2000) 155-160.
- [29] H. Zheng, D. Ma, X. Bao, J.Z. Hu, J.H. Kwak, Y. Wang, C.H.F. Peden, Direct Observation of the Active Center for Methane Dehydroaromatization Using an Ultrahigh Field <sup>95</sup>Mo NMR Spectroscopy, *Journal of the American Chemical Society*, 130 (2008) 3722-3723.

- [30] J.Z. Hu, J.H. Kwak, Y. Wang, C.H.F. Peden, H. Zheng, D. Ma, X. Bao, Studies of the Active Sites for Methane Dehydroaromatization Using Ultrahigh-Field Solid-State  $^{95}\text{Mo}$  NMR Spectroscopy, *The Journal of Physical Chemistry C*, 113 (2009) 2936-2942.
- [31] N. Kosinov, A.S.G. Wijpkema, E. Uslamin, R. Rohling, F.J.A.G. Coumans, B. Mezari, A. Parastaev, A.S. Poryvaev, M.V. Fedin, E.A. Pidko, E.J.M. Hensen, Confined Carbon Mediating Dehydroaromatization of Methane over Mo/ZSM-5, *Angewandte Chemie*, 57 (2018) 1016-1020.
- [32] V.P. Santos, T.A. Wezendonk, J.J.D. Jaén, A.I. Dugulan, M.A. Nasalevich, H.-U. Islam, A. Chojecki, S. Sartipi, X. Sun, A.A. Hakeem, A.C.J. Koeken, M. Ruitenbeek, T. Davidian, G.R. Meima, G. Sankar, F. Kapteijn, M. Makkee, J. Gascon, Metal organic framework-mediated synthesis of highly active and stable Fischer-Tropsch catalysts, *Nat Commun*, 6 (2015).
- [33] K. Xu, B. Sun, J. Lin, W. Wen, Y. Pei, S. Yan, M. Qiao, X. Zhang, B. Zong,  $\epsilon$ -Iron carbide as a low-temperature Fischer-Tropsch synthesis catalyst, 5 (2014) 5783.
- [34] V.V. Ordomsky, B. Legras, K. Cheng, S. Paul, A.Y. Khodakov, The role of carbon atoms of supported iron carbides in Fischer-Tropsch synthesis, *Catalysis Science & Technology*, 5 (2015) 1433-1437.
- [35] J.M. Gracia, F.F. Prinsloo, J.W. Niemantsverdriet, Mars-van Krevelen-like Mechanism of CO Hydrogenation on an Iron Carbide Surface, *Catalysis Letters*, 133 (2009) 257.
- [36] S. Liu, A.C. Gujar, P. Thomas, H. Toghiani, M.G. White, Synthesis of gasoline-range hydrocarbons over Mo/HZSM-5 catalysts, *Applied Catalysis A: General*, 357 (2009) 18-25.
- [37] S. Xing, D. Zhou, L. Cao, X. Li, Density Functional Theory Study on Structure of Molybdenum Carbide and Catalytic Mechanism for Methane Activation over ZSM-5 Zeolite, *Chinese Journal of Catalysis*, 31 (2010) 415-422.
- [38] D. Zhou, S. Zuo, S. Xing, Methane Dehydrogenation and Coupling to Ethylene over a Mo/HZSM-5 Catalyst: A Density Functional Theory Study, *The Journal of Physical Chemistry C*, 116 (2012) 4060-4070.
- [39] H. Zhu, Y. Zhang, D. Zhou, J. Guan, X. Bao, Density Functional Theory Study on Structure of Molybdenum Carbide Loaded on MCM-22 Zeolite and Mechanism for Methane Activation, *Chinese Journal of Catalysis*, 28 (2007) 180-186.
- [40] D. Ma, Y. Shu, W. Zhang, Xiuwen Han, Y. Xu, X. Bao, In Situ  $^1\text{H}$  MAS NMR Spectroscopic Observation of Proton Species on a Mo-Modified HZSM-5 Zeolite Catalyst for the Dehydroaromatization of Methane, *Angewandte Chemie International Edition*, 39 (2000) 2928-2931.
- [41] J. Dang, G. Zhang, L. Wang, K. Chou, P.C. Pistorius, Study on Reduction of  $\text{MoO}_2$  Powders with CO to Produce  $\text{Mo}_2\text{C}$ , *Journal of the American Ceramic Society*, 99 (2016) 819-824.
- [42] B.M. Weckhuysen, D. Wang, M.P. Rosynek, J.H. Lunsford, Conversion of Methane to Benzene over Transition Metal Ion ZSM-5 Zeolites: II. Catalyst Characterization by X-Ray Photoelectron Spectroscopy, *Journal of Catalysis*, 175 (1998) 347-351.

- [43] B.M. Weckhuysen, D. Wang, M.P. Rosynek, J.H. Lunsford, Conversion of Methane to Benzene over Transition Metal Ion ZSM-5 Zeolites, *Journal of Catalysis*, 175 (1998) 338-346.
- [44] N. Kosinov, V.G.P. Sripathi, E.J.M. Hensen, Improving separation performance of high-silica zeolite membranes by surface modification with triethoxyfluorosilane, *Microporous and Mesoporous Materials*, 194 (2014) 24-30.
- [45] J. Wang, B. McEnaney, Quantitative calibration of a TPD-MS system for CO and CO<sub>2</sub> using calcium carbonate and calcium oxalate, *Thermochimica Acta*, 190 (1991) 143-153.
- [46] B. AlSabban, L. Falivene, S.M. Kozlov, A. Aguilar-Tapia, S. Ould-Chikh, J.-L. Hazemann, L. Cavallo, J.-M. Basset, K. Takanabe, In-operando elucidation of bimetallic CoNi nanoparticles during high-temperature CH<sub>4</sub>/CO<sub>2</sub> reaction, *Applied Catalysis B: Environmental*, 213 (2017) 177-189.
- [47] T.V. Voskoboinikov, H.Y. Chen, W.M.H. Sachtler, Characterization of Fe/ZSM-5 by isotopic exchange with <sup>18</sup>O<sub>2</sub>, *Journal of Molecular Catalysis A: Chemical*, 155 (2000) 155-168.
- [48] J. Valyon, W.K. Hall, Studies of the Desorption of Oxygen from Cu-Zeolites During NO Decomposition, *Journal of Catalysis*, 143 (1993) 520-532.
- [49] T.-c. Xiao, A.P.E. York, V.C. Williams, H. Al-Megren, A. Hanif, X.-y. Zhou, M.L.H. Green, Preparation of Molybdenum Carbides Using Butane and Their Catalytic Performance, *Chemistry of Materials*, 12 (2000) 3896-3905.
- [50] T. Xiao, A.P.E. York, K.S. Coleman, J.B. Claridge, J. Sloan, J. Charnock, M.L.H. Green, Effect of carburising agent on the structure of molybdenum carbides, *Journal of Materials Chemistry*, 11 (2001) 3094-3098.
- [51] D. Ma, X. Han, D. Zhou, Z. Yan, R. Fu, Y. Xu, X. Bao, H. Hu, S.C.F. Au-Yeung, Towards Guest-Zeolite Interactions: An NMR Spectroscopic Approach, *Chemistry – A European Journal*, 8 (2002) 4557-4561.
- [52] D. Ma, Y. Shu, X. Bao, Y. Xu, Methane Dehydro-aromatization under Nonoxidative Conditions over Mo/HZSM-5 Catalysts: EPR Study of the Mo Species on/in the HZSM-5 Zeolite, *Journal of Catalysis*, 189 (2000) 314-325.
- [53] B.S. Zelakiewicz, A.C. de Dios, Tong, <sup>13</sup>C NMR Spectroscopy of <sup>13</sup>C1-Labeled Octanethiol-Protected Au Nanoparticles: Shifts, Relaxations, and Particle-Size Effect, *Journal of the American Chemical Society*, 125 (2003) 18-19.
- [54] H. Koller, A.R. Overweg, R.A. van Santen, J.W. de Haan, <sup>13</sup>C and <sup>23</sup>Na Solid-State NMR Study on Zeolite Y Loaded with Mo(CO)<sub>6</sub>, *The Journal of Physical Chemistry B*, 101 (1997) 1754-1761.
- [55] I. Vollmer, G. Li, I. Yarulina, N. Kosinov, E.J. Hensen, K. Houben, D. Mance, M. Baldus, J. Gascon, F. Kapteijn, Relevance of the Mo-precursor state in H-ZSM-5 for methane dehydroaromatization, *Catalysis Science & Technology*, 8 (2018) 916-922.
- [56] T.M. Duncan, P. Winslow, A.T. Bell, The characterization of carbonaceous species on ruthenium catalysts with <sup>13</sup>C nuclear magnetic resonance spectroscopy, *Journal of Catalysis*, 93 (1985) 1-22.
- [57] A. Mehdad, R.F. Lobo, Ethane and ethylene aromatization on zinc-containing zeolites, *Catalysis Science & Technology*, 7 (2017) 3562-3572.



## **Annex chapter 4**

**On the dynamic nature of Mo sites for methane dehydroaromatization**

## Contents

<b>A4.1 CO carburization</b>	165
A4.1.1 Quantification	166
<b>A4.2 Pulsing CH<sub>4</sub></b>	169
A4.2.1 Effect of CO-treatment	169
A4.2.2 Effect of H <sub>2</sub> -treatment	173
A4.2.3 Signals for ethylene and ethane	177
<b>A4.3 X-ray absorption spectroscopy (XAS)</b>	178
<b>A4.4 Deconvolution of <sup>13</sup>C NMR spectra</b>	185
<b>A4.5 Temperature Programmed Oxidation (TPO)</b>	186
<b>A4.6 Activity Relationships</b>	187
<b>A4.7 Catalytic performance</b>	188
<b>A4.8 CH<sub>4</sub> pulsing using labelled molecules</b>	190
A4.8.1 Benzene control experiments	190
<b>A4.9 Gas chromatography-mass spectrometry (GC-MS) analysis of the collected liquid products</b>	192
<b>A4.10 Catalyst characterization</b>	196
A4.10.1 N <sub>2</sub> Adsorption	196
A4.10.2 Powder X-Ray Diffraction (PXRD)	196
<b>A4.11 References</b>	196

### A4.1 CO carburization

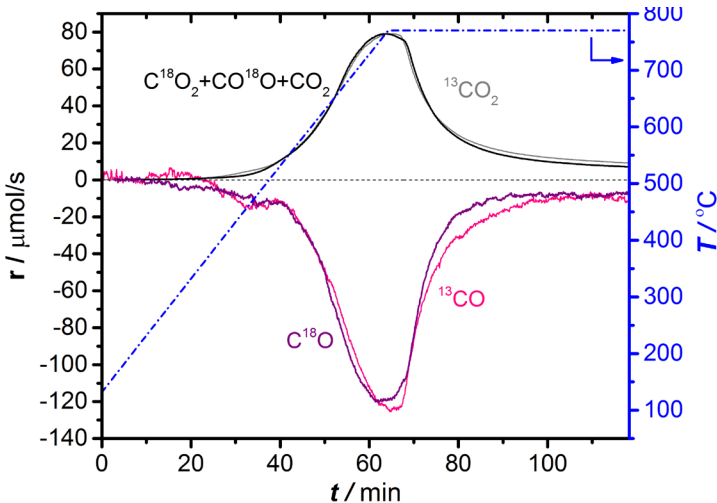


Figure A4.1.  $^{13}\text{CO}$  or  $\text{C}^{18}\text{O}$  consumption and simultaneous  $^{13}\text{CO}_2$  or  $\text{CO}_2$ ,  $\text{C}^{18}\text{O}_2$  and  $\text{CO}^{18}\text{O}$  production in TPC of **2MoHZ-13** with 30 ml/min, 2.5%  $^{13}\text{CO}$  or  $\text{C}^{18}\text{O}$  in He. The temperature was increased to  $780\ ^{\circ}\text{C}$  at a rate of  $10\ ^{\circ}\text{C}/\text{min}$  (right axis).

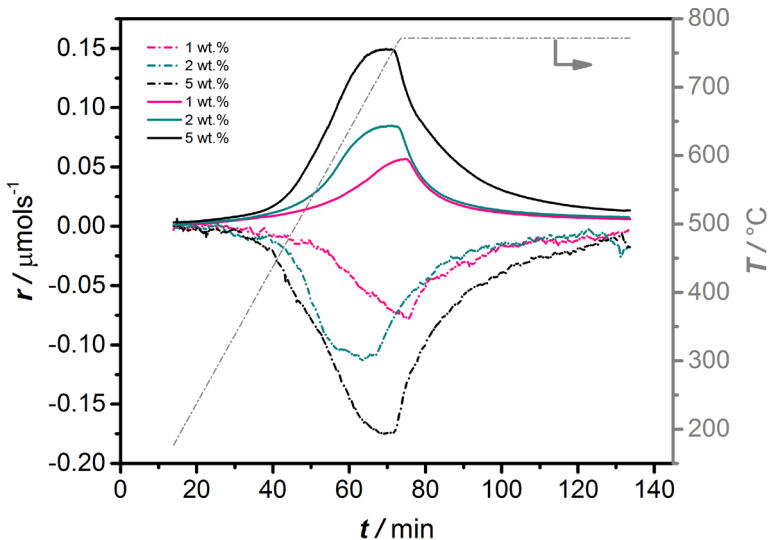
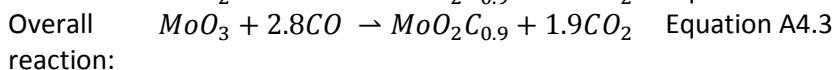
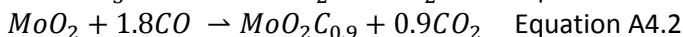
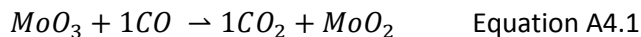


Figure A4.2. CO (dashed lines) and  $\text{CO}_2$  (solid lines) evolution for 1, 2 and **5MoHZ-13**, during TPC with 30 ml/min of 2.5% CO in He heating to  $780\ ^{\circ}\text{C}$  with  $10\ ^{\circ}\text{C}/\text{min}$ .

#### A4.1.1 Quantification

We arrive at an oxygen to molybdenum ratio of  $O/Mo = 1.09 \pm 0.15$  and a carbon to molybdenum ratio of  $C/Mo = 0.90 \pm 0.15$  based on CO uptake and  $\text{CO}_2$  calculated from **Figure 4.1** using equations 4, 6, 8-10 and 14-15. It can be seen that, even with a maximum error, still only 1.24 oxygen is removed per molybdenum, which means that oxygen is still at the Mo site, if the initial stoichiometry of the Mo oxide is at least  $\text{MoO}_2$ . We tentatively propose **Equations A4.1-3**, assuming an initial stoichiometry of  $\text{MoO}_3$ .



To estimate the accuracy of these results an error analysis was performed taking into account the errors arising from the necessary corrections due to fragmentation of  $\text{CO}_2$  into CO, baseline corrections and calibration factors. All constants used for the corrections are listed in **Table A4.1**.

Table A4.1. List of constants used for the quantification of results shown in **Figure 4.1** and their estimated errors.

Constant	Value and error
Factor for fragmentation of $\text{CO}_2$	$\alpha = 0.25 \pm 0.07$
Calibration factor CO	$K_{\text{CO}} = 24.09 \pm 0.11 \mu\text{mol}/\text{area}$
Calibration factor $\text{CO}_2$	$K_{\text{CO}_2} = 26.08 \pm 0.33 \mu\text{mol}/\text{area}$
Baseline correction $a + b * t$ for CO	$a_{\text{CO}} = 0.296 \pm 0.001 \text{ 1/s}$
Baseline correction $a + b * t$ for CO	$b_{\text{CO}} = (4.93 \pm 4.93) * 10^{-8} \text{ 1/s}^2$
Baseline correction $a + b * t$ for $\text{CO}_2$	$a_{\text{CO}_2} = (4.81 \pm 0.467) * 10^{-5} \text{ 1/s}$

Molar ratio carbon to molybdenum:	$\frac{C}{Mo} = \frac{A_{CO} + A_{CO_2}}{A_{Mo}}$	Equation A4.4
And associated error:	$\delta\left(\frac{C}{Mo}\right) = \frac{\delta C}{Mo} = \frac{\sqrt{\delta A_{CO}^2 + \delta A_{CO_2}^2}}{A_{Mo}}$	Equation A4.5
Molar ratio oxygen to molybdenum:	$\frac{O}{Mo} = \frac{A_{CO} + 2 * A_{CO_2}}{A_{Mo}}$	Equation A4.6
And associated error:	$\delta\left(\frac{O}{Mo}\right) = \frac{\delta O}{Mo} = \frac{\sqrt{\delta A_{CO}^2 + \delta 2A_{CO_2}^2}}{A_{Mo}}$	Equation A4.7
Total molar amount of CO consumed, with $\Delta t$ the time step in the measurement, which is constant and can be taken in front of the sum.	$A_{CO} = K_{CO} \sum_0^{t_{end}} r_{CO}(t)\Delta t = K_{CO}\Delta t \sum_0^{t_{end}} r_{CO}(t)$	Equation A4.8
With $r_{CO}(t)$ , the rate of CO consumption with correction for fragmentation of $CO_2$ into CO with factor $\alpha$ determined by prior calibration. $I_{CO}(t), I_{He}(t)$ and $I_{CO_2}(t)$ [A] are the MS signals for CO, He and $CO_2$ respectively	$r_{CO}(t) = \frac{I_{CO}(t)}{I_{He}(t)} - \alpha \frac{I_{CO_2}(t)}{I_{He}(t)} - baseline, CO(t)$	Equation A4.9
The sum over $r_{CO}(t)$ then becomes:	$\sum_0^{t_{end}} r_{CO}(t) = \sum_0^{t_{end}} \frac{I_{CO}(t)}{I_{He}(t)} - \alpha \sum_0^{t_{end}} \frac{I_{CO_2}(t)}{I_{He}(t)} - \sum_0^{t_{end}} baseline, CO(t)$	Equation A4.10
And the associated error arises from the correction due to fragmentation of $CO_2$ and the baseline correction and can be written as:	$\begin{aligned} \delta\left(\sum_0^{t_{end}} r_{CO}(t)\right) &= \sqrt{\left(\delta \alpha \sum_0^{t_{end}} \frac{I_{CO_2}(t)}{I_{He}(t)}\right)^2 + \left(\delta \left(\sum_0^{t_{end}} baseline, CO(t)\right)\right)^2} \end{aligned}$	Equation A4.11

Where the error associated with the baseline is estimated like this:	$\delta \left( \sum_0^{t_{end}} baseline, CO(t) \right)$ $= \sqrt{\sum_0^{t_{end}} \delta a_{CO}^2 + \sum_0^{t_{end}} t \delta b_{CO}^2}$	Equation A4.12
The relative error of $A_{CO}$ is written as:	$\frac{\delta A_{CO}}{ A_{CO} } = \sqrt{\left( \frac{\delta K_{CO}}{K_{CO}} \right)^2 + \left( \frac{\delta (\sum_0^{t_{end}} r_{CO}(t))}{\sum_0^{t_{end}} r_{CO}(t)} \right)^2}$	Equation A4.13
Total molar amount of $CO_2$ consumed.	$A_{CO_2} = K_{CO_2} \sum_0^{t_{end}} r_{CO_2}(t) \Delta t$ $= K_{CO_2} \Delta t \sum_0^{t_{end}} r_{CO_2(t)}$	Equation A4.14
Where $r_{CO_2}(t)$ , the rate of $CO_2$ consumption is defined as	$r_{CO_2}(t) = \frac{I_{CO_2}(t)}{I_{He}(t)} - baseline, CO_2(t)$	Equation A4.15
The associated error only arises from the baseline correction:	$\delta(\sum_0^{t_{end}} r_{CO_2}(t)) = \delta \left( \sum_0^{t_{end}} baseline, CO_2(t) \right)$ $= \sqrt{\sum_0^{t_{end}} \delta a_{CO_2}^2 + \sum_0^{t_{end}} t \delta b_{CO_2}^2}$ $= \sqrt{t_{end} * \delta a_{CO_2}}$	Equation A4.16
The relative error of $A_{CO_2}$ becomes:	$\frac{\delta A_{CO_2}}{ A_{CO_2} } = \sqrt{\left( \frac{\delta K_{CO_2}}{K_{CO_2}} \right)^2 + \left( \frac{\delta (\sum_0^{t_{end}} r_{CO_2}(t))}{\sum_0^{t_{end}} r_{CO_2}(t)} \right)^2}$	Equation A4.17

## A4.2 Pulsing CH<sub>4</sub>

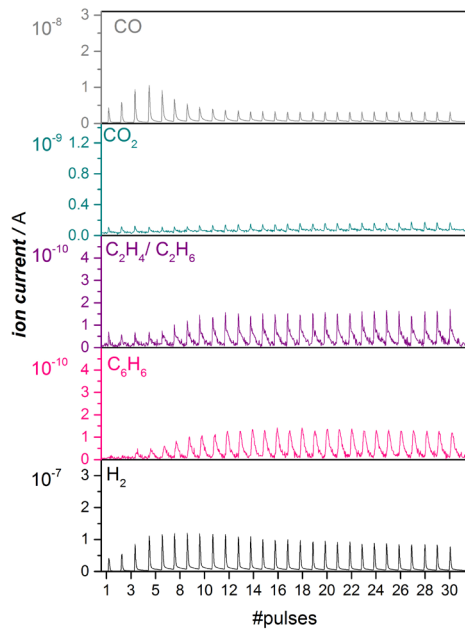
### A4.2.1 Effect of CO-treatment

CO carburization was performed as described in section "CO carburization". No corrections for fragmentation were applied in the  $m/z$  data given in **Figure A4.3**. It can be seen that the 'CO'-signal stays high throughout the experiment even after the induction period is completed. Next to a general higher background level at  $m/z = 28$  in the MS this is attributed to a pressure pulse upon injection of the 5 ml pulse of CH<sub>4</sub> into the continuous flow of 30 ml/min He, resulting in apparent 'CO' pulses. Further, the fragmentation of the products ethylene and ethane may also contribute to  $m/z = 28$  to some extent. This is evident when comparing the presented pulse experiments with a blank, where CH<sub>4</sub> is sent to an empty reactor at RT. **Figure A4.5a** compares the  $m/z = 28$  signal of the blank with pulses 16 to 19 of the pulsing experiment over untreated **1MoHZ-13**, while **Figure A4.6b** presents all signals corresponding to ethylene and ethane that were measured in our experiments, namely  $m/z = 27$ , 28 and 30, where  $m/z = 28$  was corrected by subtracting the signal during the blank experiment. Signals  $m/z = 27$  and 30 did not show any increase in signal during pulsing in the blank experiment as their background is nihil. **Figure A4.6b** represents the typical fragmentation pattern of a mixture of ethylene and ethane [1].

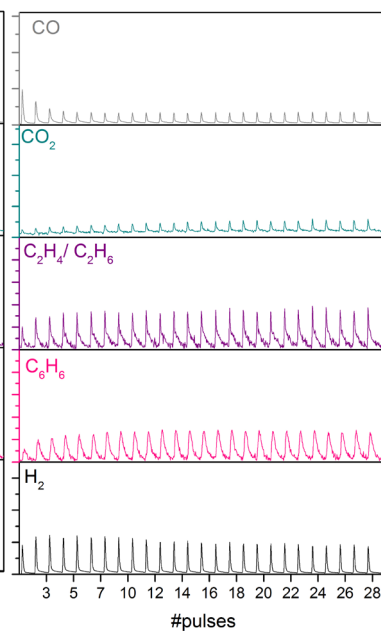
Also for the  $m/z = 44$  signal ('CO<sub>2</sub>') the increasing background during the experiment results in contributions from pressure pulses upon methane injection. The  $m/z = 44$  is part of the fragmentation pattern of any other products observed, naphthalene, benzene, toluene, ethylene and ethane.

**1MoHZ-13**

Without pre-treatment

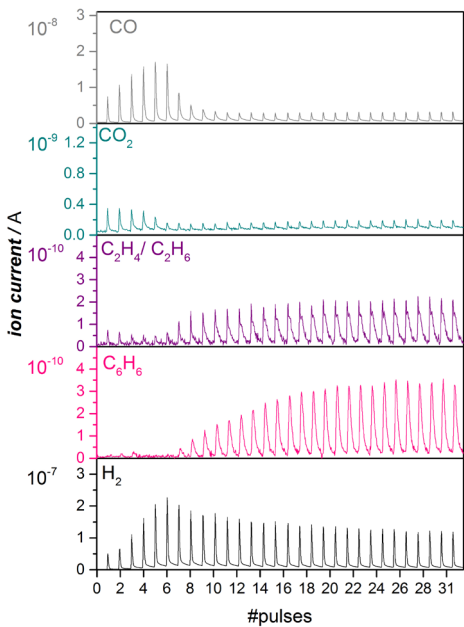


With CO-treatment

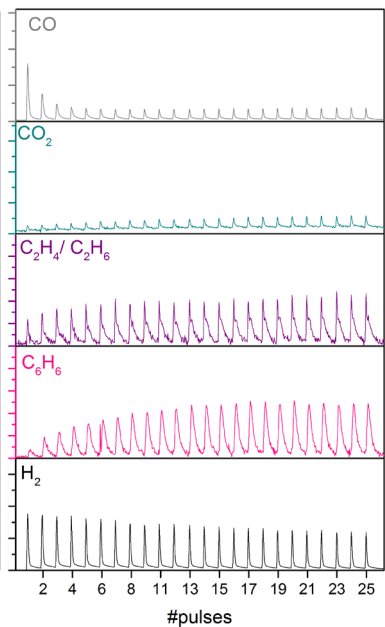


**2MoHZ-13**

Without pre-treatment

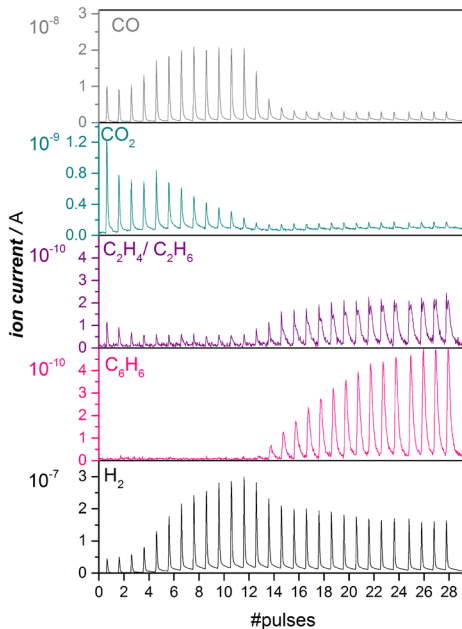


With CO-treatment



**5MoHZ-13**

Without pre-treatment



With CO-treatment

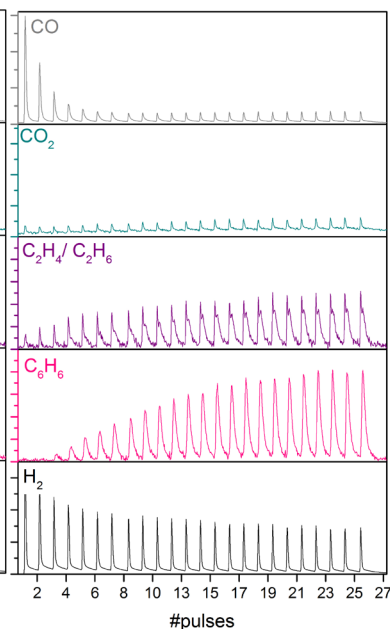


Figure A4.3. Ion current for CO,  $\text{C}_2\text{H}_4/\text{C}_2\text{H}_6$ ,  $\text{CO}_2$ ,  $\text{C}_6\text{H}_6$  and  $\text{H}_2$  ( $m/z = 28, 27, 44, 78, 2$ ) during consecutive pulsing of  $223 \mu\text{mol} \text{CH}_4$  at  $700^\circ\text{C}$  to  $300 \text{ mg}$  untreated catalyst (left column) and a catalyst pre-carburized with a  $30 \text{ ml/min}$  flow of  $2.5\%$  CO in He at  $780^\circ\text{C}$  for  $1 \text{ h}$  (right column). From top to bottom 1, 2 and 5 wt.% **MoHZ-13** samples.

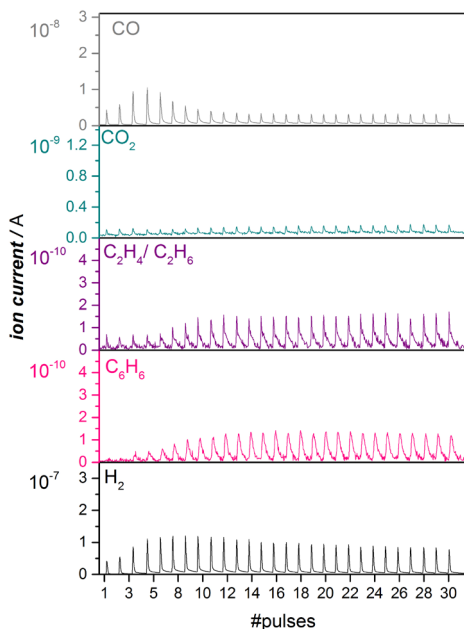
#### A4.2.2 Effect of H<sub>2</sub>-treatment

Another reduction treatment was performed to see whether a merely reduced Mo is sufficient to activate methane during consecutive pulsing of CH<sub>4</sub> described above. During this reduction treatment, a flow of 30 ml/min of 5% H<sub>2</sub> in Helium was fed to the reactor at atmospheric pressure, kept at 700 °C for 3 h, after heating at 10 °C/min. The catalyst was pre-treated at 350 °C in He overnight to desorb any gasses from the zeolite. No corrections for fragmentation were applied in the *m/z* data given in **Figure A4.4**.

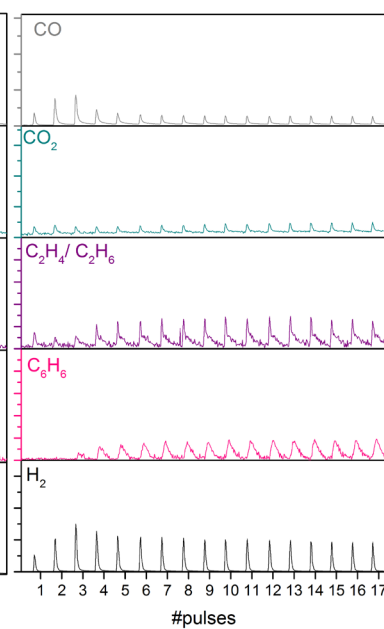
The results in **Figure A4.4** show that the activation period is somewhat reduced for **5MoHZ-13** and **2MoHZ-13**, but not for **1MoHZ-13**. The level of benzene production seems to be lower after the H<sub>2</sub> treatment indicating that this treatment creates an active site that differs from the one produced at reaction conditions. The typical maximum in H<sub>2</sub> production right before the onset of benzene production is still observed for all three Mo loadings.

#### **1MoHZ-13**

Without pre-treatment

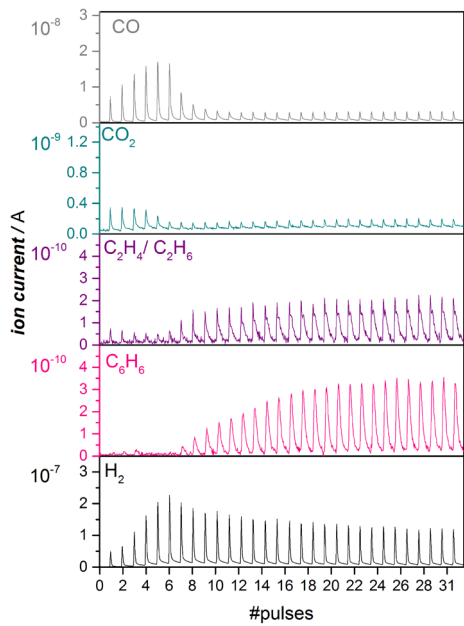
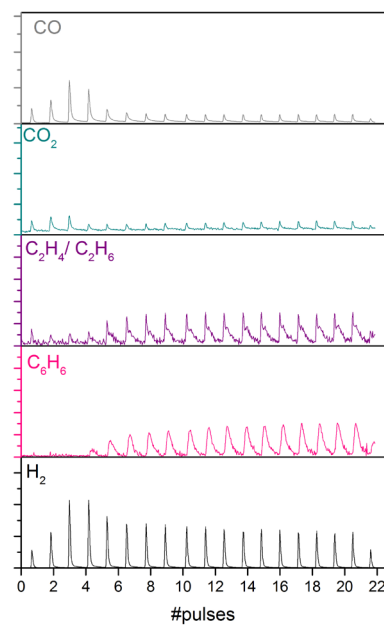


With H<sub>2</sub>-pretreatment



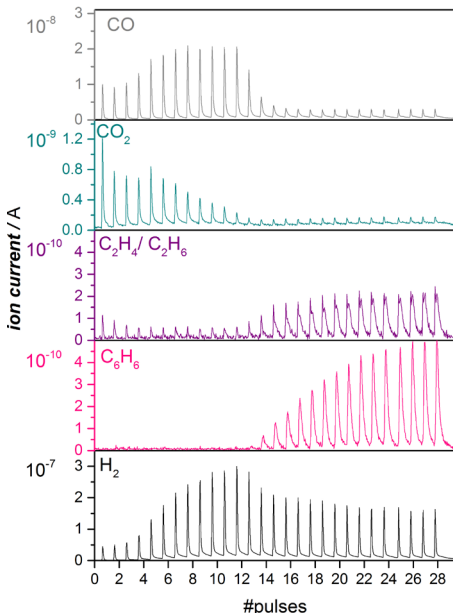
**2MoHZ-13**

Without pre-treatment

With  $\text{H}_2$ -pretreatment

## 5MoHZ-13

Without pre-treatment



With  $\text{H}_2$ -pretreatment

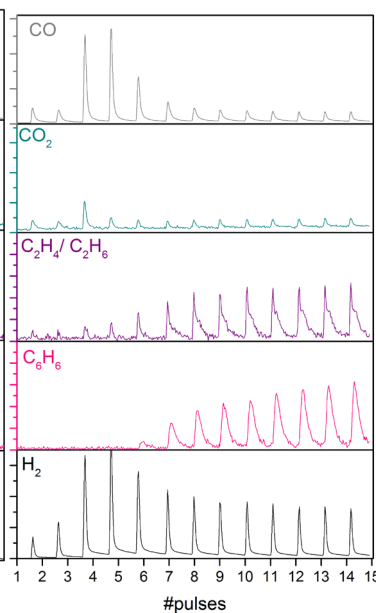


Figure A4.4. Ion current for  $\text{CO}$ ,  $\text{C}_2\text{H}_4/\text{C}_2\text{H}_6$ ,  $\text{CO}_2$ ,  $\text{C}_6\text{H}_6$  and  $\text{H}_2$  ( $m/z = 28, 27, 44, 78, 2$ ) during consecutive pulsing of  $223 \mu\text{mol}$  of  $\text{CH}_4$  at  $700^\circ\text{C}$  to  $300 \text{ mg}$  untreated catalyst (left column) and a catalyst pre-reduced with a  $30 \text{ ml}/\text{min}$  flow of  $5\%$   $\text{H}_2$  in  $\text{He}$  at  $700^\circ\text{C}$  for  $3 \text{ h}$  (right column). From top to bottom 1, 2 and 5 wt.% **MoHZ-13** samples.

To test, whether a higher temperature of  $\text{H}_2$ -reduction can lead to a shortening of the induction period, sample **1MoHZ-13** was additionally reduced at  $810^\circ\text{C}$ . The result from the pulsing experiment performed on a sample reduced at  $810^\circ\text{C}$  is shown in **Figure A4.5**. Benzene is only observed after 3 pulses of methane have been sent to the catalyst. It can be concluded that no further reduction is observed when increasing the  $\text{H}_2$ -reduction temperature to  $810^\circ\text{C}$ .

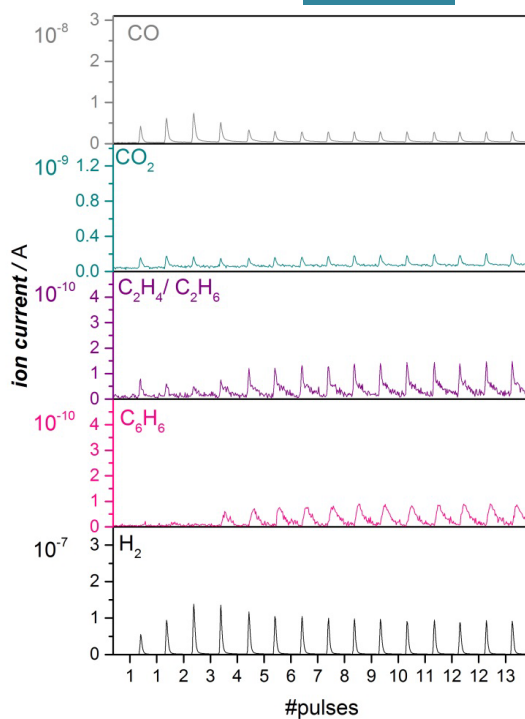


Figure A4.5. Ion current for CO, C<sub>2</sub>H<sub>4</sub>/C<sub>2</sub>H<sub>6</sub>, CO<sub>2</sub>, C<sub>6</sub>H<sub>6</sub> and H<sub>2</sub> ( $m/z = 28, 27, 44, 78, 2$ ) during consecutive pulsing of 223  $\mu\text{mol}$  of CH<sub>4</sub> at 700  $^{\circ}\text{C}$  to 300 mg **1MoHZ-13** pre-reduced in a 30 ml/min flow of 5% H<sub>2</sub> in He at 810  $^{\circ}\text{C}$  for 1 h.

## A4.2.3 Signals for ethylene and ethane

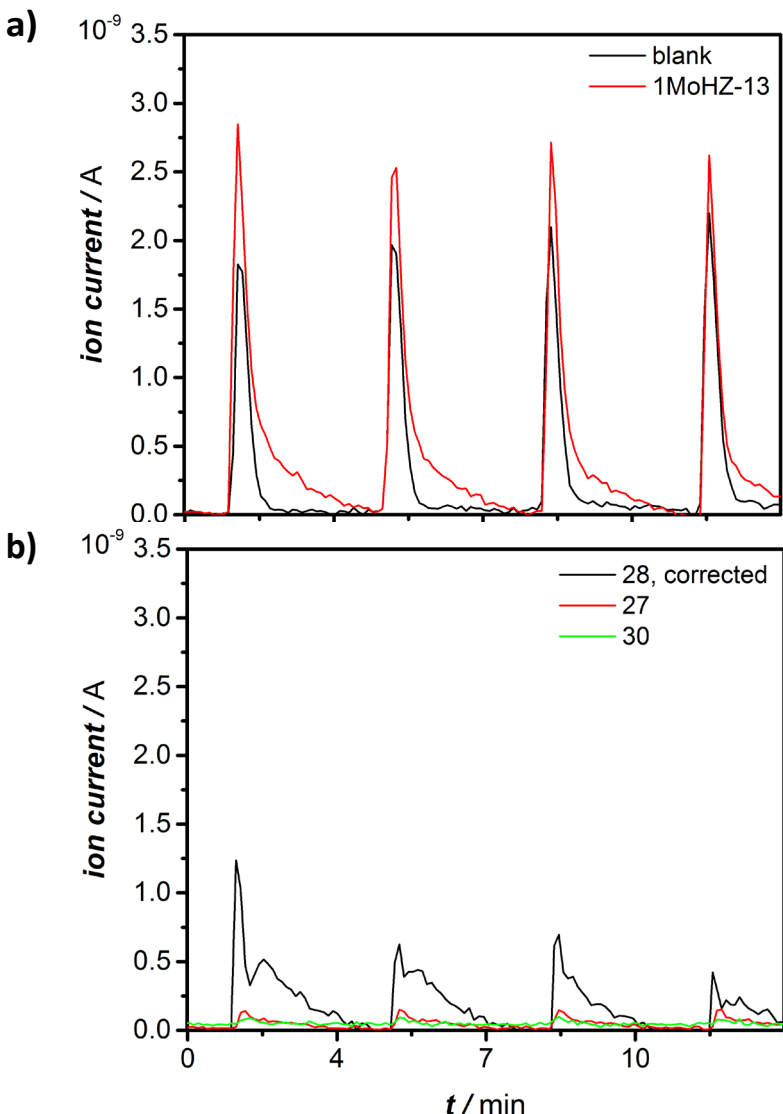


Figure A4.6. a) Ion current for  $m/z = 28$  of a blank measured during consecutive pulsing of  $223 \mu\text{mol}$  of  $\text{CH}_4$  at RT to an empty reactor compared with the ion current for  $m/z = 28$  during pulse 16-19 over **1MoHZ-13** (see Figure A4.3). b) The pressure pulse caused by the injection resulted in an apparent  $m/z = 28$  signal. Signals  $m/z = 27$ ,  $28$  and  $30$  corresponding to ethylene and ethane during pulses 16-19 over **1MoHZ-13**, where  $m/z = 28$  was corrected for the pressure pulse by subtracting the  $m/z$  signal measured during the blank experiment.

### A4.3 X-ray absorption spectroscopy (XAS)

In **Figure A4.7**, the signals of CO ( $m/z = 28$ ) and CO<sub>2</sub> ( $m/z = 44$ ) are shown in a), while the recorded XANES spectra are shown in b). The sample was left at 780 °C until a negligible amount of CO<sub>2</sub> evolved (~11 min). Then, the sample was cooled down to room temperature under CO flow and the reactor was purged with a helium flow of 10 ml/min prior to the CH<sub>4</sub> pulsing experiment.

The signals recorded during CH<sub>4</sub> pulsing for CO, C<sub>2</sub>H<sub>4</sub>/C<sub>2</sub>H<sub>6</sub>, CO<sub>2</sub>, C<sub>6</sub>H<sub>6</sub> and H<sub>2</sub> ( $m/z = 28, 27, 44, 78, 2$ ) as well as CH<sub>4</sub> conversion are shown in **Figure A4.8**. Spectra were collected right after each pulse without cooling down and are shown in **Figure A4.9** in a) for the CO treated catalyst and in b) for untreated catalyst. The spectrum highlighted in pink in **Figure A4.9**, b) signifies the spectra after the 5<sup>th</sup> pulse, where Mo sites becomes active to form benzene. This spectrum is very similar to the spectrum taken after the completion of CO carburization. It is clear that the reduction degree is very similar for the two cases, demonstrating that the same active Mo species are formed. Reference spectra for MoO<sub>2</sub>, MoO<sub>3</sub>, Na<sub>2</sub>MoO<sub>4</sub>, Mo<sub>2</sub>C and Mo-foil are shown in **Figure A4.10** together with a spectrum of **2MoHZ-13** carburized in CO recorded under *in-situ* carburization at 780 °C in fluorescence mode. The spectrum of **2MoHZ-13** carburized in CO is mostly similar to the Mo<sub>2</sub>C reference, but the post-edge features differ slightly. **Figure A4.11** shows the EXAFS spectra collected at RT right at the onset of benzene formation when pulsing CH<sub>4</sub> to the He-treated sample and after CO carburization. The Mo<sub>2</sub>C reference spectrum is added for comparison. This shows that all main vibrations are in phase with the Mo<sub>2</sub>C reference while being much lower in intensity. This is consistent with FT-EXAFS in **Figure A4.12** showing a similar Mo-Mo distance for all three samples, while the intensity of this feature is lower for the samples activated in CO and CH<sub>4</sub> compared to the Mo<sub>2</sub>C reference.

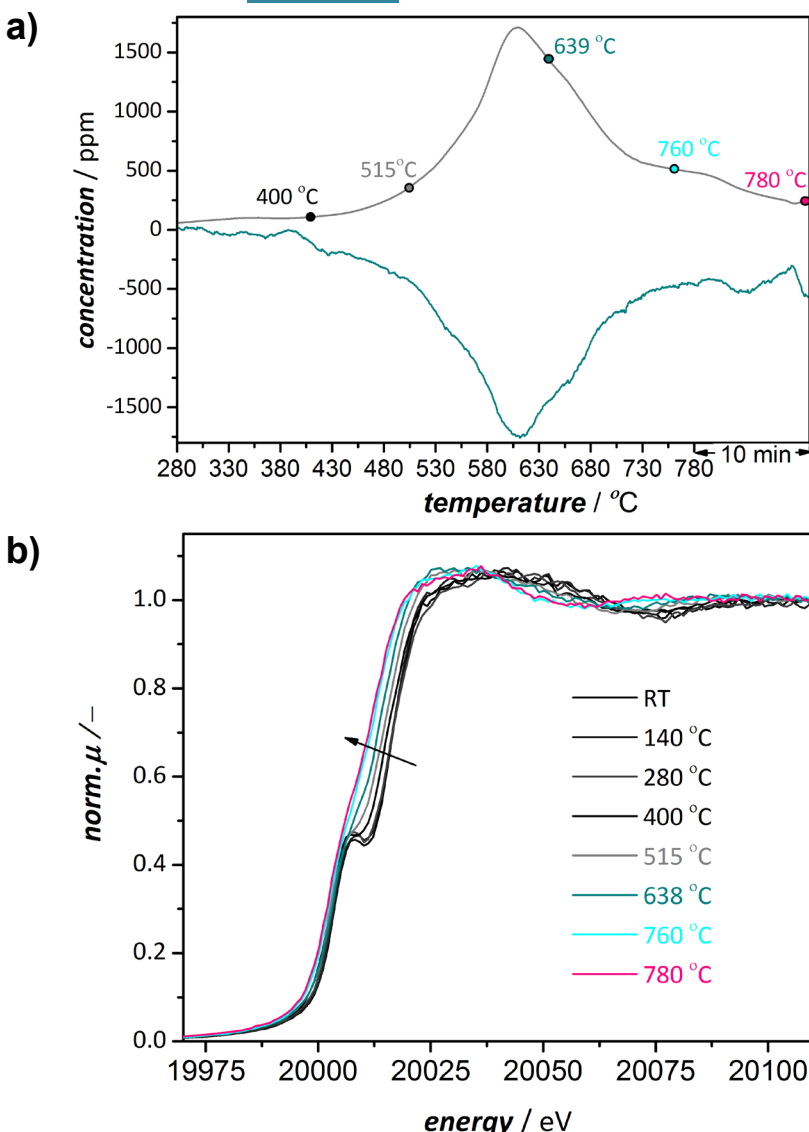


Figure A4.7. a) Concentrations of CO ( $m/z = 28$ , black) and  $\text{CO}_2$  ( $m/z = 44$ , purple) recorded by online-MS analysis during the CO carburization treatment of the **2MoHZ-13** catalyst. b) Highlighted data points in Panel A correspond to the temperatures at which Mo K-edge XANES spectra were recorded. Experimental conditions: 100 mg of catalyst were subjected to a 30 ml/min flow of 2.5%CO in He, heating up to 780  $^{\circ}\text{C}$  at 10  $^{\circ}\text{C}/\text{min}$  and cooling down after  $\text{CO}_2$  evolution ceased to be detected.

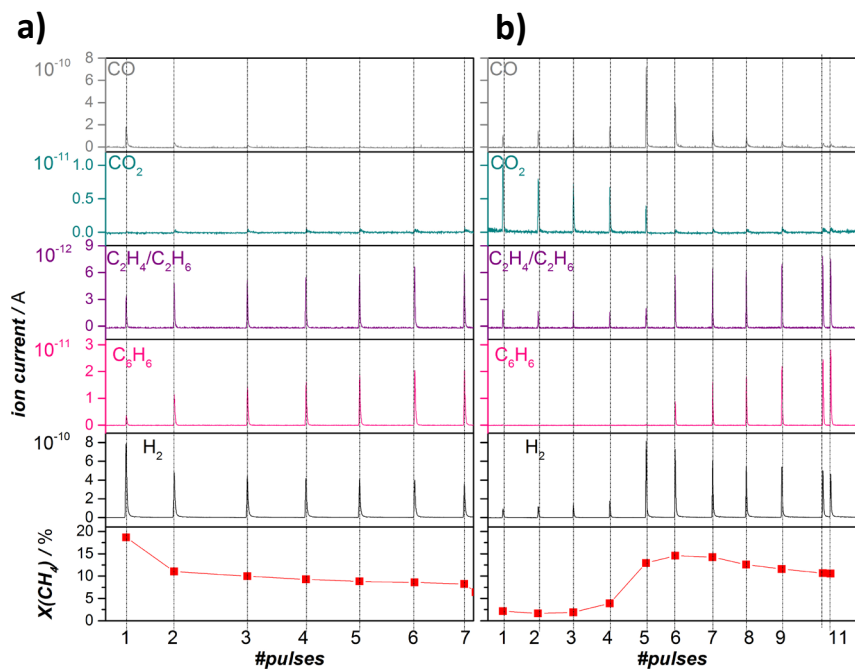


Figure A4.8. Signals for CO, C<sub>2</sub>H<sub>4</sub>/C<sub>2</sub>H<sub>6</sub>, CO<sub>2</sub>, C<sub>6</sub>H<sub>6</sub> and H<sub>2</sub> ( $m/z = 28, 27, 44, 78, 2$ ) as well as the CH<sub>4</sub> conversion recorded by online-MS analysis during the CH<sub>4</sub> pulsing for a) untreated catalyst and b) CO treated **2MoHZ-13** catalyst. Experimental conditions: 223  $\mu\text{mol}$  CH<sub>4</sub> pulses were introduced into a He flow of 10 ml/min while maintaining a temperature of 700 °C. 100 mg of catalyst were used.

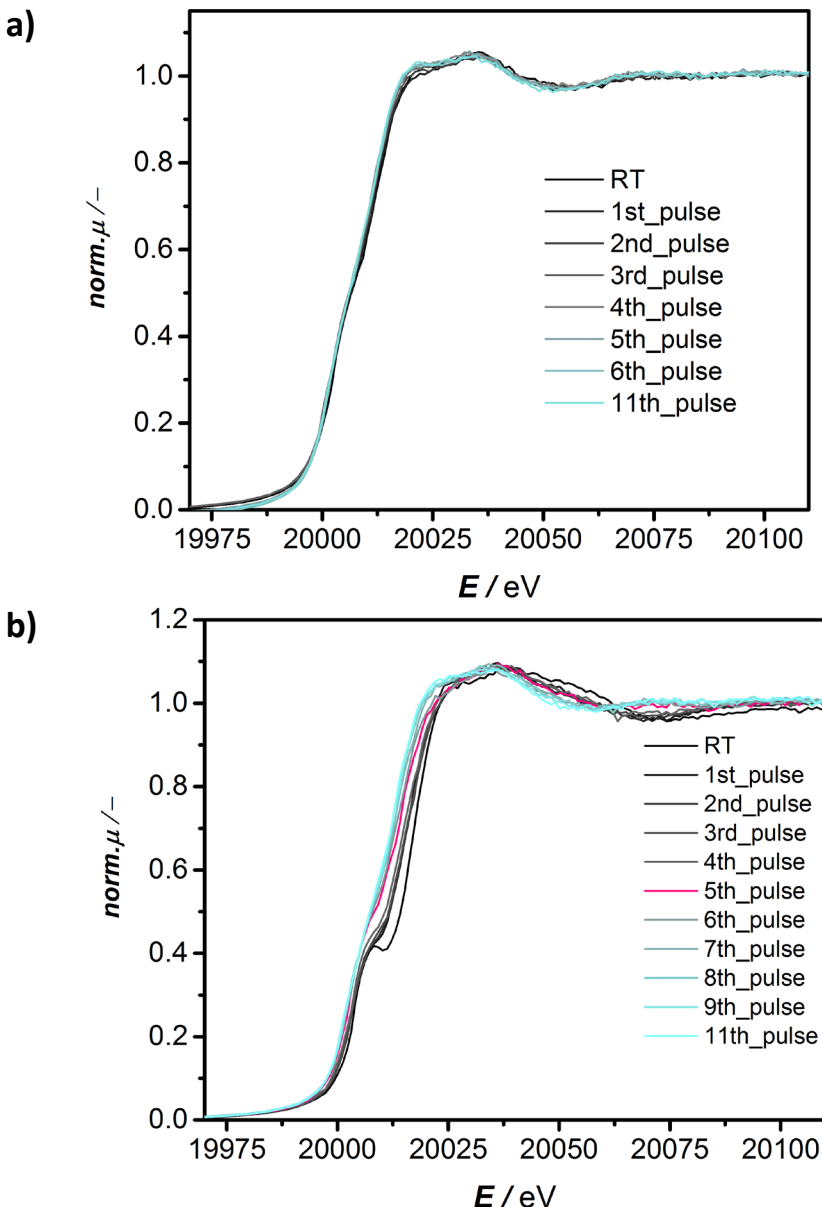


Figure A4.9. a) XANES spectra collected at Mo  $K$ -edge during  $\text{CH}_4$  pulsing at  $700\text{ }^\circ\text{C}$  with a **2MoHZ-13** catalyst pre-treated in He and b)  $30\text{ ml/min } 2.5\%\text{CO}$  in He at  $780\text{ }^\circ\text{C}$  for 1 h. Experimental conditions:  $223\text{ }\mu\text{mol}$   $\text{CH}_4$  pulses were introduced into a He flow of  $10\text{ ml/min}$  while maintaining a temperature of  $700\text{ }^\circ\text{C}$ .  $100\text{ mg}$  catalyst was used.

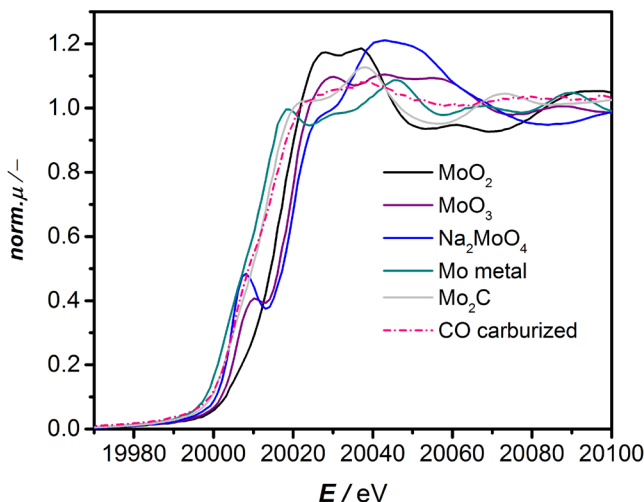


Figure A4.10. Absorption spectra collected at Mo K-edge for references measured in transmission mode and a **2MoHZ-13** carburized in CO measured in situ in fluorescence mode.

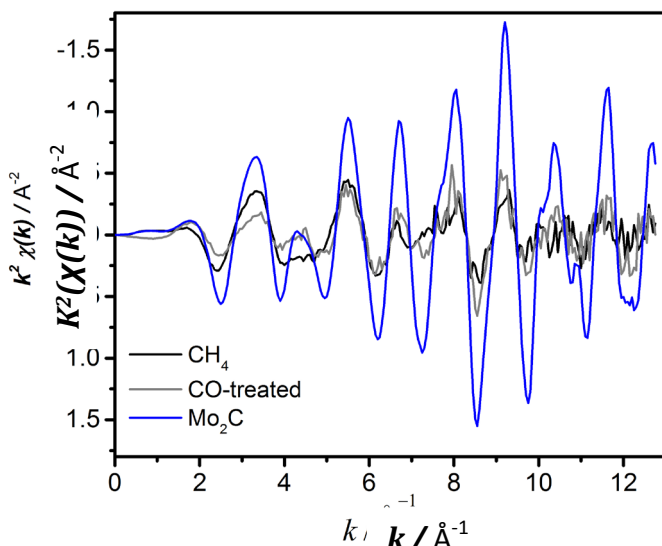


Figure A4.11. EXAFS spectra collected at Mo K-edge for references measured in transmission mode and a **2MoHZ-13** collected at RT right at the onset of benzene formation when pulsing  $\text{CH}_4$  to the He-treated **2MoHZ-13** sample and after CO carburization measured in fluorescence mode.

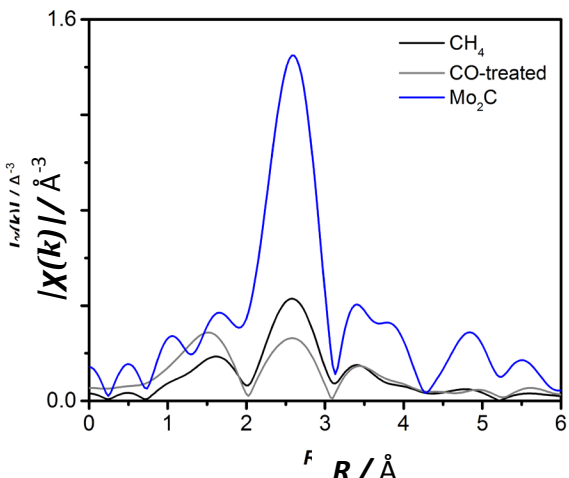


Figure A4.12. Fourier Transformed EXAFS spectra collected at Mo *K*-edge for references measured in transmission mode and a **2MoHZ-13** collected at RT right at the onset of benzene formation when pulsing  $\text{CH}_4$  to the He-treated **2MoHZ-13** sample and after CO carburization measured in fluorescence mode.

**Figure A4.13** shows the readouts on the MS during CO carburization at different temperatures. These *quasi in-situ* results are shown in **Figures 2.5** and **2.6** for the **2MoHZ-13** and **5MoHZ-13** catalysts.

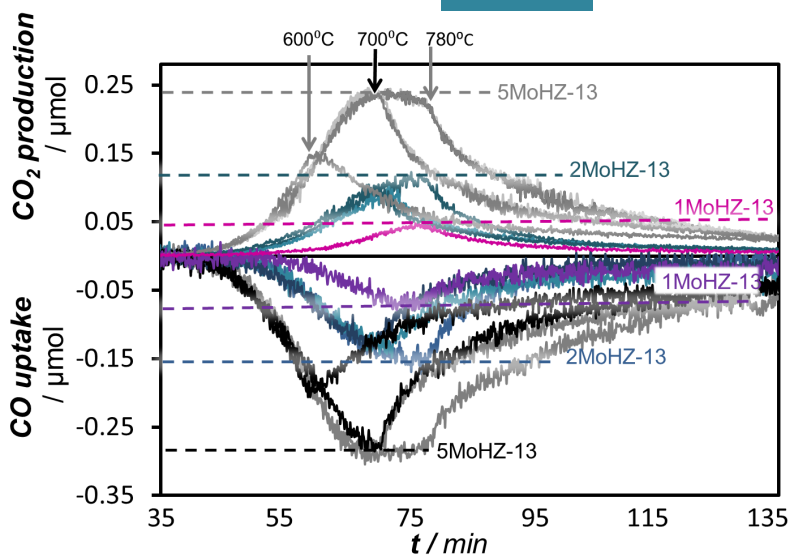


Figure A4.13.  $\text{CO}_2$  evolution (positive scale) and  $\text{CO}$  consumption (negative scale) upon  $\text{CO}$  carburization of 2 wt.% and 5 wt.% Mo on **HZ-13** with 30 ml/min 2.5%  $\text{CO}$  in He at 600  $^{\circ}\text{C}$ , 700  $^{\circ}\text{C}$  and 780  $^{\circ}\text{C}$ . Line colours correspond with the sample colours, maximum temperatures applied for the carburization are indicated with arrows at the top.

#### A4.4 Deconvolution of $^{13}\text{C}$ NMR spectra

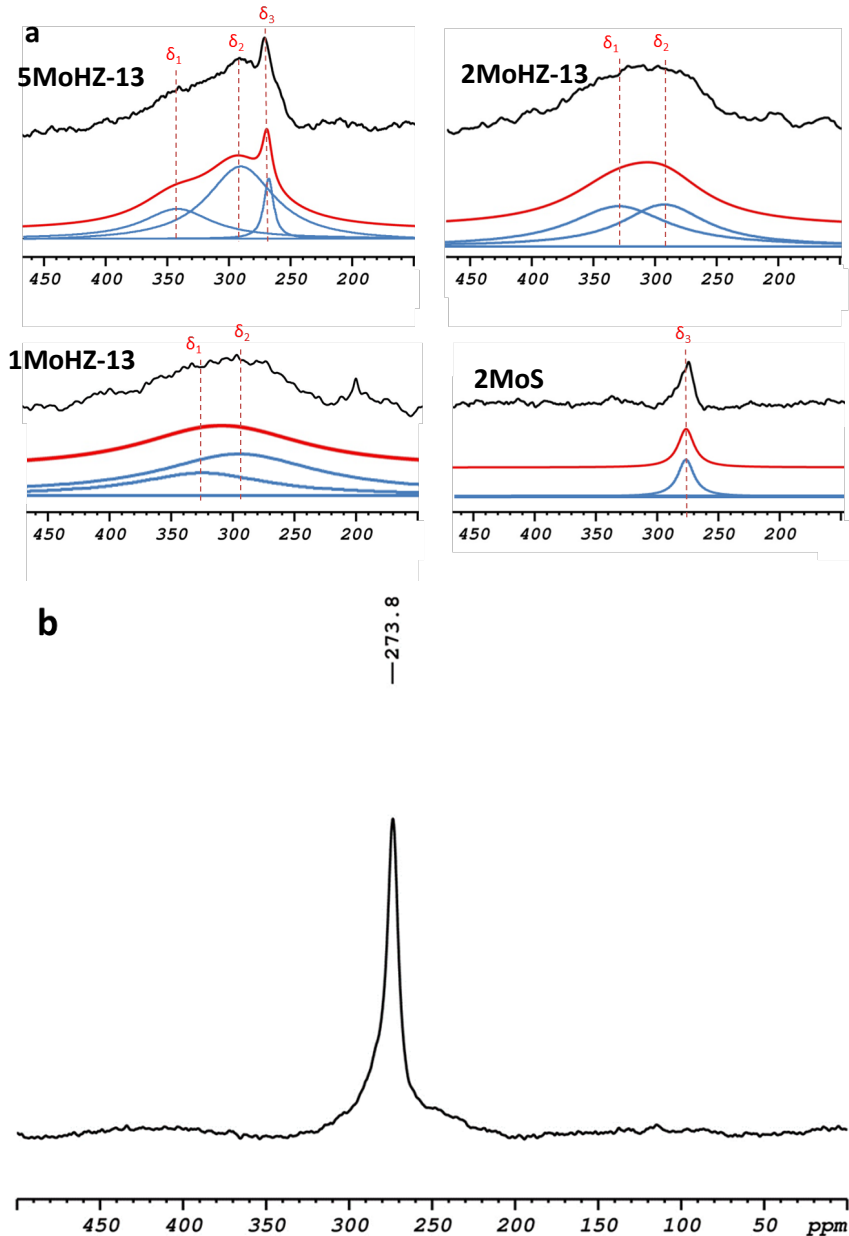


Figure A4.14. a) Deconvolution results of  $^{13}\text{C}$  MAS NMR spectra of **MoHZ-13** after  $^{13}\text{CO}$  carburization using Lorentzian-Gaussian fitting. b) Spectra collected with  $\text{Mo}_2\text{C}$  reference.

Carbon amounts obtained from the deconvolution using Gaussian-Lorentzian fitting are summarized in **Table A4.2**. Carbon amounts predicted by TPC are about 4 times higher than carbon amounts obtained by deconvolution of the  $^{13}\text{C}$  NMR spectra. The fact that this factor is the same for all three loadings of Mo suggests a systematic error in the deconvolution of  $^{13}\text{C}$  NMR. This can be due to a slight re-oxidation of the active site, although exposure to oxygen was limited as much as possible.

Table A4.2.  $^{13}\text{C}$  MAS NMR chemical shifts deconvolution and quantification of carbide species obtained after  $^{13}\text{CO}$  carburization of Mo loaded **HZ-13** and **silicalite-1** compared to carbon content determined from TPC.

Catalyst	$\delta 1$ (338 ppm)		$\delta 2$ (290 ppm)		$\delta 3$ (270 ppm)		$\sum \delta$	Carbon content from TPC
	% <sup>a</sup>	$\mu\text{mol} \cdot \text{g}^{-1}$ <sup>b</sup>	% <sup>a</sup>	$\mu\text{mol} \cdot \text{g}^{-1}$ <sup>b</sup>	% <sup>a</sup>	$\mu\text{mol} \cdot \text{g}^{-1}$ <sup>b</sup>		
<b>1MoHZ-13</b>	22	7.0	78	25.0	0	0.0	32.0	137.0
<b>2MoHZ-13</b>	53	28.3	47	25.0	0	0.0	53.3	201.9 d
<b>5MoHZ-13</b>	36	28.3	57	44.7	7	5.5	78.5	308.3
<b>2MoS</b>	0	0.0	0	0.0	100	27.5	27.5	

<sup>a</sup> Relative concentration of carbide species (%) obtained from deconvolution using mixed Gaussian-Lorentzian fitting.  
<sup>b</sup> Calculated using  $\text{Mo}_2\text{C}$  as external standard.  
<sup>c</sup> calculated from curves in Figure A4.2, see section ‘CO carburization-Quantification’ for details on calculation  
<sup>d</sup> obtained by averaging 3 experiments

#### A4.5 Temperature Programmed Oxidation (TPO)

Table A4.3. Carbon content as determined from **Figure A4.2** and **Figure 4.7** for **1, 2 and 5MoHZ-13**.

Catalyst	Carbon content from TPC	Carbon content from TPO	% difference	
			C/Mo	%
<b>1MoHZ-13</b>	1.3	1.0	25	
<b>2MoHZ-13</b>	1.1	1.0	13	
<b>5MoHZ-13</b>	0.6	0.4	27	

## A4.6 Activity Relationships

**Figures A4.15-16** relate maximum conversion of methane to total carbon content in  $\mu\text{mol/g}$  as determined by deconvolution of  $^{13}\text{C}$  NMR (section “ $^{13}\text{C}$  NMR”).

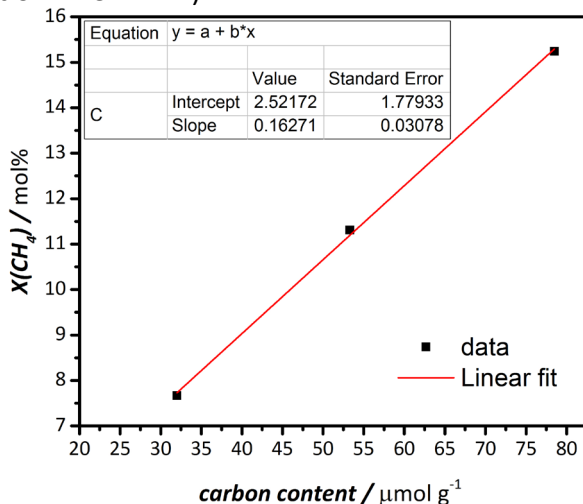


Figure A4.15. Maximum conversion of methane plotted against carbon content determined by quantification of  $^{13}\text{C}$  NMR results for **1MoHZ-13**, **2MoHZ-13** and **5MoHZ-13**.

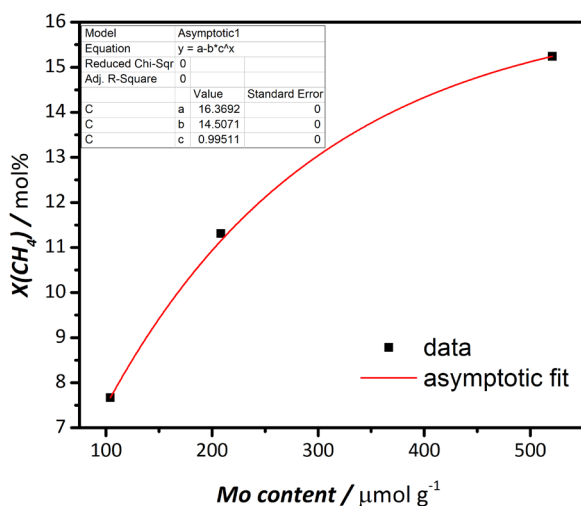


Figure A4.16. Maximum methane conversion plotted against Mo content for **1MoHZ-13**, **2MoHZ-13** and **5MoHZ-13**.

#### A4.7 Catalytic performance

Catalytic testing was performed in a quartz reactor tube with an inner diameter of 6 mm, using 500 mg catalyst pelletized to pellets of 212 to 425 µm. A weight hourly space velocity (WHSV) of 1.21 h<sup>-1</sup> (based only on methane flow) and a reaction temperature of 700 °C was applied in all tests. Product analysis was achieved on an Interscience Trace GC with a TCD and two FIDs. A mixture 5% N<sub>2</sub> in CH<sub>4</sub> was fed to the reactor, where N<sub>2</sub> was used as an internal standard. The reactor was brought to reaction temperature under the same flow with a heating rate of 10 °C/min. Although trace amount of many products were detected in the calculations only the major products were considered (hydrogen, ethylene, ethane, propylene, benzene, toluene, xylenes and naphthalene).

Product yields were calculated according to **Equation A4.18**:

$$Y_{product} [\text{mol}\%] = \frac{F_{C_i H_j}}{F_{CH_4, in}} * i * 100\% \quad \text{Equation A4.18}$$

Conversion of methane is shown in **Figure A4.17** for **1MoHZ-13**, **2MoHZ-13** and **5MoHZ-13**. While benzene yields and naphthalene yields are shown in **Figure A4.18** and **Figure A4.19** respectively.

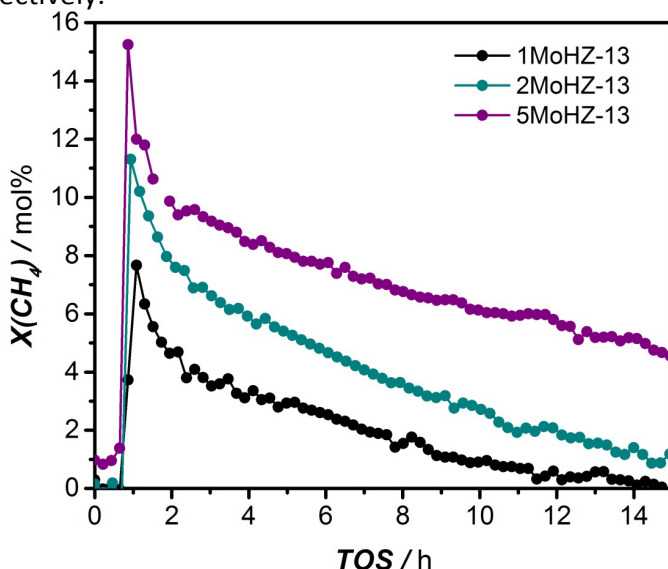


Figure A4.17: CH<sub>4</sub> conversion for **1MoHZ-13**, **2MoHZ-13** and **5MoHZ-13** tested at 700 °C with 500 mg catalyst and a WHSV = 1.21 h<sup>-1</sup>.

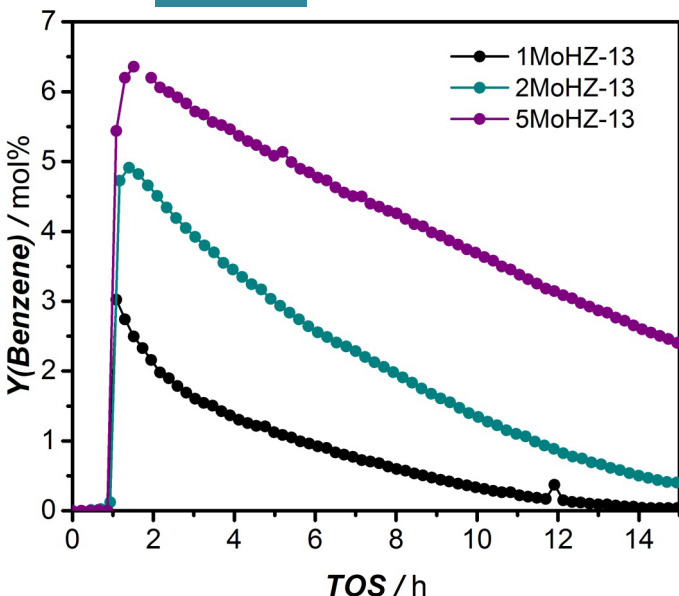


Figure A4.18. Benzene yields for **1MoHZ-13**, **2MoHZ-13** and **5MoHZ-13** tested at 700 °C with 500 mg catalyst and a WHSV = 1.21 h<sup>-1</sup>.

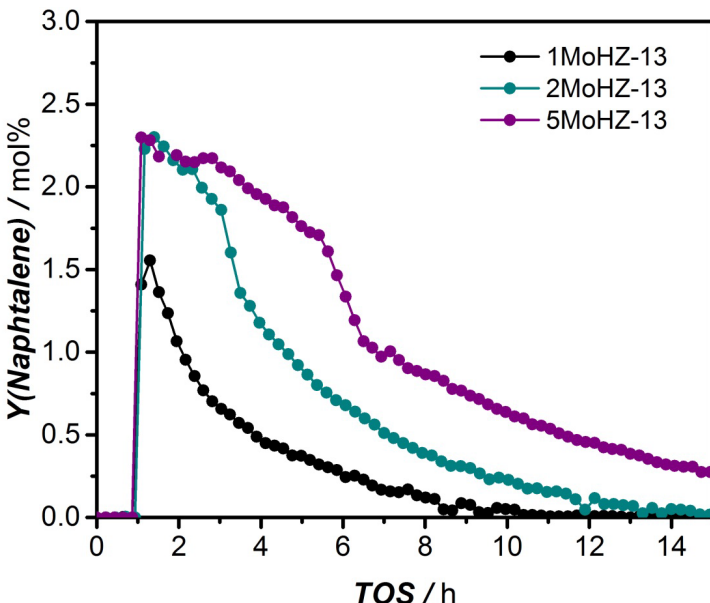


Figure A4.19. Naphthalene yields for **1MoHZ-13**, **2MoHZ-13** and **5MoHZ-13** tested at 700 °C with 500 mg catalyst and a WHSV = 1.21 h<sup>-1</sup>.

## A4.8 CH<sub>4</sub> pulsing using labelled molecules

### A4.8.1 Benzene control experiments

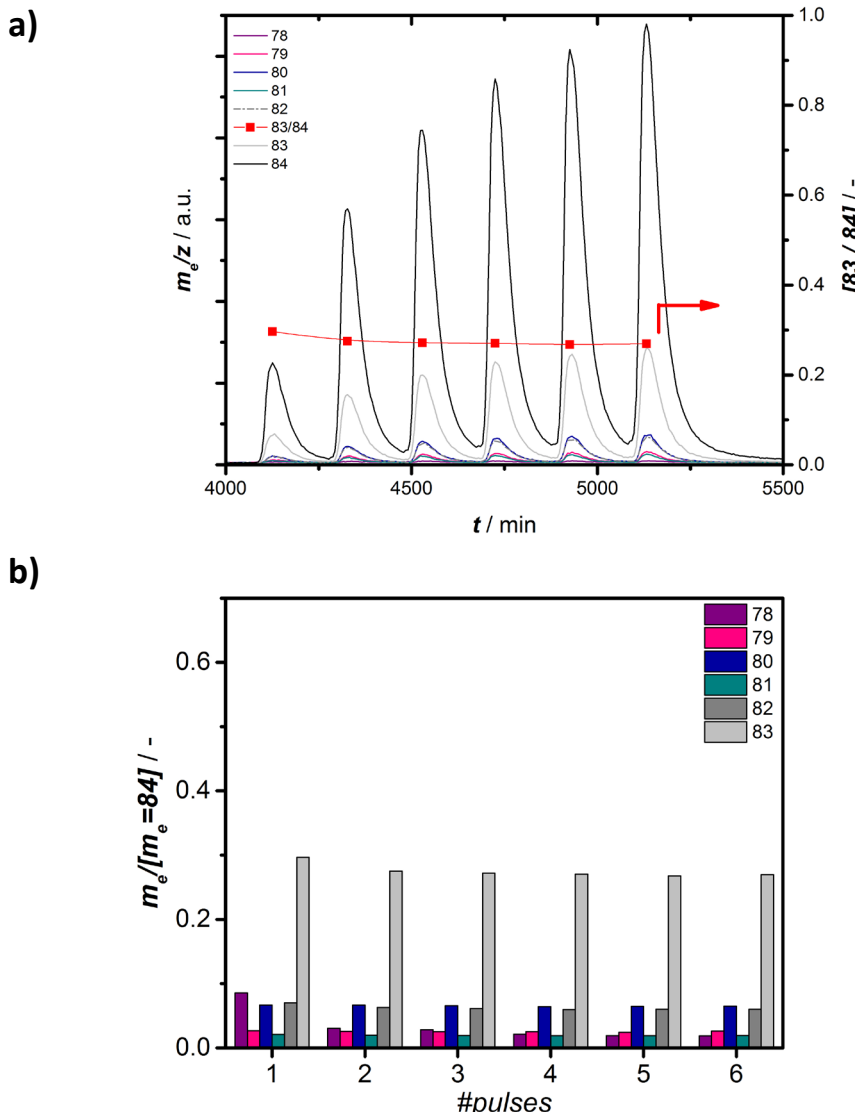


Figure A4.20. a) Development of MS readouts for several fragments representative of  $^{13}\text{C}_6\text{H}_6$  during consecutive pulsing of  $^{13}\text{CH}_4$  to 300 mg of **2MoHZ-13** carburized with 30 ml/min of 2.5%  $^{13}\text{CO}$  in He at  $780^\circ\text{C}$  for 1 h. b) Shows the integrated peak areas per pulse normalized by  $m/z = 84$ .

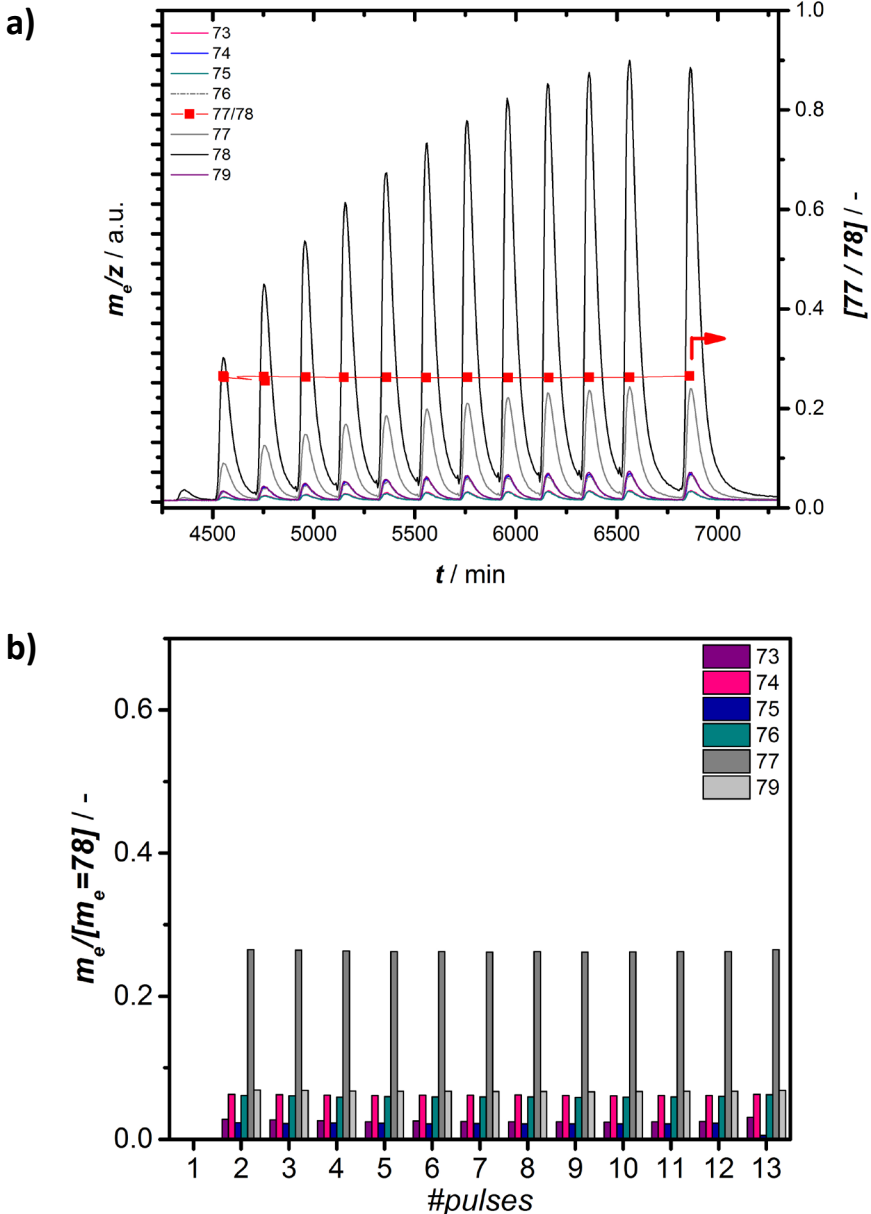


Figure A4.21. a) Development of MS readouts for several fragments representative of  $^{12}\text{C}_6\text{H}_6$  during consecutive pulsing of  $^{12}\text{CH}_4$  to 300 mg of **2MoHZ-13** carburized with 30 ml/min of 2.5%  $^{12}\text{CO}$  in He at  $780^\circ\text{C}$  for 1 h. b) Shows the integrated peak areas per pulse normalized by  $m/z = 78$ .

#### A4.9 Gas chromatography-mass spectrometry (GC-MS) analysis of the collected liquid products

To further confirm the results for the online-MS analysis of the products, the liquid products were collected at the outlet by bubbling the effluent gasses through ethyl-acetate. The collected samples were analysed on a Shimadzu GCMS-QP2010S with a split of 25, an injector temperature of 250 °C and a VF CPsil-5 25mx0.25mmx0.4 µm column. The temperature program consisted of a 5 min hold at 50 °C and then a ramp rate of 70 °C/min to ramp to 325 °C and another hold for 3 min. The MS was operated with the ion source(EI) at 200 °C and the interface at 250 °C and masses between 40 and 600 amu were measured with 0.5 sec per spectrum and a solvent cut time of 1.7 min. Collected samples were compared to a reference of unlabelled benzene.

In **Figure A4.23**, a sample collected after the first 4 pulses of  $^{13}\text{CH}_4$  to 300 mg of **2MoHZ-13** carburized with 30 ml/min of 2.5 %  $^{12}\text{CO}$  in He at 780 °C for 1 h are compared to a reference. As also observed with online MS analysis mass 83 is much higher than the fragment at 77 for  $\text{C}_6\text{H}_5$  of the reference. **Figure A4.24** shows the results of the reverse experiment where carburization was performed with  $^{13}\text{CO}$  and pulsing with  $^{12}\text{CH}_4$ , while keeping all other conditions the same. The sample collected during the first 3 pulses shows a much higher intensity for mass 79, this mass represents  $^{13}\text{C}^{12}\text{C}_5\text{H}_6$ . For the reference this mass corresponds to the natural abundance of the isotope. It is clear from **Figure A4.24** that the intensity for this mass exceeds the value for natural abundance in benzene of 6\*1.1% for the sample collected after the first 3 pulses. This value is lower for the sample collected during pulse 4 to 8, but is still above the value corresponding to natural abundance.

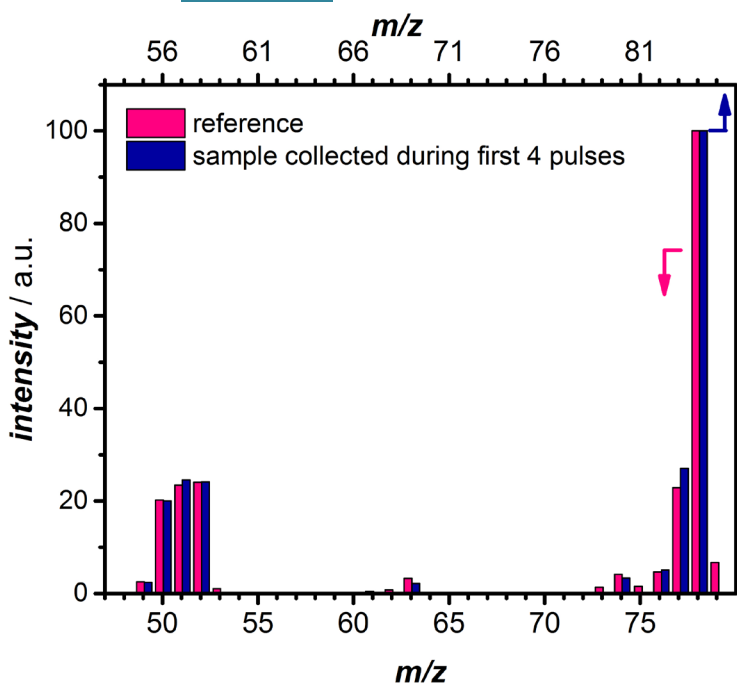


Figure A4.23. Fragmentation pattern obtained from GC-MS analysis of benzene collected during the first 4 pulses of  $^{13}\text{CH}_4$  to 300 mg of **2MoHZ-13** carburized with 30 ml/min of 2.5%  $^{12}\text{CO}$  in He at  $780\text{ }^\circ\text{C}$  for 1 h compared to unlabelled benzene as a reference. The top axis refers to the collected sample, while the bottom axis refers to the non-enriched reference.

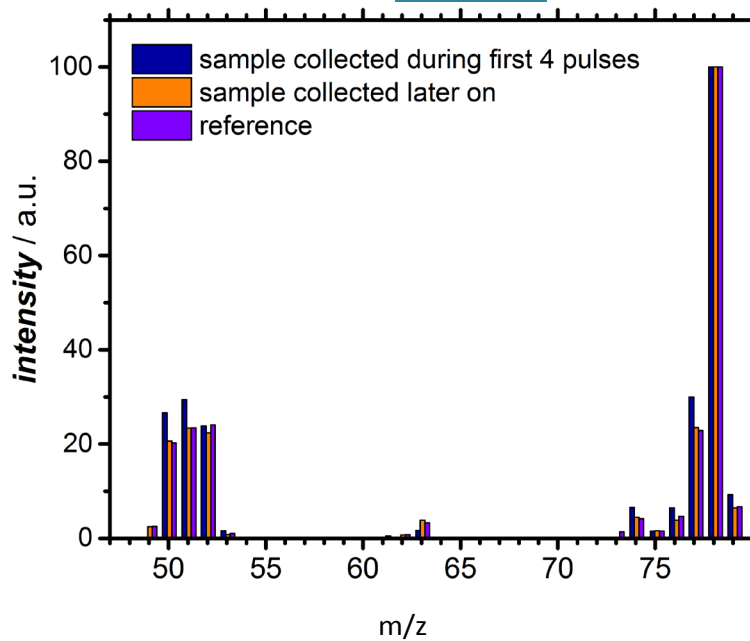


Figure A4.24. Fragmentation pattern obtained from GC-MS analysis of benzene collected during the first 3 pulses of  $^{12}\text{CH}_4$  to 300 mg of **2MoHZ-13** carburized with 30 ml/min of 2.5%  $^{13}\text{CO}$  in He at  $780\text{ }^{\circ}\text{C}$  for 1 h compared to a sample collected during pulse 4-8 and a non-enriched benzene as a reference.

## A4.10 Catalyst characterization

### A4.10.1 N<sub>2</sub> Adsorption

N<sub>2</sub> Adsorption was performed on a TriStar II 3020 Version 3.02 (Micromeritics) at liquid nitrogen temperature,  $T = -196^{\circ}\text{C}$ . The equilibration interval amounted to 12 s. Before running the adsorption, the catalyst was outgassed under a flow of N<sub>2</sub> at 350  $^{\circ}\text{C}$  for 16 h. The Brunauer-Emmet-Teller theory was applied to determine the BET area of the catalyst and the *t*-plot method to determine the micropore volume. The isotherm obtained for **HZ-13** calcined at 550  $^{\circ}\text{C}$  for 7 h, heating with 2  $^{\circ}\text{C}/\text{min}$ , is shown in **Figure A4.25**. The micropore volume was determined to be 0.132 cm<sup>3</sup>/g and the BET area 350 m<sup>2</sup>/g.

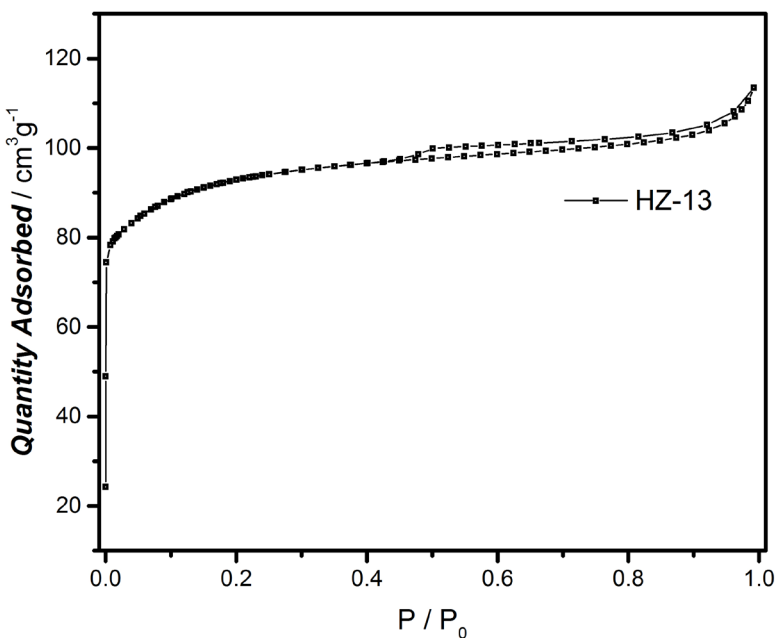


Figure A4.25. N<sub>2</sub> isotherm measured at liquid N<sub>2</sub> temperature on **HZ-13**, calcined at 550  $^{\circ}\text{C}$  for 7 h, heating with 2  $^{\circ}\text{C}/\text{min}$ .

#### A4.10.2 Powder X-Ray Diffraction (PXRD)

For Powder X-Ray Diffraction (PXRD), a Bruker D8 Advance diffractometer was used operating in Bragg-Brentano geometry using Co  $K\alpha$  radiation ( $\lambda = 0.179$  nm) and a Lynxeye position sensitive detector to collect data in the range of  $2\theta$  from  $5^\circ$  to  $50^\circ$  with a scan-speed of  $0.2^\circ\text{s}^{-1}$  and a sample rotation of 30 rpm. **Figure A4.26** shows the diffraction pattern of **HZ-13** calcined at  $550^\circ\text{C}$  for 7 h, heating with  $2^\circ\text{C}/\text{min}$ . The zeolite shows the typical diffraction pattern of a zeolite with MFI topology.

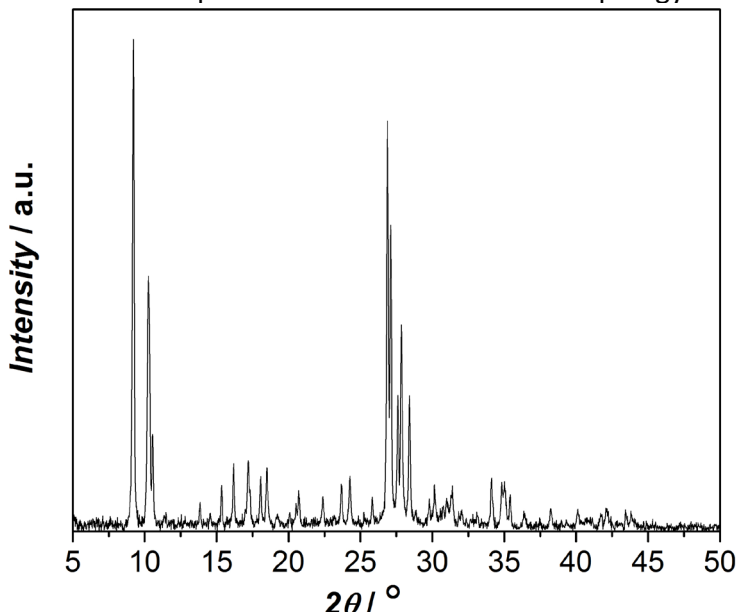
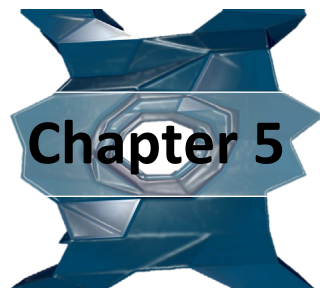


Figure A4.26. PXRD pattern of **HZ-13**, calcined at  $550^\circ\text{C}$  for 7 h, heating with  $2^\circ\text{C}/\text{min}$ .

#### A4.12 References

- [1] S.E. Stein, NIST Chemistry WebBook, The National Institute of Standards and Technology Gaithersburg MD, 2017.



---

**A site-sensitive *quasi-in situ* strategy to  
characterize Mo/HZSM-5 during activation**

The active sites on the methane dehydroaromatization (MDA) catalyst Mo/HZSM-5 are very hard to characterize, because they are present in various geometries and sizes and only form under reaction conditions with methane at 700 °C. To address these issues an experimental strategy is presented that enables distinguishing different active sites for MDA present on Mo/HZSM-5 and helps determining the Mo charge, nuclearity and chemical composition. This approach combines a CO pretreatment to separate the active Mo-site formation from coke formation, *quasi-in situ* spectroscopic observations using DNP, <sup>13</sup>C NMR, CO IR and theory. This allows the discrimination between three different types of active sites. Distinct spectroscopic features were observed corresponding to two types of mono- or dimeric Mo (oxy-)carbide sites as well as a third site assigned to Mo<sub>2</sub>C nanoparticles on the outer surface of the zeolite. Their formal Mo oxidation state was found to be between 4+ and 6+. Dynamic nuclear polarization (DNP) measurements of samples carburized in CO as well as in CH<sub>4</sub> confirm the assignment and also show that accumulated aromatic carbon covers the bigger Mo nanoparticles on the outer surface of the zeolite, causing deactivation. It was previously observed that after an initial period where no desired products are formed yet, benzene starts slowly forming until reaching its maximum productivity. Direct observation of the active site with <sup>13</sup>C NMR confirmed that Mo-sites do not transform further once benzene starts forming, meaning that they are fully activated during the period where no desired products are observed yet. Therefore, the slow increase of the benzene formation rate cannot be attributed to a further transformation of Mo sites.

This chapter is based on the following publication:

I. Vollmer, N. Kosinov, Á. Szécsényi, G. Li, I. Yarulina, E. Abou-Hamad, A. Gurinov, S. Ould-Chikh, A. Aguilar-Tapia, J.-L. Hazemann, E. Pidko, E. Hensen, F. Kapteijn, J. Gascon, (2019) "A site-sensitive quasi-*in situ* strategy to characterize Mo/HZSM-5 during activation", *Journal of Catalysis*, **370**: 321-331  
**doi: /10.1016/j.jcat.2019.01.013**

## 5.1 Introduction

Direct, non-oxidative conversion of methane provides an alternative way to obtain aromatics. If this process could be brought to commercialization, it could compensate for the decrease in production of aromatics from naphtha crackers of which many, especially in the US, are currently revamped to gas crackers [1]. Shale gas is available and cheap, which makes it an attractive feedstock [2]. Because of that, developing an active and stable methane dehydroaromatization catalyst has gained a lot of research interest since this reaction was shown to be possible over a Mo/HZSM-5 catalyst [3, 4]. Still today Mo supported on HZSM-5 remains the most researched system, because of its superior performance. It is not fully understood why this particular system performs so well and how the structure of the Mo active site looks like exactly.

Pinpointing the active site on a heterogeneous catalyst and its full spectroscopic characterization have rarely been achieved, because of the plethora of sites with different geometries and nuclearities one has to consider [5]. At the same time, only a small fraction of these sites is responsible for all catalysis [5, 6] and to spot which ones are most active is a challenge. Developing a structure-activity relationship for the methane dehydroaromatization (MDA) is further complicated because the active sites form at reaction conditions in an initial period where no desired products are observed yet [7-13]. Because of this, measurements need to be performed *operando* or *quasi-in situ* to characterize the active site, which is challenging, mostly because of the high reaction temperature of 700 to 800 °C. During the activation period, Mo was shown to reduce and carburize [7]. However, there is no agreement about the degree of reduction and carburization and several species have been proposed to constitute the active site: MoC, Mo<sub>2</sub>C, coke modified Mo<sub>2</sub>C [14], Mo<sub>2</sub>C [9, 15], any kind of Mo<sup>6+</sup> and partially reduced oxide MoO<sub>(3-x)</sub> [16, 17]. Gao *et al.* and Khan *et al.* performed DFT calculations to determine the dehydroaromatization activity of fully carbidic clusters with the formula Mo<sub>2</sub>C<sub>x</sub> and Mo<sub>4</sub>C<sub>x</sub> [18, 19]. Since these are only a few of many possible structures Mo can take on at reaction conditions, to really get valuable insight from such calculations, more direct evidence on the nuclearity and size of the Mo sites is needed. *Operando* XAS has been performed to detect Mo carbide formation [8, 13, 20], but since it is a bulk technique only an average over all active sites present can be obtained [6, 21]. We have used *operando* XAS on the

same system studied in this work and were able to track the reduction of Mo to (oxy-)carbidic species [22]. We speculated that most of the Mo was present as mono- or dimeric species even after on-stream activation, since only a low intensity for the Mo-Mo scattering path was observed in the FT-EXAFS. Information about how many different sites exist, their nuclearity and structure could not be deduced. <sup>95</sup>Mo NMR, similar to XAS also directly probes the electronic state of Mo, but leads to a very broad signal that does not allow to determine the nuclearity, stoichiometry or location of Mo inside the zeolite channels [23, 24]. EPR can also directly probe, but unfortunately does not lead to much insight on the (oxy-)carbidic species either [25, 26]. Gao *et al.*, using UV Raman, were able to gain valuable insight on the location and nature of the Mo oxidic species before reaction [27]. The bands for oxidic species disappeared upon contact with methane at reaction temperature, which lead them to speculate about the formation of Mo (oxy-)carbides. These Mo (oxy-)carbides themselves however cannot be detected by UV Raman, also demonstrating the limitations of this technique to elucidate the exact nature of the active site. Other techniques often used to determine the structure of supported organometallic compounds, like NMR and IR [28] are difficult to apply, since the catalyst experiences severe coking already during the activation period. This means that the carbon signal in <sup>13</sup>C NMR is obscured and absorption of the sample is very high, leading to weak infrared (IR) signals. Additionally, access to some of the active sites could be blocked by coke and therefore renders it inaccessible to probe molecules. As we reported, an active Mo site equivalent to the one forming under MDA conditions can also be formed using a pretreatment of the catalyst in carbon monoxide (CO). This pretreatment leads to a coke-free catalyst, which does not need further activation [22]. Herein, we used this technique to obtain active sites, freely accessible for probe molecules that can be examined by IR. CO IR spectroscopy is used to determine the oxidation state, nuclearity and uniformity of metal cations and to probe the acidity of the zeolite [29-37]. Mo is present in its oxidized form on the as-synthesized catalyst and does not adsorb CO. The more reduced a Mo species is, generally, the lower the vibrational frequency of the CO adsorbed on the Mo species [35, 38]. Information about the nuclearity of metal species can also be obtained from the full width at half maximum (FWHM) of the absorbance band [36, 37]. The broader the band, the bigger the Mo cluster, because a

bigger cluster offers many slightly different adsorption sites leading to broadening of the CO vibrational absorption band. Although not yet applied for Mo, DFT calculations can be used to calculate CO vibrational frequencies for CO adsorbed on proposed structures [39]. Comparing the experimental results with calculated values helps determine which structures are present on the catalyst. Mostly oxycarbodic structures were considered as we previously found that a considerable amount of oxygen remained at the active site during activation, accounting for an average O/Mo ratio of 1, while an average C/Mo ratio of 0.9 was found [22]. We however also considered  $\text{Mo}_4\text{C}_3$  (structure 17, **Figure A5.8**) as a structure without oxygen to be able to draw a comparison with previous DFT calculations of the methane dehydroaromatization activity over  $\text{Mo}_x\text{C}_y$  structures [18, 19]. The samples activated in CO can also be investigated by  $^{13}\text{C}$  MAS NMR to understand the chemical interaction of carbodic carbon with Mo and therefore the structure of the active site. Aside from the chemical shift itself, the anisotropy of the observed resonances can reveal the uniformity and nuclearity of the contribution.  $^{13}\text{C}$  MAS NMR, however, yields low intensity for the carbon of the Mo (oxy-)carbodic structures, because of the low amount of carbon present [22]. Dynamic nuclear polarization surface enhanced NMR spectroscopy (DNP SENS) measurements of the  $^{13}\text{C}$  chemical shift give a much enhanced signal and better resolution [40-45]. The samples are impregnated with a solution containing a stable free radical (usually bi-nitroxides), which allows transfer of polarization from its unpaired electrons to surrounding protons from either the solvent or the sample. Through cross-polarization and spin diffusion this polarization is then transferred to the nuclei of interest, in this case  $^{13}\text{C}$  [46]. To allow for the polarization to be transferred from  $^1\text{H}$  to  $^{13}\text{C}$ , the two nuclei need to be in close contact. This way information can be gained from about the proximity of protons from the Brønsted acid site (BAS) to the Mo (oxy-)carbides. If the acidic protons are not close enough to the Mo (oxy-)carbides, the polarization can be transferred through the solvent, which is also able to diffuse into the pores of the zeolite. Because the spin can diffuse via the solvent, the radical can in principle be further away from  $^{13}\text{C}$ . TEKPol, which is the radical used in this work does not fit inside of the pores of the zeolite, which is a fact that can be exploited to distinguish between Mo (oxy-)carbides on the outer surface of the zeolite and inside the pores of the zeolite [47].

In the MDA process three phases are distinguished: (i) the activation period in which Mo carburizes and reduces to its active phase on which methane can be transformed to the intermediates of the reaction, (ii) the induction period, in which the benzene production slowly reaches its maximum rate, and (iii) the reaction/deactivation period of the reaction [13]. Both phase (i) and (ii) need to be completed for the catalyst to reach full activity. In this work, the described techniques are not only used to understand which structures form during the activation period, in which the active sites are formed, but are also employed to better understand the induction period. The induction period was previously ascribed to a hydrocarbon pool formation [13], but it could also be due to a further transformation of the Mo active site. Given that  $^{13}\text{C}$  NMR and especially DNP SENS are very sensitive to the different carbidic structures in the zeolite and their carburization degree, this technique can be applied to probe the active Mo sites during different phases of the reaction. Instead of using a continuous stream of methane, samples are prepared by a pulsed reaction technique where pulses of methane are injected into a continuous flow of carrier gas. This leads to a high time resolution and good quantification [7, 13, 22].

## 5.2 Experimental Details

**Mo** was introduced to the ammonium form of a commercial ZSM-5 zeolite (Südchemie) with Si/Al = 13 or a silicalite-1 zeolite (synthesis details below) through incipient wetness impregnation (IWI) dissolving appropriate amounts of ammonium heptamolybdate (AHM) in a volume of water needed to fill the pores of the zeolite powder (210 µl/g). The samples were dried overnight at 80 °C and calcined at 550 °C for 7 h using a heating rate of 2 °C/min. Samples are denoted as **yMo-x**, where **y** denotes the wt.% of Mo introduced and **x** the pre-treatment. Catalysts were prepared with 1, 2 and 5 wt.% of Mo.

**Silicalite-1** was synthesized mixing 25.6 g TPAOH with 30.0 g distilled water, after which 36.9 g TEOS was added dropwise to the solution. The obtained mixture is aged at room temperature overnight. Afterwards the mixture was transferred into autoclaves to perform further crystallization at 150 °C for 10 days. After cooling down, the product was collected by filtration and washing, and dried in air overnight. The dried product was calcined at 550 °C for 5 h (2 °C/min) to remove the template [48].

**CO carburization** was performed in a custom-made setup, where a 30 ml/min flow of 2.5 % CO in He was continuously fed to the reactor containing 300 mg catalyst, that had been pelletized and sieved to 212 to 425 µm particles. The reactor consists of a quartz tube with an inner diameter of 6 mm. A heating rate of 10 °C/min to 800 °C (if not otherwise stated) was applied and the reactor was kept at the final temperature for 1 h. Samples subjected to this treatment are denoted as **yMo-CO**.

**H<sub>2</sub> treatment** was performed in the same setup and under the same conditions as CO carburization, but with a 30 ml/min flow of 5 % H<sub>2</sub> in He.

**CH<sub>4</sub> pulsing experiments** were performed in a custom made setup described previously [13]. A catalyst mass of 300 mg was pelletized and sieved to 212 to 425 µm particles and filled in a quartz tube with a 4 mm inner diameter. It was equipped with an injection loop in the feed line kept at atmospheric pressure, injecting 223 µmol every 200 s into a 30 ml/min flow of He by switching a multi-position valve to the reactor. The catalyst bed was heated to 700 °C under a 30 ml/min flow of He. Once the temperature was reached the first pulse was injected. Samples subjected to CH<sub>4</sub> pulsing are denoted as **yMo-zCH<sub>4</sub>** where **z** stands for the number of pulses applied.

**Fourier transformed infrared spectroscopy** (FT-IR) of the vibrations of CO adsorbed on the catalyst was measured in a custom-made stainless-steel cell with CaF<sub>2</sub> windows that could be sealed airtight inside the glovebox. Spectra were measured with the addition of 128 scans in transmission mode using a Nicolet FT-IR spectrometer equipped with a cryogenic MCT detector. Samples were transferred from either the CO pre-treatment setup, the CH<sub>4</sub> pulsing setup or the H<sub>2</sub> pre-treatment setup to the glovebox without exposure to the ambient atmosphere. Pre-treated samples were pressed undiluted into pellets with 10 mm diameter inside the glovebox and loaded into the IR cell. The sealed cell was then transferred to the spectrometer evacuated and cooled to -167 °C with liquid N<sub>2</sub> before introducing 250 µl CO pulses. The pulsing sequence for CO consisted of 6 pulses keeping the injection loop at 100 mbar, 3 pulses at 200 mbar and another 11 pulses at 1 bar. One sample with 2 wt.% Mo loading was not reduced but instead dried at 450 °C in the infrared cell under dynamic vacuum for 16 h and denoted **2Mo**. All spectra were normalized by the framework vibration intensity at 1876 cm<sup>-1</sup>.

**Dynamic Nuclear Polarization surface enhanced NMR spectroscopy** (DNP SENS) sample preparation: 3.65 mg of the radical TEKPol was first dissolved in 20 µl of 1,1,2,2-tetrachloroethylene (TCE) and then mixed well with about 20 mg of the sample inside an Ar glovebox. The impregnated samples were packed into 3.2 mm o.d. sapphire rotors capped with a Teflon plug inside the glovebox and measured the same day. Spectra were acquired using 263 GHz/400 MHz Avance III Bruker DNP solid-state NMR spectrometer ( $\nu_L(^{13}C)$  = 100.6 MHz) equipped with a 3.2 mm Bruker triple resonance low temperature magic angle spinning (LTMAS) probe. The experiments were performed at ~-173 °C with a 263 GHz gyrotron. The sweep coil of the main magnetic field was set for the microwave irradiation occurring at the <sup>1</sup>H positive enhancement maximum of the TEKPol biradical. The <sup>13</sup>C NMR experiments the acquisition parameters used are 20 s repetition delay to allow complete relaxation, a <sup>1</sup>H π/2 pulse length of 2.5 µs to afford 100 kHz <sup>1</sup>H decoupling using the SPINAL 64 decoupling method. A contact time between <sup>1</sup>H and <sup>13</sup>C was set to 8 ms. 5,000-15,000 scans were performed, the MAS frequency varied between 8 and 10 kHz. All <sup>13</sup>C NMR spectra were referenced to adamantane with the higher frequency peak set to 38.48 ppm with respect to TMS (0 ppm). DNP enhancements

factors ( $\varepsilon_H$ ) of the TCE solvent were determined by comparing the integration of the resonance of interest for the spectra acquired with and without microwave irradiation.  $^{13}\text{C}$  spin lattice relaxation times were measured using a saturation recovery experiment. Data are fitted using either a stretched-exponential (**Equation 5.1**) or a mono-exponential (**Equation 5.2**) with  $A$  being the equilibrium signal intensity when microwave irradiation is used,  $S(\tau)$  the integrated intensity at recycle delay time  $\tau$ ,  $\beta$  being the stretching parameter and  $T_1^*$  the build-up time.

$$S(\tau) = A \left[ 1 - \exp \left( -\left( \frac{\tau}{T_1^*} \right)^\beta \right) \right] \quad (\text{Equation 5.1})$$

$$S(\tau) = A \left[ 1 - \exp \left( -\frac{\tau}{T_1^*} \right) \right] \quad (\text{Equation 5.2})$$

For  $^{13}\text{C}$  NMR spectroscopy samples were prepared as described in section **CH<sub>4</sub> pulsing experiments** using  $^{13}\text{CH}_4$  and transferred from the setup to the glovebox without exposure to the atmosphere. A known amount of sample was filled into zirconia rotors inside the glovebox and tightly closed. 1D  $^{13}\text{C}$  MAS NMR spectra were recorded on a Bruker AVANCE III spectrometer operating at resonance frequencies of 100 MHz, and using a conventional double resonance 4 mm CPMAS probe. The spinning frequency was set to 15 kHz. NMR chemical shifts are reported with respect to TMS as the external reference. Spectra were recorded by a spin echo pulse sequence (pulse length 3.4  $\mu\text{s}$ ) with four-phase alternation synchronized with the spinning rate for the MAS experiments. The interscan delay was set to 30 s to allow the complete relaxation, and 5,000-30,000 scans were performed. An apodization function (exponential) corresponding to a line broadening of 80 Hz was applied prior to the Fourier transformation.

**Periodic DFT calculations** were performed to determine the vibrational frequencies of Mo clusters in different speciation and oxidation state (between +2 and +6). For this purpose extra-framework  $[\text{Mo}_x\text{O}_y\text{C}_z]^{2+}$  ( $x = 1, 2$  or 4) clusters were constructed in the ZSM-5 zeolite framework as counter-ion for two framework Al ions positioned in the six-membered ring located at the intersection of straight and zigzag channels, previously referred to as  $\delta$ -site (see **Figure A5.7**) [49]. This site was chosen as an open site allowing for anchoring of Mo species of different sizes and also leading to high symmetry of a pair of framework Al. Gao *et al.* calculated the Raman frequency for a monomeric oxide structure in this location and confirmed that it falls within the range observed experimentally [27]. The resulting ZSM-5 model

had a Si/Al ratio of 47. On the clusters one and two CO molecules were placed and their geometry optimized. All spin polarized DFT calculations were performed by using the Vienna Ab initio Simulation Package (VASP, version 5.3.5) [50-54]. The PBE functional based on the generalized gradient approximation was chosen to account for the exchange–correlation energy [55]. A plane-wave basis set in combination with the projector augmented wave (PAW) method was used to describe the valence electrons and the valence–core interactions, respectively [56, 57]. The kinetic energy cut-off of the plane wave basis set was set to 450 eV. A Gaussian smearing of the population of partial occupancies with a width of 0.05 eV was used during iterative diagonalization of the Kohn-Sham Hamiltonian. Considering the large unit cell, Brillouin zone-sampling was restricted to the  $\Gamma$  point [58]. Geometry optimizations were assumed to have converged when forces on each atom were less than 0.04 eV/Å. The Van der Waals (vdW) interactions were included by using Grimme's DFT-D3(BJ) method as implemented in VASP [59]. Geometry optimization was completed for all possible spin states for the given oxidation state which was followed by frequency analysis on the most stable spin state. Vibrational frequencies were calculated by determining the second derivatives of the Hessian matrix using the density functional perturbation theory as implemented in VASP 5.3.5. To decrease the computation costs only the CO molecules were considered in the analysis. The computed frequencies were corrected according to the following **Equation 5.3**.

$$\frac{\nu_{exp}(CO)}{\nu_{calc}(CO)} = \frac{\nu_{normalized(CO_{ads})}}{\nu_{calc}(CO_{ads})} = 1.009 \quad (\text{Equation 5.3})$$

where  $\nu_{exp}(CO)$  is the experimentally measured frequency of the gas-phase CO ( $2143\text{ cm}^{-1}$ ),  $\nu_{calc}(CO)$  is the calculated vibrational frequency ( $2124\text{ cm}^{-1}$ ),  $\nu_{calc}(CO_{ads})$  is the calculated C-O vibrational frequency of the adsorbed CO molecule and  $\nu_{normalised(CO_{ads})}$  is the corrected vibrational frequency of the adsorbed CO molecule. The difference between  $\nu_{calc}(CO)$  and  $\nu_{exp}(CO)$  is about  $19\text{ cm}^{-1}$  and provides an estimate of the expected error for the calculated frequencies. Partial charges were calculated with the atoms in molecules (AIMS) method. The program was developed by the Henkelman Group [60-63]. The orthogonal MFI unit cell with lattice parameters of  $a = 20.241$ ,  $b = 20.015$  and  $c = 13.439\text{ \AA}$  as optimized by DFT with an all-silica MFI periodic model was used for all calculations.

The optimized unit cell parameters agree well with experimental data for calcined ZSM-5.

### 5.3 Results

#### 5.3.1 CO IR

Using a CO pretreatment the active phase of Mo was created avoiding any carbonaceous deposits, which surround the active after activation under methane. The absence of those deposits allows probe molecules to absorb on the active site. CO vibrations were probed after adsorption on fresh samples as well as samples reduced in CO **Figure 5.1** (see **Figure A5.1** for full spectra). The CO activated sample shows several distinct vibrations (**Figure 5.1b**), while only the vibrations characteristic of the zeolite are observed on the fresh sample, **2Mo** (**Figure 5.1a**) namely CO adsorbed on Brønsted acid sites ( $2173\text{ cm}^{-1}$ , BAS) with a shoulder at  $2164\text{ cm}^{-1}$  which is assigned to Al-OH [64] or silanols [65] as well as a band at  $2138\text{ cm}^{-1}$  characteristic of physisorbed CO [66]. A slight decrease in acidity is observed on the CO treated sample as well, likely due to dehydration/dehydrogenation occurring at the high temperature of the activation [67-69].

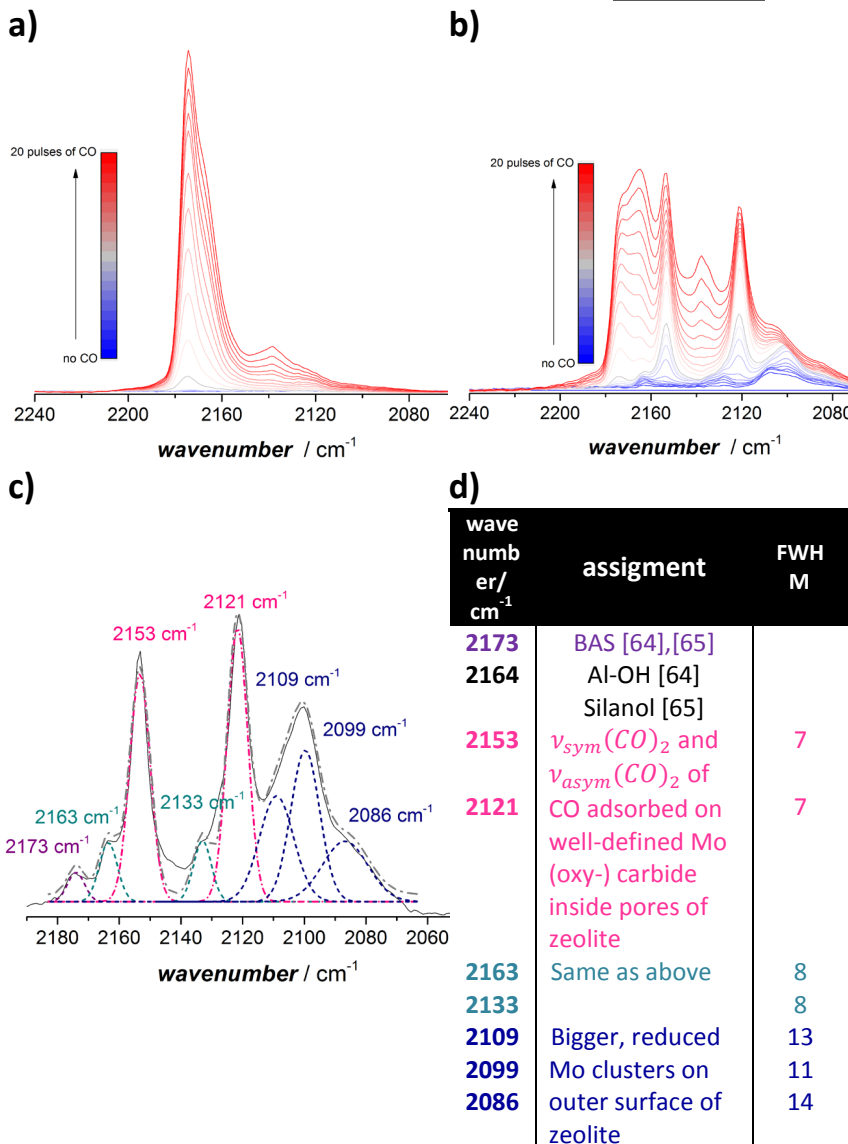


Figure 5.1. a) IR-spectra of the CO vibrations after consecutive pulsing of CO to **2Mo**. b) after consecutive pulsing of CO to **5Mo-CO**. c) Gaussian deconvolution of the spectrum taken after introducing 9 pulses of CO to **5Mo-CO**. A spectrum was taken after each pulse of CO sent to the evacuated IR cell kept at -167 °C. A total of 20 pulses was sent to the cell in a sequence described in the experimental part. The pre-treated samples were transferred to the IR cell without exposure to the atmosphere. d) Summary of all observed vibrations with assignment, references, and FWHM.

The same vibrations of CO can be observed on a sample activated in methane confirming that similar Mo species are forming with both pre-treatments (**Figure A5.1**). The absorbances however are slightly lower, maybe due to some carbonaceous deposits formed during activation in methane blocking access to the active site. More information about the different Mo sites observed can be gained from deconvolution of the vibrational spectrum as shown in **Figure 5.1c** with spectra collected at low CO coverage on **5Mo-CO**. The two pink bands ( $2121$  and  $2153\text{ cm}^{-1}$ ) and the two turquoise bands ( $2133$  and  $2163\text{ cm}^{-1}$ ), respectively, grow simultaneously with the same rate. This is demonstrated in **Figure A5.3**, which shows the intensities of each vibrational contribution plotted against the number of pulses of CO introduced to the sample. Because the intensity of the two turquoise and the two pink bands grow simultaneously, each of these pairs likely corresponds to two CO molecules adsorbed as dicarbonyls on the same Mo site. This is further supported by the fact that they are separated by  $\Delta\sigma = 33\text{ cm}^{-1}$ , a separation distance for dicarbonyl absorbances observed elsewhere [70]. The four dicarbonyl bands are rather narrow with a full width at half maximum (FWHM) of  $7$  and  $8\text{ cm}^{-1}$ . Another broad absorbance is observed at around  $2100\text{ cm}^{-1}$  and seems to comprise three rather broad contributions with a FWHM ranging between  $11$  and  $14\text{ cm}^{-1}$ . **Figure A5.4** shows the spectrum of CO adsorbed on **2Mo/silicalite-1** treated in CO. Only two broad absorbances between  $2080$  and  $2100\text{ cm}^{-1}$  are observed apart from the vibrations corresponding to the silicalite-1 support.

### 5.3.2 DFT calculation of CO vibrations

DFT calculations were performed to gain more insight into the nature of the Mo species giving rise to the CO vibrations observed experimentally. 18 different possible mono-, di- and tetrameric (oxy-)carbide structures were proposed and the vibrational frequencies of CO adsorbed on those structures calculated. Both the adsorption of one CO on one structure as well as two CO molecules on one structure was explored. When a second carbonyl is adsorbed, two new vibrations arise as the vibrations of the two CO molecules are coupled to a symmetric and an antisymmetric stretching vibration. This is the case both for monomeric and dimeric Mo-structures. When relating the wavenumber of the CO vibration and the nuclearity of the species no clear trend can be observed. Instead the wavenumber seems to increase with the partial charge of molybdenum

(Figure 5.2 and Figure A5.5). Wavenumbers of both adsorbed single carbonyls (Figure A5.5) as well as dicarbonyls (Figure 5.2) follow a linear trend with the partial charge. The separation between the dicarbonyl vibrations  $\Delta\sigma$  is inversely proportional to the partial charge for the monomers and dimers (Figure 5.2).

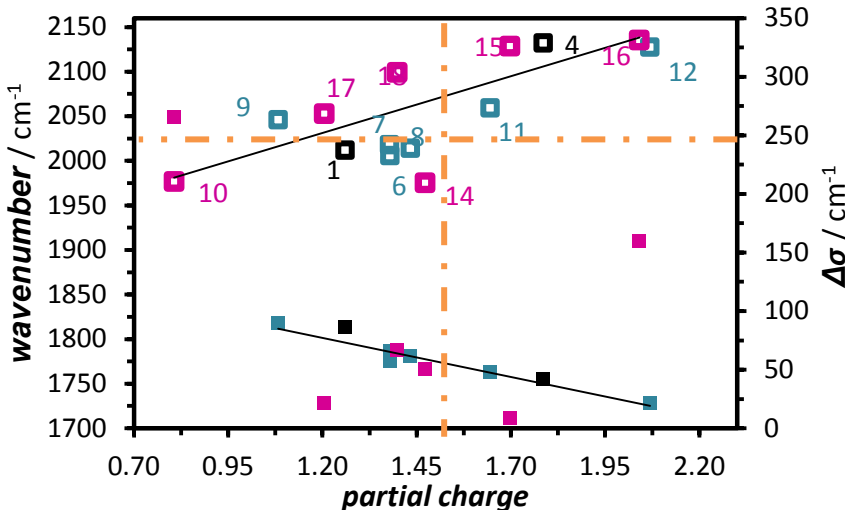


Figure 5.2. Vibrational wavenumbers of the symmetric stretching of the dicarbonyls (open symbols) and separation  $\Delta\sigma$  between the two contributions (filled symbols) as calculated by DFT plotted against partial charge. Colors key: pink: tetramers, turquoise: dimers, black: monomers. The horizontal orange line indicates the lowest wavenumber observed experimentally, while the vertical line represents the lower limit regarding partial charge. Thus all points above and to the right of the orange lines could be possible candidates of Mo structures present on the investigated samples based on this analysis. Corresponding structures are shown in Figure A5.9.

The same trend can in principle be observed for the tetramers, but the calculations for the tetramers corresponding to structure 10 and 16 (Figure A5.8), yielded very high values of  $\Delta\sigma$ , which is due to the fact that the four Mo of the tetramer have a different electronic structure. The range of wavenumbers observed ( $\sim 2060$  to  $\sim 2170$  cm $^{-1}$ ) corresponds to a partial charge between 1.5 and 2.4.

Finally this information can be used to find the formal oxidation state corresponding to the experimentally observed wavenumbers, because the partial charge of molybdenum is proportional to the formal oxidation state (Figure A5.6). From this correlation, it can be concluded that Mo has a formal oxidation state of Mo between 4+ and 6+. For a given formal

oxidation state however, the partial charge for structures containing carbon is generally lower than for structures without carbon. This is, because the formal oxidation state of carbon is -4 and for oxygen only -2, while oxygen is much more electronegative, meaning that the partial charge remains almost the same when replacing oxygen by carbon in a given structure (compare structure 6 and 8 in **Figure A5.8**). This illustrates well that the partial charge is a better descriptor compared to formal oxidation state, when one wants to correlate the charge of a metal species with the vibrational frequency of CO adsorbed on that metal species.

### 5.3.3 $^{13}\text{C}$ MAS NMR

$^{13}\text{C}$  NMR spectra collected after sending several 233  $\mu\text{mol}$  pulses of  $^{13}\text{CH}_4$  to **5Mo** during the induction period are presented in **Figure 5.3b** and **A5.14**. **Figure 5.3a** and **Figure A5.11** show the MS readouts during pulsing. During the first 14 pulses of methane sent to the catalyst, no benzene formation is observed, marking the 'activation period'. After the activation of Mo is completed, benzene starts to be produced and the rate of formation slowly increases until it reaches its steady state value at around pulse 35. This gradual increase represents the 'induction period' and was previously attributed to an accumulation of catalytically active polyaromatic coke that acts as a hydrocarbon pool [13]. The first  $^{13}\text{C}$  MAS NMR spectrum was collected right before the onset of benzene production after Mo activation was completed (**Figure 5.3b**). The same three Mo (oxy-)carbide contributions as previously observed on the **5Mo** pretreated in CO [22] can be observed on this sample activated under MDA conditions. Two broader contributions at 360 ppm and 306 ppm were attributed to well-defined mono- or dimeric Mo (oxy-)carbide species inside the pores of the zeolite and a third contribution at 270 ppm to bigger  $\text{Mo}_2\text{C}$  nanoparticles on the outer surface of the zeolite.

In addition to the signatures of the Mo (oxy-)carbides, another resonance corresponding to polyaromatic carbon is observed at 121 ppm [13, 71-75]. This polyaromatic carbon already forms while Mo is still being activated.

After 3, 9 and 20 more pulses, the resonances corresponding to Mo (oxy-)carbides do not change further. Instead accumulation of more polyaromatic carbon on the catalyst is observed. The relative amount of polyaromatic carbon on the samples taken after an increasing number of  $\text{CH}_4$  pulses was determined by deconvolution (see **Figure A5.14** for an example deconvolution of the spectra shown in **Figure 5.3b**) of the  $^{13}\text{C}$  NMR spectra and is plotted together with the MS readouts at  $m/z = 84$  in **Figure 5.3a**. Interestingly, polyaromatic carbon accumulates inside the pores of the zeolite at the same rate as benzene production goes up.

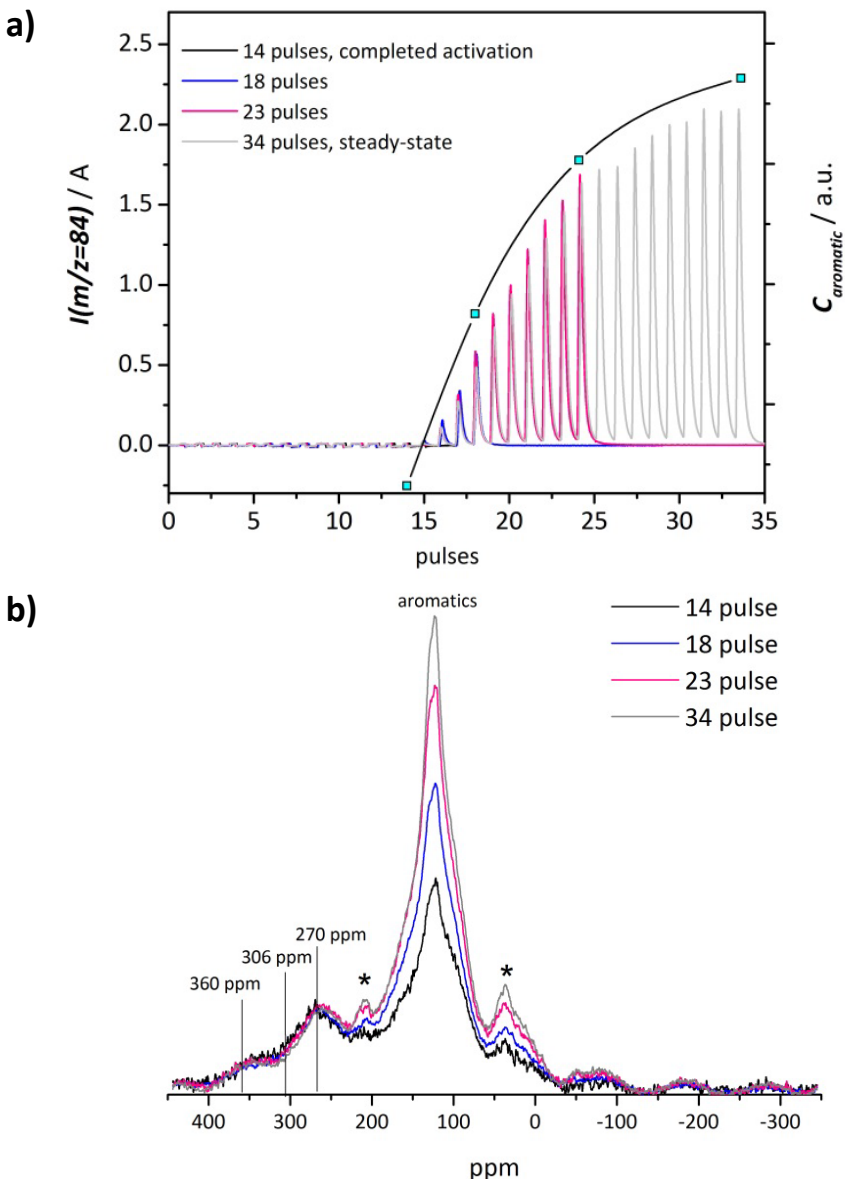


Figure 5.3. a) *left axis*: MS readout for  $C_6H_6$  ( $m/z = 84$ ) during consecutive pulsing of 233  $\mu\text{mol}$  of  $^{13}\text{CH}_4$  at 700  $^\circ\text{C}$  into a continuous flow 30 ml/min He over 300 mg of **5Mo**. *Right axis*: polyaromatic carbon content obtained from deconvolution of  $^{13}\text{C}$  MAS NMR spectra (Figure A5.14) plotted in b). b)  $^{13}\text{C}$  NMR spectra measured on the samples prepared by the pulsing experiments depicted in a). A fresh **5Mo** sample was subjected to 14, 18, 23 and 34 pulses sealed and transferred to NMR rotors without exposure to the atmosphere. Asterisks denote spinning side-bands.

### 5.3.4 DNP SENS

DNP spectra shown in **Figure 5.4** show that well-separated peaks can be resolved for Mo (oxy-)carbides, while these contributions shown in our previous publication [22] (reproduced in **Figure A5.13**) and in **Figure 5.3b** are rather broad and were only visible after collecting many scans. For the lowest loading of Mo, **1Mo-<sup>13</sup>CO** two peaks can clearly be observed at 360 and 306 ppm, where with <sup>13</sup>C NMR only one broad resonance was observed in that region (**Figure A5.13**). These resonances are assigned to well-defined species inside the pores of the zeolite [22]. Very good enhancement of  $\varepsilon_H = 90 \pm 4$  and  $105 \pm 5$  were observed in proton experiments using TCE for the low loading Mo samples, **1Mo-<sup>13</sup>CO** and **2Mo-<sup>13</sup>CO**, respectively (**Figure A5.15**). For the high loading, **5Mo-<sup>13</sup>CO** however no enhancement could be observed initially, instead the signal for the decomposed radical was observed (**Figure A5.16**) [45]. On this sample several bigger nanoparticles are present on the outer surface of the zeolite and therefore Mo is in direct contact with the radical, while for **1Mo-<sup>13</sup>CO** and **2Mo-<sup>13</sup>CO**, Mo is shielded from the radical inside the pores of the zeolite. TEKPol with  $d_{molecule} \sim 2 \text{ nm}$  is too big to penetrate the pores with  $d_{pore} \sim 0.6 \text{ nm}$  [45]. TEKPol can decompose when in direct contact with an organometallic complex immobilized on silica [45], so it is concluded that the bigger nanoparticles on the outer surface of **5Mo-<sup>13</sup>CO** fully decompose TEKPol.

After impregnating the sample a second time with the radical solution an enhancement of  $\varepsilon_H = 32 \pm 3$  was observed for **5Mo-<sup>13</sup>CO**. It is important to note that the spectra measured after the second impregnation with TEKPol (**Figure 5.4c**) still did not show the resonance corresponding to Mo<sub>2</sub>C nanoparticles at 270 ppm observed in **Figure 5.3**, because the decomposed TEKPol that is still in close proximity to the Mo<sub>2</sub>C sites has a paramagnetic character and renders the carbon next to it NMR invisible.

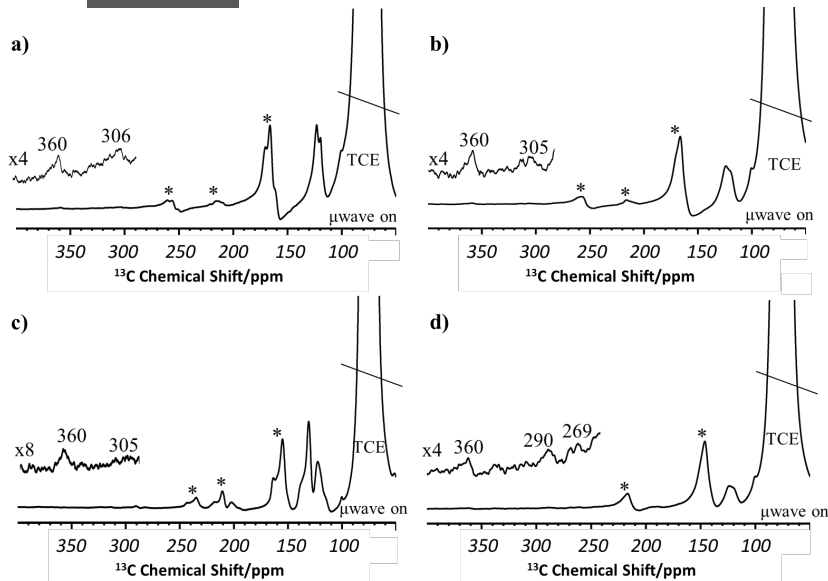


Figure 5.4. DNP SENS  $^{13}\text{C}$  MAS NMR spectra of a)  $\mathbf{1\text{Mo}-}^{13}\text{CO}$  b)  $\mathbf{2\text{Mo}-}^{13}\text{CO}$  c)  $\mathbf{5\text{Mo}-}^{13}\text{CO}$  after a second impregnation with TEKPol d)  $\mathbf{5\text{Mo-18}^{13}\text{CH}_4}$ . a) to c) were measured at a MAS frequency of 9 kHz, while d) was measured at 8 kHz. The measurement was performed at different rotation speeds to identify spinning side bands, which are indicated by the asterisks.  $\mathbf{1\text{Mo}-}^{13}\text{CO}$  measured at 8 kHz can be found in **Figure A5.17** for comparison.

When impregnating the sample  $\mathbf{5\text{Mo-18}^{13}\text{CH}_4}$  carburized by 18 pulses of  $^{13}\text{CH}_4$  (the same sample used for the  $^{13}\text{C}$  NMR measurements shown in **Figure 5.3** with the TEKPol solution) an enhancement of  $\varepsilon_{\text{H}} = 43 \pm 3$  can be observed immediately upon the first exposure to TEKPol (**Figure A5.18**) and only weak signals for degraded TEKPol are observed. At the same time **Figure 5.4d** shows that the contribution for bigger  $\text{Mo}_2\text{C}$  nanoparticles at 269 ppm can be observed.

## 5.4 Discussion

The active sites of Mo/HZSM-5 form during an initial period of the MDA reaction coined 'activation period', where no desired products are formed yet and where coking is concurring together with the transformation of Mo to its active phase. Similar Mo species are forming on a catalyst treated in CO and one that was activated in methane confirmed by the fact that the same CO vibrations and the same  $^{13}\text{C}$  NMR and DNP SENS resonances are observed for the two treatments.

While it has been proposed in literature that Mo forms (oxy-)carbidic species at reaction conditions and that some Mo stays anchored inside the pores of the zeolite while some Mo is present as bigger clusters and nanoparticles on the outer surface of the zeolite crystal, here we provide direct spectroscopic evidence showing distinct contributions that can be assigned to two different kinds of species inside the pores of the zeolite as well as the previously proposed nanoparticles on the outer surface of the zeolite. This is demonstrated using CO IR together with computational modeling as well as  $^{13}\text{C}$  NMR and DNP SENS.

The vibrations of the CO probe molecule adsorbed on the activated samples are very sensitive to the electronic structure of Mo [38] and the FWHM of the observed vibrations can give information about the nuclearity of the adsorption site [36]. The various distinct CO vibrations observed on the pretreated Mo/HZSM-5 samples, allow us to distinguish between the different activated Mo species. The narrow FWHM of the dicarbonyl species is indicative for presence of two types of sites with very similar geometry, which only contain a few atoms, previously coined 'well-defined' species [36, 37]. Such small species are created inside the pores of the zeolite through anchoring to the Al of the framework. Previous studies [13, 76, 77] suggest that these are mono- and dimeric (oxy-)carbide species. The contributions of these well-defined species are not observed when the zeolite support used does not contain any framework Al for anchoring the Mo, as is the case for **2Mo/silicalite-1** treated in CO (**Figure A5.4**) [22]. The two types of well-defined species are also observed with  $^{13}\text{C}$  NMR and DNP SENS. While three contribution could already be seen by deconvolution of the  $^{13}\text{C}$  NMR signal, the enhancement of the signal with DNP SENS enabled resolving three distinct and separated resonances.

A third species observed in all three characterization techniques is assigned to bigger Mo nanoparticles, because it

leads to a broad contribution in the CO IR, typical for a site that allows the CO to adsorb on many slightly different locations of the nanoparticle with similar electronic structure. At the same time it leads to a rather narrow resonance in  $^{13}\text{C}$  NMR, also indicative of nanoparticles. These nanoparticles were observed earlier by HR-TEM on an equivalent catalyst by Kosinov *et al.* [13]. They suggested that these nanoparticles are mainly present on the outer surface of the zeolite, since a nanoparticle of Mo should not form inside the pores of the zeolite, because of size and because it is more likely to form coordinated structures in proximity to BAS. They don't directly exclude however that some smaller nanoparticles are located inside the pores of the zeolite.

In this regard, DNP SENS proved to be a very useful technique to clearly distinguish between (oxy-)carbidic Mo located on the outer surface of the zeolite and inside the pores. The DNP SENS measurements presented here confirm that the  $\text{Mo}_2\text{C}$  nanoparticles are indeed only located at the outer surface of the zeolite particles. The biradical TEKPol decomposes, because it is in direct contact with the  $\text{Mo}_2\text{C}$  nanoparticles and TEKPol is too large to penetrate the pores. Thus the nanoparticles have to be on the outer surface. The resonance corresponding to  $\text{Mo}_2\text{C}$  also disappears, because TEKPol becomes paramagnetic when it decomposes and effectively makes carbon close by undetectable by NMR, which further confirms that the  $\text{Mo}_2\text{C}$  nanoparticles must be located close to TEKPol and thus on the outer surface of the zeolite crystals. In line with this, for the sample activated with 18 pulses of methane, **5Mo-18 $^{13}\text{CH}_4$** , the deposited aromatic carbon shields the bigger nanoparticles avoiding the decomposition of TEKPol and allowing for the resonance of  $\text{Mo}_2\text{C}$  nanoparticles to be observed.

It was speculated that different kinds of Mo sites are present on Mo/HZSM-5 after activation, while it was not known how many different sites exist. With our findings, we were able to determine that (at least) three different (oxy-)carbidic species exist on Mo/HZSM-5 after activation. Knowledge about the exact number of different types of Mo sites provides a good starting point to assign different activity to those sites. Comparing DNP SENS measurements of samples prepared with  $\text{CH}_4$  and coke-free samples prepared with CO confirm that the aromatic carbon mostly is associated with bigger  $\text{Mo}_2\text{C}$  nanoparticles on the outer surface of the zeolite, which is indication that these nanoparticles are the cause of deactivation through a kind of fouling.

As the mono- and dimeric species inside the pores of the zeolite seem to be most active for conversion of methane to valuable aromatics, we further elucidated the nature of these Mo sites using DFT calculations. Although for nanoparticles it was suggested that the wavenumber of CO generally decreases with higher Mo oxidation state, for well-defined, mono- or dimeric transition metal sites in zeolites and especially for Mo little information is available. We find a linear relationship between the observed CO vibrational wavenumber and the partial charge of Mo for well-defined sites. This partial charge can be translated to the formal Mo oxidation state (**Figures 5.2, A5.5 and A5.6**). For the experimentally observed CO vibrational wavenumbers it can be concluded that the Mo in these active sites has a formal oxidation state between 4+ and 6+. It is emphasized that simply reduced structures that do not contain any carbon can be excluded as active sites, because a sample reduced in H<sub>2</sub> does not give rise to any of the vibrations observed on the samples treated in CH<sub>4</sub> or CO (**Figure A5.9**). This H<sub>2</sub> treated sample also exhibited lower benzene yields during MDA as was shown in our previous publication [22] and the EXAFS of that sample does not match with the spectra measured on the samples treated in CO or CH<sub>4</sub> (**Figure A5.10**). Furthermore, it should be noted that the structures highlighted in **Figure 5.2** mostly contain only oxygen, but given that many (oxy-)carbidic structure calculated CO frequencies were close to the ones observed experimentally, we cannot exclude structures with similar partial charges that contain carbon. This especially in comparison to the <sup>13</sup>C NMR results and what has been proposed previously [8, 23, 24, 27, 78-80]. The choice of structures was, however, sufficient to achieve our goal of determining a formal Mo oxidation state, but we cannot claim to have exhausted all configurational possibilities.

With more information about the exact nature of the active site after completion of the activation at hand, we wanted to investigate the impact of Mo speciation on the induction period occurring right after completion of the activation period. During this period benzene formation slowly increases to its maximum. The species observed with <sup>13</sup>C MAS NMR did not transform further during this period, so no further evolution and activation of the Mo sites takes place in the induction period. Instead the build-up of (poly-)aromatic carbon on the sample follows the same trend as the increase in benzene formation rate

(Figure 5.3), suggesting that the build-up of a hydrocarbon pool [13, 81] is necessary for the catalyst to achieve maximum activity, while not leading to deactivation yet.

It has been speculated that Mo agglomerates at reaction conditions [27], our results however suggest that this agglomeration occurs later on in the process after the induction period. Figure 5.3 clearly indicates that no significant agglomeration occurs during the induction period, since the resonances corresponding to Mo (oxy-)carbide do not transform further during induction. This is also supported by CO IR. There is no change in wavenumber of the CO vibrations for a sample that has seen 5 or 10 pulses of CH<sub>4</sub> (Figure A5.12). The agglomeration of Mo might even be the cause of deactivation. The fact that the nanoparticles seem to be cause for deactivation is supported by our DNP SENS measurements, where we find that the aromatic carbon surrounds the bigger Mo<sub>2</sub>C nanoparticles (fouling) on the outer surface of the zeolite. This is concluded, because no TEKPol decomposition is observed on a sample containing aromatic carbon.

## 5.5 Conclusions

A quasi-*in situ* strategy is presented to directly probe the different types of Mo sites on the methane dehydroaromatization catalyst, Mo/HZSM-5, after activation. CO IR, <sup>13</sup>C NMR as well as DNP SENS combined with theory were used to find the nuclearity, charge and stoichiometry of the three different types of Mo sites observed. A coke-free active site was obtained using a CO pretreatment leading to very clear spectra. We provide direct spectroscopic evidence showing distinct contributions that can be assigned to two different kinds of species inside the pores of the zeolite as well as nanoparticles on the outer surface of the zeolite. The latter contribute to the deactivation of the catalyst by coke deposition.

For the observed Mo species an oxidation state between 4+ and 6+ was determined. The (oxy-)carbidic Mo species do not transform further during the induction period, but instead the build-up of a hydrocarbon pool is necessary for the catalyst to achieve maximum activity.

## 5.6 References

- [1] M. Bender, Global Aromatics Supply - Today and Tomorrow, in: New Technologies and Alternative Feedstocks in Petrochemistry and Refining DGMK Conference, Dresden, Germany, 2013.
- [2] N.E.T. Laboratory, An introduction to the science and energy potential of a unique resource, in: U.D.o. Energy (Ed.), US Department of Energy, US, 2011.
- [3] O. Bragin, T. Vasina, Y.I. Isakov, B. Nefedov, A. Preobrazhenskii, N. Palishkina, K.M. Minachev, Catalytic aromatization of methane and ethane, Russian Chemical Bulletin, 31 (1982) 847-847.
- [4] L. Wang, L. Tao, M. Xie, G. Xu, J. Huang, Y. Xu, Dehydrogenation and aromatization of methane under non-oxidizing conditions, *Catalysis Letters*, 21 (1993) 35-41.
- [5] C. Copéret, M. Chabanas, R. Petroff Saint-Arroman, J.-M. Basset, Homogeneous and Heterogeneous Catalysis: Bridging the Gap through Surface Organometallic Chemistry, *Angewandte Chemie International Edition*, 42 (2003) 156-181.
- [6] M. Nachtegaal, U. Hartfelder, J.A. van Bokhoven, From Spectator Species to Active Site Using X-ray Absorption and Emission Spectroscopy Under Realistic Conditions, in: J. Frenken, I. Groot (Eds.) *Operando Research in Heterogeneous Catalysis*, Springer International Publishing, Cham, 2017, pp. 89-110.
- [7] H. Jiang, L. Wang, W. Cui, Y. Xu, Study on the induction period of methane aromatization over Mo/HZSM-5: partial reduction of Mo species and formation of carbonaceous deposit, *Catalysis Letters*, 57 (1999) 95-102.
- [8] I. Lezcano-González, R. Oord, M. Rovezzi, P. Glatzel, S.W. Botchway, B.M. Weckhuysen, A.M. Beale, Molybdenum Speciation and its Impact on Catalytic Activity during Methane Dehydroaromatization in Zeolite ZSM-5 as Revealed by Operando X-Ray Methods, *Angewandte Chemie International Edition*, 55 (2016) 5215-5219.
- [9] F. Solymosi, A. Szöke, J. Cserényi, Conversion of methane to benzene over Mo<sub>2</sub>C and Mo<sub>2</sub>C/ZSM-5 catalysts, *Catalysis Letters*, 39 (1996) 157-161.
- [10] D. Wang, J. Lunsford, M. Rosynek, Catalytic conversion of methane to benzene over Mo/ZSM-5, *Topics in Catalysis*, 3 (1996) 289-297.
- [11] S. Liu, L. Wang, R. Ohnishi, M. Lchikawa, Bifunctional catalysis of Mo/HZSM-5 in the dehydroaromatization of methane with CO/CO<sub>2</sub> to benzene and naphthalene, *Kinetics and catalysis*, 41 (2000) 132-144.
- [12] W. Ding, S. Li, G. D Meitzner, E. Iglesia, Methane conversion to aromatics on Mo/H-ZSM5: structure of molybdenum species in working catalysts, *The Journal of Physical Chemistry B*, 105 (2001) 506-513.
- [13] N. Kosinov, A.S.G. Wijpkema, E. Uslamin, R. Rohling, F.J.A.G. Coumans, B. Mezari, A. Parastaei, A.S. Poryvaev, M.V. Fedin, E.A. Pidko, E.J.M. Hensen, Confined Carbon Mediating Dehydroaromatization of Methane over Mo/ZSM-5, *Angewandte Chemie*, 57 (2018) 1016-1020.
- [14] B.M. Weckhuysen, M.P. Rosynek, J.H. Lunsford, Characterization of surface carbon formed during the conversion of methane to benzene over Mo/H-ZSM-5 catalysts, *Catalysis Letters*, 52 (1998) 31-36.

- [15] F. Solymosi, A. Erdöhelyi, A. Szöke, Dehydrogenation of methane on supported molybdenum oxides. Formation of benzene from methane, *Catalysis Letters*, 32 (1995) 43-53.
- [16] Y. Xu, L. Lin, Recent advances in methane dehydro-aromatization over transition metal ion-modified zeolite catalysts under non-oxidative conditions, *Applied Catalysis A: General*, 188 (1999) 53-67.
- [17] H. Liu, W. Shen, X. Bao, Y. Xu, Identification of Mo active species for methane dehydro-aromatization over Mo/HZSM-5 catalysts in the absence of oxygen: <sup>1</sup>H MAS NMR and EPR investigations, *Journal of Molecular Catalysis A: Chemical*, 244 (2006) 229-236.
- [18] T.S. Khan, S. Balyan, S. Mishra, K.K. Pant, M.A. Haider, Mechanistic Insights into the Activity of Mo-Carbide Clusters for Methane Dehydrogenation and Carbon–Carbon Coupling Reactions To Form Ethylene in Methane Dehydroaromatization, *The Journal of Physical Chemistry C*, 122 (2018) 11754-11764.
- [19] J. Gao, Y. Zheng, G.B. Fitzgerald, J. de Joannis, Y. Tang, I.E. Wachs, S.G. Podkolzin, Structure of Mo<sub>2</sub>Cx and Mo<sub>4</sub>Cx Molybdenum Carbide Nanoparticles and Their Anchoring Sites on ZSM-5 Zeolites, *The Journal of Physical Chemistry C*, 118 (2014) 4670-4679.
- [20] R.O. Savinelli, S.L. Scott, Wavelet transform EXAFS analysis of mono- and dimolybdate model compounds and a Mo/HZSM-5 dehydroaromatization catalyst, *Physical Chemistry Chemical Physics*, 12 (2010) 5660-5667.
- [21] M. Agote-Aráñ, A. Kröner, H. Islam, W. Ślawinski, D. Wragg, I. Lezcano-Gonzalez, A.M. Beale, Determination of Molybdenum Species Evolution during Non-Oxidative Dehydroaromatization of Methane and its Implications for Catalytic Performance, *ChemCatChem*, 0.
- [22] I. Vollmer, B. van der Linden, S. Ould-Chikh, A. Aguilar-Tapia, I. Yarulina, E. Abou-Hamad, Y.G. Sneider, A.I. Olivos Suarez, J.-L. Hazemann, F. Kapteijn, J. Gascon, On the dynamic nature of Mo sites for methane dehydroaromatization, *Chemical Science*, 9 (2018) 4801-4807.
- [23] H. Zheng, D. Ma, X. Bao, J.Z. Hu, J.H. Kwak, Y. Wang, C.H.F. Peden, Direct Observation of the Active Center for Methane Dehydroaromatization Using an Ultrahigh Field <sup>95</sup>Mo NMR Spectroscopy, *Journal of the American Chemical Society*, 130 (2008) 3722-3723.
- [24] J.Z. Hu, J.H. Kwak, Y. Wang, C.H.F. Peden, H. Zheng, D. Ma, X. Bao, Studies of the Active Sites for Methane Dehydroaromatization Using Ultrahigh-Field Solid-State <sup>95</sup>Mo NMR Spectroscopy, *The Journal of Physical Chemistry C*, 113 (2009) 2936-2942.
- [25] D. Ma, W. Zhang, Y. Shu, X. Liu, Y. Xu, X. Bao, MAS NMR, ESR and TPD studies of Mo/HZSM-5 catalysts: evidence for the migration of molybdenum species into the zeolitic channels, *Catalysis Letters*, 66 (2000) 155-160.
- [26] D. Ma, Y. Shu, X. Bao, Y. Xu, Methane Dehydro-aromatization under Nonoxidative Conditions over Mo/HZSM-5 Catalysts: EPR Study of the Mo Species on/in the HZSM-5 Zeolite, *Journal of Catalysis*, 189 (2000) 314-325.
- [27] J. Gao, Y. Zheng, J.-M. Jehng, Y. Tang, I.E. Wachs, S.G. Podkolzin, Identification of molybdenum oxide nanostructures on zeolites for natural gas conversion, *Science*, 348 (2015) 686-690.

- [28] J.C. Fierro-Gonzalez, S. Kuba, Y. Hao, B.C. Gates, Oxide- and Zeolite-Supported Molecular Metal Complexes and Clusters: Physical Characterization and Determination of Structure, Bonding, and Metal Oxidation State, *The Journal of Physical Chemistry B*, 110 (2006) 13326-13351.
- [29] S. Bordiga, C. Lamberti, F. Bonino, A. Travert, F. Thibault-Starzyk, Probing zeolites by vibrational spectroscopies, *Chemical Society Reviews*, 44 (2015) 7262-7341.
- [30] C. Lamberti, A. Zecchina, E. Groppo, S. Bordiga, Probing the surfaces of heterogeneous catalysts by *in situ* IR spectroscopy, *Chemical Society Reviews*, 39 (2010) 4951-5001.
- [31] A. Zecchina, F. Geobaldo, C. Lamberti, S. Bordiga, G. Turnes Palomino, C. Otero Areán, Infrared studies of the interaction of carbon monoxide and dinitrogen with ferrisilicate MFI-type zeolites, *Catalysis Letters*, 42 (1996) 25-33.
- [32] K.I. Hadjiivanov, Identification of Neutral and Charged N x O y Surface Species by IR Spectroscopy, *Catalysis reviews*, 42 (2000) 71-144.
- [33] K.I. Hadjiivanov, G.N. Vayssilov, Characterization of oxide surfaces and zeolites by carbon monoxide as an IR probe molecule, in: *Advances in Catalysis*, Academic Press, 2002, pp. 307-511.
- [34] E.V. Fadeeva, O.P. Tkachenko, A.V. Kucherov, A.P. Barkova, M.N. Mikhailov, A.M. Kulizade, M.M. Akhmedov, L.M. Kustova, Investigation of the molybdenum state in the Mo(4%)/HZSM-5 catalyst for methane aromatization, *Russian Chemical Bulletin*, 61 (2012) 2230-2235.
- [35] G. Doyen, G. Ertl, Theory of carbon monoxide chemisorption on transition metals, *Surface Science*, 43 (1974) 197-229.
- [36] R.J. Lobo-Lapidus, B.C. Gates, Supported Rhenium Complexes: Almost Uniform Rhenium Tricarbonyls Synthesized from CH<sub>3</sub>Re(CO)<sub>5</sub> and HY Zeolite, *Langmuir*, 26 (2010) 16368-16374.
- [37] J.F. Goellner, B.C. Gates, G.N. Vayssilov, N. Rösch, Structure and Bonding of a Site-Isolated Transition Metal Complex: Rhodium Dicarbonyl in Highly Dealuminated Zeolite Y, *Journal of the American Chemical Society*, 122 (2000) 8056-8066.
- [38] J.B. Peri, Computerized infrared studies of molybdenum/alumina and molybdenum/silica catalysts, *The Journal of Physical Chemistry*, 86 (1982) 1615-1622.
- [39] C.O. Areán, M.R. Delgado, K. Frolich, R. Bulánek, A. Pulido, G.F. Bibiloni, P. Nachtigall, Computational and Fourier Transform Infrared Spectroscopic Studies on Carbon Monoxide Adsorption on the Zeolites Na-ZSM-5 and K-ZSM-5: Evidence of Dual-Cation Sites, *The Journal of Physical Chemistry C*, 112 (2008) 4658-4666.
- [40] B. Hamzaoui, A. Bendjeriou-Sedjerari, E. Pump, E. Abou-Hamad, R. Sougrat, A. Gurinov, K.-W. Huang, D. Gajan, A. Lesage, L. Emsley, J.-M. Basset, Atomic-level organization of vicinal acid-base pairs through the chemisorption of aniline and derivatives onto mesoporous SBA15, *Chemical Science*, 7 (2016) 6099-6105.

- [41] T. Kobayashi, F.A. Perras, I.I. Slowing, A.D. Sadow, M. Pruski, Dynamic Nuclear Polarization Solid-State NMR in Heterogeneous Catalysis Research, *ACS Catalysis*, 5 (2015) 7055-7062.
- [42] D. Lee, H. Takahashi, A.S.L. Thankamony, J.-P. Dacquin, M. Bardet, O. Lafon, G.D. Paépe, Enhanced Solid-State NMR Correlation Spectroscopy of Quadrupolar Nuclei Using Dynamic Nuclear Polarization, *Journal of the American Chemical Society*, 134 (2012) 18491-18494.
- [43] M. Lelli, D. Gajan, A. Lesage, M.A. Caporini, V. Vitzthum, P. Miéville, F. Héroguel, F. Rascón, A. Roussey, C. Thieuleux, M. Boualleg, L. Veyre, G. Bodenhausen, C. Coperet, L. Emsley, Fast Characterization of Functionalized Silica Materials by Silicon-29 Surface-Enhanced NMR Spectroscopy Using Dynamic Nuclear Polarization, *Journal of the American Chemical Society*, 133 (2011) 2104-2107.
- [44] K. Märker, M. Pingret, J.-M. Mouesca, D. Gasparutto, S. Hediger, G. De Paépe, A New Tool for NMR Crystallography: Complete  $^{13}\text{C}/^{15}\text{N}$  Assignment of Organic Molecules at Natural Isotopic Abundance Using DNP-Enhanced Solid-State NMR, *Journal of the American Chemical Society*, 137 (2015) 13796-13799.
- [45] E. Pump, J. Viger-Gravel, E. Abou-Hamad, M.K. Samantaray, B. Hamzaoui, A. Gurinov, D.H. Anjum, D. Gajan, A. Lesage, A. Bendjeriou-Sedjerari, L. Emsley, J.-M. Basset, Reactive surface organometallic complexes observed using dynamic nuclear polarization surface enhanced NMR spectroscopy, *Chemical Science*, 8 (2017) 284-290.
- [46] M. Giulia, D. Myriam, Z. Fabio, T. Pierre, V. Stéphane, Quantitative Structural Constraints for Organic Powders at Natural Isotopic Abundance Using Dynamic Nuclear Polarization Solid-State NMR Spectroscopy, *Angewandte Chemie International Edition*, 54 (2015) 6028-6031.
- [47] D. Mance, J. van der Zwan, M.E.Z. Velthoen, F. Meirer, B.M. Weckhuysen, M. Baldus, E.T.C. Vogt, A DNP-supported solid-state NMR study of carbon species in fluid catalytic cracking catalysts, *Chemical Communications*, 53 (2017) 3933-3936.
- [48] N. Kosinov, V.G.P. Srivastava, E.J.M. Hensen, Improving separation performance of high-silica zeolite membranes by surface modification with triethoxyfluorosilane, *Microporous and Mesoporous Materials*, 194 (2014) 24-30.
- [49] G. Li, E.A. Pidko, R.A. van Santen, C. Li, E.J.M. Hensen, Stability of Extraframework Iron-Containing Complexes in ZSM-5 Zeolite, *The Journal of Physical Chemistry C*, 117 (2013) 413-426.
- [50] G. Kresse, J. Hafner, Ab initio molecular dynamics for liquid metals, *Physical Review B*, 47 (1993) 558-561.
- [51] G.K.a.J. Hafner, *Phys. Rev. B*, 49 (1994) 14251-14269.
- [52] G.K.a.J. Furthmüller, *Phys. Rev. B Condens. Matter Mater. Phys.*, 54 (1996) 11169-11186.
- [53] G. Kresse, J. Furthmüller, Efficient iterative schemes for ab initio total-energy calculations using a plane-wave basis set, *Physical Review B*, 54 (1996) 11169-11186.

- [54] G. Kresse, J. Furthmüller, Efficiency of ab-initio total energy calculations for metals and semiconductors using a plane-wave basis set, *Computational Materials Science*, 6 (1996) 15-50.
- [55] J.P. Perdew, K. Burke, M. Ernzerhof, Generalized Gradient Approximation Made Simple, *Physical review letters*, 77 (1996) 3865-3868.
- [56] P.E. Blöchl, Projector augmented-wave method, *Physical Review B*, 50 (1994) 17953-17979.
- [57] G. Kresse, D. Joubert, From ultrasoft pseudopotentials to the projector augmented-wave method, *Physical Review B*, 59 (1999) 1758-1775.
- [58] H.J. Monkhorst, J.D. Pack, Special points for Brillouin-zone integrations, *Physical Review B*, 13 (1976) 5188-5192.
- [59] S. Grimme, S. Grimme, J. Antony, S. Ehrlich, and H. Krieg, A consistent and accurate ab initio parametrization of density functional dispersion correction (DFT-D) for the 94 elements H-Pu, *J. Chem. Phys.* 132, 154104 (2010), *J. Chem. Phys.*, 132 (2010) 154104.
- [60] W. Tang, E. Sanville, G. Henkelman, A grid-based Bader analysis algorithm without lattice bias, *Journal of Physics: Condensed Matter*, 21 (2009) 084204.
- [61] S. Edward, K.S. D., S. Roger, H. Graeme, Improved grid-based algorithm for Bader charge allocation, *Journal of Computational Chemistry*, 28 (2007) 899-908.
- [62] G. Henkelman, A. Arnaldsson, H. Jónsson, A fast and robust algorithm for Bader decomposition of charge density, *Computational Materials Science*, 36 (2006) 354-360.
- [63] M. Yu, D.R. Trinkle, Accurate and efficient algorithm for Bader charge integration, *The Journal of Chemical Physics*, 134 (2011) 064111.
- [64] K. Chakarova, K. Hadjiivanov, Problems in the IR measuring the acidity of zeolite bridging hydroxyls by low-temperature CO adsorption, *Chemical Communications*, 47 (2011) 1878-1880.
- [65] M.S. Holm, S. Svelle, F. Joensen, P. Beato, C.H. Christensen, S. Bordiga, M. Bjørgen, Assessing the acid properties of desilicated ZSM-5 by FTIR using CO and 2,4,6-trimethylpyridine (collidine) as molecular probes, *Applied Catalysis A: General*, 356 (2009) 23-30.
- [66] I. Yarulina, J. Goetze, C. Gucuyener, L. van Thiel, A. Dikhtarenko, J. Ruiz-Martinez, B.M. Weckhuysen, J. Gascon, F. Kapteijn, Methanol-to-olefins process over zeolite catalysts with DDR topology: effect of composition and structural defects on catalytic performance, *Catalysis Science & Technology*, 6 (2016) 2663-2678.
- [67] H.E. Bergna, The colloid chemistry of silica, in, American Chemical Society, Washington, DC (United States), 1994.
- [68] P.L.J. Gunter, J.W. Niemantsverdriet, F.H. Ribeiro, G.A. Somorjai, Surface Science Approach to Modeling Supported Catalysts, *Catalysis reviews*, 39 (1997) 77-168.
- [69] M.J. Nash, A.M. Shough, D.W. Fickel, D.J. Doren, R.F. Lobo, High-Temperature Dehydrogenation of Brønsted Acid Sites in Zeolites, *Journal of the American Chemical Society*, 130 (2008) 2460-2462.

- [70] C.C. Williams, J.G. Ekerdt, Infrared spectroscopic characterization of molybdenum carbonyl species formed by ultraviolet photoreduction of silica-supported molybdenum (VI) in carbon monoxide, *The Journal of Physical Chemistry*, 97 (1993) 6843-6852.
- [71] N. Kosinov, F.J.A.G. Coumans, E.A. Uslamin, A.S.G. Wijpkema, B. Mezari, E.J.M. Hensen, Methane Dehydroaromatization by Mo/HZSM-5: Mono- or Bifunctional Catalysis?, *ACS Catalysis*, (2016) 520-529.
- [72] J. Yang, D. Ma, F. Deng, Q. Luo, M. Zhang, X. Bao, C. Ye, Solid state  $^{13}\text{C}$  NMR studies of methane dehydroaromatization reaction on Mo/HZSM-5 and W/HZSM-5 catalysts, *Chem. Commun.*, (2002) 3046-3047.
- [73] H. Zheng, D. Ma, X. Liu, W. Zhang, X. Han, Y. Xu, X. Bao, Methane dehydroaromatization over Mo/HZSM-5: A study of catalytic process, *Catalysis Letters*, 111 (2006) 111-114.
- [74] K. Kim, T. Lee, Y. Kwon, Y. Seo, J. Song, J.K. Park, H. Lee, J.Y. Park, H. Ihee, S.J. Cho, R. Ryoo, Lanthanum-catalysed synthesis of microporous 3D graphene-like carbons in a zeolite template, *Nature*, 535 (2016) 131.
- [75] H. Okamoto, R. Eguchi, S. Hamao, H. Goto, K. Gotoh, Y. Sakai, M. Izumi, Y. Takaguchi, S. Gohda, Y. Kubozono, An Extended Phenacene-type Molecule, [8]Phenacene: Synthesis and Transistor Application, *Scientific Reports*, 4 (2014) 5330.
- [76] I. Vollmer, G. Li, I. Yarulina, N. Kosinov, E.J. Hensen, K. Houben, D. Mance, M. Baldus, J. Gascon, F. Kapteijn, Relevance of the Mo-precursor state in H-ZSM-5 for methane dehydroaromatization, *Catalysis Science & Technology*, 8 (2018) 916-922.
- [77] N. Kosinov, F.J. Coumans, G. Li, E. Uslamin, B. Mezari, A.S. Wijpkema, E.A. Pidko, E.J. Hensen, Stable Mo/HZSM-5 methane dehydroaromatization catalysts optimized for high-temperature calcination-regeneration, *Journal of Catalysis*, 346 (2017) 125-133.
- [78] S. Liu, L. Wang, R. Ohnishi, M. Ichikawa, Bifunctional Catalysis of Mo/HZSM-5 in the Dehydroaromatization of Methane to Benzene and Naphthalene XAFS/TG/DTA/MASS/FTIR Characterization and Supporting Effects, *Journal of Catalysis*, 181 (1999) 175-188.
- [79] H.S. Lacheen, E. Iglesia, Stability, structure, and oxidation state of Mo/H-ZSM-5 catalysts during reactions of CH<sub>4</sub> and CH<sub>4</sub>-CO<sub>2</sub> mixtures, *Journal of Catalysis*, 230 (2005) 173-185.
- [80] J.-Z. Zhang, M.A. Long, R.F. Howe, Molybdenum ZSM-5 zeolite catalysts for the conversion of methane to benzene, *Catalysis Today*, 44 (1998) 293-300.
- [81] N. Kosinov, E.A. Uslamin, F.J.A.G. Coumans, A.S.G. Wijpkema, R.Y. Rohling, E.J.M. Hensen, Structure and Evolution of Confined Carbon Species during Methane Dehydroaromatization over Mo/ZSM-5, *ACS Catalysis*, (2018) 8459-8467.





## Annex chapter 5

---

A site-sensitive *quasi-in situ* strategy to  
characterize Mo/HZSM-5 during activation

## Contents

<b>A5.1 CO IR</b>	229
<b>A5.2 DFT calculations of CO IR bands</b>	233
<b>A5.3 <math>^{13}\text{C}</math> MAS NMR</b>	238
<b>A5.4 DNP</b>	239
<b>A5.5 References</b>	241

## A5.1 CO IR

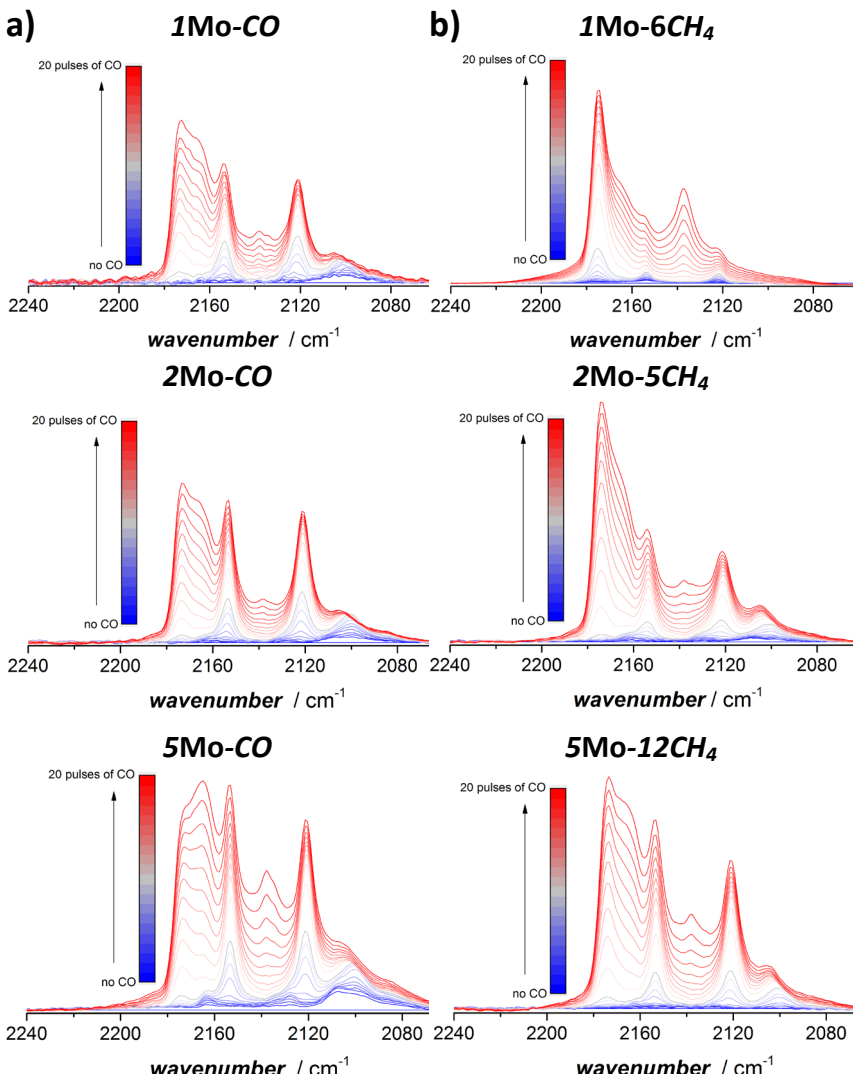


Figure A5.1. a) IR-spectra of the CO vibrations after consecutive pulsing of CO to  $x\text{Mo}-\text{CO}$ , where  $x$  denotes the loading of Mo in wt.% and CO denotes that the sample was pre-treated in CO. b) IR-spectra of the CO vibrations after consecutive pulsing of CO to  $x\text{Mo}-z\text{CH}_4$ , where  $z$  denotes the number of CH<sub>4</sub> pulses used to pre-treat the sample. A spectrum was taken after each pulse of CO sent to the evacuated IR cell kept at -167 °C. A total of 20 pulses was sent to the cell in a sequence described in the experimental part (**Fourier transformed infrared spectroscopy**). The CO-treatment and the CH<sub>4</sub> pulsing are described in the experimental part (**CO carburization** and **CH<sub>4</sub> pulsing experiments**). The pre-treated samples were transferred to the IR cell without exposure to the atmosphere. The scale is in a.u. but kept the same for all spectra.

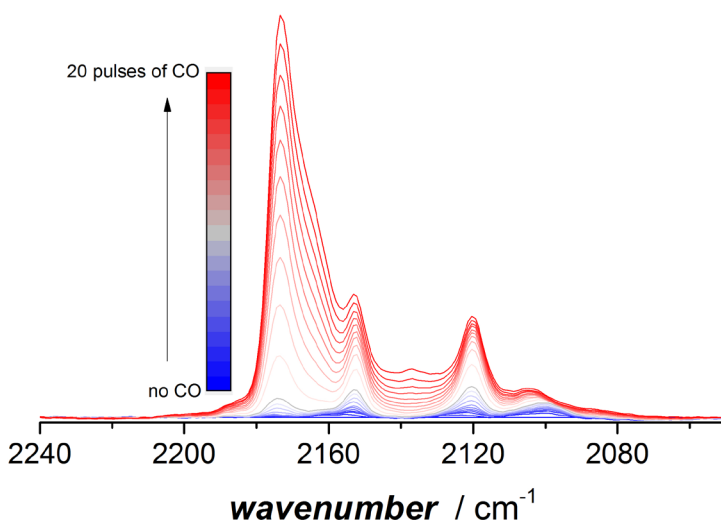


Figure A5.2. IR-spectra of the CO vibrations after consecutive pulsing of CO to **2Mo-CO** previously treated in 30 ml/min 2.5%CO in He at 700 °C for 1 h and then transferred to the IR cell without exposure to the atmosphere. A spectrum was taken after each pulse of CO sent to the evacuated IR cell kept at -167 °C. A total of 20 pulses was sent to the cell in a sequence described in the experimental part (**Fourier transformed infrared spectroscopy**).

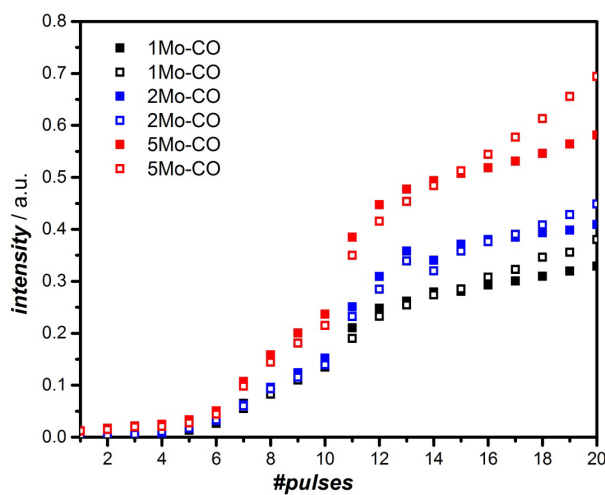


Figure A5.3. Evolution of heights of absorbance bands at 2120 cm<sup>-1</sup> (solid symbols) and 2153 cm<sup>-1</sup> (open symbols) with number of CO pulses. Full spectra are shown in **Figure A5.1a**.

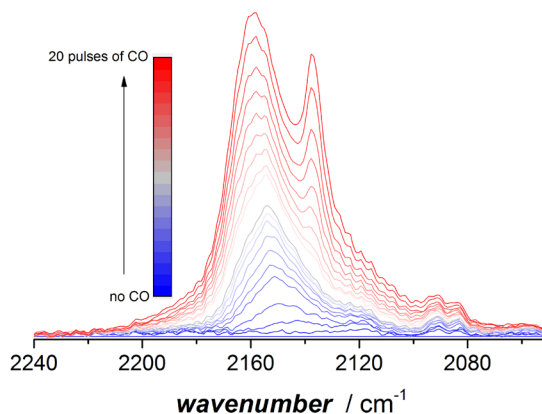


Figure A5.4. IR-spectra measured after each pulse of CO introduced into the evacuated chamber containing **2Mo/silicalite-1** pre-treated in 30 ml/min 2.5%CO in He at 800 °C for 1 h as described in the experimental part ('CO carburization') and then transferred to the FTIR cell without exposure to the atmosphere. For details of CO pulsing and IR measurement refer to the experimental part **Fourier transformed infrared spectroscopy**.

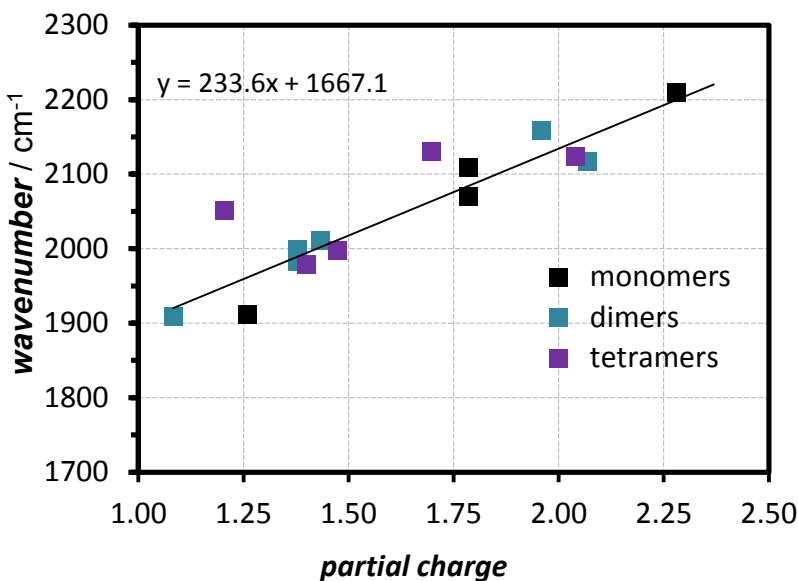


Figure A5.5: Carbonyl vibrations as calculated by DFT plotted against partial charge. Black symbols represent monomers, turquoise dimers and purple tetramers. Corresponding structures can be found in **Figure A5.8**.

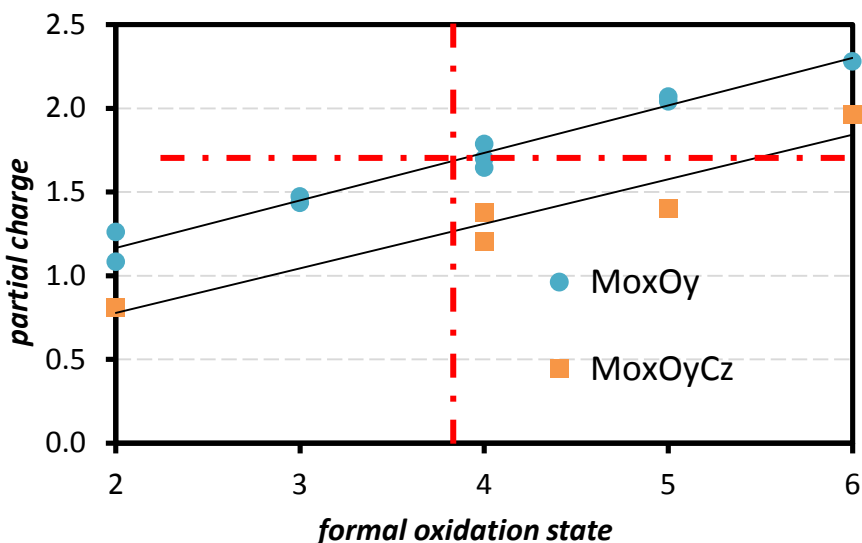


Figure A5.6: Relation between formal oxidation state and partial charge for the structures shown in **Figure A5.8** containing only oxygen as a ligand as  $\text{Mo}_x\text{O}_y$  and structures containing oxygen and carbon as  $\text{Mo}_x\text{O}_y\text{C}_z$ . Note that there are no monomeric structures containing carbon. The red lines indicate the partial charge and formal oxidation state that correspond to the wavenumbers for CO vibrations observed experimentally.

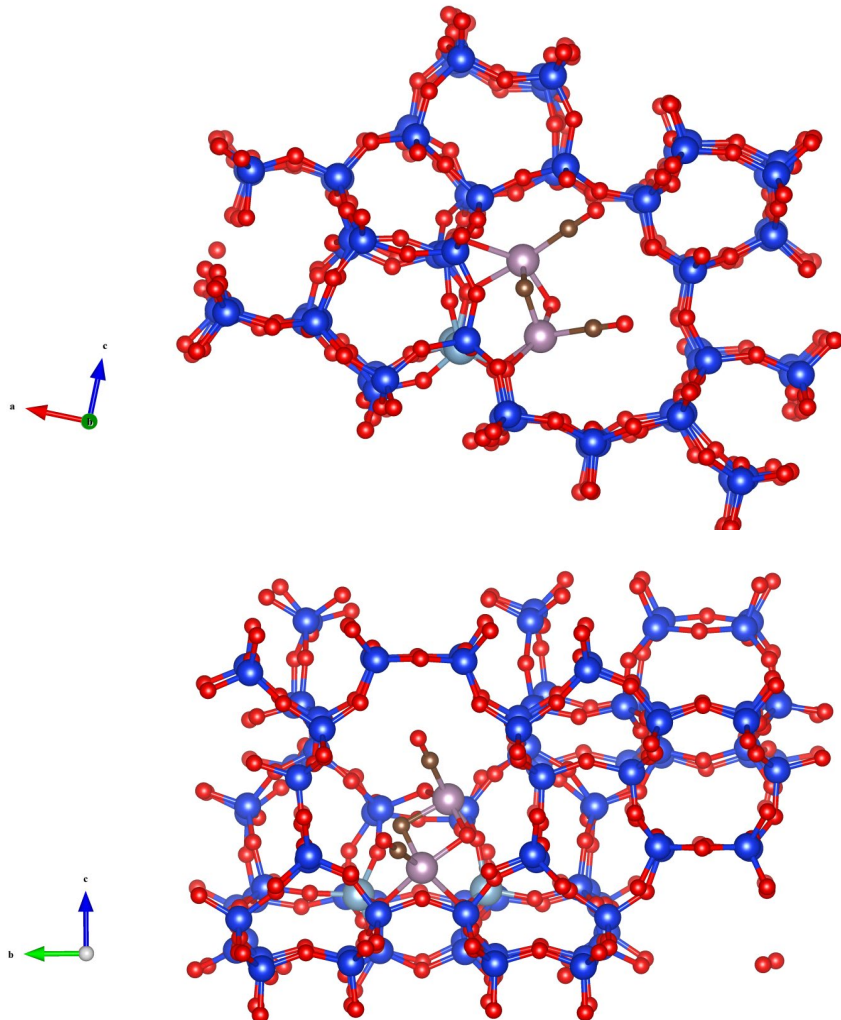
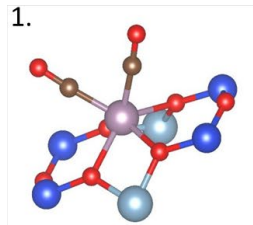
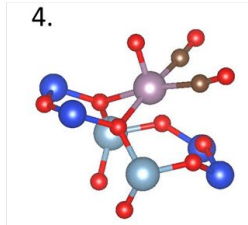
**A5.2 DFT calculation of CO IR bands**

Figure A5.7. Representation of the location of the  $\delta$ -site in the zeolite framework chosen as anchoring site for all Mo (oxy-)carbide models shown in **Figure A5.8** used for the DFT calculations of CO vibrational frequencies.

## monomers



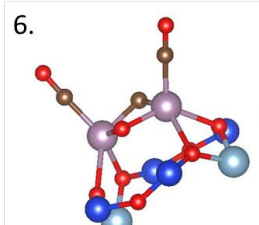
partial charge: 1.26



partial charge: 1.79

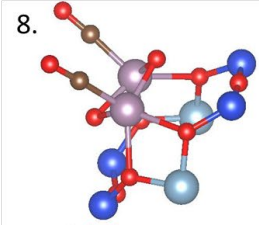
## Dimers

$\text{Mo}_2\text{OC}$



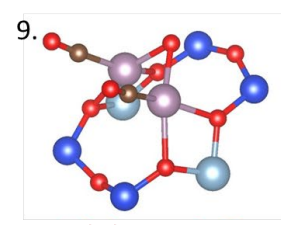
partial charge: 1.38

$\text{Mo}_2\text{O}_2$



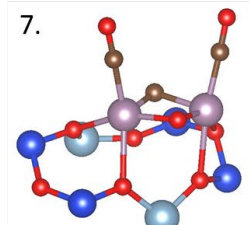
partial charge: 1.43

$\text{Mo}_2\text{O}$



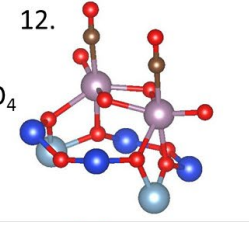
partial charge: 1.08

7.



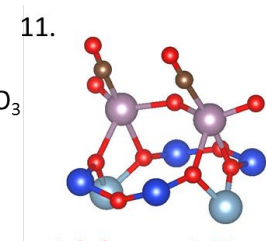
partial charge: 1.38

12.



partial charge: 2.07

11.

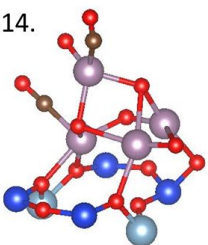


partial charge: 1.65

## Tetramers

 $\text{Mo}_4\text{O}_5$ 

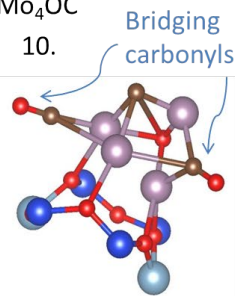
14.



partial charge: 1.47

 $\text{Mo}_4\text{OC}$ 

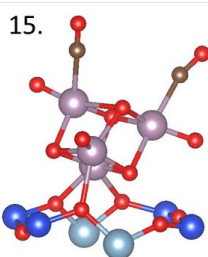
10.



partial charge: 0.81

 $\text{Mo}_4\text{O}_7$ 

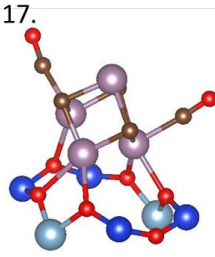
15.



partial charge: 1.7

 $\text{Mo}_4\text{C}_3$ 

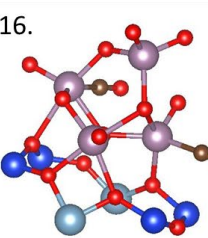
17.



partial charge: 1.21

 $\text{Mo}_4\text{O}_8$ 

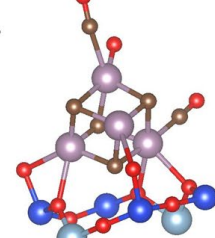
16.



partial charge: 2.04

 $\text{Mo}_4\text{OC}_4$ 

18.



partial charge: 1.4

Figure A5.8: Monomeric, dimeric and tetrameric structures with adsorbed CO as used to determine the CO vibrational frequencies through DFT calculations. Colors correspond to atoms(Mo: purple, Al: turquoise, O: red, Si: blue, C: brown).

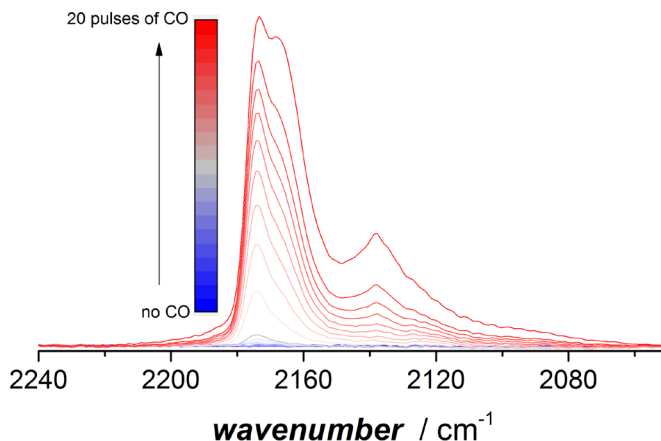


Figure A5.9: IR-spectra measured after each pulse of CO introduced into the evacuated chamber containing **2Mo-H<sub>2</sub>** pre-treated in 30 ml/min 5% H<sub>2</sub> in He heating to 800 °C with 10 °C/min for 1 h as described in the experimental part (**H<sub>2</sub> treatment**) and then transferred to the FTIR cell without exposure to the atmosphere. For details of CO pulsing and IR measurement refer to the experimental part **Fourier transformed infrared spectroscopy**.

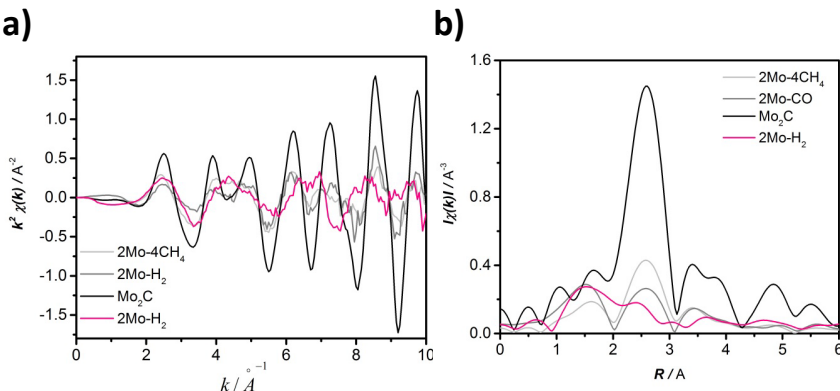


Figure A5.10: a) EXAFS and b) FT-EXAFS of spectra collected at Mo K-edge for the Mo<sub>2</sub>C reference, **2Mo-CH<sub>4</sub>**, **2Mo-CO** and **2Mo-H<sub>2</sub>**. All spectra were collected in fluorescence mode at RT, except for the Mo<sub>2</sub>C reference, which was measured in transmission mode on a pressed pellet. **2Mo-CH<sub>4</sub>** was quenched right at the onset of benzene formation when pulsing CH<sub>4</sub> to **2Mo**. The XAS measurement were performed at the CRG-FAME UHD beamline (BM16) at the European Synchrotron Radiation Facility (ESRF) in Grenoble [1]. CO carburization, the CH<sub>4</sub> pulsing experiment and the H<sub>2</sub>-treatment were performed in an operando setup[2] specifically designed for that beamline similarly to what is described in the experimental part **CO carburization, H<sub>2</sub>-treatment and CH<sub>4</sub> pulsing experiment**. For details refer to reference [3].

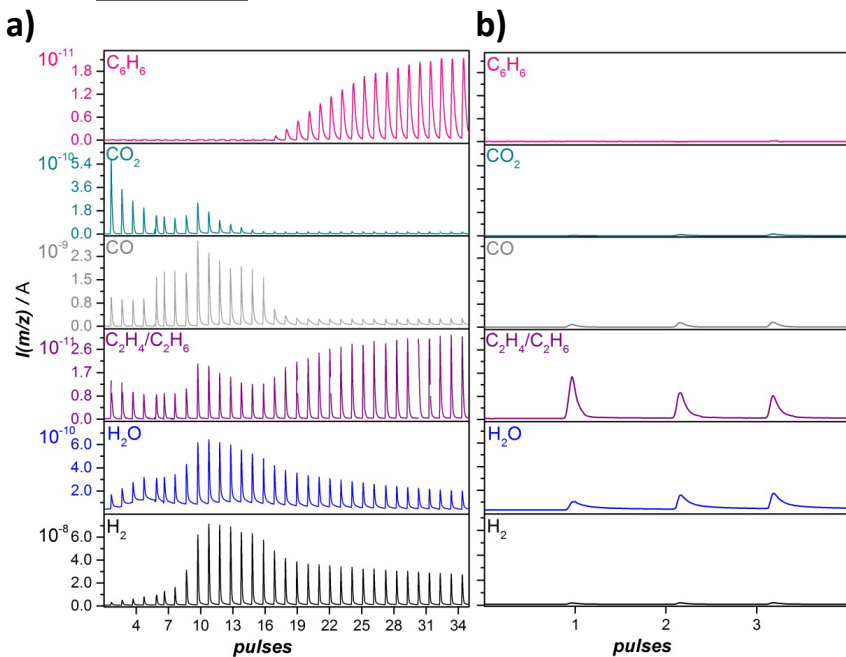


Figure A5.11: MS readouts for  $C_6H_6$ ,  $CO_2$ ,  $CO$ ,  $C_2H_4/C_2H_6$ ,  $H_2O$  and  $H_2$  ( $m/z = 78$ , 44, 28, 27, 18 and 2) during consecutive pulsing of 233  $\mu\text{mol}$  of  $CH_4$  at 700  $^{\circ}\text{C}$  into a continuous flow of 30 ml/min He. a) over 300 mg of **5Mo** and b) using an empty reactor.

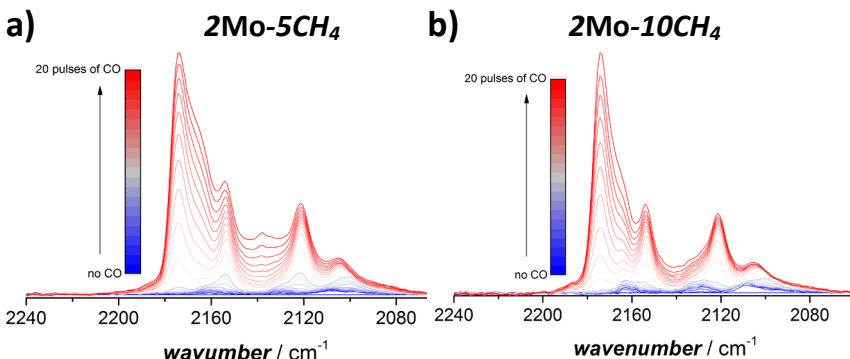


Figure A5.12: IR-spectra measured after each pulse of CO introduced into the evacuated chamber containing a) **2Mo-5 $CH_4$**  and b) **2Mo-10 $CH_4$**  at -167  $^{\circ}\text{C}$ . **2Mo-z $CH_4$**  was pretreated as detailed in **CH<sub>4</sub> pulsing experiments**. After treatment the sample was transferred to the IR cell without exposure to the atmosphere.

### A5.3 $^{13}\text{C}$ MAS NMR

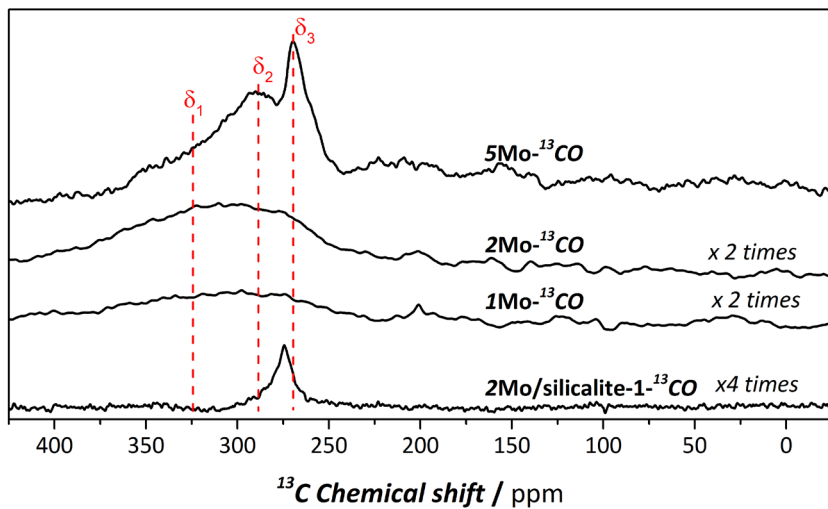


Figure A5.13.  $^{13}\text{C}$  MAS NMR spectra of  $x\text{Mo}-^{13}\text{CO}$  and  $2\text{Mo}/\text{silicalite-1}$  after  $^{13}\text{CO}$  carburization at  $780\text{ }^{\circ}\text{C}$  for 1 h using 30 ml/min, 2.5%  $^{13}\text{CO}$  in He as detailed in the experimental part **CO carburization**. Reproduced from our previous publication[3] with permission from the Royal Society of Chemistry.

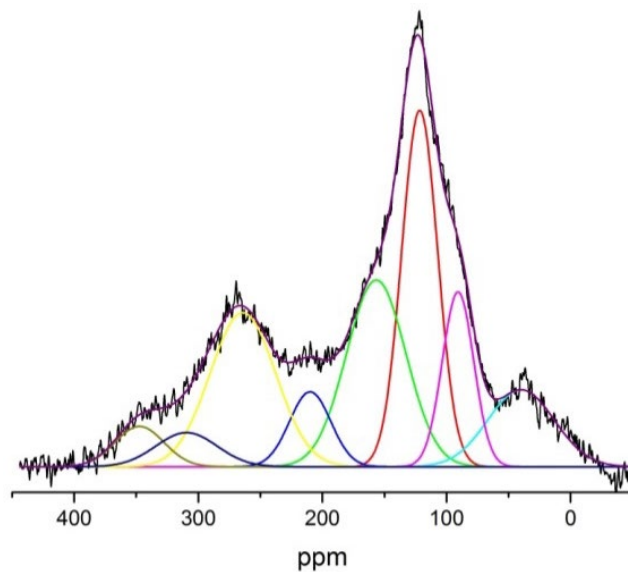


Figure A5.14. Deconvolution of the  $^{13}\text{C}$  MAS NMR spectra of  $5\text{Mo}-14^{13}\text{CH}_4$ .

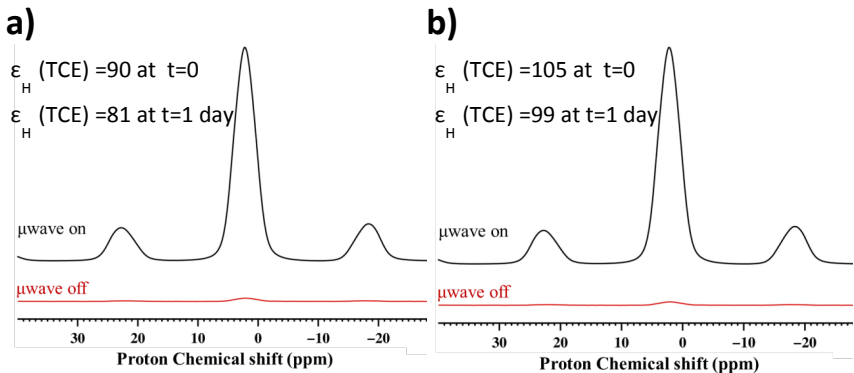
**A5.4 DNP**

Figure A5.15: Enhancement of the  ${}^1\text{H}$  MAS spectrum of the protons of the solvent TCE for samples a)  $\text{1Mo}-{}^{13}\text{CO}$  and b)  $\text{2Mo}-{}^{13}\text{CO}$  impregnated with the TEKPol solution when the microwave irradiation is switched on (black line) compared to without microwave irradiation (red line).

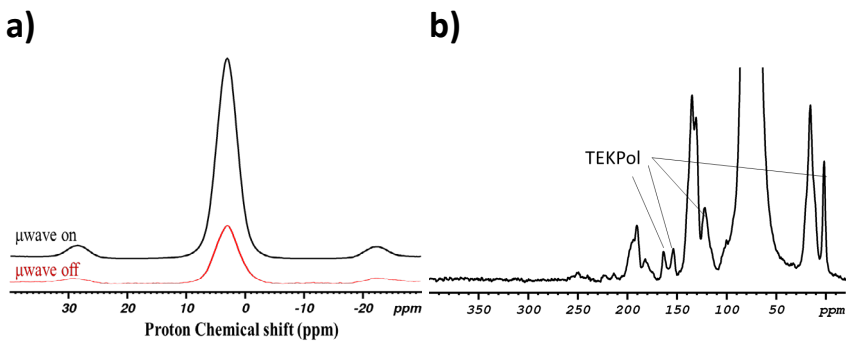


Figure A5.16: a) Enhancement of the  ${}^1\text{H}$  MAS spectrum of the protons of the solvent TCE for sample  $\text{5Mo}-{}^{13}\text{CO}$  impregnated with the TEKPol solution when the microwave irradiation is switched on (black line) compared to without microwave irradiation (red line). b) DNP SENS  ${}^{13}\text{C}$  MAS NMR spectra of  $\text{5Mo}-{}^{13}\text{CO}$ , where the signals corresponding to decomposed TEKPol are indicated.

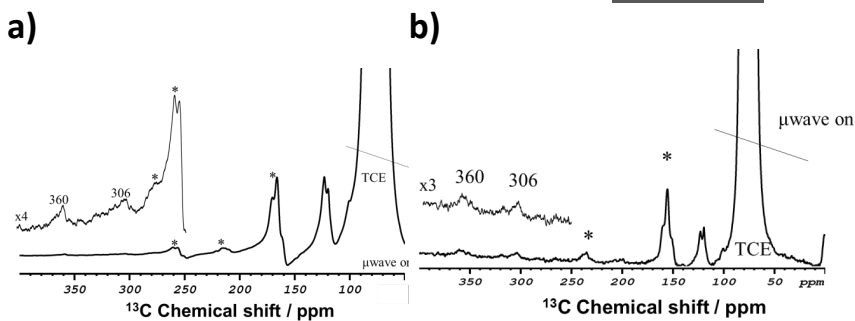


Figure 5.17: DNP SENS  $^{13}\text{C}$  MAS NMR spectra of **1Mo- $^{13}\text{CO}$**  measured at a MAS frequency of a) 9 kHz and b) 8 kHz. No bands are visible at 270 ppm when the measurement is performed at 8 kHz, confirming that the band visible at a MAS frequency of 9 kHz is a spinning sideband.

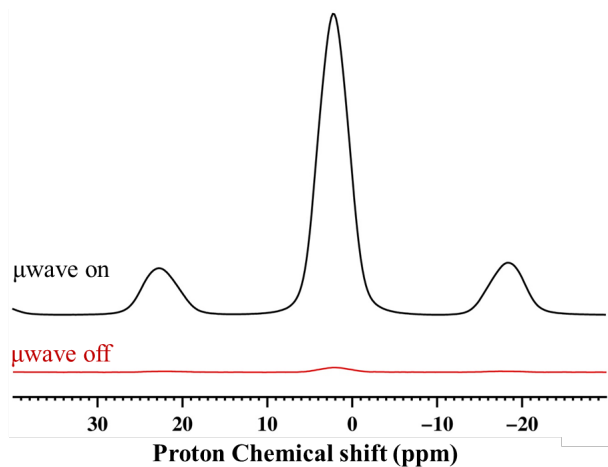


Figure A5.18: Enhancement of the  $^1\text{H}$  MAS spectrum of the protons of the solvent TCE for sample **5Mo-18 $^{13}\text{CH}_4$**  impregnated with the TEKPol solution when the microwave irradiation is switched on (black line) compared to without microwave irradiation (red line).

## A5.5 References

- [1] B. AlSabban, L. Falivene, S.M. Kozlov, A. Aguilar-Tapia, S. Ould-Chikh, J.-L. Hazemann, L. Cavallo, J.-M. Basset, K. Takanabe, In-operando elucidation of bimetallic CoNi nanoparticles during high-temperature CH<sub>4</sub>/CO<sub>2</sub> reaction, *Applied Catalysis B: Environmental*, 213 (2017) 177-189.
- [2] A. Aguilar-Tapia, S. Ould-Chikh, E. Lahera, A. Prat, W. Delnet, O. Proux, I. Kieffer, J.-M. Basset, K. Takanabe, J.-L. Hazemann, A new high temperature reactor for operando XAS: Application for the dry reforming of methane over Ni/ZrO<sub>2</sub> catalyst, *Review of Scientific Instruments*, 89 (2018) 035109.
- [3] I. Vollmer, B. van der Linden, S. Ould-Chikh, A. Aguilar-Tapia, I. Yarulina, E. Abou-Hamad, Y.G. Sneider, A.I. Olivos Suarez, J.-L. Hazemann, F. Kapteijn, J. Gascon, On the dynamic nature of Mo sites for methane dehydroaromatization, *Chemical Science*, 9 (2018) 4801-4807.





## **SUMMARY AND OUTLOOK**

## Summary

In view of rising global demand for aromatics as starting chemical for many commodity goods as well as pharmaceuticals, new routes for production are explored. Since the advent of fracking, natural gas has become increasingly cheap and direct utilization for aromatics production has gained attractiveness. Methane dehydroaromatization represents the most direct of such utilization routes and could potentially be very carbon efficient, if no oxidants are added, since byproducts such as CO and CO<sub>2</sub> are avoided. For the direct non-oxidative conversion however, fast deactivation due to coke formation and significant thermodynamic limitations still stand in the way of commercialization. Improvements of the catalysts towards coke-resistance and overall stability could significantly speed up the development towards large-scale operation of the methane dehydroaromatization process, although innovation in process development is also believed to be important. It is desirable to develop a catalyst that outperforms the state-of-the-art system Mo/HZSM-5. This system however, continues to perform better than other catalyst formulations, and for 25 years already, no significantly better system was found. Thus, this thesis focusses on developing a fundamental understanding of why this catalytic system continues to outperform other systems. The aim of this thesis was to spot the characteristic traits of this catalyst, which can then be used as guidelines for the development of novel catalysts. This was done in two parts, where the first deals with the characterization of the as-synthesized catalyst and parameters of the synthesis that influence final performance (**Chapter 2 and 3**) while *operando* and *in-situ* characterization are used in the second part to gain insight on the catalyst under reaction conditions.

**Chapter 1** describes how Mo takes on many different configurations when introduced to the zeolite support. A plethora of different geometries, nuclearities and Mo locations complicates the signal in spectroscopic techniques and it is very difficult to understand which of these sites actually catalyse the conversion of methane to aromatics. This is why in **Chapter 2** the preparation of catalysts containing Mo in a well-known geometry and location is attempted. The geometry of the Mo oxide site changes depending on whether it anchors to one or two framework Al and also depending on the location of this framework Al, *i.e.* in the straight or zig-zag channels of the MFI framework or at their intersection. Different synthesis protocols

were employed to alter the proximity of framework Al. This was successfully achieved as confirmed by UV-Vis spectroscopy on Co(II) ion-exchanged into the zeolite, which exclusively anchors to Al situated in close proximity as pairs. With the help of Py IR, it was demonstrated that one or two acidic protons were exchanged by Mo, depending on the concentration of Al pairs on the zeolite. This however had no significant impact on catalyst performance and it was concluded that as long as similar Mo dispersion is achieved on the catalyst, the catalytic performance in terms of methane conversion, benzene and naphthalene yields is also similar.

Because Mo dispersion was determined to be the most important parameter to determine catalyst performance, **Chapter 3** focusses on quantifying the relationship between Mo dispersion, acidity as well as porosity and measures of catalytic performance, such as instantaneous yields selectivity to aromatics products as well as coke. For this, a suite of 17 catalysts was synthesized using 9 different synthesis techniques. Py IR, ICP, XPS and UV-Vis were compared in their ability to reliable assess the Mo dispersion on the as-synthesized catalysts. It was found that the decrease in acidity due to the exchange of acidic protons with cationic Mo can reliably be determined by Py IR and is a good measure for Mo dispersion. Integral selectivities to naphthalene and benzene linearly increased with the concentration of highly dispersed cationic Mo and coke selectivity is related to Mo present as bigger clusters or nanoparticles on the outer surface of the zeolite crystal. This confirms what was mostly speculated in literature prior to that work. Apart from the commonly used incipient wetness impregnation and solid ion exchange, in this chapter, chemical vapor deposition (CVD) techniques using  $\text{MoCl}_5$ ,  $\text{MoO}_2\text{Cl}_2$  and  $\text{Mo}(\text{CO})_6$  as precursors are explored as well. Although rarely applied to the MDA catalyst CVD methods have been found to lead to highly dispersed metal sites on zeolites for other reactions like deNOx. This technique initially lead to a catalyst with improved dispersion and catalytic performance in terms of benzene and naphthalene yields as well as decreased coke selectivity compared to the most commonly used incipient wetness impregnation technique. However, the synthesis procedure proved to be very hard to reproduce. Adjusting several parameters of the technique, it was found to work better when used with  $\text{MoCl}_5$  as a precursor compared to  $\text{MoO}_2\text{Cl}_2$ . In

addition, *in vacuo* sublimation of the precursor was found to impair the integrity of the zeolite.

The MDA process is operated at very high temperatures over a metal zeolite system. Reactions involving hydrocarbon on zeolites involve many parallel and consecutive reactions leading to a complicated reaction network. The fact that the MDA process is performed at high temperatures, because of thermodynamic limitations, further speeds up those reactions and leads to fast coke formation. Furthermore, the active site is formed at reaction conditions. The consequence is that only very limited insight can be gained from analysing the fresh and spent catalyst and trying to relate such findings to catalytic behaviour (**Chapter 1**). Especially, if the catalyst is exposed to ambient atmosphere between on-stream operation and characterization. This was also shown in **Chapter 2**, where the differences in the geometry of the oxidic Mo in the as-synthesized samples had little influence on catalytic performance, likely because of significant transformation and even agglomeration of Mo at reaction conditions. **Chapter 4** and **5** address the challenge of meaningful characterization.

In **Chapter 4**, an alternative way of creating the active site using a CO pre-treatment is introduced. This pre-treatment stabilizes the active site for *quasi-insitu* characterization. It is effective in preparing an active catalyst, where no coke has been deposited yet. This is in contrast to activation under methane atmosphere, since coke deposition happens simultaneous with the formation of the (oxy-)carbidic active site during the so-called ‘activation period’. Using either  $\text{C}^{18}\text{O}$  or  $^{13}\text{CO}$  for the pre-treatment revealed the stoichiometry of the active site. The CO pre-treatment also allowed probing the interaction of methane directly with the carbon from the active site. This was investigated using  $^{13}\text{C}$ -labelled CO for the pre-treatment and unlabelled  $^{12}\text{CH}_4$  methane after pre-treatment, or vice versa. A pulsed reaction technique was also employed for better time resolution. The (oxy-)carbidic carbon formed during the pre-treatment was found to be incorporated into the final products of the reaction, highlighting the dynamicity of the active site and the participation of the carbon from the active site in the reaction. Relating the amount of carbon present at the active site after the pre-treatment to the initial activity of catalysts with different loadings of Mo, a linear relationship was found, highlighting the important role the (oxy-)carbidic carbon plays in activating methane. This is supported by the fact that a

pre-treatment in H<sub>2</sub> did not produce a catalyst that was able to immediately convert methane to aromatics without experiencing an activation period as was the case with the CO pre-treatment.

*Operando* XAS measurements revealed in **Chapter 4** that with the CO pre-treatment an active site is formed that is equivalent to the active site forming at reaction conditions with methane. This finding was further corroborated in **Chapter 5** by <sup>13</sup>C NMR and CO IR and exploited to gain more insight into the nature of the active site. CO IR reveals three different kind of Mo species, two corresponding to Mo anchoring to the zeolite framework inside its pores as mono- or dimeric species as well as another species corresponding to bigger clusters of Mo on the outer surface of the zeolite particle. In comparison with DFT calculations, the CO IR results point to a Mo oxidation state between 4+ and 6+. Three different (oxy-)carbidic Mo species were also observed with <sup>13</sup>C NMR on the <sup>13</sup>CO activated catalyst in **Chapter 4**. Using DNP SENS, a higher resolution of the carbon resonances was obtained leading to clear separation of the three contributions that were observed as lumped and had to be deconvoluted using Gaussians for the <sup>13</sup>C NMR spectra.

After activation of the Mo is completed, benzene production does not immediately reach its maximum, but only increases slowly to maximum production during a period termed ‘induction period’. The cause of this induction period has recently been assigned to the build-up of a hydrocarbon pool [1]. **Chapter 4** confirms that the extent of aromatics accumulation during the induction period follows the same trend as the increase in the benzene formation rate. At the same time, this experiment also confirms that the active site, once formed during the activation period, does not transform further during the induction period. This was evident from the unchanged resonances in the <sup>13</sup>C NMR spectra taken right after activation and at different points during the induction period.

## Outlook

Although the conversion of methane to aromatics was already shown to be possible in 1982[2], commercialization of this process still faces a lot of hurdles. The Mo/HZSM-5 system remains the best performing system, since it was discovered in 1993 by Wang *et al.*,[3] but only slight improvements for this catalyst were achieved since then by using different preparation techniques for Mo to achieve higher dispersion, by modifying the

support as well as by adding promoter metals. Still after those small improvements the problems of limited operational catalyst life-time and low methane conversion could not be overcome. At this moment, it remains to be seen whether innovations in process operation such as membrane reactor operation,[4-8] reactive removal of hydrogen[9] or smart regeneration techniques[10, 11] will finally allow commercialization of the MDA process with the metal zeolite system as a catalyst. It is however clear that commercialization could be significantly sped up, if the catalyst lifetime could be enhanced significantly, maintaining benzene yields at the thermodynamic maximum. One such example of a major breakthrough in methane conversion was achieved by Guo *et al.* [12]. The catalyst employed developed by Guo *et al.* is vastly different from the Mo/HZSM-5 system in that it does not exhibit any Brønsted acidity or porosity. In addition, the catalyst is effective at very high temperatures and experiences almost no coking. However, up to date this system remains to be better understood and the results obtained have not been verified by the scientific community.

To develop an entirely new system, more insight in the structure-activity relationship for the MDA reaction is needed. As both the process development as well as the catalyst developed by Guo *et al.* are out of the scope of this thesis, in the following an outlook is provided on the further development of a structure-activity relationship for the reaction over the metal zeolite system.

In **Chapter 4**, it was shown that the carbidic carbon at the active site, plays an important role in the activation of methane as a linear increase in initial activity with amount of carbidic carbon on the catalyst was observed. In addition, carbon from the active site was found to be incorporated into the final products of the reaction. It could be speculated that methane is actually activated by first forming carbidic carbon and two H<sub>2</sub> and then one H<sub>2</sub> extracts the carbidic carbon to form highly active CH<sub>2</sub> species as was proposed for the Fischer-Tropsch reaction. While this might not be the exact mechanism, it is clear that more mechanistic insight could lead to very important inside on how the initial methane activation proceeds. This could be investigated theoretically.

While the work presented in this thesis was still ongoing, a hydrocarbon pool mechanism, which is commonly accepted for the MTH process, was also proposed for the MDA process [13-]

18]. Data supporting this proposal are presented in **Chapter 5**. However, more research is necessary to confirm that the carbonaceous species that accumulate inside the zeolite pores during the induction period are indeed the cause for the asymptotic approach to the maximum of the benzene production rate. In addition, more information is needed about the type of hydrocarbon species that make up this hydrocarbon pool. This could, for example, be achieved by operando UV-Vis or UV Raman experiments. For the MTO process, it is known which hydrocarbon pool species are the main intermediate for inactive coke species. This knowledge was used to design a more selective and coke-resistant catalyst [19, 20]. A similar approach could be taken for MDA, once more knowledge about the hydrocarbon pool species is available. Which hydrocarbons make up the main intermediates of the reaction could be investigated by feeding suggested intermediates directly to the catalyst and comparing the measured selectivity to products with the selectivity obtained when feeding methane.

Although other metals have been investigated for MDA,[21] a systematic comparison of their activity on a metal-atom basis is lacking. For such a comparison, as many parameters as possible need to be kept similar among the different metals. The most important ones are molar amount of metal present on the support and dispersion. Differences in the carburizability of the metal and the geometry of the active site could have a great impact on the performance of the metal.

## References

- [1] N. Kosinov, A.S.G. Wijpkema, E. Uslamin, R. Rohling, F.J.A.G. Coumans, B. Mezari, A. Parastaei, A.S. Poryvaev, M.V. Fedin, E.A. Pidko, E.J.M. Hensen, Confined Carbon Mediating Dehydroaromatization of Methane over Mo/ZSM-5, *Angewandte Chemie*, 57 (2018) 1016-1020.
- [2] O. Bragin, T. Vasina, Y.I. Isakov, B. Nefedov, A. Preobrazhenskii, N. Palishkina, K.M. Minachev, Catalytic aromatization of methane and ethane, *Russian Chemical Bulletin*, 31 (1982) 847-847.
- [3] L. Wang, L. Tao, M. Xie, G. Xu, J. Huang, Y. Xu, Dehydrogenation and aromatization of methane under non-oxidizing conditions, *Catalysis Letters*, 21 (1993) 35-41.
- [4] J. Xue, Y. Chen, Y. Wei, A. Feldhoff, H. Wang, J. Caro, Gas to Liquids: Natural Gas Conversion to Aromatic Fuels and Chemicals in a Hydrogen-Permeable Ceramic Hollow Fiber Membrane Reactor, *ACS Catalysis*, 6 (2016) 2448-2451.
- [5] M. Sakbodin, Y. Wu, S.C. Oh, E.D. Wachsman, D. Liu, Hydrogen-Permeable Tubular Membrane Reactor: Promoting Conversion and Product Selectivity for Non-Oxidative Activation of Methane over an Fe@SiO<sub>2</sub> Catalyst, *Angewandte Chemie*, (2016) n/a-n/a.
- [6] L. Li, R.W. Borry, E. Iglesia, Design and optimization of catalysts and membrane reactors for the non-oxidative conversion of methane, *Chemical Engineering Science*, 57 (2002) 4595-4604.
- [7] M.C. Iliuta, F. Larachi, B.P.A. Grandjean, I. Iliuta, A. Sayari, Methane Nonoxidative Aromatization over Ru-Mo/HZSM-5 in a Membrane Catalytic Reactor, *Industrial & Engineering Chemistry Research*, 41 (2002) 2371-2378.
- [8] S.H. Morejudo, R. Zanón, S. Escolástico, I. Yuste-Tirados, H. Malerød-Fjeld, P.K. Vestre, W.G. Coors, A. Martínez, T. Norby, J.M. Serra, C. Kjølseth, Direct conversion of methane to aromatics in a catalytic co-ionic membrane reactor, *Science*, 353 (2016) 563-566.
- [9] A. Kumar, K. Song, L. Liu, Y. Han, A. Bhan, Absorptive Hydrogen Scavenging for Enhanced Aromatics Yield During Non-oxidative Methane Dehydroaromatization on Mo/H-ZSM-5 Catalysts, *Angewandte Chemie*, 130 (2018) 15803-15808.
- [10] C. Sun, G. Fang, X. Guo, Y. Hu, S. Ma, T. Yang, J. Han, H. Ma, D. Tan, X. Bao, Methane dehydroaromatization with periodic CH<sub>4</sub>-H<sub>2</sub> switch: A promising process for aromatics and hydrogen, *Journal of Energy Chemistry*, 24 (2015) 257-263.
- [11] N. Kosinov, F.J. Coumans, G. Li, E. Uslamin, B. Mezari, A.S. Wijpkema, E.A. Pidko, E.J. Hensen, Stable Mo/HZSM-5 methane dehydroaromatization catalysts optimized for high-temperature calcination-regeneration, *Journal of Catalysis*, 346 (2017) 125-133.
- [12] X. Guo, G. Fang, G. Li, H. Ma, H. Fan, L. Yu, C. Ma, X. Wu, D. Deng, M. Wei, D. Tan, R. Si, S. Zhang, J. Li, L. Sun, Z. Tang, X. Pan, X. Bao, Direct, Nonoxidative Conversion of Methane to Ethylene, Aromatics, and Hydrogen, *Science*, 344 (2014) 616-619.
- [13] E.G. Derouane, J.B. Nagy, P. Dejaive, J.H.C. van Hooff, B.P. Spekman, J.C. Védrine, C. Naccache, Elucidation of the mechanism of conversion of

- methanol and ethanol to hydrocarbons on a new type of synthetic zeolite, *Journal of Catalysis*, 53 (1978) 40-55.
- [14] P.W. Goguen, T. Xu, D.H. Barich, T.W. Skloss, W. Song, Z. Wang, J.B. Nicholas, J.F. Haw, Pulse-Quench Catalytic Reactor Studies Reveal a Carbon-Pool Mechanism in Methanol-to-Gasoline Chemistry on Zeolite HZSM-5, *Journal of the American Chemical Society*, 120 (1998) 2650-2651.
- [15] J.F. Haw, W. Song, D.M. Marcus, J.B. Nicholas, The Mechanism of Methanol to Hydrocarbon Catalysis, *Accounts of Chemical Research*, 36 (2003) 317-326.
- [16] U. Olsbye, M. Bjørgen, S. Svelle, K.-P. Lillerud, S. Kolboe, Mechanistic insight into the methanol-to-hydrocarbons reaction, *Catalysis Today*, 106 (2005) 108-111.
- [17] K. Hemelsoet, J. Van der Mynsbrugge, K. De Wispelaere, M. Waroquier, V. Van Speybroeck, Unraveling the Reaction Mechanisms Governing Methanol-to-Olefins Catalysis by Theory and Experiment, *ChemPhysChem*, 14 (2013) 1526-1545.
- [18] I. Yarulina, A.D. Chowdhury, F. Meirer, B.M. Weckhuysen, J. Gascon, Recent trends and fundamental insights in the methanol-to-hydrocarbons process, *Nature Catalysis*, 1 (2018) 398-411.
- [19] I. Yarulina, S. Bailleul, A. Pustovarenko, J.R. Martinez, K.D. Wispelaere, J. Hajek, B.M. Weckhuysen, K. Houben, M. Baldus, V. Van Speybroeck, F. Kapteijn, J. Gascon, Suppression of the Aromatic Cycle in Methanol-to-Olefins Reaction over ZSM-5 by Post-Synthetic Modification Using Calcium, *ChemCatChem*, 8 (2016) 3057-3063.
- [20] I. Yarulina, K. De Wispelaere, S. Bailleul, J. Goetze, M. Radersma, E. Abou-Hamad, I. Vollmer, M. Goesten, B. Mezari, E.J.M. Hensen, J.S. Martínez-Espín, M. Morten, S. Mitchell, J. Perez-Ramirez, U. Olsbye, B.M. Weckhuysen, V. Van Speybroeck, F. Kapteijn, J. Gascon, Structure-performance descriptors and the role of Lewis acidity in the methanol-to-propylene process, *Nature Chemistry*, 10 (2018) 804-812.
- [21] B.M. Weckhuysen, D. Wang, M.P. Rosynek, J.H. Lunsford, Conversion of Methane to Benzene over Transition Metal Ion ZSM-5 Zeolites, *Journal of Catalysis*, 175 (1998) 338-346.





## **SAMENVATTING & VOORUITBLIK**

## Samenvatting

De voortdurend stijgende mondiale vraag naar aromatische verbindingen als grondstof voor bulkgoederen en onder andere medicijnen geeft een impuls aan onderzoek naar nieuwe productiemethoden van deze waardevolle aromaten. De exploitatie van schaliegas heeft geleid tot een significante prijsverlaging van aardgas, wat het gebruik van gas voor de productie van aromaten aantrekkelijker heeft gemaakt. De dehydroaromatisering van methaan (MDA) is de meest directe route naar aromaten en is in principe zeer efficiënt en selectief indien er geen oxidatiemiddel gebruikt wordt, omdat dan de vorming van bijproducten als CO en CO<sub>2</sub> voorkomen kan worden. Echter, op dit moment is deze directe non-oxidatieve reactie niet industrieel toepasbaar vanwege, naast de bekende significante thermodynamische beperkingen, de zeer snelle deactivering van de katalysator door vorming van coke. De implementatie op grote schaal van het methaan-dearomatiseringsproces kan aanzienlijk versneld worden door ontwikkeling van stabielere en coke-bestendige katalysatoren, alsmede door nieuwe doorbraken op het gebied van procesontwikkeling. Het is daarom belangrijk om de momenteel beste katalysator voor dit proces, Mo/HZSM-5, te verbeteren. Ondanks grote en continue inspanningen in de afgelopen 25 jaar is dit nog niet gelukt en blijft de bekende Mo/HZSM-5-formulering superieur. Dit proefschrift beschrijft de ontwikkeling van fundamentele kennis naar de onderliggende reden van deze uitstekende prestaties ten opzichte van andere systemen. Het doel van dit promotieonderzoek was het identificeren van deze karakteristieke eigenschappen van deze katalysator, welke vervolgens gebruikt kunnen worden voor de ontwikkeling van nieuwe formuleringen. Dit onderzoek is uitgevoerd in twee delen, waarbij het eerste focus is op karakterisering van de bereide katalysatoren en specifieke condities tijdens de bereiding welke invloed hebben op de uiteindelijke werking (**Hoofdstuk 2 en 3**). Deel twee beschrijft het inzicht verkregen door *operando* en *in-situ* karakteriseringssstudies onder relevante reactiecondities.

In **Hoofdstuk 1** wordt beschreven hoe Mo verschillende configuraties aanneemt na introductie op een zeolietdrager. De grote verscheidenheid van geometrieën, nucleariteit, en centra bemoeilijkt interpretatie van spectroscopische analyses en maakt het lastig om specifieke katalytisch actieve centra te duiden. Om deze reden focus **Hoofdstuk 2** op de bereiding van katalysatoren

waarin Mo zich in een specifieke geometrie en locatie bevindt. De geometrie van het Mo-oxide verandert afhankelijk van het aantal Al-atomen waarmee het oxide verankerd is in de drager, en van de exacte locatie van deze Al-ankers, dat wil zeggen, in de rechte of zig-zag kanalen van de MFI-drager, of in hun intersecties. De nabijheid van het Al in de drager is gevarieerd door verschillende syntheseprotocollen te gebruiken. Gemaakte materialen zijn vervolgens geanalyseerd door middel van UV-Vis spectroscopie op Co(II)-iongewisseld zeoliet, waarin dit exclusief plaatsvindt waar een tweetal Al-atomen zich dicht bij elkaar bevinden. Py IR-studies demonstreren dat één of twee zure protonen gewisseld worden met Mo, afhankelijk van de concentratie van Al-paren in het zeoliet. Dit had echter geen significante invloed op katalytische resultaten en leidde daarom tot de conclusie dat zo lang Mo op eenzelfde wijze gedispergeerd is over de drager, de katalytische prestatie vergelijkbaar is in termen van methaanconversie, en opbrengsten van benzeen en naftaleen. Gezien het belang van Mo-dispersie voor het behalen van gunstige katalytische resultaten is in **Hoofdstuk 3** gericht op het kwantificeren van de correlatie tussen Mo-dispersie, zuurgraad, alsmede porositeit en verschillende maatstaven voor katalytische prestaties zoals instantane opbrengst, selectiviteit voor aromaten en cokevorming. Hiervoor is een set van zeventien katalysatoren bereid via negen verschillende synthesetechnieken. Py IR, ICP, en UV-Vis zijn gebruikt om te bepalen hoe nauwkeurig Mo-dispersie bepaald kan worden met deze technieken. Gevonden is dat Mo-dispersie goed meetbaar is met Py IR en beschreven wordt door de reductie van zuurgraad, veroorzaakt door het vervangen van zure protonen met kationische Mo-kernen. Selectiviteit voor naftaleen en benzeen namen lineair toe met de concentratie van zeer goed gedispergeerd kationisch Mo, terwijl selectiviteit voor coke vorming gerelateerd is aan Mo als onderdeel van grotere clusters of nanodeeltjes aan de buitenzijde van het zeolietkristal. Deze bevindingen bevestigen wat tot nu toe voornamelijk gespeculeerd werd in de literatuur. Naast de veelgebruikte porievolume impregnatie ('incipient wetness impregnation') en vaste stof ionenwisseling ('solid state ion exchange') beschrijft dit hoofdstuk het gebruik van 'chemical vapor deposition' (CVD) van  $\text{MoCl}_5$ ,  $\text{MoO}_2\text{Cl}_2$ , en  $\text{Mo}(\text{CO})_6$  als uitgangsmaterialen. Ondanks dat CVD zelden gebruikt wordt ter bereiding van katalysatoren voor MDA leidt het tot zeolieten met zeer gedispergeerde elementen welke bruikbaar zijn voor andere reacties zoals bijvoorbeeld deNOx. Deze techniek leidde initieel tot een katalysator met

verbeterde dispersie en katalytische prestaties in termen van benzeen- en naftaleenopbrengsten, alsmede verminderde selectiviteit voor cokevorming ten opzichte van materialen gemaakt via incipient wetness impregnation. Echter bleek de procedure zeer lastig te reproduceren. Vervolgstudies wezen uit dat de techniek beter werkt wanneer  $\text{MoCl}_5$  als uitgangsmateriaal gebruikt wordt dan  $\text{MoO}_2\text{Cl}_2$  en dat vacuumsublimatie van het materiaal de structuur van het zeoliet negatief beïnvloedt.

Het MDA-proces wordt doorgaans bedreven op hoge temperatuur met een metaal-zeoliet katalysator. Reacties van koolwaterstoffen op zeoliëten kunnen op vele manieren plaatsvinden en leiden daarom tot een gecompliceerd netwerk van reacties. Het feit dat, gezien de thermodynamische limiteringen, het MDA-proces op hoge temperatuur wordt bedreven, leidt tot versnelde reacties en vervolgens ook tot snelle vorming van coke. Daarnaast wordt ook het katalytisch actieve centrum gevormd onder de gebruikte reactieomstandigheden. Dit heeft tot gevolg dat slechts een beperkte hoeveelheid relevante informatie en inzicht geëxtraheerd kan worden uit enkel het analyseren van verse en gebruikte katalysator en het relateren van deze informatie aan katalytische resultaten (**Hoofdstuk 1**). Dit fenomeen is buitengewoon relevant wanneer de katalysator tussen de katalytische test en karakterisering wordt blootgesteld aan de lucht. Een dergelijk effect is ook beschreven in **Hoofdstuk 2**, waarin de verschillende geometrieën van oxidisch Mo in de bereide katalysatoren weinig invloed hadden op katalytische prestaties, vermoedelijk veroorzaakt door significante veranderingen en agglomeratie van Mo centra onder relevante reactiecondities. **Hoofdstuk 4** en **5** beschrijven de uitdaging in het verkrijgen van betekenisvolle karakteriseringsdata. In **Hoofdstuk 4** wordt een alternatieve methode voor het creëren van het katalytisch actieve centrum middels behandeling met CO beschreven. Deze behandeling stabiliseert het actieve centrum voor *quasi-in-situ* karakterisering en is effectief voor het bereiden van een actieve katalysator waar nog geen coke op is afgezet. Dit in tegenstelling tot activering met een atmosfeer van methaan aangezien de vorming van coke simultaan plaatsvindt met vorming van het (oxy-)carbidische actieve centrum tijdens de zogenaamde ‘activeringsperiode’. De stoichiometrie van dit actieve centrum kon worden bestudeerd door gelabeld CO ( $\text{C}^{18}\text{O}$  en  $^{13}\text{CO}$ ) te gebruiken tijdens activering. De behandeling met CO was ook nuttig voor het onderzoeken van de interactie tussen

methaan en koolstof in het actieve centrum. Deze studies zijn uitgevoerd met  $^{13}\text{C}$ -gelabeld CO tijdens activering en ongelabeld  $^{12}\text{CH}_4$  na activering, of *vice versa*. De tijdsresolutie van de experimenten kon worden verbeterd door reacties uit te voeren als een serie pulsen. (Oxy-)carbidisch koolstof gevormd tijdens activering bleek opgenomen te worden in de uiteindelijke reactieproducten, hetgeen duidelijk maakt dat het actieve centrum zeer dynamisch is en dat koolstof in dit centrum een rol speelt in de reactie. Een lineair verband relateert de hoeveelheid koolstof die aanwezig is na activering met de initiële activiteit van katalysatoren met gevarieerde Mo-lading en demonstreert het belang van (oxy-)carbidisch koolstof voor de activering van methaan. Dit wordt verder ondersteund met het feit dat activering met  $\text{H}_2$  niet direct leidde tot een katalysator welke methaan om kon zetten tot aromaten zonder additionele pre-activeringsperiode, een effect dat ook na activering met CO waargenomen kon worden.

*Operando* XAS-metingen beschreven in **Hoofdstuk 4** tonen dat activering met CO leidt tot vorming van een vergelijkbare actief centrum als wanneer activering met methaan wordt uitgevoerd onder reactiecondities. Deze vinding wordt verder ondersteund in **Hoofdstuk 5** door middel van  $^{13}\text{C}$ -NMR en CO IR, hetgeen meer inzicht in de aard van het actieve centrum gaf. Drie verschillende soorten Mo werden geïdentificeerd met CO IR; twee typen Mo verankerd als mono- of dimeer in de poriën van het zeoliet, en één soort die toegewezen kon worden aan grotere Mo clusters aan het oppervlak van het zeolietkristal. Resultaten van CO IR, na vergelijking met DFT-berekeningen, wijzen naar een oxidatietoestand van Mo tussen 4+ en 6+. In **Hoofdstuk 4** konden drie verschillende (oxy-)carbidische Mo-soorten worden geïdentificeerd met  $^{13}\text{C}$ -NMR analyse van  $^{13}\text{CO}$ -geactiveerde katalysatoren. Een hogere resolutie voor de koolstofsignalen kon worden behaald met DNP SENS, hetgeen noodzakelijk was om de drie verschillende bijdragen te kunnen onderscheiden. Gaussische deconvolutie van de  $^{13}\text{C}$  NMR spectra leidde uiteindelijk tot interpreteerbare data. Nadat Mo volledig gedeactiveerd is bereikt de productie van benzeen niet direct het maximum, maar blijft langzaam stijgen tot de maximale productie gedurende de ‘inductieperiode’. De oorzaak van deze inductieperiode is recent toegeschreven aan de opbouw van een koolwaterstofreservoir [1]. Data gepresenteerd in **Hoofdstuk 4** bevestigt dat de opbouw van aromaten gedurende de inductieperiode dezelfde trend volgt als de toename in vorming

van benzeen. Daarnaast bevestigen de resultaten ook dat het actieve centrum, eenmaal gevormd tijdens de activeringsperiode, niet verandert gedurende de inductieperiode. Onveranderde signalen in de  $^{13}\text{C}$  NMR spectra, gemeten direct na activering en op verschillende momenten tijdens de reactie ondersteunen deze conclusie.

## Vooruitblik

Ondanks dat de technische haalbaarheid van conversie van methaan naar aromaten reeds gedemonstreerd werd in 1982[2], zijn er op dit moment nog vele barrières voor commerciële implementatie van het proces. Het Mo/HZSM-5 systeem is, sinds de ontdekking door Wang *et al.* in 1993, het beste katalytische systeem [3]. Sindsdien zijn slechts kleine verbeteringen van deze katalysator bereikt, onder andere door middel van alternatieve synthesemethoden om een hogere dispersie van Mo te behalen, de drager aan te passen, alsmede toevoeging van metalen welke dienen als promotor. Echter, ook na deze verbeteringen blijft de zeer beperkte levensduur van de katalysator en lage omzetting van methaan problematisch. Op dit moment blijft het onduidelijk of innovatieve procesontwikkeling zoals bijvoorbeeld membraan-reactoren[4-8], reactieve verwijdering van waterstof[9], of slimme regeneratietechnieken[10, 11] voldoende zijn om commerciële implementatie van het MDA-proces met het metaal-zeoliet systeem mogelijk te maken. Echter, het is duidelijk dat industriële implementatie aanzienlijk versneld kan worden indien de levensduur van de katalysator kan worden verlengd, waarbij de benzeenopbrengst op het thermodynamisch haalbare maximum gehouden kan worden. Een voorbeeld van een dergelijke doorbraak in methaanconversie werd geclaimd door Guo *et al.* [12]. De katalysator ontwikkeld door Guo *et al.* verschilt drastisch van het Mo/HZSM-5 systeem aangezien het geen Brønsted-zuурte of porositeit bezit. Daarnaast is de katalysator effectief op zeer hoge temperatuur en vertoont deze vrijwel geen vorming van coke. Echter dient dit systeem nog beter bestudeerd te worden en zijn de resultaten op dit moment niet bevestigd door de wetenschappelijke gemeenschap. De ontwikkeling van een volledig nieuw systeem vereist meer inzicht in de relatie tussen katalysatorstructuur en katalytische activiteit voor MDA. Gezien het feit dat zowel procesontwikkeling als de katalysator gepubliceerd door Guo *et al.* buiten het kader van dit

proefschrift vallen wordt hier een vooruitzicht gegeven op basis van ontwikkeling van structuur-activiteit relaties voor de reactie met het metaal-zeoliet systeem. **Hoofdstuk 4** beschrijft dat carbidisch koolstof in het actieve katalysatorcentrum een belangrijke rol speelt in de activering van methaan gezien het feit dat de initiële activiteit lineair gecorreleerd is aan de hoeveelheid carbidisch koolstof in de katalysator. Daarnaast werd koolstof afkomstig van het actieve centrum gevonden in het uiteindelijke reactieproduct. Er kan gespeculeerd worden dat methaan in feite eerste geactiveerd wordt via vorming van carbidisch koolstof en twee moleculen H<sub>2</sub>, waarna één molecuul H<sub>2</sub> het carbidisch koolstof extraheert en reageert tot een zeer reactief CH<sub>2</sub>-fragment, vergelijkbaar met voorstellen voor de Fischer-Tropsch reactie. Hoewel dit wellicht niet het exacte mechanisme is, blijft het duidelijk dat inzicht in het reactiemechanisme kan leiden tot zeer belangrijk begrip in hoe activering van methaan plaatsvindt. Een dergelijk mechanisme kan door middel van simulaties bestudeerd worden. Gedurende het werk beschreven in dit proefschrift werd een mechanisme met een koolwaterstofreservoir, zoals geaccepteerd voor het MTH-proces, tevens voorgesteld voor de MDA-reactie [13-18]. Ondersteunende data voor dit voorstel zijn beschreven in **Hoofdstuk 5**. Er is echter meer onderzoek nodig om te bevestigen dat koolstof dat accumuleert in de zeolietporiën verantwoordelijk is voor de asymptotische stijging dat uiteindelijk leidt tot de maximale vorming van benzeen. Daarnaast is het belangrijk dat meer informatie vergaard wordt betreffende de aard van de koolwaterstoffen in dit koolwaterstofreservoir, hetgeen bereikt kan worden door middel van, bijvoorbeeld, *operando* UV-Vis or UV Raman studies. Voor het MTO-proces is het bekend welke koolstoffragmenten in het koolwaterstofreservoir leiden tot inactieve vormen van coke. Dit inzicht is vervolgens toegepast in de ontwikkeling van een selectievere en coke-bestendige katalysator [19, 20]. Op het moment dat inzicht in de compositie van het koolwaterstofreservoir beschikbaar is kan een vergelijkbare methode toegepast worden voor het MDA-proces. Een dergelijke studie kan uitgevoerd worden door de belangrijkste intermediairen te voeden aan de katalysator en de selectiviteit voor zekere reactieproducten te vergelijken met de selectiviteit voor diezelfde producten wanneer het proces uitgevoerd wordt met methaan als voeding.

Ondanks dat andere metalen onderzocht zijn voor MDA[21] is een systematische vergelijking van de katalytische activiteit van

verschillende metalen momenteel niet beschikbaar. Voor een dergelijke studie is het belangrijk dat zo veel mogelijk parameters onveranderd blijven, waarbij de meest belangrijke parameters de molaire hoeveelheid van het metaal op de drager en de dispersie daarvan zijn. Het is mogelijk dat verschillen in carburiseringseigenschappen van het metaal en de specifieke geometrie van het actieve centrum een significante invloed hebben op de katalytische prestaties van het metaal.

## Literatuur

- [1] N. Kosinov, A.S.G. Wijpkema, E. Uslamin, R. Rohling, F.J.A.G. Coumans, B. Mezari, A. Parastaev, A.S. Poryvaev, M.V. Fedin, E.A. Pidko, E.J.M. Hensen, Confined Carbon Mediating Dehydroaromatization of Methane over Mo/ZSM-5, *Angewandte Chemie*, 57 (2018) 1016-1020.
- [2] O. Bragin, T. Vasina, Y.I. Isakov, B. Nefedov, A. Preobrazhenskii, N. Palishkina, K.M. Minachev, Catalytic aromatization of methane and ethane, *Russian Chemical Bulletin*, 31 (1982) 847-847.
- [3] L. Wang, L. Tao, M. Xie, G. Xu, J. Huang, Y. Xu, Dehydrogenation and aromatization of methane under non-oxidizing conditions, *Catalysis Letters*, 21 (1993) 35-41.
- [4] J. Xue, Y. Chen, Y. Wei, A. Feldhoff, H. Wang, J. Caro, Gas to Liquids: Natural Gas Conversion to Aromatic Fuels and Chemicals in a Hydrogen-Permeable Ceramic Hollow Fiber Membrane Reactor, *ACS Catalysis*, 6 (2016) 2448-2451.
- [5] M. Sakbodin, Y. Wu, S.C. Oh, E.D. Wachsman, D. Liu, Hydrogen-Permeable Tubular Membrane Reactor: Promoting Conversion and Product Selectivity for Non-Oxidative Activation of Methane over an Fe@SiO<sub>2</sub> Catalyst, *Angewandte Chemie*, (2016) n/a-n/a.
- [6] L. Li, R.W. Berry, E. Iglesia, Design and optimization of catalysts and membrane reactors for the non-oxidative conversion of methane, *Chemical Engineering Science*, 57 (2002) 4595-4604.
- [7] M.C. Iliuta, F. Larachi, B.P.A. Grandjean, I. Iliuta, A. Sayari, Methane Nonoxidative Aromatization over Ru-Mo/HZSM-5 in a Membrane Catalytic Reactor, *Industrial & Engineering Chemistry Research*, 41 (2002) 2371-2378.
- [8] S.H. Morejudo, R. Zanón, S. Escolástico, I. Yuste-Tirados, H. Malerød-Fjeld, P.K. Vestre, W.G. Coors, A. Martínez, T. Norby, J.M. Serra, C. Kjølseth, Direct conversion of methane to aromatics in a catalytic co-ionic membrane reactor, *Science*, 353 (2016) 563-566.
- [9] A. Kumar, K. Song, L. Liu, Y. Han, A. Bhan, Absorptive Hydrogen Scavenging for Enhanced Aromatics Yield During Non-oxidative Methane Dehydroaromatization on Mo/H-ZSM-5 Catalysts, *Angewandte Chemie*, 130 (2018) 15803-15808.
- [10] C. Sun, G. Fang, X. Guo, Y. Hu, S. Ma, T. Yang, J. Han, H. Ma, D. Tan, X. Bao, Methane dehydroaromatization with periodic CH<sub>4</sub>-H<sub>2</sub> switch: A promising process for aromatics and hydrogen, *Journal of Energy Chemistry*, 24 (2015) 257-263.
- [11] N. Kosinov, F.J. Coumans, G. Li, E. Uslamin, B. Mezari, A.S. Wijpkema, E.A. Pidko, E.J. Hensen, Stable Mo/HZSM-5 methane dehydroaromatization catalysts optimized for high-temperature calcination-regeneration, *Journal of Catalysis*, 346 (2017) 125-133.
- [12] X. Guo, G. Fang, G. Li, H. Ma, H. Fan, L. Yu, C. Ma, X. Wu, D. Deng, M. Wei, D. Tan, R. Si, S. Zhang, J. Li, L. Sun, Z. Tang, X. Pan, X. Bao, Direct, Nonoxidative Conversion of Methane to Ethylene, Aromatics, and Hydrogen, *Science*, 344 (2014) 616-619.
- [13] E.G. Derouane, J.B. Nagy, P. Dejaifve, J.H.C. van Hooff, B.P. Spekman, J.C. Védrine, C. Naccache, Elucidation of the mechanism of conversion of methanol and ethanol to hydrocarbons on a new type of synthetic zeolite, *Journal of Catalysis*, 53 (1978) 40-55.
- [14] P.W. Goguen, T. Xu, D.H. Barich, T.W. Skloss, W. Song, Z. Wang, J.B. Nicholas, J.F. Haw, Pulse-Quench Catalytic Reactor Studies Reveal a Carbon-Pool Mechanism in

- Methanol-to-Gasoline Chemistry on Zeolite HZSM-5, Journal of the American Chemical Society, 120 (1998) 2650-2651.
- [15] J.F. Haw, W. Song, D.M. Marcus, J.B. Nicholas, The Mechanism of Methanol to Hydrocarbon Catalysis, Accounts of Chemical Research, 36 (2003) 317-326.
- [16] U. Olsbye, M. Bjørgen, S. Svelle, K.-P. Lillerud, S. Kolboe, Mechanistic insight into the methanol-to-hydrocarbons reaction, Catalysis Today, 106 (2005) 108-111.
- [17] K. Hemelsoet, J. Van der Mynsbrugge, K. De Wispelaere, M. Waroquier, V. Van Speybroeck, Unraveling the Reaction Mechanisms Governing Methanol-to-Olefins Catalysis by Theory and Experiment, ChemPhysChem, 14 (2013) 1526-1545.
- [18] I. Yarulina, A.D. Chowdhury, F. Meirer, B.M. Weckhuysen, J. Gascon, Recent trends and fundamental insights in the methanol-to-hydrocarbons process, Nature Catalysis, 1 (2018) 398-411.
- [19] I. Yarulina, S. Bailleul, A. Pustovarenko, J.R. Martinez, K.D. Wispelaere, J. Hajek, B.M. Weckhuysen, K. Houben, M. Baldus, V. Van Speybroeck, F. Kapteijn, J. Gascon, Suppression of the Aromatic Cycle in Methanol-to-Olefins Reaction over ZSM-5 by Post-Synthetic Modification Using Calcium, ChemCatChem, 8 (2016) 3057-3063.
- [20] I. Yarulina, K. De Wispelaere, S. Bailleul, J. Goetze, M. Radersma, E. Abou-Hamad, I. Vollmer, M. Goesten, B. Mezari, E.J.M. Hensen, J.S. Martínez-Espín, M. Morten, S. Mitchell, J. Perez-Ramirez, U. Olsbye, B.M. Weckhuysen, V. Van Speybroeck, F. Kapteijn, J. Gascon, Structure–performance descriptors and the role of Lewis acidity in the methanol-to-propylene process, Nature Chemistry, 10 (2018) 804-812.
- [21] B.M. Weckhuysen, D. Wang, M.P. Rosynek, J.H. Lunsford, Conversion of Methane to Benzene over Transition Metal Ion ZSM-5 Zeolites, Journal of Catalysis, 175 (1998) 338-346.

## ACKNOWLEDGEMENTS

Before I started my PhD, I asked other PhDs how it is to do one. I think the description I most agree with is a rollercoaster. There are extreme lows in your PhD that are so low that you can often not get out of them without the support of your loved ones or valuable advice from your professional mentors and colleagues. There are also extreme highs that scream for celebration and it is wonderful to have people around that are happy for and with you and who are proud of you. Shared joy is double the joy. Rollercoasters can also be extremely scary and you need people who continuously push you to ride it again and again and to believe in yourself. I consider myself extremely lucky that I had so many people around me that not only helped me to survive the rollercoaster, but who also served as constant inspiration and taught me so much.

Jorge Gascon and Freek Kapteijn, you deserve a big 'Thank you!' as the enablers of my thesis and constant support throughout my PhD work, reading, correcting and editing my work even on weekends and during conference travels. My promoter, Freek welcomed me to the group, already inviting me to the group's new year's dinner before I even joined. I want to thank you for challenging me with the difficult questions, being very attentive for all scientific details to be correct. Jorge Gascon, you always offered an open door, even after you already moved to Saudi Arabia. You taught me how to think big and that even crazy sounding ideas often work and also to take a step back, to not get lost in the details.

I am convinced that nothing is possible without our technicians in CE. Bart is so handy that I don't think there is anything that he cannot fix. I also enjoyed discussing my results with you. You taught me how to approach troubleshooting with great calm and efficiency. And Bart, can you please, someday reveal your secret of staying so calm with so many completely hysterical PhDs around? Harrie Jansma helped me a lot in the beginning of my PhD. Harrie, thank you for all the very neat tubing and heat-tracing. Willy Rook, you seem to memorize any adsorption isotherm you ever measured. Thank you for always helping me. Liliana Baron, you are wonderfully cheerful and problems seem very small after discussing them with you. You are great for getting ideas on how to solve issues in the lab and also a great person to talk to. It would have been even better, if you would have started earlier in our group. A big thanks also goes to Els Arkesteijn for making bureaucratic matters at least manageable and answering all my stupid questions about

## ACKNOWLEDGEMENTS

digiforms. And thank you, Caroline Monna for sending countless packages.

My PhD project would not have been possible without the support of SABIC and the great discussion we had with the people working there as well as the other project partners from TU Eindhoven. I especially want to thank Christoph Dittrich for managing the project from the SABIC side and his scientific input as well as being part of my defense committee. Alexander Nijhuis, I want to thank you for our nice conversations over lunch and coffee at the ACS meeting in New Orleans and your career advice as well as for your scientific input and for always asking difficult questions at the project meetings. Thanks also goes to Frank Mostert. Emiel Hensen, I want to thank you for all your support during the project, for letting me come to Eindhoven and use the equipment there and for giving advice on the obtained results. Special thanks goes to Nikolai Kosinov for teaching me a lot about zeolites, how to properly conduct catalytic experiments and other characterization techniques.

Several people from the CE group helped me during my PhD and most of them also became my friends. One of the most knowledgeable people I know is Alma Olivos Suárez. I want to thank you for all your chemistry insight, for teaching me the basics of synchrotron measurements, for always knowing yet another technique I could use to characterize my system and for helping me organize my papers. Finally, I want to thank you for a great friendship. Ági Szécsényi helped me a lot with doing theoretical calculations. Ági as an officemate and friend, you always put things in perspective. Thank you for that and for being super fun to be around especially during NIOK courses, conferences, summer schools and crochet club. Guanna Li, thank you for adding the theory backbone to my papers, teaching me everything I know about DFT. You are a great teacher and I am sure you will be a great professor. Thank you also for your positive words and for being a great friend and officemate.

My PhD rollercoaster was kind of derailed into the nearest pool, when I started to work more closely with IRina Yarulina. A very, very special thanks goes to you for teaching me all I know about IR and zeolites and for helping me write my articles. You are always full of ideas and enthusiasm. Thanks for being a great mentor and friend.

Anastasiya Bavykina, you were my first go-to person in the group. As my officemate you were always there to help orient myself in the group. Thank you also for all the support at KAUST

## ACKNOWLEDGEMENTS

and for the fun we had at the crochet clubs. Early on in my PhD, Martijn de Lange taught me how to conduct gravimetric adsorption and I thank him for that. Thank you, María José Valero-Romano for scientific discussion and for letting me collaborate with you.

There are also many people I have to thank because they really made me feel comfortable in CE. Lide Oar-Arteta Gonzalez, my Yoga and gym companion. Jara García-Santaclara with her cheerful attitude, seemingly doing her PhD easily, an organization and management talent. Eduardo for being the social driver of the group. Robert Franz, thank you for making me look less German and for being a great person to talk to. Chuncheng Liu, you are a fun person to teach and discuss things with. Good luck for your PhD. Dmitrii Osadchii as a very eccentric person always supplying me with chocolate. Thanks goes to everyone in CE. And I also want to thank Annika Krieger and Elena Khramenkova from ISE, who are always able to cheer me up by going to ballet shows or coffee with oat-milk at the Fellowship. And I especially thank you, Robbert Putten, for first of all translating the 'Summary & Outlook' in this thesis to Dutch. I also thank you for always being able to lift the mood in the room.

My Master, Bachelor and Erasmus students, Rommy Gobardhan, Zhimian Hao, Chenkun Long, Alberto Falcone, Yuri G. Sneider and Amanrita Mondal deserve lots of thanks for helping me a lot in the lab. I wish you all the best for the future.

During my PhD, I also collaborated with several people. Evgeny Pidko, thank you for your computational expertise and letting me use one of your VASP accounts. Thank you Georgy Filonenko for helping me with IR measurements.

I feel a very deep gratitude for my parents. I want to thank my mother, Annette Vollmer for all her support and love. Thank you for always believing in me, helping me when I had to make difficult decisions and teaching me how to write good motivation letters. Thank you dad for raising curiosity in me early on and always explaining how things work. Thank you Dirk for being the warm, welcoming and relaxed person that you are. I'm still trying to manage to stay as calm as you even when there is soooo much important work to do.

During most of my PhD I lived with my brother René Vollmer, who always was very supportive and to my surprise is also thinking about doing a PhD. René, I am convinced you can understand and structure anything. Isabell Trinh also lived with us. Isa, you are a design talent. Thank you both for helping me

## **ACKNOWLEDGEMENTS**

with my presentations and hugging me when I was down. I also want to thank my roommates Pablo, Daniel and Stefano for making our house the warm and lively place, which I enjoy coming home to.

I also want to thank my friends. Raphael Sprenger, I am so happy that you decided that Rotterdam is so much cooler than Düsseldorf. Our party nights were pure medicine. Thanks also goes to Manuel Baumann and Anton Kidess.

Finally, I want to thank my boyfriend, Lennart Budelmann. Lennart thank you for being ready for any adventure and making it super easy to forget the troubles of PhD-dom. You are not only a great support, but also a great inspiration.

## LIST OF PUBLICATIONS AND PRESENTATIONS

### Publications related to this thesis

- I. Vollmer, G. Li, I. Yarulina, N. Kosinov, E.J. Hensen, K. Houben, D. Mance, M. Baldus, J. Gascon, F. Kapteijn, Relevance of the Mo-precursor state in H-ZSM-5 for methane dehydroaromatization, Catalysis Science & Technology, **8** (2018) 916-922.
- I. Vollmer, B. van der Linden, S. Ould-Chikh, A. Aguilar-Tapia, I. Yarulina, E. Abou-Hamad, Y.G. Sneider, A.I. Olivos Suarez, J.-L. Hazemann, F. Kapteijn, J. Gascon, On the dynamic nature of Mo sites for methane dehydroaromatization, Chemical Science, **9** (2018) 4801-4807.
- I. Vollmer, I. Yarulina, F. Kapteijn, J. Gascon, Progress in Developing a Structure-Activity Relationship for the Direct Aromatization of Methane, ChemCatChem, **11** (2019) 39-52.
- I. Vollmer, N. Kosinov, A. Szécsényi, G. Li; I. Yarulina, E. AbouHamad, A. Gurinov, S. Ould-Chikh, A. Aguilar; J-L. Hazemann, E. Pidko, E. Hensen, F. Kapteijn, J. Gascon, A site-sensitive quasi-in situ strategy to characterize Mo/HZSM-5 during activation, Journal of Catalysis, **370** (2019) 321-331.
- I. Vollmer, A. Mondal, I. Yarulina, E. Abou-Hamad, F. Kapteijn, J. Gascon, Quantifying the impact of dispersion, acidity and porosity of Mo/HZSM-5 on the performance in methane dehydroaromatization, Applied Catalysis A: General, **574** (2019) 144-150.
- I. Vollmer, B. van der Linden, S. Ould-Chikh, A. Aguilar-Tapia, I. Yarulina, E. Abou-Hamad, Y.G. Sneider, A.I. Olivos Suarez, J.-L. Hazemann, F. Kapteijn, J. Gascon, Operando XAS observation of Mo transforming to its active phase for converting methane to aromatics, ESRF Highlights 2018, (2019), accepted

# LIST OF PUBLICATIONS AND PRESENTATIONS

## Other publications

N. Kosinov, A. Parastaev, A.S.G. Wijpkema, I. Vollmer, J. Gascon, F. Kapteijn, E.J.M. Hensen, Comment on "Efficient Conversion of Methane to Aromatics by Coupling Methylation Reaction", ACS Catalysis, **7** (2017) 4485-4487.

I. Yarulina, K. De Wispelaere, S. Bailleul, J. Goetze, M. Radersma, E. Abou-Hamad, I. Vollmer, M. Goesten, B. Mezari, E.J.M. Hensen, J.S. Martínez-Espín, M. Morten, S. Mitchell, J. Perez-Ramirez, U. Olsbye, B.M. Weckhuysen, V. Van Speybroeck, F. Kapteijn, J. Gascon, Structure–performance descriptors and the role of Lewis acidity in the methanol-to-propylene process, Nature Chemistry, **10** (2018) 804-812.

## Presentations

I. Vollmer, N. Kosinov, E. Hensen, J. Gascon, F. Kapteijn, Geometry of Molybdenum Oxide in HZSM-5 Does Not Influence Its Activity for the Aromatization of Methane, NCCC XVIII, Noordwijkerhout, the Netherlands, March 2017 (*oral*)

I. Vollmer, S. Ould-Chikh, A. Aguilar-Tapia, I. Yarulina, E. Abou-Hamad, J-L. Hazemann, Freek Kapteijn and Jorge Gascon On the Dynamic Nature of Mo sites for Methane Dehydroaromatization, KCC Symposium, King Abdullah University of Science and Technology, Saudi Arabia, January 2018 (*poster*)

I. Vollmer, B. van der Linden, S. Ould-Chikh, A. Aguilar-Tapia, I. Yarulina, E. Abou-Hamad, Y. G. Sneider, A. I. Olivos Suarez, J-L. Hazemann, F. Kapteijn, J. Gascon, On the dynamic nature of Mo sites for Methane Dehydroaromatization, 255th ACS National Meeting, New Orleans, United States, March 2018 (*oral*)

I. Vollmer, B. van der Linden, S. Ould-Chikh, A. Aguilar-Tapia, Y. G. Sneider, I. Yarulina, A. I. Olivos Suarez, J-L. Hazemann, F. Kapteijn, J. Gascon, On the Dynamic Nature of Mo sites for Methane Dehydroaromatization, TOCAT8, Yokohama, Japan, August 2018 (*oral*)

I. Vollmer, S. Ould-Chikh, A. Aguilar-Tapia, J-L. Hazemann, J. Gascon, F. Kapteijn, Activity descriptors derived from comparison of Mo and Fe as active metal for methane conversion to aromatics, CHAINS, Veldhoven, the Netherlands, December 2018 (*oral*)

I. Vollmer, F. Kapteijn, J. Gascon, Ethylene – the main intermediate of the methane dehydroaromatization reaction?, NCCC XX, Noordwijkerhout, the Netherlands, March 2019 (*oral*)

## **LIST OF PUBLICATIONS AND PRESENTATIONS**

### **Awards**

NIOK Lecture Award for the best lecture presented during the Netherlands' Catalysis and Chemistry Conference, Noordwijkerhout, the Netherlands, March 2018

'Best Presentation' of the session for the lecture entitled 'On the dynamic nature of Mo sites for me-thane dehydroaromatization', 255<sup>th</sup> ACS National Meeting, New Orleans, United States, March 2018

## ABOUT THE AUTHOR



**Ina Vollmer** was born on the 19<sup>th</sup> of July 1990 in Freiburg i. Br., Germany. She later moved to the German city of Hamburg, and graduated with a high school diploma from Wiechern-Schule in 2009. After spending the summer in Tanzania to teach 1<sup>st</sup> and 3<sup>rd</sup> grade students, she started a B. Sc. in Verfahrenstechnik (process engineering) at Hamburg University of Applied Sciences with a scholarship from the Studienstiftung des Deutschen Volkes (German Scholarship Foundation).

For her final Bachelor's project she studied zeolite heat pumps at the Fraunhofer Institute in Stuttgart.

After completion of the B. Sc. degree, she continued with an M. Sc. E. P. at Massachusetts Institute of Technology in August 2013. There she completed the Practice School Program which concluded with four consulting projects, two one-month projects at Corning and two at General Mills. During her university studies, she also completed a degree in journalism with a scholarship from the journalism education program of the Konrad-Adenauer foundation. This included several internships at news outlets in Brazil, Thailand and Germany.

On the 1<sup>st</sup> of February 2015, she started her PhD project at the Delft University of Technology under the supervision of Freek Kapteijn and Jorge Gascon. In this booklet you can read in detail about her work on methane dehydroaromatization over the Mo/HZSM-5 catalyst.